Physics of the early universe: non-singular cosmologies and multifield inflation

Swansea University
Prifysgol Abertawe

Roberta Chiovoloni

Department of Physics

Swansea University

Submitted to Swansea University in fulfillment
of the requirements for the degree of

Doctor of Philosophy

2022

Declaration

This work has not previously been accepted in substance for any degree and is not being concurrently submitted for any degree.

Signed: [redacted] (candidate)

Date: 18th May 2022

This thesis is the result of my own investigations, except where otherwise stated. Where correction services have been used, the extent and nature of the correction is clearly marked in a footnote(s). Other sources are acknowledged by footnotes giving explicit references. A bibliography is appended.

Signed: [redacted] (candidate)

Date: 18th May 2022

I hereby give consent for my thesis, if accepted, to be available for photocopying and for inter-library loan, and for the title and summary to be made available to outside organisations.

Signed: [redacted] (candidate)

Date: 18th May 2022

The University's ethical procedures have been followed and, where appropri-

ate, that ethical approval has been granted.

Signed: . [redacted] .. (candidate)

Date: 18th May 2022 .....

Contents

Acknowledgements

Firstly, I'd like to express my deepest gratitude to my supervisor Ivonne Zavala for her guidance and support over the last four years. I am really grateful for the opportunity you gave me to be part of the Swansea Cosmology Group and for the numerous insightful discussions and precious suggestions.

I would also like to thank Giovanni Montani, my former supervisor, who more often than not believed in me more than myself. You helped me to grow as a researcher and more importantly as a person, and I am incredible thankful for that. I feel privileged to have had the opportunity to continue working with you during these last years.

Grazie agli amici dell'Università, Frances, Lorenzo, Matteo, Michele e Chiara, per il supporto, le risate e i consigli.
Grazie a Sparta, Dario, Federica, Ginevra e Chiara, per esserci sempre, indipendentemente dal come, dove e quando.

Thanks to John for making me feel at home in Wales and for always giving me a reason to smile (and yes, also for your morning rhymes).

Grazie a mamma, per il supporto incondizionato e i pacchi da giù.

Grazie pà.

List of Figures

LIST OF FIGURES

Chapter 1

Introduction

Cosmology, in very few words, is the study of the Universe and its evolution, from its very first moments to its possible end. It is an incredible old science which came to life through humans' inherent curiosity to understand the world around them. Our approach to this science has changed massively over millennia before being formalised into its current model

Egyptians and Mesopotamians were among the first civilizations to keep records of stars and constellations, but, as it could be expected, their interpretation of astronomical phenomenons and their origins relied heavily on creation myths and traditionalistic beliefs.

A more intellectual approach, partially based on astronomical evidence, debate and reason was at the foundation of Greek philosophy. Aristarchus, Aristotle and Hipparchus are a few of the many great thinkers who spent their life investigating the *cosmological problem*; the advent of modern mathematics (with Pythagoras) and the use of both observations and experimentation are the underlying themes in the Greek Geometrical Cosmology. During the Hellenistic era, thanks to the advancement of numerous observational techniques, the first rudimentary heliocentric model of a spherical Earth was proposed.

However the strong religious influence and the limited experimental and observational capability slowed the evolution of Cosmology, confining it to (mostly) the area of Astronomy until more recent times. It is only after the scientific revolution, thanks to Copernicus, Kepler, Galileo and Newton, that the Universe can finally be considered as an environment where physical laws, formulated in

a mathematical language, are the same everywhere. Yet the law of the static gravitational field together with the idea of an infinite Universe still presented some problems when implemented to explain the beginning of the Universe[1].
Modern Cosmology officially began with the publication, in 1915, of Einstein's theory of General Relativity. Since then, our understanding of the history of the Universe has seen an unprecedented growth thanks to the development of new theories and the advent of new technologies which have exponentially improved our ability to collect data.
The Standard Cosmological model, or ΛCDM, is, as of today, the most widely accepted cosmological model used to describe the history of the Universe. According to this model, which has been confirmed by data[2], our Universe started in an incredibly hot and dense state (*Hot Big Bang*) and expanded to produce the observable Universe. However, there are several aspects of the ΛCDM model which are not well understood yet. For example, in order to explain today flatness, isotropy and homogeneity, the Universe is required to start with very particular initial conditions.

Starting from the '80s scientists realized that this problem could be solved introducing an early de Sitter phase of exponential expansion in the very early Universe, which takes the name of *inflation*. The most basic inflationary paradigm predicts that the exponential expansion is driven by the energy density of one or more scalar fields, called inflatons, rolling down a potential. It has been estimated, thanks to direct measurements on the Cosmic Microwave Background (CMB), that the energy scale of this mechanism is around $\sim 10^{16} Gev$. Unfortunately, even if in the last decades inflation has been one of the most widely studied phenomenon in cosmology, we still do not know how it happened. In fact different inflationary scenarios lead to very similar predictions: in particular current data do not allow us to discern between single or multifield models. To make any progress in this direction we have to wait for accurate measurements of primordial

[1] Olbers paradox, formulated in 1896 is probably the most famous problem in this sense. He questioned how it is possible that the sky is dark at night if the Universe is infinite and therefore filled with an infinite number of stars.

[2] This model agrees with measures of the current acceleration, with measures of the the Cosmic Microwave Background (CMB) and with the maps of the distributions of large scale structure

non-gaussianities or large scale structures; single field and multifield models of inflation behave very differently and produce distinctive signatures which would help us to determine how many scalars were involved during the expansion.
Until we can obtain these measurements, much of the modern day research focuses on more complex multifield models, with particular attention to non-geodesic models, for different reasons. A major advantage afforded to us is that these types of models can be easily embedded into UV theories, which is interesting given the high energy scale involved in inflation, they do satisfy recently proposed consistency conjectures and they do not require incredibly flat potentials.
The research presented in the first part of this thesis is conducted within this theoretical context. We focus on non-geodesic multifield models of inflation and the conditions needed for their realizations.

In the second part of the thesis we analyse an often overlooked consequence of the inflationary mechanism: the possibility to have general cosmologies near the singularity. In fact as recalled above, the theory of inflation, independently on how it is realised, solves the problem of the initial conditions of the ΛCDM flattening and homogenising the Universe just few moments after its beginning. As a consequence, it allows us to discuss the evolution of the Universe near the singularity, i.e. before the exponential expansion, under more general hypothesis than homogeneity and isotropy. In the last chapters we address the dynamical evolution of general cosmologies, the Bianchi models and inhomogeneous Universes, near the singularities under the semi-classical approximation.

The outline of the thesis is as follow:

1. In Chapter 2 we present an overview of modern cosmology and the inflationary theory. We discuss single field and multifield models dynamics and we conclude the chapter showing how the latters can be embedded in a high energy theory.

2. In Chapter 3 we present part of the work published in [6]. Here we derive the fat inflation attractor, a novel way to avoid the η-problem in the context of multifield inflation, where the masses of the scalar fields are heavier than the Hubble scale.

3. In Chapter 4 we present the work published in [7]. Here we focus on supergravity multifield models and we show how, while in the literature seems to be quite difficult to find models which present large turning rate, it is actually possible to construct strongly non-geodesic trajectories when two fields are orthogonal.

4. In Chapter 5 we introduce the ADM formalism, the Hamiltonian formulation of the dynamics, we briefly comment on the Wheeler-DeWitt equation and we present the Vilenkin approach to the wave function of the Universe. In the second part we review the generic cosmologies: the Bianchi models, which are homogeneous and anisotropic, and the more general inhomogeneous and anisotropic models.

5. In Chapter 6 we present the work published in [8]. Here we analyse the dynamical evolution of the Bianchi IX model in the "corner configuration" applying the Vilenkin approach. We show that, depending on the specific case analysed, the corner configurations can act as an attractor, can remove the singularity or can suppress the anisotropies.

6. In Chapter 7 we present the work published in [9], which is a follow-up of [8]. Here we develop a scenario for the emergence of a non-singular generic cosmological solution using the Vilenkin approach in the "corner configuration".

In Appendix A we present a brief summary for the computation of primordial fluctuations in single field models. Appendix B contains a table related to the results presented in Chapter 4 and in Appendix C we formulate the General Kasner solution for the inhomogeneous Mixmaster model. Finally, Appendix D contains a summary of the work done during the industrial placement at Mobileum. This is not related to the research done but it is an integral part of the PhD.

In this thesis we work in natural units, i.e $\hbar = c = 1$, unless otherwise stated, and we use the reduced Planck mass $M_{\rm Pl} \equiv 1/\sqrt{8\pi G_N}$.

Chapter 2

Inflationary Cosmology

In this chapter we review the state of modern cosmology discussing the Standard Cosmological Model (SCM) and the Inflationary paradigm. In particular, we start by reviewing the SCM and we show how, while it seems to perfectly describe the Universe and account for Hubble discovery of the cosmic expansion, it presents three major shortcomings. In the second part of the Chapter we introduce the inflationary paradigm, giving a brief historical overview, presenting its main features and showing how this exponential expansion can solve the problems of the SCM. We then discuss single field models, introducing the slow-roll conditions and describing how inflation proves to be a suitable mechanism to explain the origin of the Large Scale Structures.
After explaining some of the reasons which lead us to extend our studies behind the vanilla single field models, we introduce multifield models of inflation. The slow-roll conditions in this case prove to be more complex than in the previous case, and we analyse in detail the reason behind that. To conclude this discussion we show how these models can solve recently proposed consistency conjectures.
In the last part of the Chapter we quickly review how to embed multifield models in a supergravity framework and we discuss the η-problem in both field theory and supergravity.

2.1 Standard model of cosmology and its shortcomings

The Standard Cosmological Model (SCM), is the most widely accepted cosmological model of the Universe: it accounts for the evolution of the Universe from few moments after the Big Bang up to today.
This model is based on two main assumptions:

- the *cosmological principle*, which asserts that the Universe is homogeneous and isotropic at large scales[1].
- the universality of the physical laws.

According to this model the Universe expanded from a very hot and dense state 13.8 billion years ago.
However, this seemingly perfect cosmological model fails to provide an explanations for the almost perfect homogeneity and isotropy of the Universe at early times, the initial density perturbation and the incredibly small value of the flatness constant that we measure today. These open problems are what we refer to as the *shortcoming* of the SCM, and they are the reasons that brought scientists, between the end of the '70s and the early '80s, to develop the idea of an early phase of inflationary expansion.

In this section we briefly review the SCM model, introducing the Hubble law and the Friedmann equations and we discuss the main shortcomings mentioned above.

2.1.1 The expanding Universe and Friedmann equations

A turning point for the establishment of Cosmology as the science that we know today, has been the realization that the Universe is, contrary to what Einstein thought, *not* static.
In 1929 [10] E.Hubble was able to derive a relation between the spectral shifts

[1] One of the reason for its introduction was the Copernican Principle, according which the Earth does not occupy a special place in the Universe.

and the distances of a sample of 50 galaxies; in particular he observed that there is a *linear* relation between the recession period of a galaxy and its distance from us. This result, which today is known as *Hubble law*, can be written simply as

$$v = H(t)d \tag{2.1}$$

where v is the recession velocity of the galaxy, d is its distance and $H(t)$ is a proportional parameter called *Hubble parameter*. This equation, which since then has been tested with improved accuracy, established once and for all that we live in a dynamical Universe where distances increase with time. In particular, it tells us that not only galaxies and other astronomical objects recede from us, but the further away they are, the fastest they recede. This discovery led to the development of *The Big Bang theory*, which describes the evolution of the Universe from few instants after its birth until now.
The exact value of the Hubble parameter today, $H(t_0) = H_0$, is still object of discussion, and there are numerous experiments at work to solve this puzzle, see e.g.[11–14] and others and see [15] for a review. The current estimation, according to the last data from Planck [16] is given by $H_0 = (67.4 \pm 0.5) Km/s/Mpc$.

When Hubble published his paper, the only known solution for the Einstein Equations for a non-empty expanding Universe was the one already found independently by Friedmann in 1922 [17] and Leimatrè in 1927 [18] (for the english version see [19]). Both these solutions relied on two assumptions: an expanding and matter-filled cosmological model and the *cosmological principle*.
A decade later, in 1935 and 1937, Robertson and Walker demonstrated, respectively in [20] and [21] that the solution proposed by Friedmann was the most general possible in a spacetime with the symmetries imposed by the cosmological principle. Today we refer to this solution of the Einstein Equations as the *Friedman-Laimatrè-Robertson-Walker* (FLRW) metric

$$ds^2 = -dt^2 + a^2(t) \left[\frac{dr^2}{1 - Kr^2} + r^2 \left(d\theta^2 + \sin\theta^2 d\phi^2 \right) \right]. \tag{2.2}$$

where $a(t)$ is the *scale factor*, which describes how the spatial directions evolve in time, K denotes the spatial curvature and (r, θ, ϕ) are the spherical coordinates.

Note that, given the assumption of isometry, $a(t)$ is the same for all the spatial directions while the value of K determines the geometry of the Universe, that is open, flat or closed respectively for $K = 1$, $K = 0$ and $K = -1$.
The equations which describe the dynamics of the Universe, thus the change of the scale factor $a(t)$ in time, are the *Friedmann equations*, and they have been derived by Friedmann in 1922 [22] from the Einstein Equations for a perfect fluid[1] and for the line element in eq.(2.2):

$$H^2 = \frac{\dot{a}^2}{a^2} = \frac{8\pi G\rho}{3} - \frac{K}{a^2} \tag{2.4}$$

$$H^2 + \dot{H} = \frac{\ddot{a}}{a} = -8\pi G\frac{\rho + 3P}{6} \tag{2.5}$$

Here $H = \frac{\dot{a}}{a}$ is the *Hubble parameter* and $M_{Pl} = \sqrt{\hbar/(8\pi G)} = 1$ is the reduced Planck mass.

The above equations, derived respectively from the component $00 - th$ and $ii - th$ of the Einstein equations, can be combined into the *continuity equation*

$$\dot{\rho} + 3H(P + \rho) = 0. \tag{2.6}$$

If a cosmological fluid satisfies

$$P = \omega\rho \tag{2.7}$$

then the continuity equation describes the evolution of the energy density

$$\rho \sim \rho_0 a^{-3(1+\omega)}. \tag{2.8}$$

Here ω is called *equation of state parameter* and assumes different values for

[1]Note that under the conditions of homogeneity and isotropy the stress energy tensor $T_{\mu\nu}$ takes the form of a perfect fluid

$$T_{\mu\nu} = (\rho + P)U_\mu U_\nu - Pg_{\mu\nu}, \tag{2.3}$$

.

different forms of energy sources

$$\begin{cases} \omega = 0, & \text{matter (or when the kinetic energy is negligible)} \\ \omega = 1/3, & \text{radiation (or when the kinetic energy dominates)} \\ \omega = -1, & \text{cosmological constant.} \end{cases} \tag{2.9}$$

Plugging eq.(2.8) in the first Friedmann equation (2.4), gives the evolution of the scale factor $a(t)$ as a function of time

$$\begin{cases} a(t) \propto t^{\frac{2}{3(1+\omega)}}, & \text{if } \omega \neq -1 \\ a(t) \propto e^{Ht}, & \text{if } \omega = -1 \end{cases} \tag{2.10}$$

Note that, when $\omega = -1$, the density of energy is constant $\rho \sim \rho_0$: this cosmological fluid is called *dark energy*. When the Universe is matter or radiation dominated, the scale factor has a power law time dependency $a(t) \propto t^{\alpha}$.

Using eq.(2.8) above, the Friedmann equation (2.4) can be rewritten in terms of the density parameters: $\Omega_i \equiv \frac{\rho_i}{\rho_c}$, where $\rho_c \equiv 3M_{Pl}^2 H^2$ and ρ_i is the energy density for each different species i, i.e

$$\Omega \equiv \Sigma_i \Omega_i = 1 + \frac{K}{a^2 H^2}. \tag{2.11}$$

As discussed above, the equations derived by Friedmann describe an Universe which expands in time. Not long after the Friedmann equations were published, scientists realized that, as a direct consequence of the Universe's expansion, at the very beginning of time all the matter and radiation which today are scattered through the space were concentrated in a hot and dense initial state. In 1948 Gamow and Alpher published a paper [23] arguing that this "thermal soup" of particles was the perfect ground for the synthesis of the chemical elements present in the Universe nowadays; they also realized that, after the temperature of Universe dropped below $T \sim 0.23 - 0.28eV$, i.e. when electrons were able to combine with protons to form hydrogen atoms, the photons would have been able to start travelling in straight line. They concluded that, as a consequence, the Universe should be filled by a blackbody radiation field.
This field, known as the Cosmic Microwave Background (CMB), was measured

for the first time in 1965 [24].

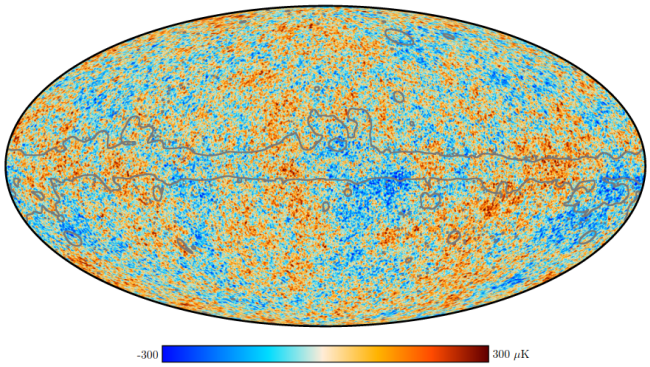

Figure 2.1: The anisotropies of the CMB as measured by Planck and WMAP. This image is taken from [1].

The CMB, as can be see in Fig.2.1 is an almost perfect black body with a temperature of $T = 2.72548 \pm 0.00057K$, and is considered one of the most important observational evidence in support of the Big Bang theory.
The SCM accounts also for the existence of large scale structures, the abundance of primordial elements (Big Bang nucleosynthesis) and most of the observational data coming from experiments such as COBE [25] and Wilkinson Microwave Anisotropy Probe (WMAP) [26, 27], are in agreement with this model predictions. However, as we show in the next section, this cosmological model cannot explain some important features present the Universe today.

2.1.2 Problems of the Standard Cosmological Model

After the discovery of the CMB, the interest in the Big Bang model grew exponentially, and while the observations agreed with the theoretical predictions of the model, it became clear that it was impossible for this theory to explain the current state of the Universe without choosing extremely specific initial conditions.
In other words, the SCM can explain some characteristic of the Universe today *only* if we fine-tune the model parameters in the early stage of the Universe; but this goes against the Copernican Principle, according which the human specie

should not occupy a special place in the Universe.

The biggest issues faced by the Big Bang theory are: *the horizon problem*, *the flatness paradox* and *the relics problem*.

All these problems find a solution thanks to the inflationary mechanism, see Sec.2.2.

2.1.2.1 Horizon problem

The horizon problem arose immediately after the discovery of the CMB and of its high degree of isotropy.
If on one side the isotropy and homogeneity of this radiation were crucial proofs for the Big Bang theory, on the other this spatial uniformity was problematic. To understand why it is necessary to relate the isotropy of the CMB to the notion of causality.

In cosmology one of the most important concept is the *comoving particle horizon* d_H, which represents the maximum (comoving) distance light can travel between two times t and $t = 0$. In particular, if the comoving distance between two particles is greater than d_H, these particles have never been in causal contact, hence they never could have communicated:

$$d_H = \int_0^t \frac{dt'}{a(t')} = \int_0^a (a'H)^{-1} d(\ln a') \tag{2.12}$$

from which, using eq. (2.10)

$$d_H \propto a^{\frac{1}{2}(1+3\omega)} \sim (aH)^{-1} \tag{2.13}$$

Note that in the last step it has been considered that for most part of its history, the Universe is dominated by matter or radiation, therefore $\omega > -1/3$ and $a(t) \propto t^{\alpha}$.

The quantity $(aH)^{-1}$ is called *comoving Hubble radius* and determines the limiting distance of causal communication.

Note that to get from d_H the *physical horizon* (hence the measurable one) r_H, it is necessary to rescale d_H for the scale factor,

$$r_H = a(t) \int_0^t \frac{dt'}{a(t')}, \tag{2.14}$$

hence eq.(2.13) can be rewritten as

$$r_H \sim H^{-1} \tag{2.15}$$

In the SCM, the Hubble radius and the particle horizon have the same evolution, as can be seen from eq. (2.13), and they both *only* increase in time. As a consequence, we can expect that scales beyond the Hubble horizon today $(a_0 H_0)^{-1}$ are not in direct causal contact and have *never* been, since the particle horizon d_H has never been bigger than the Hubble one. Since the particle horizon at the CMB time (t_{rec}) is much smaller than the CMB we see today (t_0), we can conclude that different regions of the CMB were not in causal contact at t_{rec}, see Fig.2.2

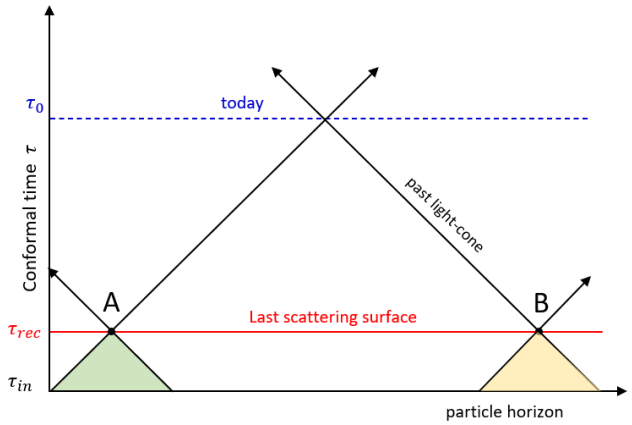

Figure 2.2: Conformal diagram of Big Bang cosmology. At the time of the recombination τ_{rec} A and B had never been in causal contact before (their past light-cone did not intersect).

Furthermore, it is possible to roughly estimate the number of causal discon-

nected patches in the CMB comparing the comoving horizon volume today V_0 to that at t_{rec}, V_{rec}.
Using the definition of the redshift $z + 1 = \frac{a_0}{a}$, from eq.(2.13) it is possible to compute the ratio V_0/V_{rec}:

$$\left(\frac{d_{H_0}}{d_{H_{rec}}}\right)^3 = \left(\frac{a_0}{a_{rec}}\right)^{\frac{3}{2}(1+3\omega)} = (1 + z_{rec})^{\frac{3}{2}(1+\omega)}. \tag{2.16}$$

At t_{rec} the redshift has been estimated to be $z \sim 1100$, and assuming that the matter component dominated between t_{rec} and t_0, i.e $\omega = 0$, we obtain:

$$\frac{V_0}{V_{rec}} \sim 10^4. \tag{2.17}$$

To summarize, the CMB spectrum, where the anisotropies in temperature are as small as 10^{-5}, is constituted by $\sim 10^4$ casually independent patches (each of which has a size of ~ 2 degrees).
"Why do these regions have such a fine-tuned temperature if they have never been in thermal contact?" is the question at the origin of the horizon problem.

A possible answer could be that homogeneity and isotropy were part of the initial conditions, but computing the energy density fluctuation $\delta\rho/\rho$ needed at the beginning in order to have today a $\delta T/T \leq 10^{-4}$ (as required by the CMB data), it results that, at the very beginning, the Universe had to have to be $\delta\rho_{in}/\rho_{in} \sim \mathcal{O}(10^{-61})$. This value is too small and to fine-tuned to be physically acceptable[1], therefore this possibility cannot be considered a solution to the problem.

2.1.2.2 Flatness paradox

The geometry of the Universe can be described by the value of the parameter Ω, introduced in eq. (2.11). The most recent *Planck* observations [16], combined with the BAO (Baryon Acoustic Oscillations) data suggest that the value of the spatial curvature of the Universe is

$$|\Omega - 1| = 0.0007 \pm 0.0019. \tag{2.18}$$

[1]See again the Copernican principle.

which suggest that the Universe is very close to being flat.
The flatness paradox arises once we compute the value of the curvature parameter in the very early stages of the Universe needed to have a (almost) flat Universe today.
Recalling eq. (2.11),

$$\Omega - 1 = \frac{K}{a^2 H^2} \propto \frac{K}{a^2 \rho} \tag{2.19}$$

and eq.(2.8), it is possible to write $(\Omega - 1)$ in terms of the redshift z, in particular, when the Universe is dominated by matter (MD) or radiation (RD), the curvature parameter is proportional to

$$MD \quad (\Omega - 1) \propto (1+z)^{-1}, \tag{2.20}$$

$$RD \quad (\Omega - 1) \propto (1+z)^{-2}. \tag{2.21}$$

Using the above equation, and knowing the value of the redshift parameter at the recombination and at the Planck time, it is possible to evolve the curvature parameter back in time. If today $(\Omega_0 - 1) \sim 10^{-3}$, at the recombination time ($z_{rec} \sim 1100$), we have

$$\frac{\Omega_0 - 1}{\Omega_{rec} - 1} = \frac{(1+z_0)^{-1}}{(1+z_{rec})^{-1}} \quad \rightarrow \quad (\Omega_{rec} - 1) \sim \mathcal{O}(10^{-7}) \tag{2.22}$$

and, at the Planck scale, where $z_{Pl} \sim 10^{31}$,

$$(\Omega_P - 1) = \frac{(1+z_{Pl})^{-2}}{(1+z_{rec})^{-1}} (\Omega_{rec} - 1) \sim \mathcal{O}(10^{-65}) \tag{2.23}$$

Again, as in the previous subsection, the initial value for the curvature parameter requested by the SCM to explain the flatness of the Universe today requires an extremely fine-tuned value.

2.1.2.3 The relics problem

Lastly, it is worth mentioning the *unwanted relics problem.*

In the very early stage of its history the Universe was incredibly hot so much that we talk about *hot Big Bang* and it is possible that the temperature and the energy scale reached the Planck scale. If this is the case, than it is possible to have new, and very heavy, degrees of freedom which obey UV theories, as for example new particle species predicted by supersymmetry .
All these new particles are massive, hence should be diluted slower than the radiation during the Universe; if Ω_X is their density parameter, since very heavy particles have a small annihilation section, $\Omega_X \ll 1$, i.e. they should have overclose the Universe.

In particular, there should be enough of them for us to detect; however this is in contrast with the observations.
Examples of these exotic objects are the *magnetic monopoles*. These are heavy particles with an isolated magnetic pole. It has been showed that they are inevitable prediction of grand unification of elementary particle interactions [28]. Unfortunately, even if they are thought to interact through the electromagnetic field and therefore they should be relatively easy to experiment on, they have never been detected.

2.2 Inflation

The theory of inflation, formulated between the end of the '70s and the beginning of the'80s, has been introduced to give an answers to the numerous problems affecting the SCM.
In the early '70 Zeldovich noticed that the problems of the SCM (see Sec.2.1.2) could be avoid if one assumes that the primordial Universe underwent a phase of accelerated (quasi-exponential) expansion.
After the model proposed by Starobinksy in [29], which still assumed a perfectly homogeneous and isotropic Universe as initial condition, the first "real" inflationary model was formalized by Guth, in 1981 [30]. Unfortunately, according to his model, quoting Guth himself, "the inflationary scenario seems to lead to some unacceptable consequences", called *graceful exit*. In the following year, A.Linde, A.Albrecht and P.Steinhardt independently proposed a new scenario, called *new*

inflation [31], which does not suffer from the graceful exit problem. In their models inflation is driven by the energy of a scalar field ϕ rolling down a potential hill.
The fundamental idea behind both these models is that this new phase of quasi-exponential expansion can change the causal structure of the spacetime, hence the way the information propagates. In the following years numerous inflationary models have been proposed, and still today this is a very active field.
In this section we introduce the inflationary dynamics, the concept of slow-roll and we analyse the easiest realizations of inflation, i.e. the single field models. In the last part we focus on the observable predictions of single field models and we discuss how the experimental data collected in the last years compare to them.

2.2.1 How does Inflation work?

To avoid the horizon and flatness problem, inflation has to allow for the different CMB regions to be casually connected; this would explain not only the homogeneity of the CMB but also and the incredibly small value of the curvature parameter $|\Omega - 1|$ without having to impose any fine-tuned initial condition.

From eq.(2.13), it is clear that the comoving particle horizon can never be larger than the Hubble radius; these quantities are proportional and they *strictly increase* with the expansion of the Universe. Therefore, to have $d_{H_{CMB}} \gg (a_0 H_0)^{-1}$, it is necessary an epoch of decreasing Hubble radius in the very early Universe:

$$\frac{d}{dt}(aH)^{-1} < 0 \tag{2.24}$$

An epoch characterized by a shrinking Hubble radius is known as *inflation*.
Using the Friedmann equations eq.(2.4) and eq.(2.5), the condition of a shrinking Hubble radius can be expressed in terms of the acceleration and the pressure of the universe. This allows to write the following equivalent conditions for inflation:

- *Inflation is a period of an accelerated expansion*: using the 2nd Friedmann

eq.(2.5), eq.(2.24) can be written as

$$-\frac{\ddot{a}}{a^2H^2} < 0 \quad \text{which implies} \quad \ddot{a} > 0. \tag{2.25}$$

- *Inflation is a period where a type of matter with negative pressure dominates*: the condition (2.24) implies that $1 + 3\omega < 0$, i.e.

$$\rho + 3P < 0 \tag{2.26}$$

From eq.(2.24), it can been seen that the inflationary period is also characterized by a slowly changing Hubble parameter. Introducing the parameter ϵ[1] as

$$\epsilon \equiv -\frac{\dot{H}}{H^2} \tag{2.27}$$

the rate of change of the Hubble radius, can be written as

$$\frac{d}{dt}(aH)^{-1} = -\frac{1}{a}(1-\epsilon). \tag{2.28}$$

It follows that having a slowly shrinking Hubble radius requires

$$\epsilon \ll 1. \tag{2.29}$$

The parameter ϵ can also be written as

$$\epsilon = -\frac{\dot{H}}{H^2} = -\frac{d\ln H}{dN} \tag{2.30}$$

where N is the *number of e-folds*, defined as

$$dN \equiv d\ln a = H dt \tag{2.31}$$

which indicates the number of expansion times of the Universe.
The limit of constant Hubble parameter, for which $\epsilon = 0$, is called *de Sitter solution* and it results in a pure exponential expansion of the scale factor: $a(t) \sim$

[1] In the rest of the thesis the parameter ϵ will be indicated as ϵ or ϵ_H indistinctly.

e^{Ht} (in this case $\omega = -1$).
However, since the mechanism of inflation needs to end in order for an apparent Big Bang to take place, we require $\epsilon \ll 1$, which describes a *quasi de Sitter solution*.
In order for inflation to last long enough to solve the problems of the SCM, it is possible to define a second parameter, η, which indicates if the condition $\epsilon \ll 1$ lasts for a sufficient amount of time. This is defined as[1]:

$$\eta \equiv \frac{d \ln \epsilon}{dN} = \frac{\dot{\epsilon}}{H\epsilon}. \tag{2.32}$$

and it quantifies the rate of change of ϵ over time.

To ensure that inflation lasts long enough $|\dot{\epsilon}| \ll \epsilon$, hence

$$|\eta| \ll 1. \tag{2.33}$$

The duration of an inflationary period is measured in e-folds, introduced in eq.(2.31), and, as we explain in the next subsection Sec.2.2.2, a successful inflationary model has to last at least $N \sim 60 - 70$.
Eq.(2.29) and eq.(2.33) are referred to as *slow-roll conditions*, and they both need to be satisfied in order to build a successful inflationary model.

2.2.2 Solution of the SCM problems

Horizon problem

During the de Sitter phase the Hubble length H^{-1} and the physical scale d_H have completely different evolution: the first one remains constant, while the second increases exponentially.

In particular, the value a_e of the scale factor at the end of the inflation is related to a_i, the scale factor's value at the beginning of the inflation, by the relation

$$a_e = a_i e^{H(t_e - t_i)} \equiv a_i e^N \tag{2.34}$$

[1] As for the parameter ϵ, the parameter η will be indicate with η or η_H indistinctly.

where $N = \ln a_e/a_i$ is the number of e-fold introduced in eq. (2.31).
The physical distance r_H that the light could have traveled just after the end of the inflation is r_{H_e}

$$r_{H_e} = a_e \int_{a_i}^{a_e} \frac{1}{(a')^2 H} da' = \frac{a_e}{H_{inf}} \left(a_i^{-1} - a_e^{-1}\right) \sim \frac{a_e}{a_i H_{Inf}} \sim \frac{e^N}{H_{Inf}} \tag{2.35}$$

where we used that $a_e \gg a_i$ and eq.(2.34). Here H_{Inf} is the value of the Hubble parameter during inflation, hence it is constant.
Comparing the above equation with eq.(2.13) and eq.(2.15) it is clear that the presence of an inflationary period allows for the particle horizon to be exponentially larger than the comoving Hubble radius, hence $r_{H_e} \gg H^{-1}$.
This means that, even if at the recombination time different Hubble spheres were outside the respective Hubble radius, they were inside the respective particle horizons. Thus they had the possibility to be in causal contact in the early Universe, see Fig.2.3.

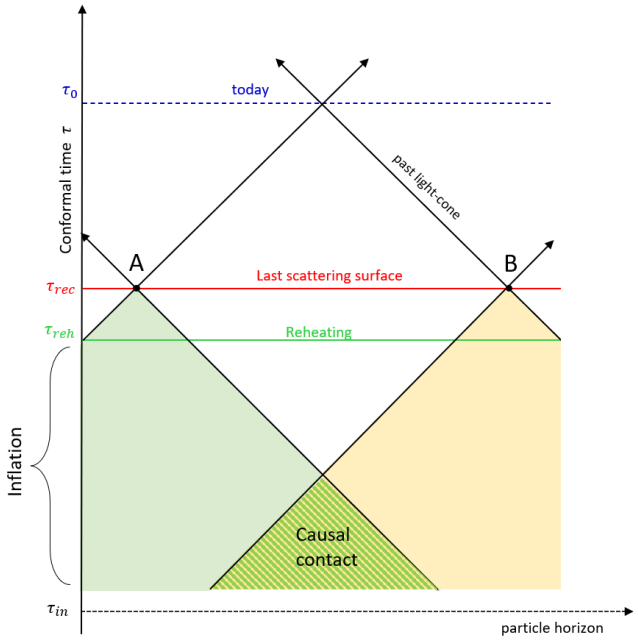

Figure 2.3: Conformal diagram of inflationary cosmology. Inflation stretches conformal time $d\tau = dt/a(t)$ to $\tau = -\infty$. This allows for the points A and B to have been in causal contact in the past.

To solve the horizon problem it is necessary that inflation lasts enough for all the points on the CMB to have been in casual contact before. In the following we compute the amount of inflation needed for the CMB to have been in casual contact at t_e.
Let us assume that inflation took place at the Planck time t_P, to give the most restrictive constraint.
At t_i, the maximum causal distance was roughly the Planck length $l_P \sim 10^{-33} cm$. After inflation, at t_e, this length has been stretched, as seen above, by a factor e^N

$$d(t_e) = e^N l_P. \tag{2.36}$$

The same length computed today, at t_0, becomes

$$d(t_0) = \frac{a_0}{a_e} d(t_e) = \frac{T_P}{T_0} e^N l_P = 10^{32} e^N l_P \sim 10^{-1} e^N cm \tag{2.37}$$

where it has been used $T_e \sim T_P$ [1], $T_0 = 10^{-13} Gev$, as estimated from the CMB, and $T_P = 10^{19} Gev$.
Finally, requiring that this distance is *at least* as large as the of the Hubble radius today

$$10^{-2} e^N cm \geq 10^{28} cm \tag{2.38}$$

gives the following condition for the number of efolds

$$N \gtrsim \ln 10^{29}, \quad \rightarrow \quad N \gtrsim 67. \tag{2.39}$$

Flatness problem

Inflation solves the flatness problem by means of the same mechanism used to solve the horizon one.
During inflation, since the Hubble parameter $H = H_{Inf}$ is constant, from eq.(2.19) it follows that $\Omega - 1 \propto 1/a^2$. The spatial curvature *after* the inflation can be written as

$$\Omega_e - 1 = (\Omega_i - 1) \left(\frac{a_i}{a_e} \right)^2 = (\Omega_i - 1)\, e^{-2N}. \tag{2.40}$$

[1] The temperature at the end of the inflation can be estimated as T_P if the reheating is maximally efficient, so that the Universe is reheated to the Planck energy.

Recalling eq.(2.20), the spatial curvature today can be written as

$$\Omega_0 - 1 = \frac{T_{equiv}}{T_0}\left(\Omega_{equiv} - 1\right) = \frac{T_{equiv}}{T_0}\left(\frac{T_P}{T_{equiv}}\right)^2 e^{-2N} \simeq 10^{60}\left(\Omega_i - 1\right) e^{-2N} \quad (2.41)$$

where $T_{equiv} = 10^4 K$ is the temperature at the matter and radiation equivalence. Knowing that $\Omega_0 - 1 \sim 10^{-4}$, it follows

$$N \geq \ln 10^{32} + \frac{1}{2}\ln\left(\Omega_i - 1\right) \sim 73 + \frac{1}{2}\ln\left(\Omega_i - 1\right). \quad (2.42)$$

If at Planck time the initial deviation from flatness is not too large, the amount of inflation needed to solve the horizon problem is enough to solve the flatness problem as well.

2.2.3 Slow roll single field inflation

In Sec.2.2.1 we showed how inflation is an epoch characterized by a shrinking Hubble radius or, equivalently, where by a type of matter with a negative pressure dominates, see eq.(2.26).
The simplest way to realize either of these scenarios is assuming that the primordial Universe is filled with *one* scalar field, called *inflaton*, which is minimally coupled to gravity:

$$S = \int d^4x\sqrt{-g}\left[\frac{M_{Pl}^2}{2}R - \frac{1}{2}g^{\mu\nu}\partial_\mu\phi\partial_\nu\phi - V(\phi)\right]. \quad (2.43)$$

In this equation $V(\phi)$ is the potential of the scalar field, R is the Ricci scalar and g is the determinant of the metric, which is assumed to be the flat FLRW metric in eq.(2.2).
In a FLRW metric $\phi(\mathbf{x}, t) = \phi(t)$, and the equation of motion for the scalar field, obtained varying the action above, becomes

$$\ddot{\phi} + 3H\dot{\phi} + V_\phi = 0. \quad (2.44)$$

where $V_\phi = dV/d\phi$. This equation describes a particle rolling down a potential $V(\phi)$ and subjected to a friction $3H\dot{\phi}$.

To rewrite the Friedmann equation eq.(2.4) as a function of ϕ, let's start by computing the energy density ρ_ϕ and the pressure P_ϕ of the inflaton. From the action eq.(2.43), the energy-momentum tensor is

$$T^{\phi}_{\mu\nu} = \partial_\mu\phi\partial_\nu\phi - g_{\mu\nu}\left(\frac{1}{2}\partial^\tau\phi\partial_\tau\phi + V(\phi)\right). \tag{2.45}$$

from which

$$\rho_\phi \equiv T_{00} = \frac{1}{2}\dot{\phi}^2 + V(\phi), \qquad P_\phi \equiv T_{ii} = \frac{1}{2}\dot{\phi}^2 - V(\phi) \tag{2.46}$$

As a consequence, equations (2.4) and (2.5) can be written as

$$H^2 = \frac{1}{3M_{Pl}^2}\left(\frac{\dot{\phi}^2}{2} + V(\phi)\right) \tag{2.47}$$

$$\dot{H} = -\frac{\dot{\phi}^2}{2M_{Pl}^2} \tag{2.48}$$

where it has been assumed $K \sim 0$[1].

Since inflation is supported by a scalar field with negative pressure, $\omega_\phi = P_\phi/\rho_\phi < 0$, and the potential energy dominates over the kinetic term:

$$\dot{\phi}^2 \ll V(\phi) \tag{2.49}$$

Note that this condition is equivalent to impose the first slow-roll condition, eq.(2.29). This can be understood by writing ϵ explicitly in terms of the scalar field:

$$\epsilon_H \equiv -\frac{\dot{H}}{H^2} = \frac{3\dot{\phi}^2}{\left(\dot{\phi}^2 + 2V(\phi)\right)} \ll 1 \quad \Rightarrow \quad \dot{\phi}^2 \ll V(\phi) \tag{2.50}$$

From the second slow-roll condition, eq.(2.33), we obtain a condition on the

[1]This can be done given the experimental data on the flatness of the Universe.

second derivative of ϕ

$$\eta_H \equiv \frac{\dot{\epsilon_H}}{H\epsilon_H} = 2\left(\frac{\ddot{\phi}}{H\dot{\phi}} + \epsilon_H\right) \ll 1 \quad \Rightarrow \quad \ddot{\phi} \ll H\phi \tag{2.51}$$

where we used $\epsilon_H \ll 1$.

Equations (2.49) and (2.51) define the *slow-roll regime*: if a scalar field satisfies both these conditions, then inflation can happen, eq.(2.49), and lasts enough to solve the SCM problems, (2.51).
The parameters ϵ_H and η_H are called *Hubble slow-roll parameters* [1].
Under the slow-roll conditions, the equation of motion for ϕ (2.44) and the Friedmann equation (2.47) can be simplified as

$$3H\dot{\phi} \simeq -V_\phi, \qquad H^2 \simeq \frac{1}{3M_{Pl}^2}V(\phi) \tag{2.52}$$

From the first of these equations it is possible to see that, in order to have the required small kinetic energy, the potential has to be flat enough. When this is the case, $H \sim \sqrt{V/(3M_{Pl}^2)}$ is almost constant, and the scale factor increases exponentially, $a(t) \sim e^{Ht}$.

In the *single field scenario* it is possible to define the *potential slow-roll parameters* ϵ_V and η_V, which express the slow-roll conditions (2.50) and (2.51) in terms of the potential shape:

$$\epsilon_V \equiv \frac{M_{Pl}^2}{2}\left(\frac{V_\phi}{V}\right)^2 \ll 1 \qquad \eta_V \equiv M_{Pl}^2\left(\frac{V_{\phi\phi}}{V}\right) \ll 1. \tag{2.53}$$

From these equations, again, it is evident that inflation requires a rather flat potential.

An example of a suitable potential for inflation is

$$V(\phi) = V_0\left(1 - e^{-\sqrt{\frac{2}{3}}\frac{\phi}{M_{Pl}}}\right) \tag{2.54}$$

[1] In the following sections these will be referred to as *slow roll parameters* except when indicated and will be indicated as ϵ and η.

which is called *Starobinsky potential*, and is represented in Fig.2.4.

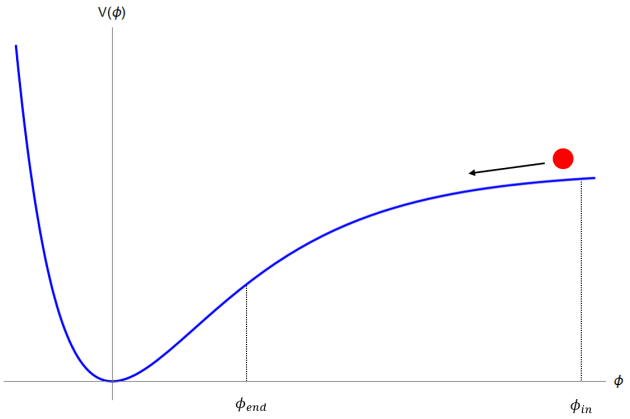

Figure 2.4: Starobinsky potential with $V_0 = 1$. The flat part of the potential, on the right side, allows for inflation to take place. The scalar field ϕ starts its journey at ϕ_{in} and then slowly rolls down until the potential becomes to steep to sustain a slow-roll, ϕ_{end}.

The inflaton, represented by the red circle, starts rolling down the flat part of the potential until it reaches $\sim \phi_{end}$ where its velocity $\dot{\phi}$ increases. This change spoils the first slow-roll condition eq.(2.49) and causes the end of inflation, which happens when $\epsilon = 1$.

2.2.4 Cosmological perturbations, observations and Planck data

One of the biggest success of inflation, besides the resolution of the SCM problems, see Sec.2.1.2, is that it provides a suitable mechanism to explain the small primordial fluctuations, which are held liable for the origin of the CMB anisotropies, see Fig.2.1, and large scale structures, such as galaxies, stars and so on.
During the inflation these primordial fluctuations are generated as quantum vacuum fluctuations of the scalar field, $\delta\phi$, in a subhorizon regime (i.e when their scales are smaller than the Hubble scale). As the exponential expansion proceeds these small fluctuations are stretched to very large scales and once the Hubble radius $1/(aH)$ drops below their scales, i.e. they become superhorizon, they freeze.

When inflation is over and the Hubble horizon expands faster than the physical scales, they re-enter the horizon and eventually become the initial density fluctuations that seed all structures in the Universe, see Fig.2.5.

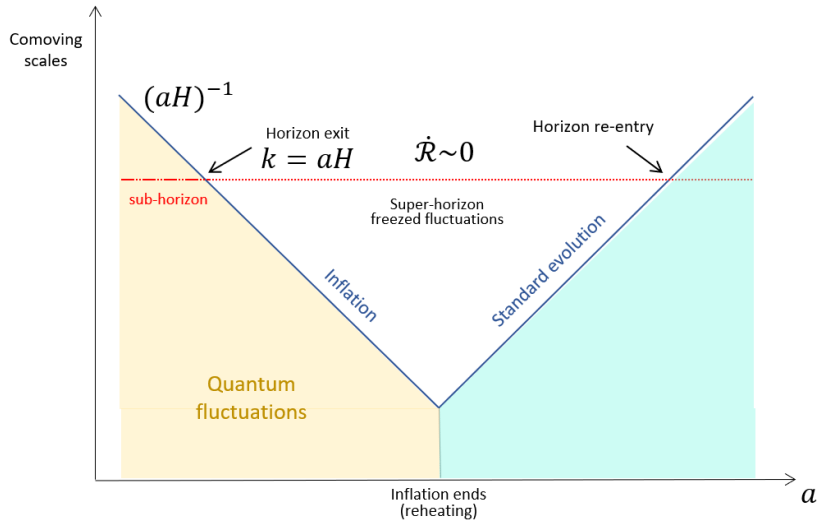

Figure 2.5: Quantum fluctuations produced during the inflation are created sub-horizon ($k \gg aH$) (left side). They freeze once they exit the horizon, hence $\dot{\zeta} \sim 0$ and they re-enter the horizon after the end of inflation becoming the seed for all the structures in the Universe (right side).

To be sure that the Universe remains homogeneous and isotropic at large scales, it is necessary that these perturbations are small relatively to the background dynamics analysed in the previous section.
In Appendix A we briefly sketch the computations for the quantum fluctuation generated during inflation in a pure de Sitter and massless case. A more extensive derivation can be found in [32–36] and in references therein.

Two of the most important results derived from the study of the primordial fluctuations are the expressions for the scalar and tensor power spectrum, derived in eq.(A.18) and eq.(A.19), i.e.

$$\Delta^2_{\mathcal{R}}(k) = \frac{H^2}{8\pi^2\epsilon}\Big|_{k=a_*H_*}, \quad \Delta^2_t(k) = \frac{2H^2}{\pi^2}\Big|_{k=a_*H_*}. \tag{2.55}$$

To derive these equation we assumed a de Sitter and massless approximation

which lead to a scale-invariant spectrum.
However, as seen in Sec.2.2.1 inflation takes place in a quasi de Sitter space, therefore the results obtained requires small corrections, of order slow-roll. Because during inflation the Hubble parameter is *nearly* constant, different modes crossing the horizon at different times, are "subject" to slightly different H; this can be taken into account introducing the *scalar spectral indices* n_s, defined as

$$n_s - 1 \equiv \frac{d \ln \Delta^2_{\mathcal{R}}}{d \ln k} \tag{2.56}$$

Using this parameter the scalar power spectrum can be parameterized as

$$\Delta^2_{\mathcal{R}}(k) = A_{\mathcal{R}}(k') \left(\frac{k}{k'}\right)^{n_s - 1} \tag{2.57}$$

where k' is the *reference scale*.
Analogously, it is possible to introduce a *tensor spectral index* n_t to parameterize the tensor power spectrum

$$n_t \equiv \frac{d \ln \Delta^2_t}{d \ln k}, \qquad \Delta^2_t(k) = A_t(k') \left(\frac{k}{k'}\right)^{n_t}. \tag{2.58}$$

The ratio between the amplitude of the tensor perturbations respect to the scalar perturbations is called *tensor-to-scalar-ratio*, is indicated by r and is defined as

$$r \equiv \frac{\Delta^2_t(k')}{\Delta^2_{\mathcal{R}}(k')} \tag{2.59}$$

Using the slow-roll parameters definition, eq.(2.50) and eq.(2.51), the above parameters can be written as

$$n_s = 1 - 2\epsilon - \eta, \quad n_t = -2\epsilon, \quad r = 16\epsilon. \tag{2.60}$$

An other important parameter is the *running of the spectral index* α_s defined as

$$\alpha_s = \frac{dn_s}{d \ln k} \tag{2.61}$$

The majority of cosmological data that we have today have been deduced

studying the power spectrum of the temperature fluctuations in the CMB, see Fig.2.1. Since this provides us with a picture of the Universe when it was only 380'000 years old, its study is our best possibility to determine the inflationary parameters introduced above.
The Planck satellite in particular has mapped the Universe with incredible precision and the data provided by the Planck collaboration [1, 2] can be used to make a selection of inflationary models, see Fig.2.6.

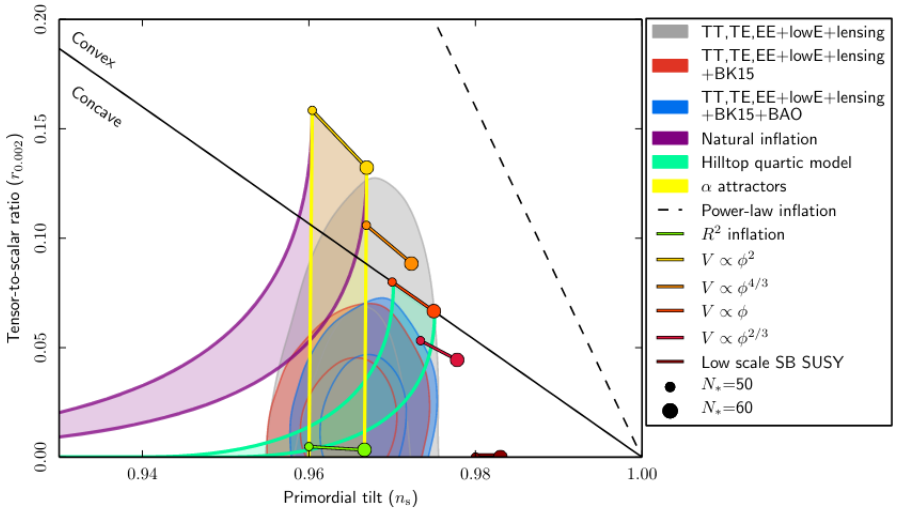

Figure 2.6: Planck 2018 results [2] for n_s and r combined with the theoretical predictions of different inflationary models. The predictions are calculated for $k' = 0.002 Mpc^{-1}$.

The scalar power spectrum's amplitude $A^2_{\mathcal{R}}(k)$, see eq.(2.57), which has been detected for the first time by COBE [25], has been determined to be

$$A^2_{\mathcal{R}}(k') = (2.14 \pm 0.10) \times 10^{-9}, \qquad k' = 0.05 Mpc^{-1} \tag{2.62}$$

and the scalar spectral index n_s and α_s have been measured to be

$$n_s = (0.9649 \pm 0.0042) \quad (68\% CL)\,, \qquad \alpha_s = (-0.005 \pm 0.013)\,(95\% CL) \tag{2.63}$$

These values suggest that the inflationary power spectrum is nearly scale invari-

ant.
The value of r has also been tested studying the CMB's polarization. Light coming from the CMB has two polarization, called E-modes and B-modes and, while the E-mode polarization can be sourced by both tensor and scalar perturbations, the B-mode one is only characteristic of the tensor fluctuations. Since no B-mode has been detected as of now, the current Planck data [2] set an upper limit for r, which strictly depends on the sensitivity of the satellite

$$r_{0.002} < 0.1 \quad (95\% CL)\,. \tag{2.64}$$

Here they assumed that $n_t = -r/8$ and the subscript indicates that the value has been calculated at the pivot scale $k' = 0.002 Mpc^{-1}$.
However, combining this result with the data collected by the BICEP2-Keck experiment [37], a tighter limit is obtained

$$r_{0.002} < 0.056 \quad (95\% CL)\,. \tag{2.65}$$

In [38] the authors provided an upper bound for r for $k' = 0.05 Mpc^{-1}$ adding to the Planck data to the *Keck Array* data taken during the observational season ended in 2018:

$$r_{0.05} < 0.036 \quad (95\% CL)\,. \tag{2.66}$$

In Fig.2.6 we can see which are the predictions for n_s and r for different inflationary models and how they compare respect to the different Planck constraints. In this case n_s and r are evaluated at the pivot scale of $k' = 0.002 Mpc^{-1}$ which corresponds to a horizon crossing between 50 and 60 e-folds.

To conclude this paragraph, it is worth mentioning that, measuring the power spectrum amplitude $A^2_{\mathcal{R}}$ (eq.(2.62)) it is possible to set an upper bound on the value of the inflationary energy. In particular, using the definition of r

$$r = \frac{A_t^2}{A^2_{\mathcal{R}}} = \frac{1}{A^2_{\mathcal{R}}} \frac{2}{3\pi^2 M_{Pl}^4} V \quad \Rightarrow \quad V^{1/4} \simeq \left(\frac{3}{2} \pi^2 r A^2_{\mathcal{R}} \right)^{1/4} M_{Pl} \tag{2.67}$$

from which, using $M_{Pl} = \sqrt{1/(8\pi G)} = 2.45 \times 10^{18} GeV$, we obtain

$$V^{1/4} \simeq 3.2 \times 10^{16} \, (r)^{1/4} \, GeV. \tag{2.68}$$

This result suggests that inflation should happen at very high energy scale, slightly below the Planck scale, around $10^{15} - 10^{16} GeV$.

2.2.4.1 Primordial non-Gaussianities

In the previous subsection it was shown how the observational data from the CMB agree with the predictions of many single field inflationary models, see Fig.2.6. In particular these vanilla models agree with two well tested observations: a nearly scale invariant spectrum ($n_s \sim 1$) and a small tensor to scalar ratio $r < 0.1$.
However, there are some physical observables which, if detected, would rule out most of the singlefield models. One of these observables are *Non-gaussianities*.
The power spectra computed in Appendix A can capture the properties of Gaussian statistics, however non-gaussian statics could present new interesting information [39–44].
In particular, they could provide new insights into inflationary dynamics which cannot be present in the scalar or tensor power spectra, as explained in [45].

To study deviation from the Gaussian distribution we need to look into higher order correlation functions. The bispectrum of the curvature perturbation, i.e the Fourier transform of the three-point correlation function, is defined by

$$\langle \mathcal{R}(\mathbf{k}_1)\mathcal{R}(\mathbf{k}_2)\mathcal{R}(\mathbf{k}_3)\rangle \equiv (2\pi)^3 \delta^{(3)} \left(\mathbf{k}_1 + \mathbf{k}_2 + \mathbf{k}_3\right) \mathcal{B}_{\mathcal{R}} \left(k_1, k_2, k_3\right) \tag{2.69}$$

where the delta function denotes the momentum conservation, hence the three momenta are bounded to form a triangle in k-space.
The bispectrum can have many possible shapes depending on the three momenta and the overall factors. It is therefore convenient to introduce a *shape function*, $S(k_1, k_2, k_3)$, to represent the different triangular shapes and a non-linear parameter f_{NL} to describe the size of the non Gaussian signal:

$$\mathcal{B}_{\mathcal{R}}(k_1, k_2, k_3) = \frac{18}{5} f_{NL} S(k_1, k_2, k_3) \Delta^2_{\mathcal{R}}. \tag{2.70}$$

Note that the shape function is scale-dependent while the the amplitude does not depend on k.

The most studied templates for the bispectrum are three: *local*, *orthogonal* and *equilateral*. See [46] for a detailed review.
In Table 2.1, it is possible to find a summary of the characteristic of these templates and the data collected by Planck for each of them [47].

Shape	Relationship between momenta	Planck data (CL 68%)
Local	$k_1 \ll k_2, k_3$	$f_{NL}^{loc} = -0.9 \pm 5.130$
Equilateral	$k_1 = k_2 = k_3$	$f_{NL}^{eq} - 26 \pm 47$
Orthogonal	$k_1 = k_2 + k_3$	$f_{NL}^{orth} = -38 \pm 24$

Table 2.1: Shapes of non-gaussianity and Planck constraints [47] for each of them.

But which information can we derive from f_{NL} for the different templates? The behavior of the bispectrum for different triangle configurations encodes information about various physical effects that took place during the inflation.
The most famous exaple in this sense, is the *consistency relation* derived by Maldacena in [39]. In the *squeezed configuration*, where one of the wavenumbers is much smaller than the others, he showed that the amplitude of the bispectrum is proportional to the tilt of the power spectrum, i.e

$$\lim_{k_1 \ll k_2 = k_3} \mathcal{B}_{\mathcal{R}}(k_1, k_2, k_3) \propto \frac{d \ln \Delta^2_{\mathcal{R}}(k_3)}{d \ln k_3} \tag{2.71}$$

Since $d \ln \Delta^2_{\mathcal{R}} / d \ln k \sim (n_s - 1)$ in the vanilla models, this quantity is of order slow-roll. As a consequence, any detection of a signal in the squeezed limit would rule out *all* single field models of inflation.
Similarly, in [48] the author demonstrated that single field models of inflation produce $f_{NL}^{equil} < 1$, hence any detection of $f_{NL}^{equil} > 1$ would imply that the inflation becomes strongly coupled or it is realized by a multifield scenario, [49, 50].

The Planck collaboration has tested non-gaussianity through CMB measurements providing us with very accurate data, see Table 2.1, which helped to rule out many multifield models with more than one light fields.

Given the complexity and the limitations that these type of measurements on the CMB are subject to, today the experimental attention is shifting toward the study of large scale structures (LLS) where it is possible to use the galaxies distribution to infer statistics of the primordial perturbations. Using LLS it is possible to use a three-dimensional dataset (the distribution of matter) which is much larger the two dimensional one from the CMB. Experiments working in this direction, which can help shedding light on the driving interactions during the inflationary era [45] include DESI [51], LSST [52], Euclid [53] and SKA [54].
It is thus essential to understand, from a theoretical point of view, what scenarios and observables we may expect from models which go beyond the simple single field vanilla model. This is one of the main reasons (as we are going to see in the next section) which brought us to focus on the study of more general multifield models of inflation.

2.3 Multifield Inflation

After more than 40 years from Guth's paper [30], inflation has revealed to be so successful that, still today, it is the most widely accepted theory for the explanation of the Big Bang. Over the decades, however, the vanilla single field models described in the previous section, have showed some weakness and shortcomings which brought the scientific community to start investigating more general and complex inflationary scenarios: multifield models.
In this section we describe the main reasons for which it is important to study more general inflationary dynamics, we describe their dynamics and show how their slow-roll conditions differ from the single field case, Sec.2.3.3.1. We also introduce multifield inflationary models in supergravity; we explain why it is natural to embed multifield models in a high-energy theory and we derive their equations of motion in such setting.
Finally we introduce the η-problem for both field theory models and supergravity embedded ones.

2.3.1 Why should we consider multifield inflation?

Cosmological inflation, introduced as a natural explanation for the homogeneity and flatness problem, has been validated by the most recent observations from the Planck, COBE and WMAP satellites.
All these observations, including the near scale invariance of the power spectrum of the primordial density fluctuations, are consistent with the single field slow-roll inflationary model described in the previous section, which is the simplest inflationary scenario, see Sec.2.2.4.
However, there are good reasons to think that a more complex model might be needed:

- Single field models are not always natural, especially considering the very high energy scales involved during inflation, see eq.(2.68). Many high energy theories, which aim to extend the Standard Model of particle physics, e.g. string theory or supergravity, require the presence of multiple scalar fields. Hence it is important to understand how the dynamics of the inflation would change if we consider multiple scalars coupled to the inflaton. In particular it is interesting to explore how the observational predictions (n_s, r, Non-gaussianities, etc.) would change following the presence of these extra degrees of freedom.

- Recently proposed consistency conjectures [55, 56] on the low energy effective theories derived from quantum gravity imply that the simple single scalar field inflation belongs to the *swampland*, a set of effective field theories which cannot be consistently embedded in a theory of quantum gravity. However, in [57] it was shown that multifield models of inflation, which can follow curved, non-geodesic trajectories, are instead not ruled out by the swampland conditions.

- The vanilla single field model inflationary paradigm is well supported by the observations, however the data collected until now are not able to give us an explanation of how inflation happened. In particular, they do not provide a definitive answer to the question: *"How many fields were involved?"*, since also many multifield models of inflation lead to very similar predictions.

However, major experimental efforts are being pursued in this direction hoping to get some anwers in the next decades thanks to experiments such as the stage four CMB-S4 [58] or CLASS [59], LiteBIRD [60], the Simons Observatory [61] and Probe Inflation and Cosmic Origins (PICO [62]), which aim to detect the B-mode polarization in the CMB induced by primordial gravitational waves.
Moreover, Large Scale Structure observations by forthcoming experiments, such as DESI [51], LSST [52], Euclid [53] or SKA [54], may also find the existence of primordial non-Gaussianities, see Sec.2.2.4.1, shedding light on the driving interactions during the inflationary era [45].
Therefore it is essential to have a deep theoretical knowledge of what scenarios and observables we may expect from models which go beyond the simple single field slow-roll.

- One of the criticisms moved to the theory of inflation is that it requires an incredibly flat potential, almost fine-tuned.
  However, as it will be shown in Sec.2.3.3.1, there are multifield models which can evade this problem allowing for the inflation to take place with potentials that would be too steep for a slow-roll.

Given the above reasons, recent years have seen a surge in the study of multifield models of inflation.

2.3.2 Generalities

In this section we will present the basic aspects of multifield inflation following the formalism developed in [63], [64], [65] and [66].
Considering a set of n scalar fields $\phi^a = (\phi^1, \phi^2, ..., \phi^n)$ minimally coupled to gravity, with possible non canonical kinetic terms, the action S equivalent to (2.43) can be written as

$$S = \int d^4x\sqrt{-g}\left[\frac{M_{Pl}^2}{2}R - \frac{1}{2}G_{ab}\partial_\mu\phi^a\partial^\mu\phi^b - V(\phi^a)\right] \tag{2.72}$$

where G_{ab} is the field space metric, which accounts for non trivial coupling between the n fields, and $V(\phi^a)$ is a function of the n scalar fields.
As in the single field case, the spacetime metric can be assumed to be homogeneous and isotropic, hence we consider a flat FLRW metric

$$ds^2 = -dt^2 + a(t)^2 \delta_{ij} dx^i dx^j. \tag{2.73}$$

With this setup, the equations of motion and the Friedmann equations become

$$\ddot{\phi}^a + 3H\dot{\phi}^a + \Gamma^a_{bc}\dot{\phi}^b\dot{\phi}^c + G^{ab}\frac{\partial V}{\partial \phi^b} = 0 \tag{2.74}$$

$$H^2 = \frac{1}{3M_{Pl}^2}\left(\frac{1}{2}\dot{\varphi}^2 + V(\phi^a)\right) \tag{2.75}$$

$$\dot{H} = -\frac{1}{2M_{Pl}^2}\dot{\varphi}^2. \tag{2.76}$$

where

$$\dot{\varphi}^2 = G_{ab}\dot{\phi}^a\dot{\phi}^b \tag{2.77}$$

and the Christoffel symbols Γ^a_{bc} are the ones associated with the field space metric G_{ab}:

$$\Gamma^a_{bc} = \frac{1}{2}G^{as}\left(\partial_b G_{as} + \partial_c G_{bs} - \partial_s G_{bc}\right). \tag{2.78}$$

Note that eq.(2.76) can easily be obtained by combining the previous two, therefore specifying G_{ab} and the shape of the potential $V(\phi^a)$, equations eq.(2.74) and eq.(2.75) can be solved.

The above system, written in the field basis, is not particularly helpful in providing an intuition for the system evolution. It is difficult to understand how the fields interact, making it hard to know how the different $\delta\phi^a$ combine to give the curvature perturbations and which is the field hierarchy if the mass-matrix is not diagonal.
It is therefore preferable to study multifield inflation using the basis which is actually induced by inflationary trajectory itself, the *kinematic basis*: in this case the equations of motion eq.(2.74) are projected onto the tangential and normal directions to the inflationary trajectory.

In this dissertation we focus on two-fields models, hence we will consider only one vector normal to the trajectory, for a generalization to more fields see [67].

If a curve is parameterized as $\phi^a(t)$, the square root of eq.(2.77) defines a field speed along the curve, and can be used to define the tangent vector T^a:

$$T^a = \frac{\dot{\phi}^a}{\dot{\varphi}} \tag{2.79}$$

which is automatically normalized, $T^a T_a = 1$.
The normal vector N^a is defined such that $T_a N^a = 0$:

$$N^a \equiv s_N(t) \left(G_{bc} \frac{DT^b}{dt} \frac{DT^c}{dt} \right)^{-1/2} \frac{DT^a}{dt} = \pm \frac{D_t T^a}{|D_t T|} \tag{2.80}$$

where $s_N(t) = \pm 1$ denotes the orientation of N^a respect to the vector $D_t T^a$. Also in this case the vector is normalized, $N^a N_a = 1$. N^a is well defined only where $D_t T^a \neq 0$, but since $D_t T^a$ can become zero for finite values of t, $s_N(t)$ is allowed to flip signs each time this happens, so that N^a is a continue functions of t.
An equivalent definition of the vector N^a, the one which will be predominantly be used in this thesis, is the following

$$N_a = \sqrt{G} \epsilon_{ab} T^b, \qquad N^a = G^{ab} N_b. \tag{2.81}$$

To have a clearer understanding of the vectors T^a and N^a see Fig.2.7.

Projecting the equations of motion eq.(2.74) along T^a and N^a yields respectively the following equations:

$$\ddot{\varphi} + 3H\dot{\varphi} + V_T = 0 \tag{2.82}$$

$$D_t T^a = -\frac{V_N}{\dot{\varphi}} N^a \tag{2.83}$$

where $V_T = T^a V_a$, $V_N = N^a V_a$ and $D_t T^a = \dot{T}^a + \Gamma^a_{bc} T^b \dot{\phi}^c$.
Eq. (2.82) is the multifield generalization of eq.(2.44), while eq.(2.83) describes the deviation of the inflationary trajectory from a geodesic. In particular, using

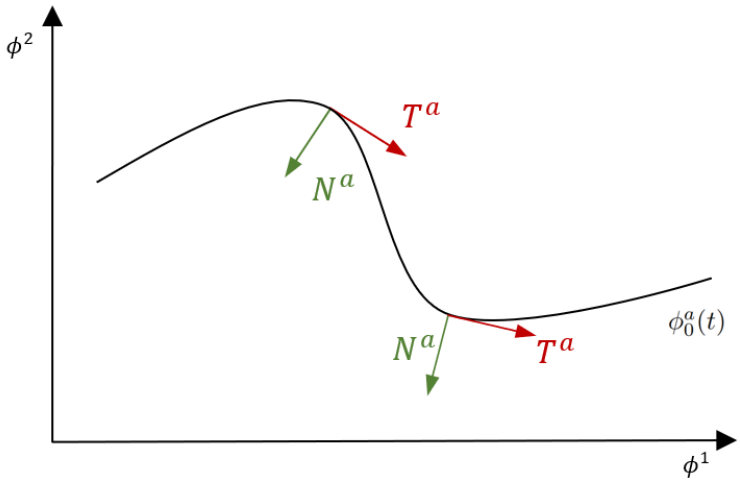

Figure 2.7: Relative orientation of the tangent vector field T^a and the normal vector field N^a with respect to the background solution $\phi_0^a(t)$.

eq.(2.80), eq.(2.83) can be written as

$$|D_t T| = -\frac{V_N}{\dot{\varphi}} \quad \Rightarrow \quad |D_N T| = -\frac{V_N}{H\dot{\varphi}} \equiv \frac{\Omega}{H} \tag{2.84}$$

where Ω/H is the *dimensionless turning rate* of the trajectory: it describes how fast the tangent vector T^a rotates in time, i.e. how much the inflationary trajectory departs from a geodesic.

In particular, if $\Omega/H = 0$, the trajectory follows a geodesic and the inflationary dynamics is not really different from a single field one, while, when $\Omega/H \neq 0$, the second field involved plays an important role. The parameter Ω is the turning parameter and is defined as

$$\Omega = \frac{V_N}{\dot{\varphi}} \tag{2.85}$$

Mass Matrix

To study the masses of the scalar fields we need to compute the eigenvalues of the *Mass Matrix*, defined as:

$$\mathbb{M}^a_b \equiv M_{Pl}^2 \nabla^a \nabla_b V. \tag{2.86}$$

In the specific case of two fields inflation it is useful to write the above expression in different basis: the field base and the kinetic one. The two expressions are clearly equivalent, but, as we will see later in the thesis (chapter 3 and 4) in some cases one of them might be preferred to the other.
In the field base, assuming that $\phi^a = (\rho, \theta)$, eq.(2.86) becomes

$$\mathbb{M} = M_{\rm Pl}^2 \begin{pmatrix} V_{;\rho\rho} & V_{;\theta\rho} \\ V_{;\rho\theta} & V_{;\theta\theta} \end{pmatrix} = M_{\rm Pl}^2 \begin{pmatrix} \partial_\rho V_\rho - \Gamma^k_{\rho\rho} V_k & \partial_\theta V_\rho - \Gamma^k_{\theta\rho} V_k \\ \partial_\rho V_\theta - \Gamma^k_{\rho\theta} V_k & \partial_\theta V_\theta - \Gamma^k_{\theta\theta} V_k \end{pmatrix} \tag{2.87}$$

where the Christoffel can be computed using the field space metric G_{ab}.

Introducing the kinetic frame, $\mathbb{M}$ can be written as

$$\mathbb{M} = M_{Pl}^2 \begin{pmatrix} V_{TT} & V_{TN} \\ V_{NT} & V_{NN} \end{pmatrix} \tag{2.88}$$

where $V_{TT} = T^a T^b \nabla_a \nabla_b V$, $V_{TN} = T^a N^b \nabla_a \nabla_b V$, etc.., and its eigenvalues result to be:

$$\begin{aligned} \lambda_\pm &= M_{\rm Pl}^2 \frac{1}{2} \left[V_{TT} + V_{NN} \pm \sqrt{(V_{TT} - V_{NN})^2 + 4V_{TN}^2} \right] \\ &= \frac{1}{2} \left[Tr\mathbb{M} \pm \sqrt{Tr\mathbb{M}^2 - 4det\mathbb{M}} \right] \end{aligned} \tag{2.89}$$

To write the eigenvalues of the mass matrix explicitely in terms of slow-roll parameters and Ω/H, it is sufficient to take the time derivative of eq.(2.82), which provides an expression for the tangent projection V_{TT} [3], [66], [68] :

$$\frac{V_{TT}}{3H^2} = \frac{\Omega^2}{3H^2} + \epsilon - \delta_\varphi - \frac{\xi_\varphi}{3} \tag{2.90}$$

where

$$\delta_\varphi \equiv \frac{\ddot{\varphi}}{H\dot{\varphi}} \qquad \xi_\varphi \equiv \frac{\dddot{\varphi}}{H^2\dot{\varphi}} \tag{2.91}$$

Next, taking the time derivative of eq.(2.85), it is possible to obtain an expression for the diagonal element of the mass matrix, V_{TN} (see [68], [66]):

$$\frac{V_{TN}}{H^2} = \frac{\Omega}{H} \left(3 - \epsilon + 2\delta_\varphi + \nu \right), \tag{2.92}$$

where ν describes the variation of the dimensionless turning rate

$$\nu \equiv \frac{\omega'}{\omega} \tag{2.93}$$

where $\omega \equiv \Omega/H$ and the prime $'$ denotes a derivative respect to N.

Note that the above expressions for V_{TT} and V_{TN} are *exact* since they have been derived without using any slow roll approximation.

2.3.3 Slow roll conditions

Using the equations of motion, the slow roll conditions, eq.(2.29) and eq.(2.33), can be written as

$$\epsilon = -\frac{\dot{H}}{H^2} = -\frac{\dot{\varphi}^2}{2M_{pl}^2 H^2} \ll 1 \quad \Rightarrow \quad \dot{\varphi}^2 \ll V \tag{2.94}$$

$$\eta = \frac{\dot{\epsilon}}{H\epsilon} = 2\frac{\ddot{\varphi}}{H\dot{\varphi}} + 2\epsilon \ll 1 \quad \Rightarrow \quad \delta_\varphi \ll 1. \tag{2.95}$$

and it can easily be noticed that they have exactly the same form of eq.(2.49) and eq.(2.51).
However in multifield inflation, given the possibility for the different scalar fields involved to interact and give rise to non geodesic-trajectories, there is a third condition which needs to be satisfied in order to have a long sustained period of inflation.
In [69] it has been shown that, to ensure that $\partial_t \dot{\phi}^a \sim \mathcal{O}\left(\epsilon H \dot{\phi}^a\right)$, i.e that the acceleration terms are negligible compared to the fields' velocities, the parameter ν introduced in eq.(2.93) has to be small, hence the dimensionless turning rate has to vary slowly along the inflationary direction:

$$\nu \ll 1. \tag{2.96}$$

Using the slow-roll conditions, the equations of motion can be simplified. In particular from the first equation

$$H^2 \simeq \frac{V}{3M_{Pl}^2} \tag{2.97}$$

while $\delta_\varphi \ll 1$ implies that eq.(2.82) becomes

$$3H\dot{\varphi} + V_T \simeq 0. \tag{2.98}$$

Going back to eq.(2.95), this condition is satisfied if

$$\frac{\ddot{\varphi}}{H\dot{\varphi}} = \frac{2\dot{\phi}_a D_t(\dot{\phi}^a)}{H\dot{\varphi}^2} \ll 1 \quad \Rightarrow \quad \left|\dot{\phi}_a D_t(\dot{\phi}^a)\right| = \frac{1}{2}\left|D_t(\dot{\varphi}^2)\right| \ll H\dot{\varphi}^2 \tag{2.99}$$

While this equation, in the single field case, can be satisfied only if $\ddot{\phi}^2 \ll H\dot{\phi}$, in the multifield models there are two possible options:

1. *Slow-roll, Slow-turn inflation* (SRST) when $\left|D_t(\dot{\phi}^a)\right| \ll H\dot{\varphi}$. This condition is equivalent to the single field $\ddot{\phi} \ll H\dot{\phi}$.
2. *Slow-roll, Rapid turn inflation* (SRRT) when $D_t(\dot{\phi}^a)$ is almost orthogonal to $\dot{\phi}^a$. In this case $\left|\dot{\phi}_a D_t(\dot{\phi}^a)\right| \ll 1$ is satisfied, but it is not necessary for $D_t(\dot{\phi}^a)$ to be small.

Before going into detail on the differences between SRSR and SRRT models, let us introduce two new slow-roll parameters which will be used in Chapter 3 and 4. From eq.(2.97) and eq.(2.98) it is possible to define ϵ_T, which expresses the first slow-roll condition in terms of the potential shape:

$$\epsilon \sim \frac{V_T^2}{9H^2(2H^2)} \quad \Rightarrow \quad \epsilon_T \equiv \frac{M_{\rm Pl}^2}{2}\left(\frac{V_T}{V}\right)^2 \ll 1. \tag{2.100}$$

Note that, while in the single field case the slow-roll parameter ϵ_V was written in terms of the gradient flow of the potential V_ϕ, in the multifield case the slow-roll parameter ϵ_T depends only on the projection of the potential along the tangent direction. As we will show later in this section, ϵ_V can no longer be used as a slow-roll parameter when there is more than one scalar field involved.
Similarly, it can be noticed that the physical interpretation of η_V in multifield inflation differs from that of the single field one, eq.(2.53).

In particular in multifield inflation η_V is defined as

$$\eta_V \equiv |\text{min.eigenvalue}\{\mathbb{M}\}|, \tag{2.101}$$

which is not equivalent to the second slow-roll parameter defined in eq.(2.95). However, analogously to ϵ_T it is possible to define a parameter η_T in terms of the derivative of the potential along the tangent direction and which can be used to ensure the slow-roll condition:

$$\eta_T \equiv -M_{\rm Pl}^2 \frac{V_{TT}}{V} \ . \tag{2.102}$$

The η parameter, defined as in eq.(2.95) becomes

$$\eta = 2M_{Pl}^2 \left(-\frac{V_{TT}}{V} + \left(\frac{V_T}{V} \right)^2 \right) = -2\eta_T + 4\epsilon_T \tag{2.103}$$

2.3.3.1 SRST and SRRT

To distinguish between these two regimes, it is necessary to write explicitly the expression of ϵ_V in the multifield case.
In two fields models, ϵ_V is defined as

$$\epsilon_V \equiv \frac{1}{2} \frac{V_a V^a}{V^2}, \quad a = 1, 2 \tag{2.104}$$

or, equivalently,

$$\epsilon_V = \frac{1}{2} \left(\frac{V_T^2 + V_N^2}{V^2} \right). \tag{2.105}$$

The first part of the above equation can be derived using eq.(2.82) and eq.(2.95):

$$V_T = -\ddot{\varphi} - 3H\dot{\varphi}, \qquad \ddot{\varphi} = (\eta - 2\epsilon) \frac{H\dot{\varphi}}{2} \tag{2.106}$$

which, if combined, lead to

$$\frac{1}{2} \frac{V_T^2}{V^2} = \epsilon \left[1 + \frac{\eta}{2(3-\epsilon)} \right]^2 . \tag{2.107}$$

Note that this result has been obtained without assuming *any* slow-roll.

The second part of eq.(2.105) can be written in terms of the dimensionless

turning rate, see eq.(2.83):

$$V_N = \frac{\Omega}{H}\left(H\dot{\varphi}\right) \quad \Rightarrow \quad \frac{1}{2}\frac{V_N^2}{V^2} = \frac{\Omega^2}{9H^2}\frac{\epsilon}{\left(1-\epsilon/3\right)^2}. \tag{2.108}$$

As a result,

$$\epsilon_V = \epsilon\left[\left(1+\frac{\eta}{2(3-\epsilon)}\right)^2 + \frac{\Omega^2}{9H^2}\frac{\epsilon}{\left(1-\epsilon/3\right)^2}\right]. \tag{2.109}$$

Assuming the slow-roll conditions $\epsilon \ll 1$ and $\eta \ll 1$, this can be reduced to [68].

$$\epsilon_V \simeq \epsilon\left[1+\frac{\Omega^2}{9H^2}\right]. \tag{2.110}$$

This expression is key to understand the difference between SRST and SRRT models:

1. When

$$\Omega/H \sim 0 \quad \Rightarrow \quad \epsilon_V \sim \epsilon, \tag{2.111}$$

we have a SRST inflation. In this case the parameter ϵ_V can be used to determine if the inflationary model admits a slow roll regime, as in the single field case, and it is possible to solve the system simply solving the n equations of motion for the fields

$$3H\dot{\phi}^a + V^a \simeq 0. \tag{2.112}$$

2. When

$$\Omega/H \gtrsim \mathcal{O}(1) \quad \Rightarrow \quad \epsilon_V > \epsilon \tag{2.113}$$

we have a SRRT inflation. In this case $V_N \gg V_T$, therefore the inflationary trajectory is aligned mostly on the direction orthogonal to V_a and does *not* follow a geodesic. As a consequence, the slow roll condition $\epsilon_T \ll 1$ can remain true even if ϵ_V is too big for slow roll slow turn inflation.
The peculiarity of this type of models is that they do not require a very flat potential to realize inflation. As a consequence, SRRT models "solve"

the conceptual problem discussed in Sec.2.3.1 of having to fine tuned the inflationary potential to solve the problems of the SCM.

In Chapter 3 and 4 we mainly focus on two fields models which present a rapid turn.

2.3.4 Adiabatic and entropic perturbations

In this section we derive the linear perturbations for multifield models. For a comprehensive review see [70].
To study the dynamics of scalar linear fluctuations, the first step is to derive the second-order action $S_{(2)}$, [71–75]

$$S_{(2)} = \int dt d^3x a^3 \left(G_{ab} D_t Q^a D_t Q^b - \frac{1}{a^2} G_{ab} \partial_\mu Q^a \partial^\mu Q^b - M_{ab} Q^a Q^b \right). \quad (2.114)$$

In the above equation Q^a are the field fluctuations, i.e. $\phi^a = \phi_0^a + Q^a$, and the squared mass matrix M_{ab} is given by

$$M_{ab} = V_{;ab} - \mathcal{R}_{acbd} \dot{\phi}^c \dot{\phi}^d + (3 - \epsilon) \dot{\phi}^a \dot{\phi}^b \quad (2.115)$$

with $V_{;ab} = V_{,ab} - \Gamma^c_{ab} V_b$.
The equations of motion for the linear fluctuations can be deducted from eq.(2.114) and, in Fourier space, they are:

$$D_t D_t Q^a + 3H D_t Q^a + \frac{k^2}{a^2} Q^a + M^a_b Q^b = 0 \quad (2.116)$$

We see, from the above equation, that the field fluctuations are coupled to each other through the mass matrix M_{ab}.

To gain a better insight of the equations above, eq.(2.114) and eq.(2.116), these can be rewritten using the local orthonormal vielbein frame e^I_a [70], which in the specific case of two-fields can be defined as

$$e^a_T = T^a, \quad e^a_N = N^a. \quad (2.117)$$

Doing so, eq.(2.116) can be rewritten as the following system (see also [74]):

$$\ddot{Q}_T + 3H\dot{Q}_T + \left(\frac{k^2}{a^2} + m_T^2\right) Q_T = (2\Omega Q_N)^{\cdot} - \left(\frac{\dot{H}}{H} + \frac{V_T}{\dot{\varphi}}\right) 2\Omega Q_N \tag{2.118}$$

$$\ddot{Q}_N + 3H\dot{Q}_N + \left(\frac{k^2}{a^2} + M^2\right) Q_N = -2\Omega\frac{\dot{\varphi}}{H}\dot{\mathcal{R}} \tag{2.119}$$

where $Q_N = N_a Q^a$ and $Q_T = T_a Q^a$ are respectively the entropic and adiabatic mode[1] and $\mathcal{R}$ is the comoving curvature perturbation which, in the spatially flat gauge, is defined as

$$\mathcal{R} = \frac{H}{\dot{\varphi}} Q_T. \tag{2.120}$$

The adiabatic mass m_T^2 is given by

$$\frac{m_T^2}{H^2} \equiv -\frac{3}{2} - \frac{1}{4}\eta^2 - \frac{1}{2}\epsilon\eta - \frac{1}{2}\frac{\dot{\eta}}{H} \tag{2.121}$$

and the entropy mass M^2 is given by

$$\frac{M^2}{H^2} = \frac{V_{NN}}{H^2} + M_{Pl}^2\epsilon R - \frac{\Omega^2}{H^2} \tag{2.122}$$

In multifield inflation, besides defining $\mathcal{R}$ as in eq.(2.120), it is possible to define an equivalent quantity for the adiabatic mode, the *isocurvature perturbation* $\mathcal{S}$:

$$\mathcal{S} = \frac{H}{\dot{\varphi}} Q_N. \tag{2.123}$$

This can be used to write the first integral for ζ on super Hubble scales $k \ll aH$ as [76]

$$\mathcal{R} \approx 2\Omega\mathcal{S}. \tag{2.124}$$

Substituting the definition of $\mathcal{S}$ in the last equation, and replacing the result obtained in eq.(2.119), this becomes

$$\ddot{Q}_N + 3H\dot{Q}_N + \left(M^2 + 4\Omega^2\right) Q_N \approx 0, \tag{2.125}$$

[1] In the single field case the entropy perturbations vanish on large scale, see [76].

which can be used to define the *effective entropic mass* as

$$M_{eff}^2 = M^2 + 4\Omega^2. \tag{2.126}$$

If there is no turning rate, hence the inflationary trajectory follows a geodesic, $M_{eff}^2 = M^2$.
The relative size of M^2 and M_{eff}^2 plays a crucial role as it is related to the speed of sound for the adiabatic perturbation [66, 77, 78]:

$$c_s^{-2} = \frac{M_{eff}^2}{M^2} \tag{2.127}$$

Looking closely at eq.(2.122), the dynamics of the linear perturbations and therefore the cosmological predictions will depend on the hierarchies of the adiabatic and entropy modes' masses relative to each other, the Hubble parameter and the turning rate Ω. Moreover, the curvature of the field space manifold R might play a role, if negative and large enough, to compensate the smallness of ϵ, as this can trigger geometric destabilization of entropy modes, as described in [79].

2.3.5 Multifield inflation and Swampland conjectures

In Sec.2.3.1 we mentioned that one of the reasons for which it is important to move on from the vanilla single field models to focus on the realization of multifield models of inflation is because of the possibility to avoid the swampland conditions, as demonstrated in [57].
In this section we give a brief review of the swampland conjectures, and we show how multifield models can successfully satisfy them according to [57].
Firstly, what is the *swampland*?
By definition [80] this is the set of apparently consistent effective field theories (EFTs) which, however, *do not* have a UV completion. In other words, the EFTs belonging to the swampland meet the consistency requirements for low energy observers, but result inconsistent with a quantum gravity theory. Theories which instead can be UV completed belong to the *landscape*.

Over the years people proposed different guidelines to discern between swampland and landscape ETFs, however most of these criteria are *conjectures*, not being supported by rigorous proofs.

The conjectures we are concerned about for the rest of the thesis, given their consequences for a possible inflationary scenario, are the *Swampland distance conjecture* (SDC), presented in [81], and *de Sitter swampland conjectures* (dSCs), presented in [55] and then revisited in [56]:

1. The SDC states that the field range traversed by the fields in field space has to be smaller of a constant Δ of order 1

$$\Delta\phi < \Delta \sim \mathcal{O}(1). \tag{2.128}$$

   If this condition is not satisfied the low energy description of the theory can no longer be a valid approximation for the theory itself due to quantum gravity effects.

2. The dSCs suggest that, given the difficulty in constructing meta-stable dS vacua in string theory, *all* dS solutions belong to the swampland. In [55], this idea is formalized conjecturing that the scalar potential V of any low energy theory of a consistent quantum gravity origin, has to satisfy:

$$\frac{|\nabla V|}{V} \geq \frac{c}{M_{Pl}} \tag{2.129}$$

   where $c \geq 0$ and it is of order 1 in Plank units. This condition restricts both de Sitter minima *and* maxima to be in the swampland.
   In [56] the authors proposed a refined version of this conjecture using the SDC (eq.(2.128)) and the covariant entropy bound [82]:
   a potential V for scalar fields in a low energy effective theory with a consistent UV completion has to satisfy either

$$|\nabla V| \geq \frac{c}{M_{Pl}} V \tag{2.130}$$

or

$$\min(\nabla_i \nabla_j V) \leq -\frac{c'}{M_{Pl}^2} V \tag{2.131}$$

where $c, c' > 0$ and of order 1.
Note that, using the definition for the second slow-roll parameter $\eta_V = V''/V$, eq.(2.131) implies that $\eta_V \leq -c'/M_{Pl}^2$, hence the redefined version accepts dS maxima.

The cosmological implications of the conjectures in eq.(2.128) and eq.(2.129) have been studied in [83], where the authors proved that inflationary models are generally in tension with these criteria:

1. The field displacement $\Delta\phi$ can be written as

$$\Delta\phi \sim \sqrt{2\epsilon} N_{end} \sim \sqrt{2} N_{end}^{1-k/2} \tag{2.132}$$

where $N_{end} \geq 60$, $\epsilon = r/16 \sim 1/N_{end}^k$ and $k = 1, 2$ depending on the inflation potential[1]. Therefore, assuming the minimum number of efolds $N_{end} \sim 60$, it results $\Delta\phi \geq 5$, already in contrast with the SDC.

2. From eq.(2.53), eq.(2.129) becomes

$$\sqrt{2\epsilon_V} \geq \frac{c}{M_{\rm Pl}}, \tag{2.133}$$

but $\epsilon_V \geq \mathcal{O}(1)$ violates the first slow-roll condition.

However in [84] and [57] the authors showed that, while the analysis conducted in [83] argues that single field model of inflation are in tension with the swampland criteria (2.128) and (2.129), multifield models can circumvent them. In [84] the authors focused on solving the SDC conjecture. Eq.(2.128) has been derived for single inflation model, when the inflationary trajectory follows a geodesic. However, in presence of more than one field, the inflationary trajectory can be non geodesic, and in [84] the authors derived a relation between the geodesic and non-geodesic field displacements. In particular they showed that there exists, for

[1] $k = 1$ if the potential scale roughly like an exponent or a power-law to leading order in ϕ, $k = 2$ if $V(\phi)$ is nearly constant during inflation.

non-geodesic inflationary trajectories, a set of parameters which can simultaneously satisfy both the SDC and the Lyth bound.
In [57], the authors focused on the original dSC conjecture.
In multifield models, as seen in Sec.2.3.3.1, it is possible to have SRST or SRRT inflation, depending on the value of the turning rate parameter Ω/H, which allows to discern between ϵ and ϵ_V, as can be seen in eq.(2.110):

$$\epsilon_V \simeq \epsilon \left(1 + \frac{\Omega^2}{9H^2}\right) \tag{2.134}$$

In particular, in the SRRT case $\Omega/H \gg 1$ and it is possible to have $\epsilon \ll 1$ and $\epsilon_V \sim \mathcal{O}(1)$.

Furthermore, considering eq.(2.132) and eq.(2.134), it follows that both the conjectures are satisfied if

$$\frac{\Omega}{H} \geq 3\sqrt{\left(\frac{cN_{end}}{\Delta}\right)^2 - 1}, \tag{2.135}$$

which can be satisfied by having $\Omega/H \geq 180$, considering $c/\Delta \sim 1$ and $N_{end} \sim 60$.

2.4 Multifield inflation in supergravity

The Standard Model of particle (SM) summarizes, as of today, our best understanding of elementary particle physics.
However it is now well known that the SM is an incomplete theory: it does not account for gravity and it does not give an explanation for dark matter nor dark energy and for neutrino oscillations.
Moreover, the SM presents additional problems: the cosmological constant problem [85], the Higgs mass hierarchy problem [86] and the strong CP problem, see [87] for a review. All of these problems arise as we cannot explain the magnitude of coefficients of relevant and marginal operators involved in the renormalization process.
In particular, the cosmological constant problem and the Higgs mass hierarchy

one, are related to the concept of *naturalness*: this asks for the value of the cosmological constant and the bare Higgs mass to be "natural" and not fine-tuned.

Supersymmetry (SUSY) is an extension of the SM which can provide an answer to some of these problems. SUSY postulates a new symmetry in the theory, which relates bosons and fermions introducing new particles: in particular, in this theory each particle from one class has an associated particle in the other.

The supersymmetric particles are the key to solve the hierarchy problem as explained in [88, 89]. At loop level the Higgs mass receives contributions from self interactions, gauge loops and fermion loops, especially the heaviest, i.e the top quarks, which are divergent and proportional to a cut-off scale Λ^2. Considering $\Lambda \sim M_{Pl}$, the Higgs mass comes to be incredible heavy, but the mass measured by LHC is "only" $\sim$ 125Gev. To explain this discrepancy, the Higgs *bare mass* is required to be (almost) exactly as large as the mass corrections, which would be "unnatural".

However, if we include the supersymmetric particles in this computation, the quantum corrections due by the fermions are (almost) exactly canceled by those of their superpartners; in this way the Higgs bare mass does not need to be fine tuned. Moreover, supersymmetric partners include some electrically neutral and light particles (LSPs) which are good candidates for dark matter.

Combining principles of SUSY and general relativity, which is not included in the SM, Freedman, Ferrara and Nieuwenhuizen constructed the minimal version of 4D Supergravity (SUGRA), a gauged local version of SUSY, [90, 91]. SUGRA, which can be embedded in a UV complete theory and includes gravity, would govern the dynamics of the early Universe and therefore it seems quite natural to extend the idea of inflation in the context of SUGRA.
The inflationary models developed in this context will naturally be multifield models of inflation, and this is the subject of the next subsection.

2.4.1 Generalities

To build an inflationary model from a high-energy theory it is necessary to derive the Lagrangian for $\mathcal{N} = 1$ $D = 4$ supergravity theory.
The scalar part of the Lagrangian is determined by three functions: the Kähler

potential $K(\Phi^i, \bar{\Phi}^i)$, which provides the kinetic term, the superpotential $W(\Phi^i)$, which describes the interactions of the scalar fields, and a gauge kinetic function $f(\Phi^i)$, which provides the coupling between the scalars and the gauge fields. Note that W and f are holomorphic functions of the complex scalar fields Φ^i, while K depends on both Φ^i and their conjugate $\bar{\Phi}^i$.
The action of complex scalar field minimally coupled to gravity is [92]

$$S = \int d^4x\sqrt{-g}\left[\frac{1}{\sqrt{-g}}\mathcal{L}_\Phi - V(\Phi^i, \bar{\Phi}^i)\right] \tag{2.136}$$

where

$$\frac{\mathcal{L}_\Phi}{\sqrt{-g}} = -K_{i\bar{j}}\partial_\mu\Phi^i\partial^\mu\bar{\Phi}^{\bar{j}}. \tag{2.137}$$

and $i, j = 1, ..., n$. In the above equation $K_{i\bar{j}}$ is the Kähler metric, which can be defined as

$$K_{i\bar{j}} = \frac{\partial^2 K}{\partial\Phi^i\partial\bar{\Phi}^{\bar{j}}} \tag{2.138}$$

From the properties of the Kähler manifolds, see [93],

$$K_{\bar{i}j} = K_{\bar{j}i}, \quad K_{ij} = K_{\bar{i}\bar{j}} = 0 \tag{2.139}$$

The scalar potential $V(\Phi^i, \bar{\Phi}^i)$ is given by

$$V = V_F + V_D \tag{2.140}$$

$$V_F = e^K\left(K^{i\bar{j}}D_iWD_{\bar{j}}\bar{W} - 3|W|^2\right) \tag{2.141}$$

$$V_D = \frac{1}{2}\sum_a \frac{1}{Re(f_a(\Phi^i))}g_a^2D_a^2 \tag{2.142}$$

where $K^{i\bar{j}}$ is the inverse of the Kähler metric, D_iW and its conjugate are defined as

$$D_iW = \frac{\partial W}{\partial\Phi^i} + \frac{\partial K}{\partial\Phi^i}W, \qquad D_{\bar{j}}\bar{W} = \frac{\partial\bar{W}}{\partial\bar{\Phi}^{\bar{j}}} + \frac{\partial K}{\partial\bar{\Phi}^{\bar{j}}}\bar{W}, \tag{2.143}$$

g_a is a gauge coupling constant and D_a is a Killing potential.
In the following chapters we will take into account only the V_F term, hence the

total potential V reduces to

$$V = e^{K/M_{Pl}^2}\left(K^{i\bar{j}} D_i W D_{\bar{j}} \bar{W} - 3|W|^2 M_{Pl}^2\right) \tag{2.144}$$

To study inflation in this framework, we consider a FLRW spacetime, see eq. (2.2), and the equations of motion for the scalar fields can be written, in analogy with eq.(2.74), as

$$\ddot{\Phi}^i + 3H\dot{\Phi}^i + \Gamma^i_{jk}\dot{\Phi}^j\dot{\Phi}^k + K^{i\bar{j}}V_{\bar{j}} = 0 \tag{2.145}$$

$$\ddot{\bar{\Phi}}^{\bar{i}} + 3H\dot{\bar{\Phi}}^{\bar{i}} + \Gamma^{\bar{i}}_{\bar{j}\bar{k}}\dot{\Phi}^{\bar{j}}\dot{\Phi}^{\bar{k}} + K^{\bar{i}j}V_j = 0. \tag{2.146}$$

The only Christoffel symbols in the above equations are Γ^i_{jk} and $\Gamma^{\bar{i}}_{\bar{j}\bar{k}}$ since they are the only non-null Christoffel for a Kähler manifold [93]:

$$\Gamma^i_{jk} = K^{i\bar{l}}\partial_j K_{k\bar{l}}, \qquad \Gamma^{\bar{i}}_{\bar{j}\bar{k}} = K^{\bar{i}l}\partial_{\bar{j}} K_{\bar{k}l} \tag{2.147}$$

The simplest realization of inflation in a SUGRA framework is the *sGoldstino inflation* [94–96], a minimal inflationary scenario which involves a single superfield Φ, hence two real scalar fields. The sGoldstino is the scalar partner of the goldstino and belongs to the chiral superfield which F-term breaks SUSY, thus it can be identified with the sGoldstino field, meaning that *the inflaton and the sgoldstino are aligned*. However this type of inflation is not easy to realize and in [97, 98] the authors showed that the model proposed in [96] is only possible with severe restrictions. An example of this will be studied in Chapter 4.
To avoid these restrictions, the next possibility is to introduce a second superfield. The pioneering model in this sense is presented in [99] where the authors included next to Φ a second superfield S. Adding a term proportional to $(S\bar{S})^2$ to the Kähler potential it is possible to stabilize $\mathrm{Im}(\Phi)$ and S, so that inflation can take place along $\Phi - \bar{\Phi} = S = 0$ direction. In this model the superfield S, which belong to the sGoldstino direction, is *orthogonal* to the inflationary direction.
Building on this model, in [100] the authors proposed a new class of models of chaotic inflation in SUGRA, which included previous work presented in [101–104], where the inflaton potential can be modified defining $W = Sf(\Phi)$ and choosing

arbitrarily the function $f(\Phi)$.
The same authors, in [105], proposed a strategy to realize single field inflation in SUGRA with an arbitrary inflaton potential $V(\phi)$, along the direction orthogonal to the sGoldstino. As in the previous case the inflaton is $\mathrm{Re}(\Phi) = \phi$. The Kähler potential and the superpotential are generalized to

$$K = K((\Phi - \bar{\Phi})^2,\ S\bar{S},\ S^2,\ \bar{S}^2), \qquad W = Sf(\Phi) \tag{2.148}$$

so that K is separately invariant under

$$S \to -S, \quad \Phi \to -\Phi, \quad \Phi \to \Phi + a, \quad a \in \mathbb{R} \tag{2.149}$$

and inflaton potential $V(\phi)$ has always the form

$$V(\phi) = |f(\phi)|^2 \tag{2.150}$$

They also show that, in this class of models, the other three scalar fields, $\mathrm{Im}(\Phi)$ and S, can be stabilized at the inflationary trajectory with a suitable choice of Kähler potential.
Another possibility is presented in [106] where the sGoldstino was eliminated by introducing a nilpotent condition to the goldstino superfield.
Finally, it is worth mentioning that an additional possibility to build an inflationary model in SUGRA using two superfields, is to combine two real (or imaginary) fields from two different superfields, e.g. using $\mathrm{Re}(\Phi)$ and $\mathrm{Im}(S)$ or any other combination. In this case the inflationary model would be a two-field inflation.

In chapter 4 we focus on the orthogonal models of inflation, introducing the nilpotent condition to set $S = \bar{S} = 0$.

2.5 η problem

In the standard scenario, to have a successful inflationary model, the inflaton has to be *light*, i.e

$$M_{Inf}^2 \ll H^2. \tag{2.151}$$

This condition applies to both single and multi-fields models.

In single field inflation, Sec.2.2.3, this constraint is a direct consequence of the second slow-roll condition eq.(2.53)

$$\eta_V \equiv M_{Pl}^2 \left| \frac{V''}{V} \right| \sim \frac{M_{Inf}^2}{3H^2} \ll 1 \tag{2.152}$$

which directly implies

$$M_{Inf}^2 \ll H^2. \tag{2.153}$$

Therefore, to realize inflation, the following inequality has to hold

$$M_{Inf} < H < M_{heavy}. \tag{2.154}$$

Note that the above equation has to hold also for tachyonic model of inflation.

In an EFT theory of inflation however the inflaton mass is subject to corrections produced by higher dimension operators [107].

To understand this, let us write the EFT Lagrangian minimally coupled to gravity

$$S_{eff}(\phi) = \int d^4x\sqrt{-g}\left[\frac{M_{Pl}^2}{2}R + \mathcal{L}_c + \sum_i c_i \frac{\mathcal{O}_i(\phi)}{\Lambda^{\delta_i-4}}\right] \tag{2.155}$$

where $\mathcal{L}_c$ includes canonical terms and renormalizable interactions while the summation includes all the operators $\mathcal{O}_i$ consistent with the considered symmetries of the UV theory, which parameterizes the effects of massive fields on the EFT of light ones. Usually these terms are irrelevant corrections to the leading dynamics of the system which we are considering, however when realizing EFTs of inflation some of these operators become incredibly important: they can change the zeroth order dynamics, bringing a correction to the inflaton mass and no symmetry prohibits their appearance [108–111].
In particular, the flatness of the potential $V(\phi)$, is particularly sensitive to Planck-suppressed operators with dimension $\delta_i \geq 6$

$$\mathcal{O}_{\delta_i \geq 6} = cV(\phi)\left(\frac{\phi}{M_{Pl}}\right)^{\delta_i-4}. \tag{2.156}$$

If $c \sim \mathcal{O}(1)$ this correction modifies the potential of a small quantity $\Delta V \ll V$. However, provided that $\phi < \Lambda$ since its vev is smaller than the cut-off energy, the variation for η_V, $\Delta\eta$, is anything but negligible and it reads as:

$$\Delta\eta \sim c\,(\delta_i - 4)\,(\delta_i - 5)\left(\frac{M_{Pl}}{\Lambda}\right)^2\left(\frac{\phi}{\Lambda}\right)^{\delta_i - 6} \sim \mathcal{O}(1). \tag{2.157}$$

This can be neglected only if $\delta_i \gg 6$. Therefore, for $c \sim \mathcal{O}(1)$ and $\Lambda < M_{Pl}$ the theory suffers from the eta problem.

2.5.1 η problem in SUGRA

In $\mathcal{N} = 1$ SUGRA the Lagrangian for inflation can be written as [112]

$$\mathcal{L} \approx -K_{i\bar{j}}\partial\Phi^i\partial\bar{\Phi}^{\bar{j}} - e^{K/M_{Pl}^2}\left(K^{i\bar{j}}D_iW\,D_{\bar{j}}\bar{W} - \frac{3}{M_{Pl}^2}|W|^2\right). \tag{2.158}$$

where $\Phi_i = (\Phi_1, \Phi_2, ..., \Phi_n)$. It is always possible, at any point in the scalar fields space, make a field redefinition such that the scalar fields have canonically normalized kinetic terms at that point [112]. In the specific case of a single complex field Φ, expanding the Kähler potential in a neighborhood of that point, this can be written as

$$K = |\Phi|^2 + ... \tag{2.159}$$

It follows that the F-term potential can be written as[1]

$$\begin{aligned} V &= e^{|\Phi|^2 + \cdot\cdot}\left[(1 + ...)\left(W_\Phi + W\left(\bar{\Phi} + ...\right)\right)\left(\bar{W}_{\bar{\Phi}} + \bar{W}\left(\Phi + ...\right)\right) - 3W\bar{W}\right] \\ &= V_0\left(1 + \Phi\bar{\Phi} + ...\right) \end{aligned} \tag{2.160}$$

and computing the slow-roll parameter η_V, we obtain

$$\eta_V \sim \frac{V''}{V} = 1 + ... \tag{2.161}$$

[1]Here we are not explicitly showing $M_{\rm Pl}$.

Thus the second slow-roll condition $|V''/V| \ll 1$ is not satisfied. This computation can be easily generalized to n superfields, see [92], therefore any generic inflationary model in $\mathcal{N} = 1$ SUGRA seems to inevitably suffer from the η problem.

Different approaches have been proposed to evade this problem thus far: tuning in W, see for example [113–115], or using particular choices for K [116, 117] or impose some symmetries on both K and W to guarantee the flatness of the potential [99, 100, 105] and the use of D-term potential [118, 119].

In chapter 4 we give a further interpretation and possible solution to this problem.

Chapter 3

Fat inflation, Large Turns and the η problem

This chapter is based on part of the work published in [6].

As mentioned in Sec.2.5, it is commonly believed that a successful period of inflation, in both single field and multifield models, requires a specific hierarchy of masses, that is

$$M_{Inf} \ll H \ll M_{heavy} \tag{3.1}$$

where M_{Inf} can correspond to several or a single *light* field and M_{heavy} corresponds to any *heavy* field which can be integrated out if it satisfies suitable conditions. In this chapter however, we show that, while this is an unavoidable conclusion in single field inflation, in multifield inflation, *heavy* fields as defined above, may be *fully* responsible for a successful period of inflation which we refer to as *fat slow-roll inflation*. This can be proven starting from the multifield equations of motion in the kinetic base, eq.(2.82) and (2.83), and simply implementing the slow-roll conditions.
As we see in Sec.3.2 this type of inflationary attractor requires for the dimensionless turning rate to be larger than 1, i.e. $\Omega/H > 1$, hence fat slow-roll inflation follows highly non-geodesic trajectories.

The chapter is organized as follow. In sec.3.1 we introduce the reasons which

bring us to focus on rapid-turn multifield models and present the main question we attempt to answer in [6].
In Sec.3.2 we introduce the new fat inflationary attractor, show how it requires large turning rates and discuss its consequences on the dynamics of the linear perturbations. In Sec.3.3 we describe how to construct such a model in the two fields case and we present some field theory models already appeared in the literature which happen to belong to the fat inflationary attractor. In Sec.3.4 we comment on the connection between fat inflation and the swampland conjecture. Finally we end by discussing our findings and future directions in Sec.3.5.

3.1 Introduction

In Sec.2.2.1 it has been discussed how cosmological inflation [30, 31, 120] has been introduced to solve the problems of the SCM and it was shown, see Fig.2.6, how some of the most studied inflationary models agree with the most recent observations performed by the Planck satellite [1, 2, 47].
Observations are fully consistent with the simplest inflationary scenario, i.e the single field model, as the leading mechanism to account for the origin of the anisotropies in the CMB radiation and, thus, the formation of the large scale structures. In particular, they agree with two robust predictions of inflation, that is, a nearly scale invariant spectrum of density perturbations, i.e $n_s \sim 1$, and a stochastic background of gravitational waves.
However, there are several reasons to study more complex inflationary models involving more than one scalar field, as described in Sec.2.3.1. Therefore, it becomes essential to move on from the vanilla single field models, both from theoretical and experimental points of view, to understand what scenarios and observables we may expect from more complex models.

In this chapter we take a further step in understanding multifield inflation [1] in view of forthcoming experimental efforts as well as recently proposed theoretical constraints.

[1] Multifield inflation has been extensively studied over the last 20+ years. Thus the existing literature is vast and it would be impossible to include every reference in the present chapter. We therefore only refer to those papers which are most relevant for our present discussion.

Our starting discussion is motivated by the following simple question: *given a multiscalar Lagrangean, what are the conditions that the parameters and fields need to satisfy in order to drive a period of successful slow-roll inflation?*
We show that contrary to usual belief, a long period of slow-roll inflation does *not* require any of the scalar fields' masses to be light (w.r.t. the Hubble scale), that is $M_{inf} < H < M_{heavy}$. On the contrary, we show that slow-roll inflation is possible also when the masses of *all* scalar fields are heavier than the Hubble scale, that is

$$H \ll M^a_{Inf}, \quad \text{for all fields,} \quad a = 1, .., n \tag{3.2}$$

We call this new type of inflationary attractor *fat inflation* to stress the fact that it is the mass of the scalar fields themselves which is heavy (w.r.t. the Hubble scale)[1]. As we will show, fat inflation belongs to the recently discussed rapid-turn attractors [121] since it requires *large dimensionless turning rates*

$$\frac{\Omega}{H} \gg 1. \tag{3.3}$$

Summarising, our most important finding is that the existence of a fat inflation attractor suggests that the η-problem, which arises when large contributions to the masses of the scalar fields spoil standard slow-roll inflation, can be evaded thanks to the large turning rates [2].

3.2 Fat Inflatons and large turns

The general framework for multifield models of inflation is described in Sec.2.3.2, therefore in the first part of this section we simply review the main equations.

[1] A lot of work was been done regarding the hierarchy of the fluctuations's masses, which can be classified into adiabatic and entropic. Depending on the masses of the perturbation modes, heavy fields (with respect to the Hubble scale) may, or not, have a strong effect on the cosmological predictions [66, 67, 77, 78]

[2] For an example of single field inflation where the η-problem is avoided with a fat inflaton in the framework of warm inflation see [122, 123].

Assuming a FLRW metric the equations of motion are

$$H^2 = \frac{1}{3M_{Pl}^2}\left(\frac{\dot{\varphi}^2}{2} + V(\phi^2)\right)$$
$$\ddot{\phi}^a + 3H\dot{\phi}^a + \Gamma^a_{bc}\dot{\phi}^b\dot{\phi}^c + G^{ab}V_b = 0$$

where $\dot{\varphi}^2 \equiv G_{ab}\dot{\phi}^a\dot{\phi}^b$ and G_{ab} is the field space metric.
The same equations, projected onto the kinematic base $\{T^a, N^a\}$, see eq.(2.79) and (2.80), can be written as

$$\ddot{\varphi} + 3H\dot{\varphi} + V_T = 0 \tag{3.4}$$
$$D_t T^a = -\frac{V_N}{\dot{\varphi}}N^a \equiv -\Omega N^a. \tag{3.5}$$

where the turning rate Ω has been defined in terms of the potential projection onto N^a, V_N. Note that at this point we are focusing on the two field case.

Starting from the last two equations, in this section we aim to answer to the question presented in the introduction and to show how, in doing that, it can be proven that heavy fields can give rise to slow-roll inflation without incurring in the η problem.
The first step is to carefully analyse the conditions that a multifield scalar theory needs to satisfy to drive a successful period of inflation [1].
In Sec.2.2.1 we introduced the slow-roll conditions, which ensure that the phase of nearly exponential expansion has a slowly changing Hubble parameter and that it lasts enough time for the SCM problems to be solved. From Sec.2.3.3, these conditions read as

$$\epsilon \equiv -\frac{\dot{H}}{H^2} = \frac{\dot{\varphi}^2}{2M_{Pl}^2H^2} \ll 1 \quad \Rightarrow \quad \dot{\varphi}^2 \ll V \tag{3.6}$$
$$\eta \equiv \frac{\dot{\epsilon}}{\epsilon H} = \frac{\ddot{H}}{H\dot{H}} + 2\epsilon = 2\frac{\ddot{\varphi}}{H\dot{\varphi}} + 2\epsilon \ll 1 \quad \Rightarrow \quad \ddot{\varphi} \ll H\dot{\varphi} \tag{3.7}$$

[1] See [124] for related work.

An additional slow-roll parameter, ξ, can be defined as

$$\xi \equiv \frac{\dot{\eta}}{H\eta} = \frac{\dddot{H}}{H^2\ddot{H}} + \mathcal{O}(\epsilon,\eta) \sim 2\frac{\dddot{\varphi}}{H^2\dot{\varphi}} \ll 1 \quad \Rightarrow \quad \dddot{\varphi} \ll H^2\dot{\varphi} \tag{3.8}$$

From the slow-roll conditions, the Friedmann equation and eq.(3.4) reduce to the following expressions, see Sec.2.3.3:

$$H^2 \simeq \frac{V}{3M_{Pl}^2} \tag{3.9}$$

$$3H\dot{\varphi} + V_T \simeq 0, \quad \Rightarrow \quad \dot{\varphi} = -\frac{V_T}{3H} \tag{3.10}$$

Therefore, the slow-roll equations to solve at the background level are eq.(3.9), (3.10), and (3.5).
Before moving forward, let us briefly recall why in the single field case, the slow-roll conditions imply that the mass of the inflaton has to be much smaller than the Hubble scale, see Sec.2.5. For the single field case, we simply consider φ as the inflaton, $V_T = V_\varphi = V'$ and there is no third equation eq.(3.5). The slow-roll conditions eq.(3.6) and eq.(3.7) simplify to the potential slow-roll conditions

$$\epsilon_V \equiv \frac{M_{Pl}^2}{2}\left(\frac{V'}{V}\right)^2 \ll 1, \quad \eta_V \equiv M_{pl}^2\left|\frac{V''}{V}\right| \ll 1 \tag{3.11}$$

thus the smallness of the η parameter implies $M_{Inf}^2 \sim V'' \ll H^2$.

In the following we are going to show how, only using the slow-roll approximation, this conclusion can be avoided in the multifield case.
First, as seen in Sec.2.3.3.1, in multifield inflation it is possible to define ϵ_T and ϵ_V as

$$\epsilon_T \equiv \frac{M_{Pl}^2}{2}\left(\frac{V_T}{V}\right)^2, \quad \epsilon_V \equiv \frac{M_{Pl}^2}{2}\frac{V_a V^a}{V^2} \tag{3.12}$$

where the slow-roll condition eq.(3.6) implies that $\epsilon_T \ll 1$.
The next step is to use the slow-roll-approximation to relate the dimensionless turning rate Ω/H with the scalar fields' masses to study their scale w.r.t H^2.

Taking the time derivative of eq.(3.10), this becomes:

$$3\dot{H}\dot{\varphi} + 3H\ddot{\varphi} + (V_T)^{\cdot} \simeq 0 \quad \rightarrow \tag{3.13}$$

$$3\dot{H}\dot{\varphi} + 3H\ddot{\varphi} + \dot{T}^a V_a + T^a V_{ab}\dot{\phi}^b \simeq 0 \tag{3.14}$$

which, knowing that $T^a V_{ab}\dot{\phi}^b = T^a T^b V_{ab}\dot{\varphi}$, gives the following expression for $\ddot{\varphi}$:

$$\ddot{\varphi} \simeq -\frac{1}{3H}\left[\frac{3}{2}\frac{\dot{\varphi}^2}{M_{pl}^2}\dot{\varphi} + T^a T^b V_{ab}\dot{\varphi} + \left(D_t T^a + \Gamma^a_{bc} T^b \dot{\phi}^c\right)\right] \tag{3.15}$$

where we also used that $D_t T^a = \dot{T}^a + \Gamma^a_{bc} T^b \dot{\phi}^c$ and $\dot{H} = -\dot{\varphi}^2/(2M_{Pl}^2)$.
To rewrite this expression in terms of the projection of the potential onto the tangent trajectory, let us define

$$V_{TT} \equiv T^a T^b \nabla_a \nabla_b V = T^a T^b V_{ab} - T^a T^b \Gamma^k_{ab} V_k. \tag{3.16}$$

Substituting this expression in eq.(3.15), and using the definition of $\Omega = V_N/\dot{\varphi}$, from eq.(3.7)

$$\ddot{\varphi} = -\frac{\dot{\varphi}}{3H}\left[\frac{3}{2}\frac{\dot{\varphi}^2}{M_{Pl}^2} + V_{TT} - \frac{\Omega V_N}{\dot{\varphi}}\right] \ll H\dot{\varphi} \tag{3.17}$$

$$\Rightarrow \quad -M_{Pl}^2\frac{V_{TT}}{V} + \frac{\Omega^2}{3H^2} + \epsilon \ll 1 \tag{3.18}$$

where we also used eq.(3.9).
Since $\epsilon \ll 1$ we arrive at the first important result, that is :
slow-roll multifield inflation implies[1]:

$$\left|-M_{Pl}^2\frac{V_{TT}}{V} + \frac{\Omega^2}{3H^2}\right| \ll 1 \tag{3.19}$$

which means

$$M_{Pl}^2\frac{V_{TT}}{V} \simeq \frac{\Omega^2}{3H^2}. \tag{3.20}$$

Before moving further it is worth to highlight that the only simplifications used

[1] A similar expression appeared in footnote 9 of [3] without derivation. In this paper, large turn models were not discussed.

to obtain this result are the slow-roll conditions. In particular there has been no assumptions on the fields masses.

Clearly eq.(3.20) can be satisfied when both terms on the left hand side are small. However, a much more interesting possibility arises when the two terms on the left hand side are large and cancel each other. This of course requires that $V_{TT} > 0$. In the following we analyse the physical implication of having a large value of V_{TT}/H^2.
Let us call the minimal eigenvalue of the field's mass matrix λ, i.e

$$\lambda \equiv \min\left(\nabla^a \nabla_b V\right). \tag{3.21}$$

where we used the general definition of the mass matrix provided in eq.(2.86).

Given any unit vector U^a, the following relation holds

$$\lambda \leq U_a \left(\nabla^a \nabla_b V\right) U^b \tag{3.22}$$

Taking $U^a = T^a$, which is legit since the tangent vector defined in eq.(2.79) is normalized, the above equation can be rewritten as

$$\lambda \leq V_{TT}. \tag{3.23}$$

Suppose now that $H^2 \ll \lambda$, meaning that *all the scalar fields* are heavier than the Hubble scale. It follows

$$H^2 \ll \lambda \quad \Rightarrow \quad H^2 \ll V_{TT} \quad \Rightarrow \quad M_{Pl}^2 \frac{V_{TT}}{V} \gg 1. \tag{3.24}$$

Therefore, when the lightest scalar field is heavier than the Hubble scale $\lambda \gg H^2$, the slow-roll condition eq.(3.19) can be satisfied when the dimensionless turning rate is large, i.e

$$H^2 \ll \lambda \quad \Rightarrow \quad \frac{\Omega^2}{H^2} \gg 1 \tag{3.25}$$

which is our second important result.

Let us summarize: the multifield slow-roll condition eq.(3.19), which again, has been obtained simply applying the slow-roll conditions to the equations of motion eq.(3.4), can be satisfied when *all* the scalar fields are heavy, $\lambda \gg H^2$. We call this *fat slow-roll inflation*, and as we show above, this type of inflationary attractor requires large dimensionless turning rates Ω/H.
Note that this new inflationary attractor is also possible for tachyonically fat field, see Sec.3.3.2 hence

$$\left|\frac{\lambda}{H^2}\right| \gg 1. \tag{3.26}$$

Notice that eq.(3.19) implies a cancellation between V_{TT}/V and Ω/H, when $V_{TT} > 0$. Thus, it is possible that $V_{TT}/V > 1$ thus having large turns, while $\lambda < 0$ and small (see Sec.3.3.2 for an example of this (AAW2)). However our point is that even when all fields are heavy, slow-roll is possible and it requires large turns[1]. Let us also point out that when more than two fields are present, one can define a turning rate associated to every normal direction and they will all contribute to the total turning rate (see Sec.3.3.2 for an example (APR)).
Note that large turning rates Ω/H do not imply large Ω. Indeed, since Ω has dimensions of mass, it is measured in Planck units and thus we expect $\Omega \lesssim M_{Pl}$ in a consistent model. Let us finally note that the geodesic displacement is measured by $|D_t T| = 0$. The departure from a geodesic can be thus measured by the dimensionless Ω/H through $|D_{\rm N} T| = \Omega/H$, where we have changed to derivatives w.r.t. the number of efolds $d\mathrm{N} = Hdt$. We therefore see that fat inflation trajectories follow highly *non-geodesic* trajectories[2]. In table 3.1 in Sec.3.3.2 we list a multifield inflationary example of this type (racetrack).

[1]Recent multifield inflation investigations have pointed out that small turning rates are not necessary for a successful period of slow-roll inflation [74, 121, 125–128], as we showed explicitly above. Most of these studies focus on the case of non-zero negative curvature of the scalar manifold. As we have shown above, large turning rates do not require a non-zero scalar curvature (see Sec.3.3.2 for explicit field theory examples). Moreover, as we discuss in the main text, large turning rates are possible even when the standard hierarchy of masses holds ($M_{inf} < H < M_{heavy}$), which is not fat slow-roll inflation.

[2]In fact geodesic inflationary trajectories require very small turning rates $\Omega/H \ll 1$.

3.2.1 Dynamics of linear perturbations

As seen in Sec.2.3.4, in multifield inflation it is standard to decompose the linear perturbations Q^a in terms of the adiabatic and entropic modes Q_T, Q_N, defined as the projection of Q^a onto T_a and N_a in spatially flat gauge [64, 72, 73, 76]. Summarising, the dynamics of the primordial linear perturbations for Q_T and Q_N is given by the equations: [64, 72, 73]:

$$\ddot{Q}_T + 3H\dot{Q}_T + \left(\frac{k^2}{a^2} + m_T^2\right) Q_T = \left(2\Omega Q_N\right)^{\cdot} - \left(\frac{\dot{H}}{H} + \frac{V_T}{\dot{\varphi}}\right) 2\Omega Q_N \,, \tag{3.27}$$

$$\ddot{Q}_N + 3H\dot{Q}_N + \left(\frac{k^2}{a^2} + M^2\right) Q_N = -2\Omega\frac{\dot{\varphi}}{H}\dot{\mathcal{R}} \tag{3.28}$$

and the adiabatic mass squared m_T^2 and the entropy mass M are given by

$$\frac{m_T^2}{H^2} \equiv -\frac{3}{2}\eta - \frac{1}{4}\eta^2 - \frac{1}{2}\epsilon\eta - \frac{1}{2}\frac{\dot{\eta}}{H} \,, \tag{3.29}$$

$$\frac{M^2}{H^2} = \frac{V_{NN}}{H^2} + M_{Pl}^2\,\epsilon\,R - \frac{\Omega^2}{H^2} \,. \tag{3.30}$$

At superhorizon scales, eq.(3.28) becomes

$$\ddot{Q}_N + 3H\dot{Q}_N + \left(M^2 + 4\Omega^2\right) Q_N \approx 0 \,, \tag{3.31}$$

and it is possible to define an effective entropy mass as $M_{eff}^2 = M^2 + 4\Omega^2$, which can be used to write the speed of sound c_s for the adiabatic perturbations as [66, 77, 78]

$$c_s^{-2} = \frac{M_{eff}^2}{M^2} \,. \tag{3.32}$$

The dynamics of the linear perturbations and cosmological predictions will depend on the hierarchies of the adiabatic and entropy modes' masses relative to each other, the Hubble parameter and the turning rate Ω. The curvature of the scalar manifold R may also play an important role if negative and large, as it may trigger geometric destabilisation of the entropy modes [79].

Notice that the adiabatic mode will be light (w.r.t. H) as long as slow-roll is satisfied (see (3.29)), which is the case in the fat field inflation scenario we are

discussing. On the other hand, the mass of the entropic mode will depend on the size of Ω/H, the curvature of the scalar manifold R and V_{NN}/H^2. For example, if besides $M \gg H$, the hierarchy $M_{eff} \gg M$ holds, the speed of sound in eq.(3.32) can be reduced, with observable consequences [66, 77, 129]. Other possibilities can arise as discussed in sidetracked inflation [74] and orbital inflation [130, 131] where the mass of the entropic modes is (much) smaller than H.

Let us see what possibilities may arise in the heavy inflation model. Note first that we can take N^a as a unit vector, instead of T^a as we did above, to write an analogous inequality to eq.(3.23) in terms of V_{NN}, that is $\lambda \leq V_{NN}$. Imposing eq.(3.24) also implies that $H^2 \ll V_{NN}$, which could dominate or not over the other terms in the entropic mass (3.30).

If the scalar manifold curvature is negative and very large, M may in principle become small or even tachyonic. On the other hand, note that for the effective entropic mass to be much larger than M, ($M_{eff} \gg M$) thus having a smaller than unity speed of sound, it is necessary that Ω^2 be larger than M^2, which implies that $5\Omega^2 \gg V_{NN} + H^2\epsilon R$.

3.2.2 Fat inflation and the η-problem

Let us briefly comment on the relevance of the heavy field inflationary attractor we have discussed for the so called η-problem, see Sec.2.5. As we have shown, fat inflation has the unusual hierarchy of masses $H \ll M_{Inf}$, where M_{Inf} corresponds to the mass of the "lightest" field driving inflation. As seen in Sec.2.5, such hierarchy of masses cannot drive a period of successful inflation, since large contributions to the masses of the inflatons might spoil the required flatness and therefore slow-roll conditions required for inflation. However, we have seen that fat inflation works with *large masses* when the turning rates are large. Therefore, previous statements on inflation bases on light inflatons need to be revisited. In particular, in supergravity inflationary constraints were discussed long ago in [132], assuming the need for light fields. We leave for future work (see [7] discussed in Chapter 4) a detailed analysis of these constraints and more generally of fat inflation and large turns in supergravity.

3.3 Field theory models of fat inflation

In the first part of this section we describe how to construct the simplest field theory model for two fields leading to the fat inflation attractor with large turning rate. We then collect some field theory multifield inflation examples present in the literature which happen to be fat field inflation models. We analyse some of them in details, heightening their most important properties, and we compare them with some "light field" (that is where $M_{inf} < H$) examples also in the literature.

3.3.1 Constructing a simple two fields model of fat inflation

As discussed in Sec.3.2, when the minimal eigenvalue of the mass matrix λ is larger than the Hubble parameter, the multifield slow-roll condition is satisfied and the turning rate is large, indicating a non-geodesic trajectory, see eq.(3.19) and eq.(3.20).
It is thus clear that some interaction between the scalar fields is necessary, which can either come from the kinetic terms or the scalar potential.
To illustrate this idea, we consider a toy model in flat field space, i.e $R = 0$, in polar coordinates $\phi^a = (\rho, \theta)$. The Lagrangian and the field metric describing this model are respectively

$$\mathcal{L} = -\frac{1}{2}\left((\partial\rho)^2 + \rho^2\,(\partial\theta)^2\right) - V(\rho,\theta) \tag{3.33}$$

$$G_{ab} = \begin{pmatrix} 1 & 0 \\ 0 & \rho^2 \end{pmatrix} \tag{3.34}$$

and the only non-vanishing Christoffel symbols for G_{ab} are:

$$\Gamma^{\rho}_{\theta\theta} = -\rho, \quad \Gamma^{\theta}_{\rho\theta} = \Gamma^{\theta}_{\theta\rho} = \frac{1}{\rho} \tag{3.35}$$

The eigenvalues of the mass matrix eq.(2.87) take the simple form[1]

$$\lambda_{\pm} = \frac{1}{2}\left(V_{\rho\rho} + \frac{V_\rho}{\rho} + \frac{V_{\theta\theta}}{\rho^2} \pm \sqrt{\left(V_{\rho\rho} - \frac{V_\rho}{\rho} - \frac{V_{\theta\theta}}{\rho^2} \right)^2 + \frac{4}{\rho^2}\left(V_{\theta\rho} - \frac{V_\theta}{\rho} \right)^2} \right) \tag{3.36}$$

where V_a, V_{ab} denote partial derivatives of V with respect to the scalar fields. If we now consider a scalar potential of the form

$$V = \frac{1}{2}M^2\rho^2 + W(\theta), \tag{3.37}$$

the eigenvalues simplify to

$$\lambda_{\pm} = M^2 + \frac{W_{\theta\theta} \pm \sqrt{W_{\theta\theta}^2 + 4W_\theta^2}}{2\rho^2}. \tag{3.38}$$

As we mentioned, the fat inflationary attractor occurs when $\lambda_- > H^2 \sim V/3$. Therefore, the fat inflation condition can be satisfied when

$$M^2 + \frac{W_{\theta\theta} - \sqrt{W_{\theta\theta}^2 + 4W_\theta^2}}{2\rho^2} > \frac{1}{6}M^2\rho^2 + \frac{1}{3}W \tag{3.39}$$

which is satisfied when ρ is close to its minimum, hence $\rho \sim 0$ and for a sufficiently large value of the parameter M. Moreover, the potential for θ, $W(\theta)$, is taken such that successful inflation does indeed occur. The simplest possibility is to take $W(\theta)$ as an even monomial function of θ, for example

$$W(\theta) = \frac{m^2\theta^2}{2}, \quad M \gg m \tag{3.40}$$

$$W(\theta) = \frac{\Lambda^4\theta^4}{4}, \quad M \gg \Lambda \tag{3.41}$$

or, an other possibility includes

$$W(\theta) = \Lambda^4\left(1 + \cos m\theta\right), \quad M \gg \Lambda. \tag{3.42}$$

This last example is listed in the next section in Table 3.1 as AAW2.

[1]Here we set $M_{Pl} = 1$ for simplicity.

3.3.2 Examples of fat inflation present in the literature

In Table 3.1 we collect some examples of field theory multifield inflation models present in the literature which happen to be fat inflation models. We list the model's name, the value of Ω/H at ~ 60 efolds before the inflation ends, the mass hierarchy and scalar curvature R (note that in these models $\Omega < M_{Pl}$).
In the same table we also include a multifield supergravity "light field" inflationary example, in which the fields follow an almost geodesic trajectory, that is, where $\Omega/H \ll 1$.
The first models in 3.1, *Orbital Inflation* [130], *Spiral Inflation* [133] and *Racetrack inflation* [134], together with AAW2 [129] have all the usual mass hierarchy [1]. Compared to the other models, racetrack inflation has a very small turning rate $\Omega/H \sim \mathcal{O}(10^{-4})$ and thus follows an almost geodesic trajectory. Example AAW2, on the other hand, is characterized by $\Omega/H \sim 2$; this is possible when $V_{TT}/V > 1$ even when $\lambda < 0$ and thus smaller than H^2.
As fat inflation models with large turning rates, we show an example of two-field natural inflation model discussed in [129] (AAW1), the recent three field model in [135] (APR) and the sidetrack models in [74]. These all have large Ω/H and only the sidetrack models have a non-zero negative curvature R. In table 3.2 we show the ratio between the masses and the Hubble parameter for AAW1, APR and the sidetrack models (both the minimal an hyperbolic examples have similar mass hierarchies).
The AAW1 model has a reduced speed of sound as in this case it holds that $M_{eff} > M$, that is $\Omega > M$ with both $M, M_{eff} \gg H$. It has a relatively mild hierarchy of masses, comparable with the hyperbolic sidetrack models. The hierarchy of masses results to be way more dramatic in the APR three-field model, where it is worth noticing that the potential does not have a minimum and therefore inflation does not end.

[1] For AAW2 we use the Lagrangean presented in [129], which is a two field model with a flat scalar manifold ($R = 0$) written in polar coordinates with a potential $V = V_0\left[M^2/2(\rho-\rho_0) + (1+\cos m\theta)\right]$. For the values we give in tables 3.1, 3.2, we use the following parameters ($m = 0.002$, $\rho_0 = 0.0001$) and $M = 100$ for AAW1 while $M = 0.15$ for AAW2 in Planck units (V_0 can then be adjusted to match the amplitude of the power spectrum.

In Fig.3.1 it is possible to see the ratio between the eigenvalues and the Hubble parameter for the AAW1 model and the value of Ω/H. In Fig.3.2 we also plotted the slow-roll parameters to show that, even if $M_{Inf} > H$, both the slow-roll conditions are still valid.

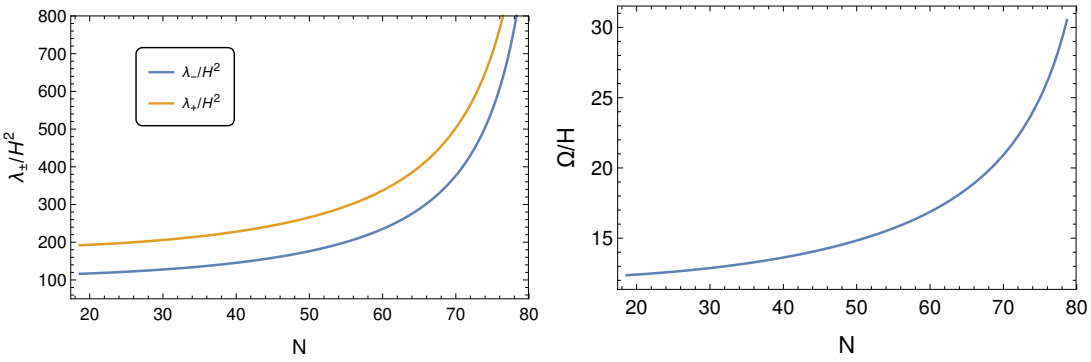

Figure 3.1: On the left: Plot of ratio between the scalar fields masses $\lambda_\pm$ and the Hubble parameter H^2 for AAW1 in 3.1. On the right: Plot of the dimensionless turning rate Ω/H for the same model.

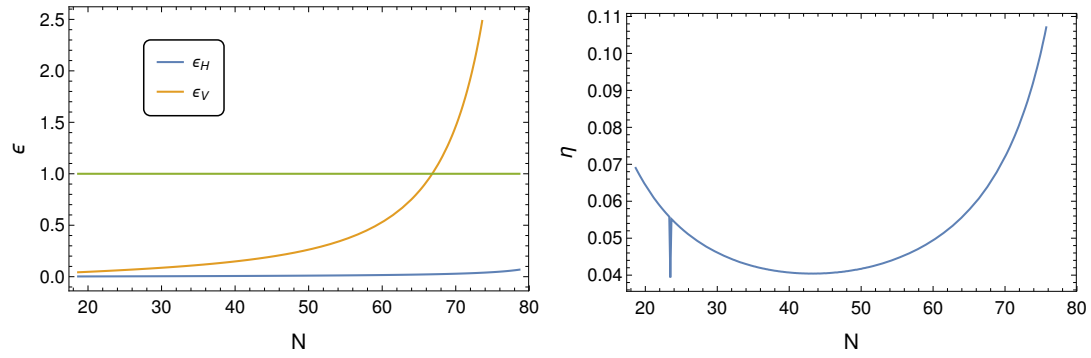

Figure 3.2: Plots of the slow-roll parameters for the example AAW1 in Table 3.1. On the left we plot the first SR parameter ϵ_H and ϵ_V. $\epsilon_H \ll 1$, hence inflation is possible, and it remains smaller than ϵ_V for all the inflationary period. On the right side we plotted η_H, which, being $\eta_H \ll 1$ ensures that inflation lasts long enough.

The sidetrack model is the only one among these three to have a negative Ricci scalar $R < 0$, and this determines a particular behavior.
In Fig.3.3 it is possible to see that, during the inflationary evolution, there is a

change of attractor. For $N \lesssim 90$, one of the the field is light, hence $\lambda_-/H^2 < 1$, while it becomes *fat* for $N \gtrsim 90$. In this model the negative scalar curvature triggers an instability which sends the light field inflationary attractor (for which $M_{Inf} < H$) to the heavy field inflationary attractor we introduced in Sec.3.2. Comparing the plot of λ_-/H^2 with the plot of Ω/H, it is clear that they have the same behavior; in particular Ω/H is small during the light field attractor while it becomes large when the fields settle into the fat field attractor.

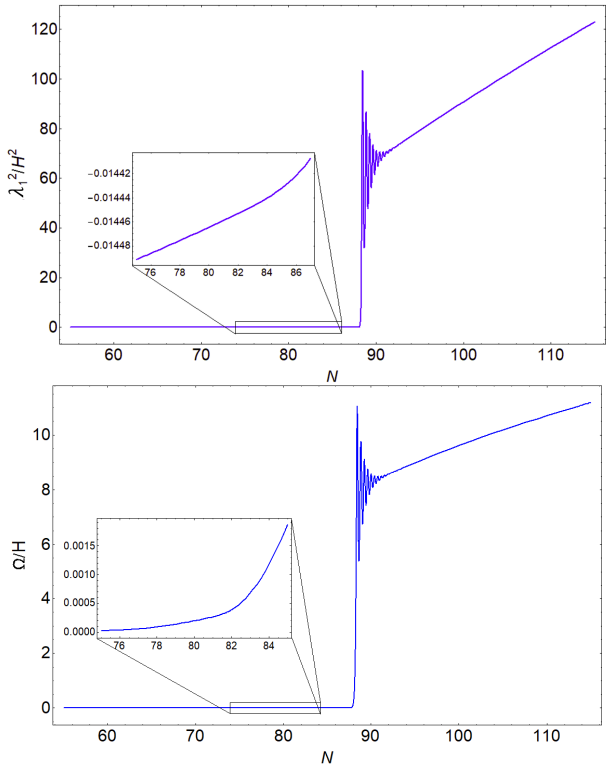

Figure 3.3: Plot of the ratio of the lightest scalar field's mass and the Hubble parameter $(\lambda_-/H)^2$ (upper) and plot of the dimensionless turning rate Ω/H (lower) for the minimal sidetrack (NI) model during the first part of inflation (inflation for this model ends for $N \sim 990$).

The plot of the the ratio $\lambda_\pm^2/H^2$ for the last 70 efolds of inflation for this model is presented in Fig.3.4. As it is possible to see, $\lambda_\pm/H^2$ present a similar behavior to the one shown in Fig.3.1, but the values of the ratio are much higher, as noted also in Table 3.1.

Finally, in Fig.3.5 we plotted the full inflationary trajectory on the potential, to highlight when, along the trajectory, the instability which causes a change in the attractor appears.

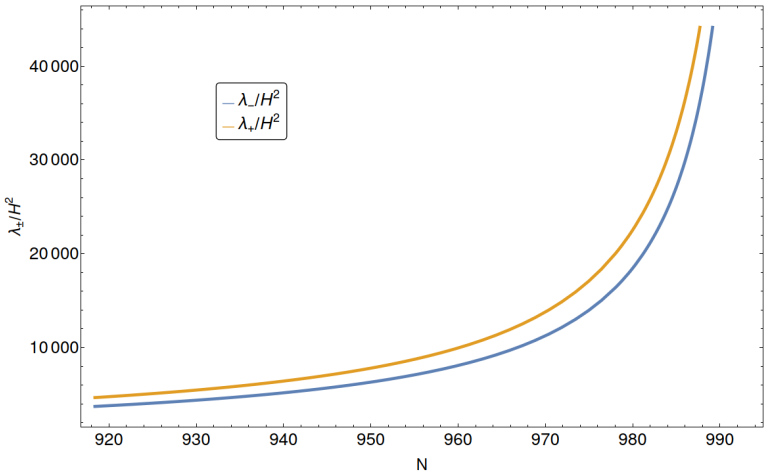

Figure 3.4: Plot of ratio between the scalar fields' masses $\lambda_\pm$ and the Hubble parameter H for the minimal Sidetrack (NI) model for the last 70 e-folds.

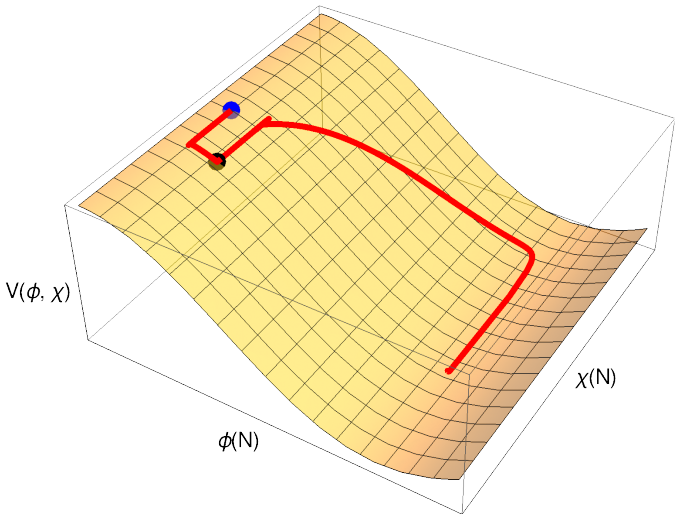

Figure 3.5: Inflationary trajectory for the minimal sidetrack (NI) model. The blue point represents the initial conditions while the black one shows where the instability due to the Ricci scalar appears.

Summarizing, for the sidetrack models, when the mass hierarchy changes from the standard $m_1 < H < m_2$ to the fat hierarchy $H < m_1 < m_2$, the Ω/H changes from $\Omega/H < 1$, to $\Omega/H > 1$. When there is this change of attractor there is also an abrupt change of direction in the inflationary trajectory, see Fig.3.5.

Finally, it is worth to briefly analyse the *Angular Inflation model* [3]. This is a supergravity inspired α-attractor and, as for the minimal sidetrack model analyzed above, has a negative curvature $R = -4/(3\alpha)$, where $\alpha > 0$, and shows a change in attractor.
The potential is relatively simple being the sum of two quadratic potential:

$$V(\phi, \chi) = \frac{\alpha}{2}\left(m_\phi^2 \phi^2 + m_\chi^2 \chi^2\right). \tag{3.43}$$

The plot of the evolution of the fields can be seen in Fig.3.6. The instability which causes a change in attractor appears for $N \sim 50$.

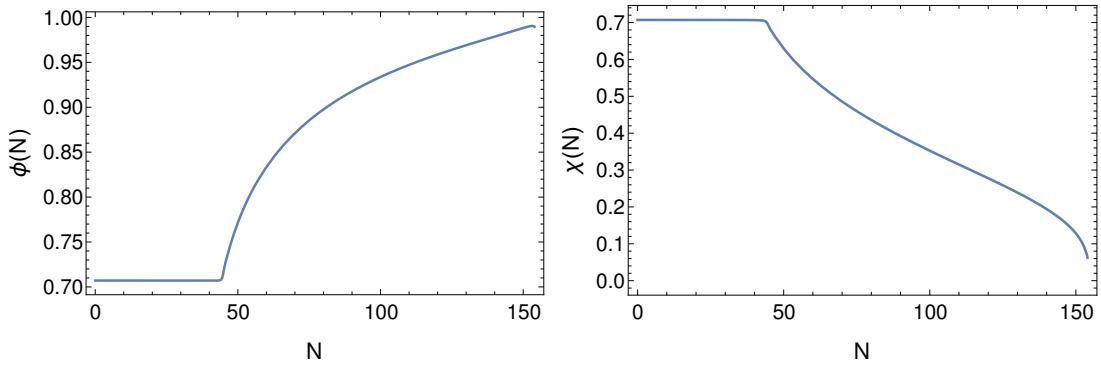

Figure 3.6: Evolution of the trajectories for the fields $\phi(N)$ and $\chi(N)$ in the angular inflation model [3]. Note that $N_{Inf} \sim 150$. Values of the parameter used: $m_\chi = m_\phi\sqrt{10}$, $m_\phi = 10$, $\alpha = 1/600$, $\phi_i = r_0 \cos\theta_0$, $\chi_i = r_0 \sin\theta_0$, $r_0 = 0.99997$, $\theta_0 = \pi/4$.

The Ω/H parameters behaves consistently, and changes drastically at $N \sim 50$ going from $\Omega/H < 1$ to $\Omega/H \sim 3$.
The evolution of the ratio $\lambda_\pm/H^2$ can be seen in Fig.3.7. In this case *both* fields are light in the first part of the inflationary evolution, however, when the attractor changes, *both* of them become fat in module, hence $H < |M|$.
This example shows that fat inflation can be realized also in models which present

tachyonic fields.

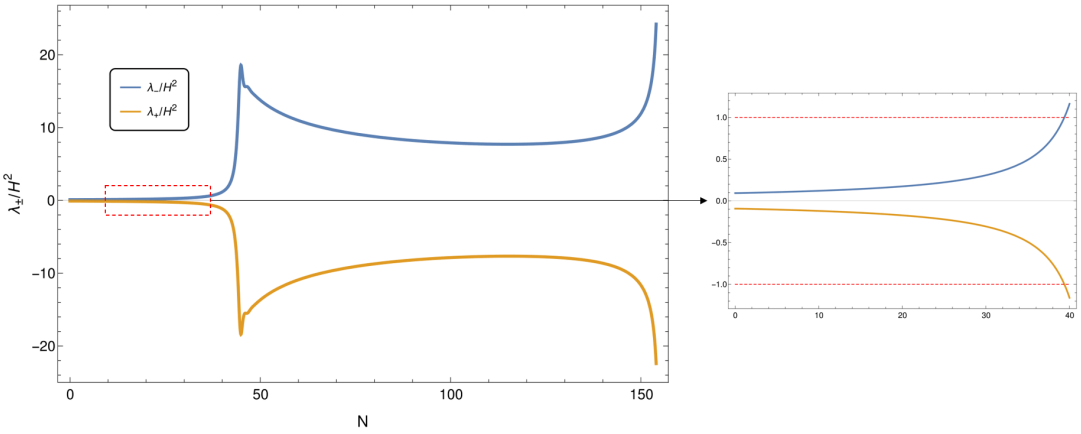

Figure 3.7: Plot of ratio between the scalar fields masses $\lambda_{\pm}$ and the Hubble parameter H for the model presented in [3]. The plot on the left shows the change of attractor at $N \sim 50$. For $N > 50$ *both* the fields are fat. On the right we show a zoomed plot of the first 50 e-fold. The dotted red lines represent $+1$ and -1. Here it is clear that both the fields are lighter than H.

3.4 Fat Inflation and the Swampland

In this section we make a connection between fat inflation and the recently proposed dSCs[1], see Sec.2.3.5, that require

$$\frac{\nabla V}{V} \geq \frac{c}{M_{Pl}} \qquad \text{or} \tag{3.44}$$

$$\frac{\min(\nabla^a \nabla_b V)}{V} \leq -\frac{c'}{M_{Pl}^2} \tag{3.45}$$

where $\nabla V \equiv \sqrt{G^{ab} V_a V_b}$ and c, c' are some $\mathcal{O}(1)$ constants. It was shown in [57] that in multifield inflation, the first condition can be satisfied, so long as Ω/H is sufficiently large, as showed in Sec.2.3.5 and in particular eq.(2.134). From this

[1] One should keep in mind that these conjectures have not been proved, and should therefore be considered with care.

Model	Ω/H	**mass spectrum**	$R(M_{Pl}^{-2})$
Orbital Inflation [130]	~ -0.2	$m_1 < m_2 < H$	0
Spiral Inflation [133]	~ -0.12	$m_1 < H < m_2$	0
Racetrack [134]	$\sim 6 \times 10^{-4}$	$m_1 < H < m_2$	$-\frac{2}{3}$
AAW2 [129]	~ 2	$m_1 < H < m_2$	0
Minimal sidetrack (NI) [74]	~ 70	$H < m_1 < m_2$	$-\frac{4\mathcal{M}^2}{(\mathcal{M}^2+2\chi^2)^2}$
Hyperbolic sidetrack (NI) [74]	~ 163	$H < m_1 < m_2$	$-\frac{4}{(\mathcal{M})^2}$
Minimal sidetrack (Staro) [74]	~ 16	$H < m_1 < m_2$	$-\frac{4\mathcal{M}^2}{(\mathcal{M}^2+2\chi^2)^2}$
Hyperbolic sidetrack (Staro) [74]	~ 150	$H < m_1 < m_2$	$-\frac{4}{(\mathcal{M})^2}$
AAW1 [129]	~ 12	$H < m_1 < m_2$	0
APR [135]	~ 61	$H < m_1 < m_2 < m_3$	0
Angular Inflation [3]	~ -2	$H < m_1 < m_2$	$-4/(3\alpha)$

Table 3.1: Inflationary models illustrating fat and light field inflation. Here $\mathcal{M}$ is the curvature scale and χ is one of the fields. For all the models (except APR) we give the value of Ω/H at the start of the last 60 e-folds before the end of inflation (where $\epsilon \sim 1$), after which these parameters increase). In the APR model inflation does not end, so the values of the parameters are given at the start of inflation. In this example, Ω decreases, while Ω/H remains almost constant (see [135]).

Model	m_3/H	m_2/H	m_1/H
Sidetrack (NI-Staro)	–	$\gtrsim 35$	$\gtrsim 30$
AAW1	–	$\gtrsim 13$	$\gtrsim 10$
APR	$\gtrsim 4500$	$\gtrsim 632$	$\gtrsim 60$
Angular	–	$\gtrsim 8$	$\gtrsim 8$

Table 3.2: Ratio of masses to the Hubble parameter for the fat inflationary models as indicated. Again, we give the value of the masses at the start of the last 60 e-folds before the end of inflation (and at the start of inflation for APR). For the angular model, we considered the absolute value of the ratio for the tachyonic field.

one sees that in a multifield inflationary model, where $\Omega \neq 0$, for sufficiently large turning rate Ω/H (and suitable values of ϵ), ϵ_V can be of order one[1].
However, eq.(2.134) does not tell us how to achieve large turns given a multifield model of inflation. We have provided an answer above in eq. (3.24) and (3.19): in order to get large turns, a sufficient condition is to consider models where

$$H^2 \ll \lambda \leq V_{TT}\,, \tag{3.46}$$

that is, multifield *fat field inflation*. Clearly in this case, the second condition (3.45) is not satisfied.
Let us also comment on another conjecture, the SDC [81], already presented in eq.(2.128), which claims that, in Planck units, $\Delta\phi \lesssim \Delta M_{Pl}$ (with $\Delta \sim \mathcal{O}(1)$) has to hold. A recent discussion on multifield inflation and the SDC has appeared in [84]. So here we simply stress that inflationary trajectories with large turning rates $\Omega/H \gtrsim 1$ differ strongly from a geodesic and thus (2.128) does not apply. Moreover, an almost geodesic trajectory requires a very small turning rate value $\Omega/H \ll 1$. (See Sec.3.3.2 for a concrete example).

3.5 Conclusion

In this Chapter we have shown that a successful period of slow-roll inflation can be achieved in multifield scenarios even when the masses of the scalar fields are heavier than the Hubble scale, that is, $H < M_{inf}$, where M_{inf} is the mass of the "lightest" field. We call this attractor *fat inflation* to stress that it is the masses of all the scalar fields which are heavier than the Hubble scale, rather than the masses of the quantum fluctuations. Indeed, in terms of the masses of the fluctuations, the mass of the adiabatic mode eq.(3.29) is given in terms of the slow-roll parameters, and therefore it is always smaller than H during slow-roll, while the isocurvature mass(es) eq.(3.30) might be heavy or light, with different cosmological implications [66, 67, 74, 77, 130].

[1]Since there is no calculation of the constant c an order one parameter can fall in a large range of values.

This is a non-trivial result, as it is commonly believed that large contributions to the masses of the inflatons causes the η-problem, see Sec.2.5, which might spoil slow-roll inflation. However, in Sec.3.2 we have seen that this can be avoided in fat inflation. In particular we showed that the slow-roll conditions, expressed as (3.19), can still be satisfied even if all the fields are fat. This scenario unavoidably requires large turning rates Ω/H and therefore non-geodesic trajectories.
In Sec.3.3 we provided a recipe to construct a fat field model in the simple setting of a flat field space in polar coordinates. In particular we showed how to fine-tune the potential and its parameters so that the smaller eigenvalues λ_- results to be $\lambda_-/H^2 > 1$.
Moreover, in Sec.3.3.2, we collected examples of field theory multifield models in the literature, which happen to belong to the fat slow-roll attractor. These include a recently discussed three field model in [135] (APR) where the lightest field is sixty times the Hubble scale, $m_1/H \gtrsim 60$, while the heaviest is thousand times heavier $m_3/H \gtrsim 4500$. Other interesting models are the sidetrack models; they show where there is a transition from a standard slow-roll trajectory with a light and a heavy field, to a fat slow-roll trajectory, with both scalar fields having larger masses than the Hubble scale. This change of attractor during the inflationary trajectory is present also in the angular inflation. However for this model one of the field is fat but tachyonic.
In conclusion, fat inflation thus *evades* the η-problem with large turns in multifield scenarios. Moreover, this type of attractor opens up a new possibility for multifield inflation in which large turns and thus non-geodesic motion are unavoidable, with interesting implications for the dS swampland conjectures and possible cosmological implications that may be testable in the forthcoming years. More generally, in view of our present results, it would be interesting to investigate the existence of fat multifield inflation in a UV complete setting, such as SUGRA or string theory. This will also be important in view of the recent theoretical constraints on standard slow-roll inflation and forthcoming experiments.
In the next chapter, Chapter 4, we partially investigate this problem focusing on the realization of large-turn inflationary models.

Chapter 4

Rapid-turn inflation in supergravity is rare and tachyonic

This chapter is based on the work published in [7].

Strongly non-geodesic, or rapidly turning, trajectories in multifield inflation have attracted much interest recently from both theoretical and phenomenological perspectives. Most models with large turning rates in the literature are formulated as effective field theories. In this chapter we investigate rapid-turn inflation in supergravity as a first step towards understanding them in string theory. We find that large turning rates can be generated in a wide class of models, at the cost of high field space curvature. In these models, while the inflationary trajectories are stable, one Hessian eigenvalue is always tachyonic and large, in Hubble units. Thus, these models satisfy the de Sitter swampland conjecture along the inflationary trajectory. However, the high curvatures underscore the difficulty of obtaining rapid-turn inflation in realistic string-theoretical models. In passing, we revisit the η-problem in multifield slow-roll inflation and show that it does not arise, inasmuch as the inflatons, ϕ^i, can all be heavier (in absolute value) that the Hubble scale: $|m_i|/H > 1$, $\forall i$.

The chapter is organized as follow. In Sec.4.1 we give a brief summary of the SRRT inflationary models, highlighting how most of the literature focuses on field theory models, leaving out SUGRA based models. We conclude the section presenting the question we intend to answer in the rest of the chapter. In Section 4.2.1, we expand on the result obtained in the previous chapter, showing how the η-problem does not arise. That is, the masses of all the inflaton fields do *not* need to be smaller than the Hubble parameter for a sustained period of inflation when more than one scale field is present. In Section 4.2.2, we discuss possible two-field trajectories in detail, and we apply these results to the supergravity case in Section 4.3. Before doing that, in Sec.4.3.1 we present a survey of broad set of SUGRA models in the literature, showing that, with the exception of only one model, these seem to present neither large turning rates nor fat fields. Finally in Sec.4.3.3 we show how to construct rapid-turn trajectories in a large class of supergravity models, in which the inflaton superfield does not mix with the supersymmetry breaking direction, that is the inflaton and Goldstino superfields are orthogonal. We finish with a summary and discussion in Sec.4.4

4.1 Introduction

Cosmological inflation is the leading mechanism for explaining the origin of primordial perturbations which seeded the large-scale structures that we observe today as seen in Sec.2.2. Multifield models of inflation with strongly non-geodesic trajectories have received recent interest, motivated by theoretical and phenomenological constraints. Strongly non-geodesic inflationary trajectories in-fact can satisfy the recently proposed consistency conjectures on the inflationary scalar potential, see Sec.2.3.5 and [55–57, 68, 136]. Moreover, rapid-turn models can admit fat fields, which are heavier than the Hubble scale thus avoiding the η-problem, as seen in Chapter 3, based on [6].
Phenomenologically, strongly non-geodesic motion can have interesting observational implications such as breaking single field consistency relations between observables [3, 127, 137, 138], leaving signature features in the primordial power spectrum [139–143], producing primordial black holes [144–147], and sourcing a stochastic background of gravitational waves [148–151].

In an effective derivative expansion, multifield physics is characterized by a field space metric, a potential, and couplings to the spacetime metric via the Ricci scalar. The true multifield nature of the trajectory manifests when the trajectory strongly deviates from geodesic motion in field space. This deviation is measured by the dimensionless turning rate Ω/H, where H is the Hubble parameter. For minimally coupled scalars, one finds, see Sec.2.3.3.1, that along solutions to the equations of motion, eq.(2.109) holds:

$$\epsilon_V = \epsilon \left\{ \left(1 + \frac{\eta}{2(3-\epsilon)} \right)^2 + \frac{\Omega^2}{9H^2} \frac{1}{(1-\epsilon/3)^2} \right\}, \tag{4.1}$$

where, again, the slow-roll and gradient parameters are defined as:

$$\epsilon \equiv -\frac{\dot{H}}{H^2}, \quad \eta \equiv \frac{\dot{\epsilon}}{H\epsilon}, \quad \epsilon_V \equiv \frac{M_{\rm Pl}^2}{2} \frac{|\nabla V|^2}{V^2}. \tag{4.2}$$

As discussed in Sec.2.3.3.1, slow-roll inflation, with $\epsilon \ll 1$ and $\eta \ll 1$, can happen in different regions of the Ω/H and ϵ_V plane. In particular, potentials and metrics for which $\epsilon_V \ll 1$ allow for an effective single-field, slow-roll trajectory, whereas steep potentials ($\epsilon_V \gtrsim 1$) can feature rapid-turn, slow-roll trajectories (SRRT) ($\Omega/H \gg 1$, $\epsilon \ll 1$) [57, 68]. The conditions for rapid-turn, slow-roll trajectories are known in the two-field case [121, 126], see also Chapters 3, while the conditions for three or more fields in the low-torsion limit[1] are discussed in [135].

Moreover, in Chapter 3, it was shown that a sufficient condition for strongly non-geodesic trajectories is to have all fields heavier than the Hubble scale, i.e. *fat inflation*. This is a remarkable result, as it effectively evades the η-problem in multifield inflation, see Sec.2.5. As we show in section 4.2.1, more generally, multifield inflation does not have an η-problem, in as much as all the inflatons can be heavier than the Hubble parameter ($|m_i|/H \ll 1$). In Chapter 3 it was also shown that fat inflatons are sufficient, but not necessary for rapid-turn inflation. An example of this is orbital inflation [131], which produces rapid-turn inflation with a large negative mass-squared along the inflationary trajectory [135] (se also

[1] See also [152] for a discussion on multifield inflation with any number of fields.

[130]). Note that the tachyons along the inflationary trajectory do not imply an instability[1]. Indeed, the trajectory can be stable in that the Lyupanov exponents contain a compensating term from the turn rate [128, 138].

As seen in Sec.2.4, multifield models of inflation arise naturally in SUGRA and string theory compactifications. Thus, it is sensible to ask how common is strongly non-geodesic, slow-roll behavior in supergravity, being a low energy effective theory description of string theory. In this chapter we aim at addressing precisely these two questions.

4.2 Slow-roll multifield in kinetic base

In this section we focus on multifield inflation in field theory, see Sec.2.3.2.
In the first part we show how these type of models do not present the η-problem. In sec.4.2.2 we analyse in detail the different types of multifield inflationary models and derive the expressions for ϵ, η, Ω/H and $\lambda_{\pm}$ as a function of the scalar fields potential.

4.2.1 No η problem in multifield inflation

In Sec.2.3.3, we derived the conditions for long lasting slow-roll multifield inflation, i.e. eq.(2.94), eq.(2.95) and eq.(2.96).

When these inequalities are satisfied the equations of motion and the expressions for Ω/H, V_{TT} and V_{TN}, derived in eq.(2.90) and (2.92), can be simplified. In particular, as already seen, the equations of motion become:

$$H^2 \simeq \frac{V}{3M_{\rm Pl}^2}$$
$$3H\dot{\varphi} + V_T \simeq 0$$

and the expressions for the dimensionless turning rate and the projection of the

[1]This is standard for concave potentials, such as in single field Starobinsky inflation [29].

potential onto T^a and N^a can be written simply as

$$\frac{\Omega}{H} \simeq -3\frac{V_N}{V_T} \tag{4.3}$$

$$\frac{V_{TT}}{3H^2} \sim \frac{\Omega^2}{3H^2} \tag{4.4}$$

$$\frac{V_{TN}}{3H^2} \sim \frac{\Omega}{H} \tag{4.5}$$

In the previous chapter we noticed that the slow-roll conditions do not impose any constraint on η_V, defined in eq.(2.101). Indeed, the minimal eigenvalue of $\mathbb{M}$ satisfies the condition seen in eq.(3.22), hence:

$$\lambda_{\rm min} \leq U_a V^a_{\ b} U^b \,. \tag{4.6}$$

Taking $U^a = T^a$, we have that $\lambda_{\rm min} \leq V_{TT}$. Thus, there arises the possibility of fat inflation, see Chapter 3. In Chapter 3 we showed that a sufficient condition to obtain large turns is to have the minimal eigenvalue of $\mathbb{M}$ much larger than one, that is $\lambda_{\rm min} \gg H^2$, which thus implies $V_{TT}/V \gg 1$. From eq.(4.4) this implies $\Omega/H \gg 1$. As a consequence it is possible to have all fields heavier than the Hubble scale, without spoiling long lasting slow-roll. Moreover, one can also check that this also holds when the minimal eigenvalue is negative. That is, slow-roll inflation with fat tachyonic fields, $|\lambda_{\rm min}| \gg H^2$, and large turning rates, $\Omega/H > 1$. Note that these models satisfy the dSCs [55, 56, 136], since $\lambda_{\rm min} \leq -\mathcal{O}(1)$. An example of this type of inflationary attractor, is angular inflation [3], see Sec.3.3.2. More generally, we see that η_V can be either large or small, without affecting the inflationary attractor. In particular, it is not necessary to fine tune the masses of the inflatons to be small (in Hubble units) to ensure a successful period of multifield inflation.

Using the slow-roll expressions for the mass matrix elements V_{TT} and V_{TN}, we can express the eigenvalues purely in terms of Ω and V_{NN}, see Sec.4.2.3. If all the eigenvalues, eq.(2.89) are positive, as in the case of fat inflation, we have that $0 < \det \mathbb{M} < {\rm Tr}\mathbb{M}^2/4$. Since $\det \mathbb{M} \simeq \Omega^2(V_{NN} - 9H^2)$, positive eigenvalues require

$$V_{NN} > 9H^2. \tag{4.7}$$

In the opposite case, $V_{NN} < 9H^2$, the minimal eigenvalue will be negative[1]. This condition will be further analysed in Sec.4.4.

4.2.2 Two-field inflation in field theory

Starting with the generic multifield Lagrangian as in eq. (2.72), in this section we focus on the two field case $\phi^a = (r, \theta)$. In anticipation of examining inflation in supergravity, we refer to these fields as the *saxion* and *axion* fields, respectively. For a broad class of highly symmetric field space geometries, the kinetic term can be written as [2]

$$\mathcal{L}_\phi \supset -\frac{f^2(r)}{2}\left[(\partial r)^2 + (\partial\theta)^2\right] . \tag{4.11}$$

Note that the field space metric is independent of the coordinate θ, indicating an isometry direction. The equations of motion (2.74) and (2.75) in terms of r and θ take the form

$$r'' + \left(3 - \frac{\varphi'^2}{2M_{\rm Pl}^2}\right) r' - \frac{f_r}{f}\left(\theta'^2 - r'^2\right) + \frac{V_r}{H^2 f^2} = 0 \tag{4.12}$$

$$\theta'' + \left(3 - \frac{\varphi'^2}{2M_{\rm Pl}^2}\right) \theta' + 2\frac{f_r}{f}\theta' r' + \frac{V_\theta}{H^2 f^2} = 0 \,, \tag{4.13}$$

[1] Recall that a tachyon along the inflationary trajectory does not indicate an instability. The criteria for the stability of the trajectory are discussed e.g. in [128].

[2] Note that this metric can be written in several other equivalent forms by suitable redefinition of the field r:

$$\mathcal{L}_\phi \supset -\frac{1}{2}\left[(\partial R)^2 + f^2(R)(\partial\theta)^2\right] \tag{4.8}$$

$$\supset -\frac{f^2(\rho)}{2}\left[(\partial\rho)^2 + \rho^2(\partial\theta)^2\right] . \tag{4.9}$$

Hence, we focus on (4.11) and transform to either (4.8) or (4.9) by a simple redefinition of the *radial* coordinate. Note further that in some cases [3], the scalar metric allegedly depends on both scalar fields. However, it only depends on a single combination of them:

$$g_{ab} = f(\phi,\chi)\mathrm{diag}(1,1) = \frac{1}{1-(\phi^2+\chi^2)}\mathrm{diag}(1,1) . \tag{4.10}$$

Therefore, it is possible to change coordinates to $\phi = r\sin\theta$ and $\chi = r\cos\theta$, such that the metric takes the form of (4.9), which in turn is equivalent to (4.11).

where primes denote e-fold derivatives, $f = f(r)$, $f_r = \partial_r f(r)$ and φ' reduces to

$$\varphi'^2 = f^2(r)(r'^2 + \theta'^2). \tag{4.14}$$

Inflationary Solutions

We now consider the possible inflationary solutions to (4.12) and (4.13).

1. *Saxion inflation.* Single field saxion inflation can occur for $\theta' \simeq 0$, with θ fixed at θ_0 such that $V_\theta(r, \theta_0) = 0 \ \ \forall \ \ r$. In this case (4.13) is automatically satisfied, while (4.12) admits slow-roll solutions given a suitable potential. An example in supergravity is discussed in [98, 105].

2. *Axion inflation.* A more interesting possibility occurs for solutions with $r' \simeq 0$ [1]. In this case, imposing slow-roll in θ on the equations of motion yields:

$$-\frac{f_r}{f}\theta'^2 + \frac{V_r}{H^2 f^2} = 0 \tag{4.15}$$

$$(3 - \epsilon)\,\theta' + \frac{V_\theta}{H^2 f^2} = 0\,. \tag{4.16}$$

These two equations give independent constraints on θ', which must coincide along the inflationary trajectory. Demanding them to be equal gives the following consistency condition:

$$(\theta')^2 = \frac{V_\theta^2}{(3-\epsilon)^2 H^4 f^4} = \frac{V_r}{H^2 f f_r}\,, \tag{4.17}$$

$$\Rightarrow \frac{V_\theta^2}{(3-\epsilon)^2 H^2 V_r} = \frac{f^3}{f_r}\,. \tag{4.18}$$

This relationship vastly restricts the regions of field and parameter space satisfying slow-roll, and can be used to identify the inflationary trajectory. We can also have different scenarios depending on the initial conditions for the saxion:

[1] While $\theta = \theta_0$ (i.e. $\theta' = 0$) is always a geodesic, $r = r_0\,(r' = 0)$ is only a geodesic when $(f_r/f)\,|_{r_0} = 0$.

(a) *Single field axion inflation.* Single field axion inflation occurs when the saxion is fixed to r_0 such that $V_r(r_0, \theta) = 0$ and $(f_r/f)|_{r_0} = 0$ so as to satisfy (4.15).

(b) *Multifield axion inflation.* Multifield inflation will occur whenever (4.15) is satisfied with both terms *non-vanishing*. This can happen in two scenarios: either $V_r(r_0, \theta) \neq 0$ and $(f_r/f)|_{r_0} \neq 0$, or $V_r(r_0, \theta) = 0$ and $(f_r/f)|_{r_0} = 0$ with $r = r_{shift} \neq r_0$. The minimal sidetrack models of [74] are an example of this case. In this situation, one can in principle compute the value of r_{shift} during the multifield evolution. Note that in this case the axion follows slow-roll inflation assisted by the saxion, which can give rise to large turning rates. These are the type of solutions we examine in the next sections.

3. *Multifield inflation.* By appropriately choosing the initial conditions and potential, it is possible to have *double inflation* without substantial turning (see e.g. Sec.3.3.2 and [153] for an example in supergravity) or genuinely multifield evolution where both axion and saxion act as inflatons with interesting phenomenology.

In the rest of the chapter we will focus on the *multifield axion inflation* models. Note that it is not possible to have a similar "assisted saxion" multifield inflation. Note also that all two-field rapid-turn models described by the actions (4.11), (4.8), and (4.9) exhibit multifield axion inflation (e.g. supergravity inspired angular inflation [3], orbital inflation [131], hyperinflation [125], sidetrack inflation [68]).

4.2.3 Rapid-turn, multifield axion inflation

In this section we build the foundations to study the multifield axion models in the SUGRA framework.
In order to do that, we are going to derive the expressions for the slow-roll parameters, the dimensionless turning rate and the mass matrix's eigenvalues as a function of the scalar fields potential V and the field space metric G_{ab}.
As mentioned above, in the multifield axion case, the inflationary trajectory is

mostly aligned with the axion direction, while the saxion stays approximately constant and constitutes the direction normal to the trajectory.

From eq.(4.11), the field space metric is

$$G_{ab} = \begin{pmatrix} f^2 & 0 \\ 0 & f^2 \end{pmatrix} \quad \Rightarrow \quad G^{ab} = \frac{1}{f^2}\begin{pmatrix} 1 & 0 \\ 0 & 1 \end{pmatrix} \tag{4.19}$$

Using the *kinematic basis* description in Sec.2.3.2, we can express the trajectory's unit tangent and normal vectors as:

$$T^a = \frac{1}{\varphi'}(r', \theta')\,, \qquad N^a = \frac{1}{\varphi'}(\theta', -r')\,. \tag{4.20}$$

Since $r' \sim 0$ in multifield axion inflation, the field velocity simplifies as

$$\varphi' \sim f\theta' \tag{4.21}$$

, which reduces the unit vectors to

$$T^a \sim (0, \frac{1}{f}), \qquad N^a \sim (\frac{1}{f}, 0). \tag{4.22}$$

Using these expression, the first slow-roll parameter ϵ_T eq.(2.100) can immediately be written as a function of the derivative of the potential along θ:

$$\epsilon_T = \frac{M_{\rm Pl}^2}{2}\left(\frac{T^a V_a}{V}\right)^2 = \frac{M_{\rm Pl}^2}{2f^2}\left(\frac{V_\theta}{V}\right)^2 \ll 1 \tag{4.23}$$

The computation for η is slightly more complicated:

$$\eta = \frac{\dot{\epsilon_T}}{H\epsilon_T} = \\ = \frac{1}{\epsilon_T H}\left[\frac{V_\theta V_{\theta\theta}\dot{\theta}}{f^2V^2} - \frac{V^2}{f^2}\left(\frac{V_\theta\dot{\theta}}{V^3}\right) - \frac{V_\theta^2}{V^2}\left(\frac{f_r\dot{r}}{f^3}\right)\right]$$

where $\dot{\theta}$ can be obtained from eq.(4.16). Finalizing the computations, we have

$$\begin{aligned}\eta &= \frac{1}{\epsilon_T H}\left[-2\epsilon_T \frac{V_{\theta\theta}}{3Hf^2} + 4\epsilon_T^2 \frac{V}{3H} - 2\epsilon_T \frac{f_r \dot{r}}{Hf}\right] \\ &\simeq -2\eta_T + 4\epsilon_T \end{aligned} \tag{4.24}$$

where $\dot{r} \simeq 0$, since we are focusing on axion models and where

$$\eta_T \equiv \frac{M_{\rm Pl}^2}{f^2}\frac{V_{\theta\theta}}{V} \tag{4.25}$$

which should be $\eta_T \ll 1$ during inflation. The last two equations are respectively, eq.(2.103) ad eq.(4.24), in the specific case of a two field model with G_{ab} given by (4.19).

Using the same procedure it is possible to rewrite Ω/H. Using eq.(4.16) and the definition of the tangent vector, eq.(4.22), one can show that [74]

$$\frac{\Omega}{H} \simeq \frac{V_r}{H^2 f^2 \theta'} \simeq -\frac{V_r}{V_\theta}(3-\epsilon)\ . \tag{4.26}$$

Using equation (4.18), we can further write:

$$\frac{\Omega}{H} \simeq -\frac{V_\theta}{H^2}\frac{f_r}{f^3}\frac{1}{(3-\epsilon)} \simeq -M_{\rm Pl}\sqrt{2\epsilon_T}\,\frac{f_r}{f^2}\,. \tag{4.27}$$

This expression for Ω/H explicitly shows that a change in the kinetic term, hence in the function $f(r)$ in which define the field space metric, directly affects the turning rate. We will later make use of this when showing how to generate large turning rates in supergravity.
It is also possible to give an expression of Ω/H as a function of the Ricci scalar. Given the field space metric in eq.(4.19), the scalar of curvature is

$$R = 2\frac{f_r^2}{f^4} - 2\frac{f_{rr}}{f^3} \tag{4.28}$$

and, substituting this expression into eq.(4.27), Ω/H becomes

$$\frac{\Omega}{H} \simeq -3\frac{V_\theta}{V}\frac{1}{3-\epsilon}\frac{\pm}{f}\sqrt{\frac{R}{2}+\frac{f_{rr}}{f^3}}. \tag{4.29}$$

From this equation it is possible to say that a scalar manifold with negative curvature is a priori not required for large turning rate, as seen in the previous chapter (see the examples in Table 3.1).

As mentioned in Sec.2.3.3, in multifield inflation, $\nu \ll 1$. Also this condition can be re-written in term of the potential derivative. Expanding eq.(2.93) or, equally, using equation eq.(2.92), this becomes

$$\nu = \frac{\dot{\omega}}{H\omega} \sim -3\frac{V_{;r\theta}}{V_\theta}\frac{f}{f_r} - 3 + \mathcal{O}(\epsilon,\eta). \tag{4.30}$$

If $\epsilon_T \ll 1$ and $\eta_T \ll 1$, then the slow-roll condition for ν requires that

$$\frac{V_{;r\theta}}{V_\theta} \simeq -\frac{f_r}{f}. \tag{4.31}$$

Lastly, recalling that the eigenvalues of the mass matrix are given by eq.(2.89), we note that, to have *both* the scalar fields positive masses, the following inequality has to be satisfied:

$$V_{TT} + V_{NN} > \sqrt{(V_{TT}-V_{NN})^2 + 4V_{NT}^2} \tag{4.32}$$

Substituting eq.(4.4) and eq.(4.5), this translates in

$$V_{NN} > 9H^2. \tag{4.33}$$

For negative eigenvalues, following a similar computation,

$$V_{NN} < 9H^2. \tag{4.34}$$

In terms of the derivative of the potential respect to the scalar fields involved,

r and θ, V_{NN} can be written as

$$V_{NN} = N^a N^b V_{;ab} = \frac{1}{f^2}\left(V_{,rr} - \Gamma^k_{rr} V_k\right) \tag{4.35}$$

which simplify to

$$V_{NN} = \frac{1}{f^2}\left(V_{,rr} - V_r \frac{f_r}{f}\right). \tag{4.36}$$

Equally, given eq.(2.87), the eigenvalues can be written as

$$\lambda_\pm = \frac{1}{2f^2}\left(V_{rr} + V_{\theta\theta} \pm (V_{rr} - V_{\theta\theta})\sqrt{1+\beta^2}\right), \quad \text{where} \quad \beta \equiv \frac{2V_{r\theta}}{V_{rr} - V_{\theta\theta}} \tag{4.37}$$

From here it is possible to see that one possibility for the eigenvalues to be both positive and large is to have $V_{rr} \sim V_{\theta\theta}$ and $V_{r\theta}$ small.

4.3 Large turning rates in supergravity

In this section we are going to investigate the viability of rapid-turn inflation in supergravity. For a review of multifield inflation in SUGRA see Sec.2.4.

Our starting point was the observation that numerical scans of supergravity models in the literature failed to find trajectories with large turning rates as we show in the next Section. However, in Sec.4.3.3 we show how to understand the small turning rates of most models and we provide a method to increase the turning rate using the formulas obtained in Sec.4.2.3. As we will discuss, these rapid-turn examples have consistently a fat tachyonic direction, (that is $|\lambda_{\rm min}| > H^2$, $\lambda < 0$) along the inflationary trajectory[1]. We therefore conjecture that rapid-turn inflationary trajectories in supergravity always occur in the presence of tachyonic directions, potentially satisfying the dSCs, Sec.2.3.5.

As mentioned in Sec.2.4, the simplest SUGRA inflationary setup involves a single superfield, i.e. two real scalar fields, however inflation is generally difficult to realize with only a single superfield. In Sec.4.3.2 we explore this possibility to

[1]Recall that this does not indicate an instability, similar to concave potential inflation, such as Starobinsky inflation [29].

understand the viability of large turning rates analytically. In Sec 4.3.3 we focus instead on models with two superfields.

4.3.1 Results from survey of supergravity models

To study the possibility of rapid-turn inflation in supergravity models, we surveyed several models from the literature ([4, 100, 154–158]), as well as studied several ad-hoc models of our own creation.

After constructing the potential and field space metric in terms of real fields, we scanned a wide region of allowed field and parameter space for each model. This was achieved using an efficient differential-evolution optimizer in `BlackBoxOptim.jl`[1], assuming "good" initial inflationary points minimized one of several cost functions. We performed several scans with each choice of cost function, first assuming the initial velocities to follow the rapid-turn solution [69, 121]. This cost function can be written

$$\text{cost}_{\text{rapid-turn}}(\vec{\phi},\text{parameters}) = \tag{4.38}$$

$$= \frac{\ddot{\phi}_v}{3H\dot{\phi}_v} + A\epsilon + B|\eta| + C|\nu| + D(\Omega/H)^{-2}, \tag{4.39}$$

where v^a is the potential gradient unit vector and $\dot{\phi}_v = v^a \dot{\phi}_a$[2]. This expression is small when the solution admits both slow-roll and rapid-turn, and with A, B, C, D chosen to weight each term's relative contribution. Typical values chosen were $A = 100, B = 10, C = D = 1$, though small changes in these values did not affect the result. For details on our numerical method of constructing the zero-torsion rapid-turn inflationary solution at a given point in parameter space, see [69].

As alternatives, we also examined cost functions to prefer high masses, with

[1] `https://github.com/robertfeldt/BlackBoxOptim.jl`

[2] This notation has been introduced in [126] and it relies on the so called "potential gradient basis" where the basis vectors are $v^a = V^{,a}/\sqrt{V^{,b}V_{,b}}$ and w^a a second unit vector orthogonal to v^a.

no inflationary considerations:

$$\text{cost}_{\text{fat}}(\vec{\phi}, \dot{\vec{\phi}}, \text{parameters}) = 10^{10}(\#\text{ negative eigvals of } V_b^a) + \frac{1}{|\text{min. eigval of } V_b^a|}, \tag{4.40}$$

and an empirical cost function, with no assumptions about the initial conditions other than the velocities were small enough to allow inflation to begin, i.e. the initial $\epsilon < 1$:

$$\text{cost}_{\text{empirical}}(\vec{\phi}, \dot{\vec{\phi}}, \text{parameters}) = \frac{1}{N_{\text{end}}} + \frac{J}{\omega_{\text{end}}}, \tag{4.41}$$

where $J = 10^6\omega_{\text{end}}$ if the total number of efolds $N_{\text{end}} < 60$ and $J = 1$ otherwise, and ω_{end} is the lowest value of ω recorded during the final 10 e-folds of evolution. Numerical integration was paused when $\epsilon = 1$ or after 60 e-folds, whichever occurred first. The empirical and high-mass scans treated the fields' initial velocities as free parameters, rather than determining them with the rapid-turn solution.

For each choice of cost function, at several hundred of its minimizing field and parameter values, we evolved the classical equations of motion using the publicly-available multifield inflationary dynamics code `Inflation.jl` [159] and recorded the number of e-folds as well as the lowest turn rate recorded during the final 10 e-folds, ω_{end}. The empirical cost function proved to be the most successful at finding inflationary points with slow-turn inflation, while the rapid-turn cost function was comparably effective at finding rapid-turn inflation. The fat cost function was the least effective at finding inflationary initial conditions, suggesting the correlation between high mass points and inflationary points is not a strong one in these models.

In Appendix B we present each scanned model's Kähler and superpotential, its reference when available, and the best solution as ranked by the empirical cost function, even if found in a scan using one of the other cost functions. Many published models restrict the field space to the regime with $S = 0$, but in these scans we have avoided that limitation when possible, rendering some of these models non-inflationary. Because the scale of the inflationary potential does not affect the background evolution, coefficients common to all terms in the superpotential

have been neglected when possible. Although not indicated in the table, none of the found rapid-turn phases were fat inflation. In each model, its real fields are defined from the complex fields as $\Phi = \phi^1 + i\phi^2$, $S = \phi^3 + i\phi^4$. We denote the initial e-fold velocities by $\pi^a \equiv \dot{\phi}^a/H$. For notational convenience we set $M_{\rm Pl} = 1$. We report in Fig.4.1 an example of the plots obtained for the various models analysed. In particular, we report the values of $\omega^2 = \Omega^2/H^2$ for the EGNO model, which we analyse in detail in Sec.4.3.5.2, for different values of the parameter p. We can see that the larger turning rates are obtained whenever $p \sim K\pi$, with $K \in \mathbb{N}$.

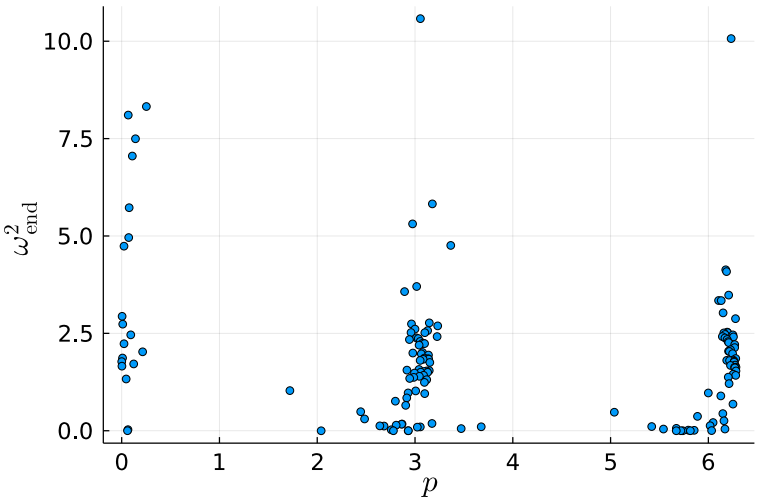

Figure 4.1: Behaviour of $\omega^2_{\rm end}$ for different values of p in the EGNO model in Table B.1.

4.3.2 Single superfield model

In order to understand the viability of large turning rates analytically, we start by examining models consisting of a single superfield Φ, i.e. multifield sGoldstino inflation. We consider model with a Kähler potential given by

$$K = -3\alpha \log[(\Phi + \bar{\Phi})/M_{\rm Pl}]. \tag{4.42}$$

For simplicity, we take the superpotential to be a monomial in Φ,

$$W = M^{3-n}\Phi^n, \tag{4.43}$$

where n is an integer. Expanding the superfield into real and imaginary parts, $\Phi = r + i\theta$, the resulting scalar potential is

$$V = 3M^{2(3-n)}\frac{(\theta^2+r^2)^{n-1}}{2^{3\alpha}r^{3\alpha}}\left[\left(\frac{(\alpha-2n/3)^2}{\alpha}-1\right)r^2+(\alpha-1)\theta^2\right], \tag{4.44}$$

and the metric on real fields takes the form of eq.(4.11) with $f = \sqrt{\frac{3\alpha}{2r^2}}$.

Axion inflation solutions require the consistency of both θ' expressions in eq.(4.15) and eq.(4.16). Denoting these expressions as θ'_1 and θ'_2 respectively, we find them to be

$$\theta'_1 = \sqrt{\frac{2}{\alpha\left(\theta^2+r^2\right)\left(9\alpha^2\left(\theta^2+r^2\right)-3\alpha\left(3\theta^2+(4n+3)r^2\right)+4n^2r^2\right)}} \tag{4.45}$$

$$\times\Bigg[r^2\Big(-27\alpha^2\left(\theta^2+r^2\right)\left(\theta^2+(2n+1)r^2\right)+27\alpha^3\left(\theta^2+r^2\right)^2 + 6\alpha n r^2\left(\theta^2(2n+7)+(6n+3)r^2\right)-8n^2r^2\left(\theta^2+nr^2\right)\Big)\Bigg]^{1/2} \tag{4.46}$$

$$\theta'_2 = -\frac{4\theta n r^2\left(9\alpha^2\left(\theta^2+r^2\right)-9\alpha\theta^2+3\alpha(1-4n)r^2+4(n-1)nr^2\right)}{3\alpha\left(\theta^2+r^2\right)\left(9\alpha^2\left(\theta^2+r^2\right)-3\alpha\left(3\theta^2+(4n+3)r^2\right)+4n^2r^2\right)}. \tag{4.47}$$

When these expressions are equal, slow-roll trajectories are constrained to be of the form

$$r = c_n\theta, \tag{4.48}$$

where c_n is a proportionality constant depending on the order n of the monomial superpotential and α. Although the expressions are unwieldy for $n \geq 2$, we present the proportionality constant for the $n = 1$ case below:

$$c_1 = \pm\sqrt{3}\alpha^{3/4}\sqrt{\frac{\sqrt{\alpha}(-81\alpha^3+297\alpha^2-303\alpha+87)+\sqrt{3}\sqrt{(-405\alpha^3+1242\alpha^2-933\alpha+288)(\alpha-1)^2}}{(3\alpha-2)(9\alpha^2-21\alpha+4)^2}}. \tag{4.49}$$

These solutions are only real-valued for $1 < \alpha < \frac{7+\sqrt{33}}{6}$, which corresponds to a negative potential. Hence, we can exclude slow-roll axion inflation from models with an $n = 1$ monomial superpotential. For higher order monomials with $n = 2, 3, 4, 5$, our numerical scans similarly find that the potential is either negative or complex wherever the solutions are real-valued. We therefore expect slow-roll axion inflation to be forbidden in this entire class of models with monomial superpotentials.

4.3.3 Rapid-turn attractor in supergravity

We saw in Section 4.2.3 that slow-roll in the $r' \sim 0$ attractor implies $\epsilon_T \ll 1$ which can be written in terms of V_θ as in eq.(4.23), and $\eta_T \ll 1$, see eq.(4.25). In supergravity inflationary models, where we deal with Φ and $\bar{\Phi}$, we can use the information in the previous section on the large turn attractor solutions to write eq.(4.23), (4.25) and Ω/H in terms of the derivative of the Kähler potential and superpotential. Part of the aim of this and the next section is to understand if it is possible to find an expression for Ω/H and the scalar fields eigenvalues such that we can constraint K and W to obtain a large turning rate and a fat model.

For this, let us introduce the real scalar fields r and θ defined as:

$$\Phi = r + i\theta, \quad \bar{\Phi} = r - i\theta \quad \rightarrow \quad r = \frac{\Phi + \bar{\Phi}}{2}, \quad \theta = \frac{\Phi - \bar{\Phi}}{2i} \tag{4.50}$$

From the above system it follows that

$$\frac{\partial V}{\partial \theta} = \frac{\partial \Phi}{\partial \theta}\frac{\partial V}{\partial \Phi} + \frac{\partial \bar{\Phi}}{\partial \theta}\frac{\partial V}{\partial \bar{\Phi}}, \qquad \frac{\partial V}{\partial r} = \frac{\partial \Phi}{\partial r}\frac{\partial V}{\partial \Phi} + \frac{\partial \bar{\Phi}}{\partial r}\frac{\partial V}{\partial \bar{\Phi}}. \tag{4.51}$$

In SUGRA models of inflation, the field space metric can be written from the Kähler potential, see Sec.2.4, thus eq.(4.19) becomes:

$$G_{ab} = \begin{pmatrix} 2K_{\Phi\bar{\Phi}} & 0 \\ 0 & 2K_{\Phi\bar{\Phi}} \end{pmatrix}. \tag{4.52}$$

Substituting eq.(4.51) and (4.52) into the expression of ϵ_T and η_T. these can

be written as

$$\epsilon_T \simeq \frac{M_{\rm Pl}^2}{2}\frac{1}{2K_{\Phi\bar{\Phi}}}\left(\frac{i(V_\Phi - V_{\bar{\Phi}})}{V}\right)^2 \tag{4.53}$$

$$\eta_T \simeq \frac{M_{\rm Pl}^2}{2K_{\Phi\bar{\Phi}}}\frac{(2V_{\Phi\bar{\Phi}} - V_{\Phi\Phi} - V_{\bar{\Phi}\bar{\Phi}})}{V} \tag{4.54}$$

Using the same substitution, ν in eq.(4.30) becomes

$$\nu \simeq \frac{1}{2V\left(V_\Phi + V_{\bar{\Phi}}\right)K_{\Phi\bar{\Phi}}}\cdot \tag{4.55}$$

$$\cdot\left[\left(V_\Phi - V_{\bar{\Phi}}\right)\left(V_{\Phi\Phi}K_{\Phi\bar{\Phi}} - V_{\bar{\Phi}\bar{\Phi}}K_{\Phi\bar{\Phi}} + V_{\bar{\Phi}}K_{\Phi\bar{\Phi}\bar{\Phi}} - V_\Phi K_{\Phi\Phi\bar{\Phi}}\right)\right]. \tag{4.56}$$

Transforming the expression for Ω/H in eq.(4.27) to complex coordinates and neglecting factors of order ϵ, we obtain two equivalent expressions:

$$\frac{\Omega}{H} \simeq -3\frac{V_\Phi + V_{\bar{\Phi}}}{i(V_\Phi - V_{\bar{\Phi}})} \tag{4.57}$$

$$\frac{\Omega}{H} \simeq -M_{\rm Pl}^2\frac{i(V_\Phi - V_{\bar{\Phi}})}{V}\frac{\left(K_{\Phi\bar{\Phi},\Phi} + K_{\Phi\bar{\Phi},\bar{\Phi}}\right)}{(2K_{\Phi\bar{\Phi}})^2}. \tag{4.58}$$

Using eq.(4.53), Ω/H can be written in terms of the first slow-roll parameter and eq.(4.58) becomes

$$\frac{\Omega}{H} \simeq -M_{\rm Pl}\sqrt{2\epsilon_T}\,\frac{\left(K_{\Phi\bar{\Phi},\Phi} + K_{\Phi\bar{\Phi},\bar{\Phi}}\right)}{(2K_{\Phi\bar{\Phi}})^{3/2}}\,. \tag{4.59}$$

From this equation it is evident that large turning rates can be adjusted by tuning the expression of Kähler potential. Meanwhile, the superpotential can be tuned to ensure slow-roll, i.e. $\epsilon_T \ll 1$, see eq.(4.53). In Sec.4.3.4 this is used in a concrete example. Note that the above equations for the turning rate are *general*: there was no assumption on either K or W.

In Sec.4.3.4, we consider large turning rates in specific supergravity models. As we have identified above, tuning the Kähler potential and superpotential suitably can in principle generate strongly non-geodesic inflationary trajectories. In all these examples, we find fat tachyonic fields along the trajectory.

4.3.4 Orthogonal inflation

As described previously, we consider two "orthogonal" chiral superfields: the goldstino and inflaton superfields S and Φ, respectively. We can eliminate S by either introducing a suitable Kähler potential to stabilise it to $S = 0$, or by introducing a nilpotent condition $S^2 = 0$ [105, 106].

Consider a general Kähler potential and a superpotential of the form

$$K(\Phi, \bar{\Phi}; S, \bar{S}) \,, \qquad W = SF(\Phi) \,, \tag{4.60}$$

where the Kähler potential is separately invariant under the transformations

$$S \to -S. \tag{4.61}$$

This ensures that the Kähler potential is a function of $S^2 + \bar{S}^2$ and $S\bar{S}$; in particular, if S is nilpotent,

$$K\left(\Phi, \bar{\Phi}, S, \bar{S}\right) = K\left(\Phi, \bar{\Phi}, S\bar{S}\right) . \tag{4.62}$$

In this section we make assumption on the superfield S but we do not impose any symmetry for Φ. Under the assumptions for S, $K_S = K_{\bar{S}} = 0$ at $S = 0$, and derivatives of the superpotential reduce to:

$$D_S W = F(\Phi) \,, \qquad D_\Phi W = 0 \,, \tag{4.63}$$

and the scalar potential then takes the simple form:

$$V = e^{K(\Phi,\bar{\Phi},0,0)/M_{\rm Pl}^2} K^{-1}_{S\bar{S}}(\Phi, \bar{\Phi}, 0, 0) \, |F(\Phi)|^2 \,. \tag{4.64}$$

Without any further assumption on the Kähler potential, ϵ_T becomes:

$$\epsilon_T = -\frac{M_{\rm Pl}^2}{4K_{\Phi\bar{\Phi}}} \left(\frac{\left(F_\Phi \bar{F} - F\bar{F}_{\bar{\Phi}} + F\bar{F} \left(K_\Phi - K_{\bar{\Phi}} \right) + \frac{F\bar{F}}{K_{S\bar{S}}} \left(K_{S\bar{S},\Phi} - K_{S\bar{S},\bar{\Phi}} \right) \right)}{F\bar{F}} \right)^2 \tag{4.65}$$

and eq.(4.57) and eq.(4.58), respectively, can be written as[1]

$$\frac{\Omega}{H} \simeq 3i \frac{F_\Phi \bar{F} + F\bar{F}_{\bar{\Phi}} + F\bar{F}\left(K_\Phi + K_{\bar{\Phi}}\right) - \frac{F\bar{F}}{K_{S\bar{S}}}\left(K_{S\bar{S},\Phi} + K_{S\bar{S},\bar{\Phi}}\right)}{F_\Phi \bar{F} - F\bar{F}_{\bar{\Phi}} + F\bar{F}\left(K_\Phi - K_{\bar{\Phi}}\right) + \frac{F\bar{F}}{K_{S\bar{S}}}\left(K_{S\bar{S},\Phi} - K_{S\bar{S},\bar{\Phi}}\right)} \tag{4.66}$$

$$\frac{\Omega}{H} \simeq -i \frac{\left(F_\Phi \bar{F} - F\bar{F}_{\bar{\Phi}} + F\bar{F}\left(K_\Phi - K_{\bar{\Phi}}\right) - \frac{F\bar{F}}{K_{S\bar{S}}}\left(K_{S\bar{S},\Phi} - K_{S\bar{S},\bar{\Phi}}\right)\right)}{F\bar{F}} \frac{K_{\Phi\bar{\Phi},\Phi} + K_{\Phi\bar{\Phi},\bar{\Phi}}}{\left(2K_{\Phi\bar{\Phi}}\right)^2} \tag{4.67}$$

The main purpose of these computations is to use the expressions of ϵ_T and Ω/H to constraint the Kähler potential and the superpotential, hence $F(\Phi)$, such that inflation an take place ($\epsilon_T \ll 1$) and $\Omega/H > 1$. However the above equation are unwieldy to work with and do not provide any clear indication in that sense.

For this reason in the next section we impose additional symmetries on the Kähler potential.

Mass Matrix for SUGRA inflationary models

Here we are going to write the expression for the eigenvalues of the mass matrix along the inflaton direction Φ, similarly to what we did in eq.(4.37). The full 4x4 mass matrix is given by

$$M^I_J = \begin{pmatrix} M^I_J & M^I_{\bar{J}} \\ M^{\bar{I}}_J & M^{\bar{I}}_{\bar{J}} \end{pmatrix} \tag{4.68}$$

where in the particular case in which we have two complex superfields, ϕ and s, each element of M is a 2x2 matrix.
In detail:

$$M^I_J = \begin{pmatrix} M^\phi_\phi & M^\phi_s \\ M^s_\phi & M^s_s \end{pmatrix}, \quad M^I_{\bar{J}} = \begin{pmatrix} M^\phi_{\bar{\phi}} & M^\phi_{\bar{s}} \\ M^s_{\bar{\phi}} & M^s_{\bar{s}} \end{pmatrix} \tag{4.69}$$

$$M^{\bar{I}}_J = \begin{pmatrix} M^{\bar{\phi}}_\phi & M^{\bar{\phi}}_s \\ M^{\bar{s}}_\phi & M^{\bar{s}}_s \end{pmatrix} \quad M^{\bar{I}}_{\bar{J}} = \begin{pmatrix} M^{\bar{\phi}}_{\bar{\phi}} & M^{\bar{\phi}}_{\bar{s}} \\ M^{\bar{s}}_{\bar{\phi}} & M^{\bar{s}}_{\bar{s}} \end{pmatrix} \tag{4.70}$$

Each of the above matrices can be written using the Kähler potential K and

[1] neglecting again factors of order ϵ, η

the Hessian of the potential V as:

$$M^I_J = K^{I\bar{L}}\nabla_{\bar{L}}\nabla_J V = K^{I\bar{L}}(V_{J\bar{L}} - \Gamma^k_{\bar{L}J}V_k) \tag{4.71}$$

$$M^I_{\bar{J}} = K^{I\bar{L}}\nabla_{\bar{L}}\nabla_{\bar{J}} V = K^{I\bar{L}}(V_{\bar{J}\bar{L}} - \Gamma^k_{\bar{J}\bar{L}}V_k) \tag{4.72}$$

$$M^{\bar{I}}_J = K^{\bar{I}L}\nabla_L\nabla_J V = K^{\bar{I}L}(V_{JL} - \Gamma^k_{LJ}V_k) \tag{4.73}$$

$$M^{\bar{I}\bar{J}} = K^{\bar{I}L}\nabla_L\nabla_{\bar{J}} V = K^{\bar{I}L}(V_{\bar{J}L} - \Gamma^k_{L\bar{J}}V_k) \tag{4.74}$$

where $\Gamma^k_{\bar{L}J}V_k = \Gamma^K_{\bar{L}J}V_K + \Gamma^{\bar{K}}_{\bar{L}J}V_{\bar{K}}$ and so on.

As a consequence, it is possible to check that the original 4x4 matrix becomes block diagonal at $S = 0$ under the nihil condition assumption, eq.(4.62) and the mass matrix takes the simple form

$$\nabla^a\nabla_b V = \begin{pmatrix} K^{\Phi\bar{\Phi}}V_{\Phi\bar{\Phi}} & K^{\Phi\bar{\Phi}}V_{\bar{\Phi}\bar{\Phi}} \\ K^{\bar{\Phi}\Phi}V_{\Phi\Phi} & K^{\bar{\Phi}\Phi}V_{\Phi\bar{\Phi}} \end{pmatrix} \tag{4.75}$$

where all the derivatives are covariant. The eigenvalues thus can be written as

$$\lambda_\pm = K^{-1}_{\Phi\bar{\Phi}}\left(V_{\Phi\bar{\Phi}} \pm \sqrt{V_{\Phi\Phi}V_{\bar{\Phi}\bar{\Phi}}}\right) \tag{4.76}$$

It is possible to compute the expressions for $\lambda_\pm$, however they are complicated and do not provide additional information.

4.3.4.1 Shift symmetric Kähler potential

In this section we impose an additional symmetry on the Kähler potential. In particular we assume that it is shift symmetric in Φ, such that it is a function of $(\Phi + \bar{\Phi})$ only. This gives the following simplifications

$$K_\Phi = K_{\bar{\Phi}} \qquad K_{S\bar{S},\Phi} = K_{S\bar{S},\bar{\Phi}}, \quad ...., \quad . \tag{4.77}$$

Within this framework the expressions for ϵ_T in eq.(4.53) reduces to:

$$\epsilon_T = -\frac{M^2_{Pl}}{4K_{\Phi\bar{\Phi}}}\left(\frac{F_\Phi\bar{F} - F\bar{F}_{\bar{\Phi}}}{F\bar{F}}\right)^2, \tag{4.78}$$

and the expressions for Ω/H, eq.(4.57) and (4.58) become:

$$\frac{\Omega}{H} \simeq 3i\frac{F_\Phi \bar{F} + F\bar{F}_{\bar{\Phi}} + 2F\bar{F}\left(K_\Phi - \frac{K_{S\bar{S},\Phi}}{K_{S\bar{S}}}\right)}{F_\Phi \bar{F} - F\bar{F}_{\bar{\Phi}}} \tag{4.79}$$

$$\frac{\Omega}{H} \simeq -M_{\rm Pl}^2 \frac{i\left(F_\Phi \bar{F} - F\bar{F}_{\bar{\Phi}}\right)}{F\bar{F}} \frac{\left(2K_{\Phi\bar{\Phi},\Phi}\right)}{(2K_{\Phi\bar{\Phi}})^2} \simeq -M_{\rm Pl}\sqrt{2\,\epsilon_T}\,\frac{\left(2K_{\Phi\bar{\Phi},\Phi}\right)}{(2K_{\Phi\bar{\Phi}})^{3/2}}, \tag{4.80}$$

while ν, eq.(4.55), can be written as:

$$\begin{aligned}
\nu = \{&(\bar{F}F' - F\bar{F}')\cdot \\
&[\bar{F}(F'' K_{S\bar{S}} K_{\Phi\bar{\Phi}} + F'(-2K_{\Phi S\bar{S}} K_{\Phi\bar{\Phi}} + K_{S\bar{S}}(2K_\Phi K_{\Phi\bar{\Phi}} - K_{\Phi\bar{\Phi}\bar{\Phi}})))+ \\
&F(\bar{F}'' K_{S\bar{S}} K_{\Phi\bar{\Phi}} + \bar{F}'(+2K_{\Phi S\bar{S}} K_{\Phi\bar{\Phi}} + K_{S\bar{S}}(-2K_\Phi K_{\Phi\bar{\Phi}} + K_{\Phi\bar{\Phi}\bar{\Phi}})))]\}\cdot \\
&[2F\bar{F}(F\bar{F}' K_{S\bar{S}} + \bar{F}(\bar{F}' K_{S\bar{S}} + 2F(K_{S\bar{S}} K_\Phi - K_{\Phi S\bar{S}})))K_{\Phi\bar{\Phi}}^2]^{-1}
\end{aligned} \tag{4.81}$$

From eq.(4.78) it is clear that the first slow-roll parameter can be fine-tuned acting only on the superpotential W, hence on $F(\Phi)$, while, from eq.(4.80) we observe that large turning rates can be obtained by tuning the Kähler potential. Unfortunately the expression for ν, again, is too complicated to provide any insights.
Following the above expressions, we wrote explicitly the eigenvalues in terms of derivatives of K and W, making use of the slow-roll conditions, hoping to understand how to obtain fat inflationary model. However these expressions were not useful.

Trying to simplify the expressions for $\lambda_\pm$ we made further assumptions on both the Kähler and the superpotential:

- F is a first order monomial, hence $F_{\Phi\Phi} = \bar{F}_{\bar{\Phi}\bar{\Phi}} = 0$
- K is separable in Φ and S, hence $K = K_1(\Phi, \bar{\Phi}) + K_2(S, \bar{S})$ so that mixed derivatives are null $K_{\Phi\bar{\Phi}S\bar{S}} = ... = 0$.

Using these simplification, the expanded expression for $\lambda_\pm$ is given by

$$\lambda_\pm = \frac{K_{\Phi\bar{\Phi}}}{K_{S\bar{S}}} e^K \Big[F_\Phi \bar{F}_{\bar{\Phi}} + \left(\bar{F} F_\Phi + \bar{F}_{\bar{F}} F\right) K_\Phi + F\bar{F}\left(K_\Phi^2 - K_{\Phi\bar{\Phi}}\right) \Big] \tag{4.82}$$

$$\pm K_{\Phi\bar{\Phi}} e^K \sqrt{F\bar{F}} \Big[\left(2K_\Phi K_{\Phi\bar{\Phi}} + K_{\Phi\bar{\Phi}}^2 - K_\Phi K_{\Phi\Phi\bar{\Phi}}\right)\left(F_\Phi \bar{F} + F\bar{F}_{\bar{\Phi}}\right) + \tag{4.83}$$

$$+ F_\Phi \bar{F}_{\bar{\Phi}} \left(2K_\Phi K_{\Phi\bar{\Phi}} - K_\Phi K_{\Phi\Phi\bar{\Phi}}\right)^2 + F\bar{F}\left(K_\Phi^2 K_{\Phi\bar{\Phi}} + K_{\Phi\bar{\Phi}}^2 - K_\Phi K_\Phi K_{\Phi\Phi\bar{\Phi}}\right) \Big]^{1/2}. \tag{4.84}$$

Also with the additional constraints it is difficult to have a clear picture on how to choose K and W to have fat inflation.

Before moving on to the next section and analyse two specific SUGRA model, it is interesting to write eq.(4.33) as a function of K, W and their derivatives. Imposing the shift symmetry for K and the additional constraints listed above, $V_{NN} > 9H^2$ becomes

$$\left(\frac{F\bar{F}_{\bar{\Phi}} + \bar{F}F_\Phi}{F\bar{F}}\right)\left(\frac{2}{3} - \frac{1}{K_{\Phi\bar{\Phi}}}\right) + \frac{1}{3}K_\Phi \left(2K_\Phi + 2K_{\Phi\bar{\Phi}} - \frac{1}{K_{\Phi\bar{\Phi}}}\right) > 1 \tag{4.85}$$

Summarizing, in order to have a SUGRA inflationary model which presents large turning rate *and* positive fields masses, eq.(4.79) (or equivalently eq.(4.80)) has to be larger than 1, and eq.(4.85) and eq.(4.78) have to be satisfied.

However, all the models presented in Table B.1 do not satisfy eq.(4.85), hence they present a tachyonic mass.

4.3.5 Generating large turning rates in supergravity

In this section we discuss two models where it is possible to demonstrate how to implement the results obtained in the previous section to generate large turning rates. Both of these models are stable and they always feature a fat tachyonic Hessian element along the inflationary trajectory.

4.3.5.1 No-scale inspired model

Let us consider eq.(4.60) with the following Kähler potential:

$$K = -3\,\alpha M_{\rm Pl}^2 \log[(\Phi+\bar{\Phi})/M_{\rm Pl}] + S\bar{S}\,, \tag{4.86}$$

which corresponds to no-scale supergravity for $\alpha = 1$ [160]. For a general $\alpha > 0$, the field space curvature is given by $R = -4/(3\alpha)$. The potential (4.64) becomes

$$V = \frac{M_{\rm Pl}^{3\alpha}\,|F|^2}{(\Phi+\bar{\Phi})^{3\alpha}}\,, \tag{4.87}$$

and the turning rate in eq.(4.80) is

$$\frac{\Omega}{H} \simeq \frac{2\sqrt{\epsilon_T}}{\sqrt{3\,\alpha}}\,. \tag{4.88}$$

As anticipated, choosing an appropriate Kähler potential allows us to generate large turning rates. In this example, this requires a sufficiently small $\alpha \ll 1$, which consequently yields a large negative curvature. We have checked that this is the case for a wide variety of superpotentials $F(\Phi)$.[1]. For clarity we now concentrate on the simple choice[2]:

$$F(\Phi) = p_0 + p_1\Phi\,. \tag{4.89}$$

In terms of real fields $\Phi = r + i\theta$, the field space metric and the scalar potential are given by

$$G_{ab} = \frac{3\,\alpha\,M_{\rm Pl}^2}{2r^2}\delta_{ab}, \quad V = M_{\rm Pl}^{3\alpha}\,\frac{[p_1^2\theta^2 + (p_0+p_1 r)^2]}{8^\alpha r^{3\alpha}}. \tag{4.90}$$

Before examining inflationary solutions, we first consider the masses of the inflatons studying the quantity V_{NN}, see eq.(4.33). As seen in Sec.4.2.3, for the attractor with $r' \sim 0$, V_{NN} can be written as in eq.(4.36).

[1] However, as we show in the next subsection, this is not always the case: it is possible to have large turning also for non-negative curvature.

[2] The exact form of $F(\Phi)$ is unimportant for supporting inflation, as can be seen in several of the families of models in Table B.1.

In particular, from eq.(4.90), V_{NN}/H^2 becomes:

$$\frac{V_{NN}}{H^2} = 18\alpha + \frac{4p_1 r\left(p_0 + 2p_1 r - 6\left(p_0 + p_1 r\right)\alpha\right)}{\alpha\left(\left(p_0 + p_1 r\right)^2 + p_1^2\theta^2\right)} \tag{4.91}$$

To write this expression in terms of the ϵ_T, it is possible to use that $\epsilon_T \simeq \frac{\epsilon_V}{1+\Omega^2/(9H^2)} = \frac{1}{2}\left(\frac{V_a V^a}{V^2}\right)\left(1+\Omega^2/(9H^2)\right)^{-1}$, which, in the small α limit, leads to:

$$\epsilon \simeq -3\frac{p_1 r}{p_0} + \mathcal{O}(\alpha) \quad \Rightarrow \quad p_1 = -\frac{p_0\epsilon}{3r} \tag{4.92}$$

Moreover, from eq.(4.88), it follows that

$$\frac{\Omega}{H} = \frac{4}{3\alpha}\sqrt{\frac{2}{3}}\sqrt{\frac{p_1^4 r^2\theta^2}{\alpha\left(\left(p_0 + p_1 r\right)^2 + p_1^2\theta^2\right)^2}} \quad \Rightarrow \quad \frac{4\sqrt{2}p_1^2 r\theta}{3\Omega/H} = \alpha\left(\left(p_0 + p_1 r\right)^2 + p_1^2\theta^2\right)^2. \tag{4.93}$$

Substituting eq.(4.93) into eq. (4.91), expanding at first order in α and finally substituting p_1 as in eq.(4.92), we obtain that, in the small-α limit $V_{NN}/H^2 - 9$ simplifies to

$$\frac{V_{NN}}{H^2} - 9 \simeq \frac{3\,r\omega}{\theta}\left(\sqrt{2} - \frac{3}{\epsilon}\right) - 9 + \mathcal{O}(\alpha). \tag{4.94}$$

where $\omega = \Omega/H$.
The sign of the expression (4.94) determines the sign of the determinant, and the number of positive eigenvalues. When ϵ is small as required for inflation, eq.(4.94) is manifestly negative. Additionally, whenever ϵ is small, ω is large, and α is small, we find that $V_{NN} < 9H^2$. This fixes the Hessian's eigenvalues to have opposite signs, implying the existence of a tachyonic direction, which, as we will see, is large in Hubble units.

In Figure 4.2, we show the turning rate for different values of α; these agree with the prediction of eq.(4.88), hence Ω/H increases as $\alpha \to 0$. For all the values of α shown, inflation lasts at least 60 e-folds and in Fig.4.2 we plot the turning rate in the last 60 e-folds. For values of $\alpha \gtrsim 10^{-2}$, inflation lasts less than 60 e-folds for the same values of the parameters (p_0, p_1), therefore they have not be plotted.

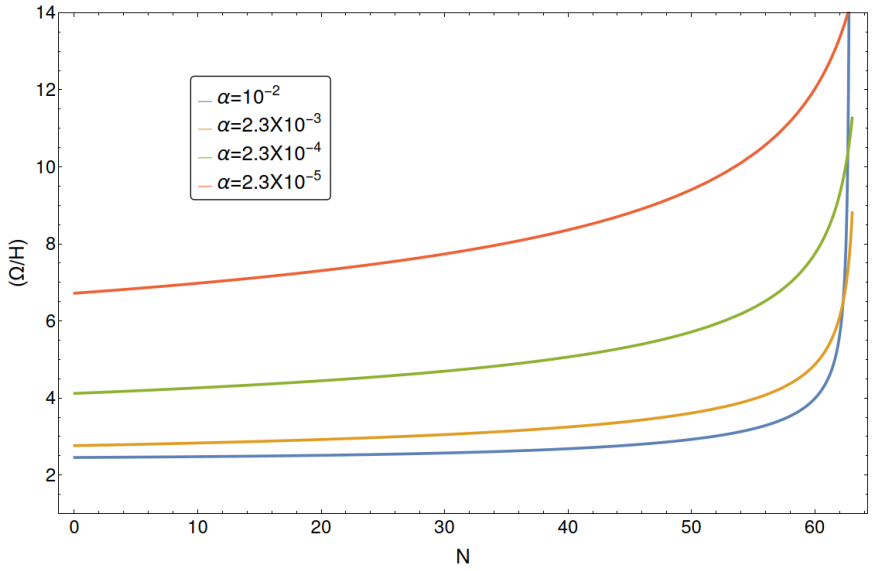

Figure 4.2: We plot the value of the dimensionless turning rate Ω/H for different values of α. In all these cases, inflation lasts at least 60 e-folds and we plot the turning rate in the last 60 e-folds. For $\alpha \gtrsim 10^{-2}$, inflation lasts less than 60-folds for the same values of the parameters $p_0 = 47.4$ and $p_1 = -8.4$).

As discussed previously, it is possible to generate strongly non-geodesic trajectories by tuning α, which changes the field space curvature, $R = -4/(3\alpha)$. In particular, the values of α which produce a large turning rate are those related to large field space curvature. On the other hand, one of the masses is always tachyonic and large along the inflationary trajectory. We show in Figure 4.3 the minimal eigenvalue of (2.101), which satisfies the dSCs.

4.3.5.2 The EGNO model

We now discuss the only supergravity model we are aware of with a dimensionless turning rate larger than one: the EGNO model of [4]. The original Lagrangian obeys the symmetries of $K(S, \bar{S})$ discussed previously in Sec.(4.62) and in principle there is not necessarily a shift symmetry in Φ. However, the parameters that yield turning rates larger than one and long-lasting inflation do admit a shift symmetry. In this region of parameter space, we can make use of the expressions found in our above analysis of rapid-turn inflation in supergravity, see 4.3.4.1.

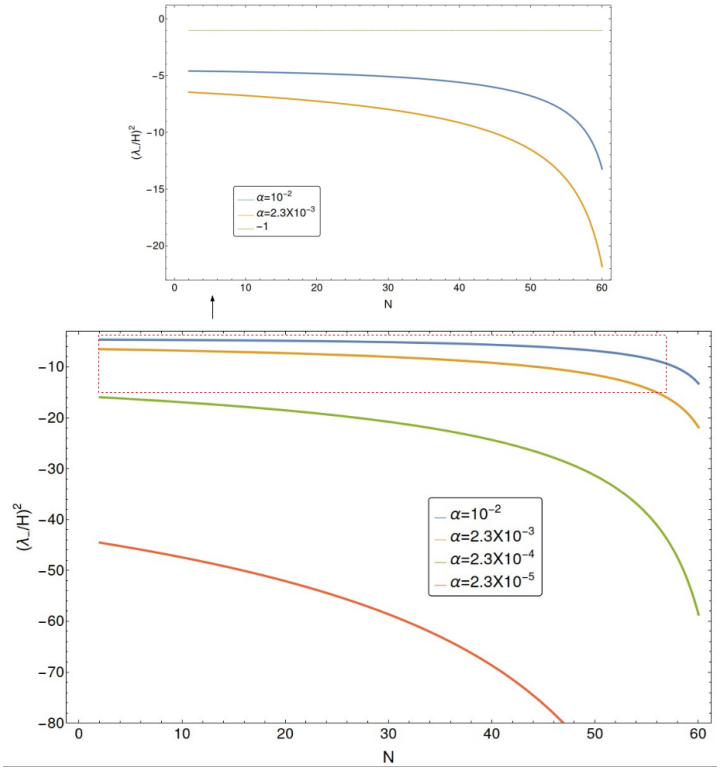

Figure 4.3: We show here the plot of λ_- for different values of α for the no-scale inspired model, eq.(4.90). They are always fat and tachyonic and they increase (in absolute value) as the turning rate increases. We see also that these models satisfy the dSSC along the inflationary trajectory.

The Lagrangian

Setting $M_{\rm Pl} = 1$ in this subsection for simplicity, the Kähler potential and superpotential for the EGNO model are

$$K = -3\,\alpha\,\log\left[\Phi+\bar{\Phi}-c\left[(\Phi+\bar{\Phi}-1)\cos(p)-i(\Phi-\bar{\Phi})\sin(p)\right]^4\right]+\frac{S\bar{S}}{(\Phi+\bar{\Phi})^3}\,, \tag{4.95}$$

$$W = SF(\Phi)\,, \qquad F(\Phi) = \sqrt{\frac{3}{4}}\frac{M}{a}(\Phi-a)\,. \tag{4.96}$$

Following our previous discussion, we introduced the parameter α[1], which allows for tuning to obtain large turning rates. The parameters p, c, a, and M are arbitrary constants.

For $p = 0$, the Kähler potential and superpotential satisfy the symmetries discussed previously[2]. The scalar potential is given by eq.(4.64):

$$\begin{aligned} V &= \frac{3}{4}\frac{M^2}{a^2}\frac{(\Phi+\bar{\Phi})^3\,(a-\Phi)(a-\bar{\Phi})}{\left(\Phi+\bar{\Phi}-c\left[(\Phi+\bar{\Phi}-1)\right]^4\right)^{3\alpha}} \\ &= \frac{6M^2r^3\,(2r-c(1-2r)^4)^{-3\alpha}\,((a-r)^2+\theta^2)}{a^2}\,, \end{aligned} \tag{4.97}$$

where, again, the superfield Φ is expanded as $\Phi = r + i\theta$. We observe that the potential has a minimum at $(r_{\min}, \theta_{\min}) = (a, 0)$ for any value of α.

This model, contrary to the simpler model of the previous section, has a non-trivial field space curvature, R, along $S = \bar{S} = 0$; it is not constant because it change with r and it depends on the value of α and c. When $c = 0$ we have $R = -4/3\alpha$, while for $c \to \pm\infty$ the curvature is $R = -1/3\alpha$. Additionally, $R \to -1/3\alpha$ as $r \to \infty$. Interestingly, the curvature can be very large and positive or negative depending on the values of c and α. In particular, the $\alpha = 1$ inflationary trajectory in [4] has $R > 0$ (see Figure 4.5). Note that although the curvature changes sign, the metric is always positive.

The EGNO model has $\alpha = 1$, $a = 1/2$, $c = 1000$, and $p = 0$, which sets the dimensionless turning rate $\Omega/H \simeq 1.5$ (see the left panel of Figure 4.7). For $p \neq 0$, our scan described in Sec.4.3.1 found smaller turning rates whenever p is far from a multiple of π (see Fig. 4.1).

We emphasize that Ω/H can be increased or decreased by tuning the Kähler potential as in (4.80). Since it depends on c, we may increase or decrease Ω/H by increasing or decreasing c. For example, when $c = 10$, the turning rate drops below one, $\Omega/H \lesssim 1$. In Figure 4.4 we show the potential and inflationary trajectory for the example in [4] with $\alpha = 1$, $a = 1/2$, $M = 10^{-3}$, $c = 1000$, $p = 0$, and initial conditions as indicated in the figure. The evolution of the fields r and θ for this example is shown in Figure 4.6.

[1] In [4] $\alpha = 1$.

[2] In Sec 4.3.1 we scan over p as a free parameter.

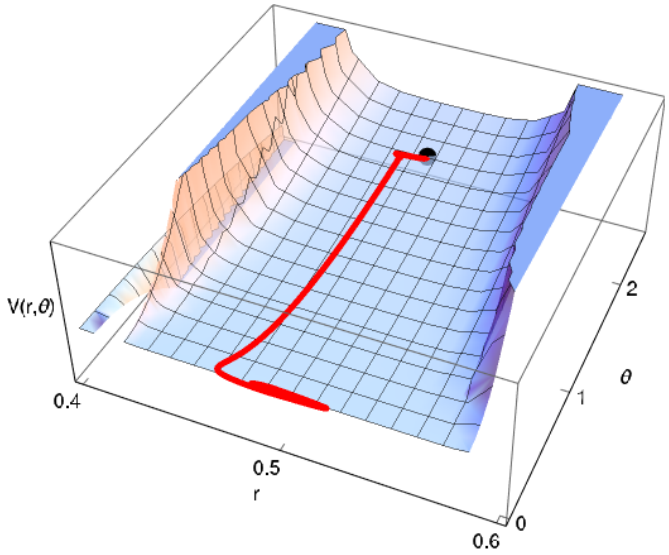

Figure 4.4: EGNO potential and inflationary trajectory for the parameters $\alpha = 1$, $a = 1/2$, $M = 10^{-3}$, $c = 1000$, and $p = 0$ as in the original model [4]. The initial conditions are $r_{\rm ini} = a$, $\theta_{\rm ini} = 5a\sqrt{2/3}$, yielding $N_{tot} = 87$.

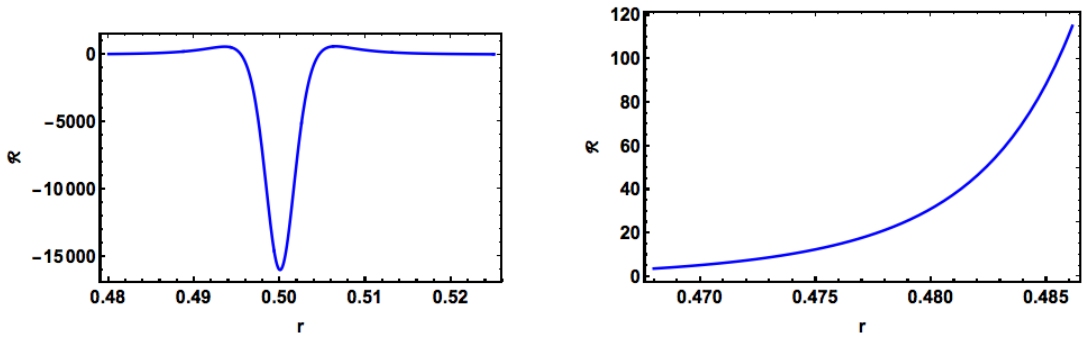

Figure 4.5: Curvature around the inflationary region (right) and during the last 60-efolds of inflation (left) in the EGNO model for the parameter values given in Figure 4.4.

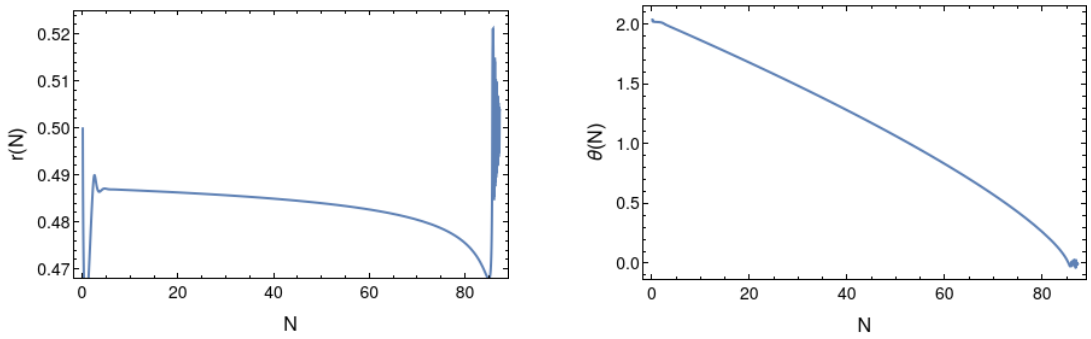

Figure 4.6: Trajectories for r and θ in the original EGNO model for the parameters and initial conditions given in Figure 4.4.

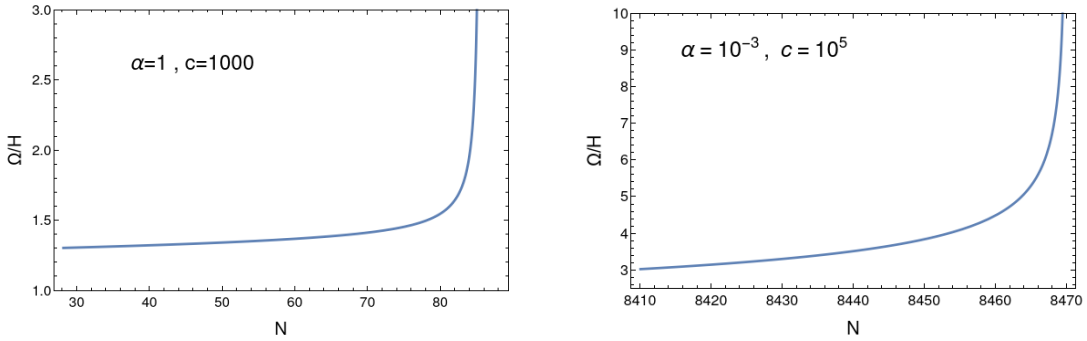

Figure 4.7: Turning rate in the original EGNO model for two sets of parameters for the last 60 efolds. On the left, we use the parameters and initial conditions given in Figure 4.4 and find $\omega(N^*) \simeq 1.3$, where N^* is $(N_{end} - 60)$. On the right, we use $\alpha = 10^{-3}$, $c = 10^5$ to increase the turn rate up to $\omega(N^*) \simeq 3$.

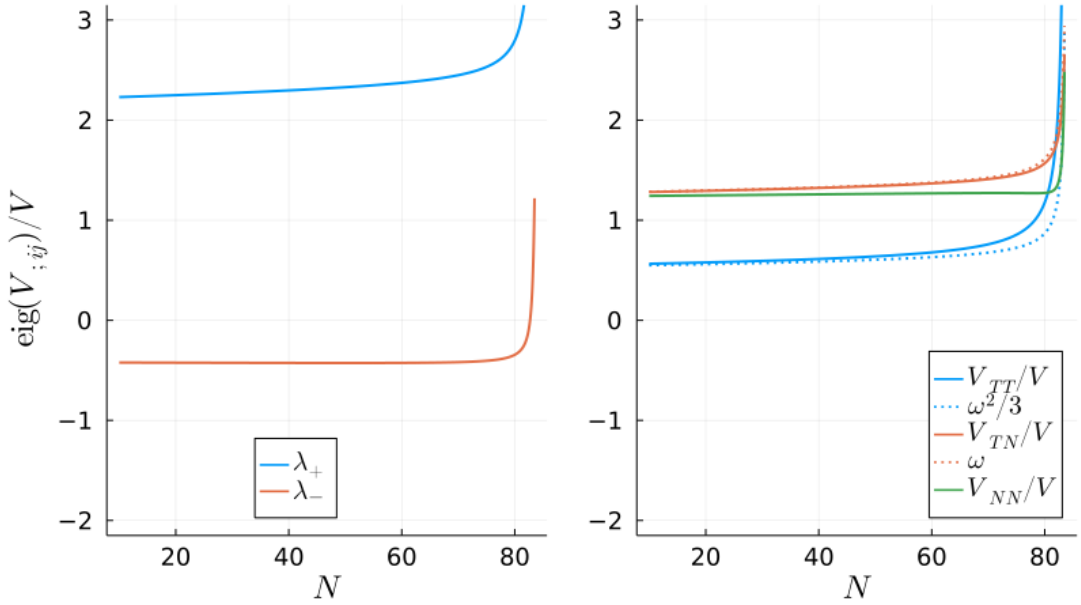

Figure 4.8: On the left, we show the Hessian eigenvalues on the trajectory of the EGNO model for the parameters and initial conditions of Figure 4.4. On the right, for the same initial conditions, we show the kinematic-basis Hessian elements during the evolution and compare them to their dynamical equivalents when available (i.e., eq.(4.4) and eq.(4.5)).

It is now evident that in the EGNO model, we can turn on α to generate rapidly turning trajectories. As a concrete example, in the right panel of Figure 4.7 we show the value of Ω/H for a smaller value of α and a larger value of c. The field space curvature *increases* for these values, but as in the original model the metric is always positive. This is consistent with what we found in the previous subsection for the no-scale inspired model; we conclude that it is possible to obtain large turning rate at the price of large (in absolute value) field space curvature $\mathcal{R}$.

Moreover, in the original EGNO model, the minimal eigenvalue is negative and of order $\lambda_- \sim -0.4$ (see Figure 4.8), while for the modified EGNO model with larger turning rate (left panel, Figure 4.7), the smallest eigenvalue is larger in absolute value, $\lambda_- \sim -3$ thus satisfying the dSSC along the inflationary trajectory. Nevertheless the potential does not satisfy it globally. Away from the trajectory, the potential has neither a large gradient parameter ϵ_V nor a large tachyonic direction.

4.4 Conclusions

Strongly non-geodesic inflationary trajectories in multifield inflation have attracted revived interest recently from theoretical and phenomenological perspectives. However to date, rapid-turn multifield models in supergravity and string theory are scarce. On the supergravity side, the only model we are aware of with an order one turning rate $\Omega/H \gtrsim 1$ is the EGNO model [4] that we discussed in Section 4.3.5.2. On the string theory side, the only available model is the multifield fat inflation D5-brane model introduced in [6].

In the present work we have systematically analysed rapid-turn inflation in supergravity as a first step toward understanding multifield inflationary attractors in string theory. In Section 4.2.1, we showed that light inflatons (in Hubble units) are not required to ensure sustained inflation. That is, the η_V parameter (2.101) does not need to be small in multifield inflation as commonly assumed. We further discuss in detail the large turn inflationary attractor in effective field theory and study the forms of two-field inflation that may occur in supergravity Lagrangeans and focus on multifield axion inflation for its relation to well-known rapid-turn inflationary models in the literature.

In Section 4.3 we then introduce multifield inflation in supergravity. For concreteness, we focus on a large class of two-superfield supergravity models, in which the inflaton is orthogonal to the sGoldstino direction [98, 105, 106]. In this class of models, inflation occurs along a single superfield direction, i.e. along two real directions. Using our discussion in effective field theory, we find expressions for the slow-roll parameter ϵ and dimensionless turning rate Ω/H in terms of derivatives of the Kähler potential (4.78) and the superpotential (4.80). From these expressions we observe that one can tune the superpotential $F(\Phi)$ to ensure a small ϵ, while independently tuning of the Kähler potential to increase the turning rate.

We find a large class of models with a high turn rate, a large field space curvature and a fat tachyonic mass. This class matches all instances of rapid-turn inflation found in our survey of supergravity models in Sec.4.3.1. We study in detail two of these models: a no-scale-inspired model and the EGNO model. In both cases, we show that the turn rate increases as the field space curvature

increases. In particular to obtain $\Omega/H > 1$, we found that it is necessary to finetune the Kähler potential's parameter which is related to the field space curvature (α in the cases analysed in the Chapter) such that $\mathcal{R}$ increases in absolute value. Moreover we observed that one of the masses is always tachyonic when slow-roll and rapid-turn are valid approximations, however this tachyon does not destabilize the trajectory.
In both these models we tuned by hand the parameters need to get strongly non-geodesic inflationary trajectories[1]. However, these can only be considered as toy models, as such small values of α do not occur in theoretically motivated models of supergravity or string theory. Interestingly, tuning of the superpotential and Kähler potential to achieve long lasting inflation and large turns, gives rise to fat tachyonic fields.

In the main text, we focused on a large class of supergravity models that were useful to illustrate our findings. We expect however that similar arguments apply to more general models[2]. In Sec. 4.3.2, we also discuss a single superfield example where we can see that inflation with large turns cannot be achieved.

These results, together with our survey of a wide variety of supergravity models, lead us to conjecture that rapid-turn inflation is rare in theoretically motivated supergravity constructions. This is the primary conclusion of this chapter. When allowing for large field space curvature, rapid-turn inflation becomes possible with $\eta_V \lesssim -\mathcal{O}(1)$. This appears to be a ubiquitous feature of rapid-turn inflation in supergravity; tachyons are also a feature of de Sitter constructions in supergravity [165]. The models we have examined in Section 4.3 do not satisfy the refined de Sitter conjecture globally as they have points with positive masses and $\epsilon_V \sim \mathcal{O}(10^{-4})$; however, rapid-turn inflationary trajectories do not exist in that region.

[1]Non-geodesicity constraints were recently studied in [161] for trajectories that asymptote to infinity, which therefore cannot be applied to inflation where all trajectories end at the minimum of the scalar potential.

[2]For example, Kähler inflation [162] is a small turn attractor with a light tachyonic inflaton (that is, $\eta_V \ll 1$) in the two field case [163, 164]. Following our discussion, tuning the Kähler potential by hand, it should be possible to find a strong non-geodesic inflationary attractor.

Chapter 5

Canonical quantization and general cosmologies

In this Chapter we introduce different topics which play a fundamental role in both Chapter 6 and 7. In the first part we review the ADM formalism and the Hamiltonian formulation of General Relativity (GR). We then define the *synchronous reference system*, which is the one we are going to adopt throughout the remaining part of the thesis, and we use the Dirac approach to derive the Wheeler-DeWitt equation. This equation, considered a fundamental step towards a theory of quantum gravity, is key to understand the Vilenkin approach to the wave function of he Universe, which we discuss in detail. In the second part of the Chapter we introduce the Bianchi Universes, hence homogeneous and anisotropic cosmological models, focusing in particular on the Bianchi I and the Bianchi IX (or Mixmaster) ones. After having analysed in detail the dynamical evolution of the Mixmaster, introducing the Misner variables and showing that its dynamics resembles that of a point-particle in a potential well, we discuss the particular case of the Taub Universe. In the last part of the Chapter we review the extension of the Bianchi IX model dynamics to the inhomogeneous sector and we present the Generic Cosmological Solution. Finally, we conclude this Chapter describing the *fragmentation process*.

5.1 Hamiltonian formulation of the dynamics

5.1.1 ADM formalism

The ADM formalism has been introduced in 1959 [166] in the wake of the numerous 3+1 formalism of GR which started to be developed in the 1920's as a procedure to reduce the Einstein-Hilbert action S_{EH} to its canonical form.
This particular formalism, proposed by R.Arnowitt, S.Deser and C.W. Misner is based on a foliation of the spacetime manifold $\mathcal{M}$, with metric g_{ij}, by a family of three dimensional spacelike hypersurfaces Σ parameterized by a time function $t \in \mathbb{R}$:

$$\mathcal{M} = \mathbb{R} \times \Sigma. \tag{5.1}$$

The hypersurfaces Σ have timelike normal vectors and spacelike tangent ones and each of them is equipped with its own Riemannian structure; we define the induced metric on Σ as h_{ij}. Note that while g_{ij} is the spacetime metric, h_{ij} is a spatial metric, hence it is three-dimensional.
The foliated spacetime can be characterized introducing the *lapse function* N and the *shift vector* N^i, see Fig.5.1 which can be defined using the four-dimensional spacetime metric as

$$N \equiv \left(-{}^{(4)}g^{00}\right)^{-1/2}, \qquad N_i \equiv {}^{(4)}g_{0i} \tag{5.2}$$

Let n^i be the unit normal vector field to Σ_t and y^i a general vector field on the spacetime manifold, y^i can be decomposed into its normal and tangential part with respect to Σ_t:

$$y^i = Nn^i + N^i. \tag{5.3}$$

In the above equation N measures the proper time separation between two adjacent hypersurfaces Σ_t and $\Sigma_{t+\delta t}$ in the direction n^i, while N^i quantifies how much the local coordinate system shifts tangentially passing from Σ_t to $\Sigma_{t+\delta t}$.

The spacetime line element ds^2, adapted to the ADM foliation, can be written as

$$ds^2 = N^2dt^2 - h_{\alpha\beta}(dx^\alpha + N^\alpha dt)(dx^\beta + N^\beta dt) \tag{5.4}$$

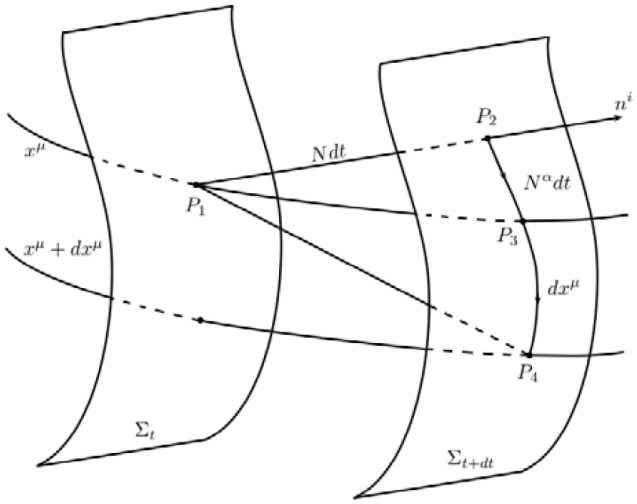

Figure 5.1: ADM foliation of the spacetime.

where we introduces Greek indices in $h_{\alpha\beta}$ to indicate that the spatial metric has three spatial component, hence $\alpha, \beta = 1, 2, 3$. The spatial metric $h_{\alpha\beta}$ can be related to the spacetime one as follows:

$$g_{00} = h_{\alpha\beta}N^{\alpha\beta} - N^2, \quad g_{0\alpha} = h_{\alpha\beta}N^\beta, \quad g_{\alpha\beta} = h_{\alpha\beta}, \quad \sqrt{g} = N\sqrt{h}. \tag{5.5}$$

The importance of the ADM formalism relies on the fact that the $h_{\alpha\beta}$ metric on Σ_t plays the role of the fundamental configuration variable in the canonical analysis of GR as we can see in the following subsection. In the following section we use the Greek indices to indicate three dimensional components.

5.1.2 Canonical general relativity

In this section we discuss the *Hamiltonian formulation of GR* following [167].

Canonical gravity is a reformulation that puts the Einstein Equations in the form of a constrained Hamiltonian system, so that General Relativity can be realized as an initial value problem. The theory, once written in the canonical form, is written without any redundant variables and it contains only the true dynamical information.

The Hamiltonian formulation of a field theory requires to choose a preferred time variable; thus to write GR in the canonical form, we separate the spacetime in a 3+1 foliation.

Therefore the first step to derive the Hamilton's equations is to recast the Einstein-Hilbert action S_{EH} in the ADM formalism. Introducing the extrinsec curvature tensor $K_{\alpha\beta}$ and using the Gauss-Codazzi relation, S_{EH} becomes

$$S_{EH}(h, N, N^\alpha) = \int_{\mathbb{R}\times\Sigma} \mathcal{L}_{3+1} dt d^3x = -\frac{1}{2k} \int_{\mathbb{R}\times\Sigma} N\sqrt{h} \left((K)^2 - K_{\alpha\beta}K^{\alpha\beta} - {}^3R \right) dt d^3x. \tag{5.6}$$

where $k = 8\pi G$.

The Hamiltonian density is then recovered performing a Legendre transformation of the Lagrangian density $\mathcal{L}_{3+1}$.

In Hamiltonian mechanics, given a configuration variable q, its canonically conjugate momentum density π is defined as the partial derivative of the Lagrangian density respect to $\dot{q}$, so in this case

$$\Pi^{\alpha\beta} \equiv \frac{\delta \mathcal{L}_{3+1}}{\delta \dot{h}_{\alpha\beta}}, \qquad \Pi_\alpha \equiv \frac{\delta \mathcal{L}_{3+1}}{\delta \dot{N}^\alpha}, \qquad \Pi \equiv \frac{\delta \mathcal{L}_{3+1}}{\delta \dot{N}} \tag{5.7}$$

Since eq.(5.6) does not depend on $\dot{N}$ and $\dot{N}^i$ and ${}^3R$ does not contain time derivatives it follows that not all the conjugate momenta are independent, and

$$C^\alpha(x,t) \equiv \Pi_\alpha(x,t) = 0, \qquad C(x,t) \equiv \Pi(x,t) = 0. \tag{5.8}$$

These are called *primary constraints*.

According to the theory of constrained Hamiltonian system, it is possible to introduce λ and λ^α as Lagrange multipliers for the primary constraints in order to make the Legendre transformation invertible. The action is given by

$$S_{EH} = \int_{\mathbb{R}} dt \int_\Sigma d^3x \left[\dot{h}_{\alpha\beta}\Pi^{\alpha\beta} + \dot{N}\Pi + N^\alpha \Pi_\alpha - (\lambda C + \lambda^\alpha C_\alpha + N\mathcal{H} - N^\alpha \mathcal{H}_\alpha) \right] \tag{5.9}$$

where

$$\mathcal{H} \equiv \mathcal{G}_{\alpha\beta\gamma\delta}\Pi^{\alpha\beta}\Pi^{\gamma\delta} - \frac{\sqrt{h}}{2k}^3 R \tag{5.10}$$

$$\mathcal{H}_\alpha \equiv -2h_{\alpha\gamma}\nabla_\beta\Pi^{\beta\gamma} \tag{5.11}$$

$$\mathcal{G}_{\alpha\beta\gamma\delta} \equiv \frac{k}{\sqrt{h}}\left(h_{\alpha\gamma}h_{\beta\delta} + h_{\beta\gamma}h_{\alpha\delta} - h_{\alpha\beta}h_{\gamma\delta}\right). \tag{5.12}$$

$\mathcal{H}$ is the *Super-Hamiltonian*, $\mathcal{H}_\alpha$ is the *Super-momentum* and $\mathcal{G}_{\alpha\beta\gamma\delta}$ is the *Super-metric*, which are defined on the space of the three-metrics.
The Hamiltonian of the system therefore is

$$H \equiv \int_\Sigma \left(\lambda C + \lambda^\alpha C_\alpha + N^\alpha\mathcal{H}_\alpha + N\mathcal{H}\right) d^3x \tag{5.13}$$

The fundamental Poisson Brackets (PB) are

$$\{h_{\alpha\beta}(x,t), h_{\gamma\delta}(x',t)\} = 0 \tag{5.14}$$

$$\{\Pi^{\alpha\beta}(x,t), \Pi^{\gamma\delta}(x',t)\} = 0 \tag{5.15}$$

$$\{h_{\alpha\beta}(x,t), \Pi^{\gamma\delta}(x',t)\} = \delta^\alpha{}_{(\gamma}\delta^\beta{}_{\delta)}\delta^3(x-x'). \tag{5.16}$$

To ensure the consistency of the dynamics it is necessary preserve the primary constraints in eq.(5.8) during the evolution, i.e

$$\dot{C} = \{C(x,t), H\} = 0, \qquad \dot{C}^i = \{C^\alpha(x,t), H\} = 0. \tag{5.17}$$

The above PB do not vanish, but are equal to $\mathcal{H}$ and $\mathcal{H}^\alpha$ respectively, hence eq.(5.17) leads to the *secondary constraints*:

$$\mathcal{H} = 0, \qquad \mathcal{H}^\alpha = 0. \tag{5.18}$$

These constraints are going to be key in the next Chapters.

5.1.3 Synchronous reference system

The synchronous reference system, which is used in Chapter 6 is one of the most interesting reference system. It is defined by

$$g_{00} = 1, \qquad g_{0\alpha} = 0 \tag{5.19}$$

and, in the canonical framework, leads to the following line element

$$ds^2 = dt^2 - h_{\alpha\beta}(x,t)dx^\alpha dx^\beta. \tag{5.20}$$

Comparing the last equation with eq.(5.4), we notice that in the synchronous reference system $N = 1$, $N^\alpha = 0$.
This is easily explained looking at the relation between the synchronous time and the lapse function:

$$t_s = \int N(t')dt'. \tag{5.21}$$

Note that the first condition in eq.(5.19) can be set since the time variable t can be rescaled as $\sqrt{g_{00}}dt$ to reduce g_{00} to unity.
It is always possible to define such a reference system, however its choice is not unique.

5.2 Canonical quantization and Vilenkin approach

Quantum cosmology is based on the idea that quantum physics should apply to everything in nature, including the whole Universe.
While this might seem a bizarre idea, since quantum physics seems to be applicable only at microscopical scales while cosmology deals with large scale objects, this is not the case. If the SCM, modified in such a way to include inflation, is the correct description of the beginning of the Universe, and there is an overwhelming number of evidence in this sense as we saw in Chapter 2, then at the very start the Universe was incredibly small and it should be treated like a quantum object as a whole.
Since gravity is the dominant interaction at large scales it is natural to think

that a realistic formulation of quantum cosmology should be based on a quantum theory of gravity.
In this Section we describe how to use the Dirac approach to quantize the canonical variables obtained in the previous section (Sec.5.1.2) in the metric formalism. We derive the Wheeler-DeWitt (WdW) equation and we introduce the concept of *wave function* of the Universe, Ψ, and the idea of *minisuperspace*, a restriction to a finite dimensional subspace of the Wheeler infinite dimensional superspace. Finally, we discuss the semi classical approximation of the wave function of the Universe introduced by Vilenkin in 1989.

5.2.1 Wheeler-DeWitt equation and its implementation in cosmology

The configuration space on which quantum dynamics is defined is called *Superspace*. This can be defined starting from the Riemannian three-metric and matter configurations on the hypersurfaces Σ introduced in 5.1.1

$$\mathrm{Riem}(\Sigma) \equiv \{h_{\alpha\beta}(x), \Phi(x) | x \in \Sigma\}. \tag{5.22}$$

This is an *infinite*-dimensional space on account of $x = \{x^i\}$, but with a finite number of degrees of freedom in each $x \in \Sigma$.
The *Superspace* is then defined as the set of all the $\mathrm{Riem}(\Sigma)$ related by a diffeomorphism:

$$\{h_{\alpha\beta}\} = \frac{\mathrm{Riem}(\Sigma)}{\mathrm{Diff}(\Sigma)} \tag{5.23}$$

The canonical quantization is performed taking the wave function of the Universe $\Psi(h_{\alpha\beta})$ as a functional on the superspace eq.(5.23). Note that Ψ does not depend explicitly on time, since this is contained implicitly in $h_{\alpha\beta}$.

To implement the quantization of a constrained system, see eq.(5.8) and eq.(5.18), it is possible to use the *Dirac approach*, where the quantum theory is constructed without solving the classical constraints. The first step is to replace the canonical momenta

$$\Pi^{\alpha\beta} \to -i\frac{\delta}{\delta h_{\alpha\beta}}, \qquad \Pi_\alpha \to -i\frac{\delta}{\delta N^\alpha}, \qquad \Pi \to -i\frac{\delta}{\delta N} \tag{5.24}$$

and demand that, following eq.(5.8),

$$\hat{\Pi}\Psi = -i\frac{\delta\Psi}{\delta N} = 0, \quad \hat{\Pi}^{\alpha}\Psi = -i\frac{\delta\Psi}{\delta N_{\alpha}} = 0. \tag{5.25}$$

The above result implies that Ψ is independent of N and N^{α}.
To select the physically allowed states, we impose the constraints in eq.(5.18) in their operators version, i.e:

$$\widehat{\mathcal{H}}(\hat{h}, \hat{\Pi})\Psi = 0 \tag{5.26}$$

$$\widehat{\mathcal{H}}_{\alpha}(\hat{h}, \hat{\Pi})\Psi = 0 \tag{5.27}$$

From eq.(5.26), eq.(5.27), and writing the above system in a Schröedinger-like equation, i.e.

$$i\frac{\partial}{\partial t}\Psi_t = \widehat{H}\Psi_t = 0 \tag{5.28}$$

we can see that Ψ_t results independent of time.
Note that eq.(5.26) is the scalar constraint equation, which generates the dynamics. Recalling eq. (5.10), eq.(5.26) explicitly reads as:

$$\widehat{\mathcal{H}}\Psi = \mathcal{G}_{\alpha\beta\gamma\delta}\frac{\delta^2\Psi}{\delta h_{\alpha\beta}\delta h_{\gamma\delta}} - \frac{\sqrt{h}}{2k}\,{}^{3}R\Psi = 0. \tag{5.29}$$

which is the famous *Wheeler-DeWitt* equation, derived by Wheeler in 1967. It is worth mentioning that eq.(5.29) is not a single equation, but one equation for each space point $x \in \Sigma$.

Once the WdW equation is derived, it is possible to apply the quantum framework to cosmological models. These arise when spatially homogeneous (or homogeneous and isotropic) space times are taken into account. Imposing this symmetry (or these symmetries) allows to "freeze" a number of the degrees of freedom in the original superspace, leaving a finite dimensional configuration space known as *minisuperspace*. In this case one deals with a constrained quantum mechanical system described by a *single* WdW equation.
In a generic n-dimensional homogeneous minisuperpsace we can assume that the three metric $h_{\alpha\beta}$ is described by n functions of t, $q^{A}(t)$, which conjugate momenta

are $p^A(t)$, and that the lapse function is space independent, i.e. $N = N(t)$, and that $N^\alpha = 0$.
The action for this model becomes

$$S = \int dt(p_A \dot{q}^A - N\mathcal{H}) = \int dt \left[p_A \dot{q}^A - N(G^{AB} p_A p_B + U(q))\right] \tag{5.30}$$

where $U(q)$ denotes the potential term and G^{AB} is the the reduced version of $G_{\alpha\beta\gamma\delta}$, is called *minisupermetric* and its components run over the independent components of $h_{\alpha\beta}$.
The WdW equation of this system becomes

$$\widehat{\mathcal{H}}\Psi = \left(-\nabla^2 + U\right)\Psi = 0 \tag{5.31}$$

where $\Psi = \Psi(q)$ is the wave function of the Universe and $\nabla^2 = \nabla_A \nabla^A = 1/\sqrt{G}\partial_A(\sqrt{G}G^{AB}\partial_B)$.

5.2.2 Vilenkin interpretation of the wave function of the universe

In this subsection we discuss the *semiclassical approximation* of the wave function of the Universe, proposed by Vilenkin in [168], which leads to a probabilistic interpretation of the wave function of the Universe Ψ.
Conventionally, in quantum mechanics, the probability to find a system, described by $\Psi(x,t)$, in a configuration-space element $d\Omega_x$ is given by

$$dP = |\Psi(x,t)|^2 d\Omega_x \tag{5.32}$$

from which $dP \geq 0$.
In quantum cosmology the wave function of the Universe, as seen in the previous section, depends only on the three-metric $h_{\alpha\beta}$ (and on matter fields if considered) but not on the time, as seen in eq.(5.28). Therefore, the analogue of eq.(5.32) in this case would be:

$$dP = |\Psi(q)|^2 \sqrt{G} d^n q, \tag{5.33}$$

where q are the coordinates as described in the last part of the previous section. However, it is easy to see that eq.(5.33) is not normalizable since, integrated on the minisuperspace, it diverges.
In 1967, in order to avoid this problem, DeWitt proposed an alternative approch based on the use of the conserved current j^A [169], defined as:

$$\nabla_A j^A = 0, \quad j^A = -\frac{i}{2} G^{AB} \left(\Psi^* \nabla_B \Psi - \Psi \nabla_A \Psi *\right) \tag{5.34}$$

Using these definitions he obtained the following probability definition:

$$dP = j^A d\Sigma_A. \tag{5.35}$$

Here the current's conservation guarantees the conservation of the probability, but unfortunately, this can still be negative.
In 1989 Vilenkin proposed an alternative approach, following DeWitt's idea, which is illustrated in [168] and partly based on an early work [170].
The main new ingredient is the idea that in quantum cosmology it is possible to obtain a semidefinite probability if we divide the space variables in semiclassical and quantum ones. The m quantum variables are indicated as ρ^I, $(I = 1, ..., m)$ and the $n - m$ semiclassical variables as q^A, $(A = 1, ..., n - m)$.

Vilenkin's work is based on two fundamental assumptions:

1. WKB approximation of Ψ:

$$\Psi(q, \rho) = A(q) e^{\frac{i}{\hbar} S(q)} \chi(q, \rho), \tag{5.36}$$

2. Adiabatic approximation of Ψ. This requires that the semiclassical evolution is principally contained in the semiclassical part of the wave function, i.e:

$$|\partial A(q)| \gg |\partial \chi(q, \rho)|. \tag{5.37}$$

In the following we show how Vilenkin demonstrates that the probability distribution for Ψ can be written as the product of the probability distribution for the semiclassical part of the wave function with the probability distribution for the quantum one.

Given the adiabatic approximation the effects of the quantum variables on the dynamics of the semiclassical ones is negligible, which suggests that ρ^I correspond to a small subset of the Universe.
The WdW equation in this case can be written as

$$\left(\nabla_0^2 - U_0 - H_\rho\right)\Psi(q,\rho) = \left(H_0 - H_\rho\right)\Psi(q,\rho) = 0. \tag{5.38}$$

The operator $H_0 \equiv \nabla_0^2 - U_0$ is the semiclassical operator and it is obtained neglecting ρ^I and their momenta while H_ρ is the quantum operator, and given the smallness of the quantum subsystem, it is true that

$$\frac{H_\rho \Psi}{H_0 \Psi} = \mathcal{O}\left(\hbar\right) \tag{5.39}$$

so that $H_\rho \propto \mathcal{O}(\hbar^{-1})$. [1]
The wave function of the Universe can be written as in (5.36)

$$\Psi \equiv \Psi_0 \chi = A(q) e^{\frac{i}{\hbar}S(q)} \chi(q,\rho) \tag{5.40}$$

where $\chi(q,\rho)$ depends only parametrically from the q^A.
The semiclassical wavefunction Ψ_0 satisfies the semi classical WdW equation $(\nabla_0^2 - U)\Psi_0 = 0$. This leads to the following two equations

$$G^{AB}\left(\nabla_A S\right)\left(\nabla_B S\right) + U = 0 \tag{5.41}$$

$$2\nabla_A A \nabla^A S + A \nabla_A \nabla^A S = 0 \tag{5.42}$$

which are, respectively, the Hamilton-Jacobi equation for S and the continuity equation for the amplitude A, which expresses the conservation of the current $j^A = |A^2|\nabla^A S$. The equation that the quantum part of the wave function has to solve is

$$\nabla_0^2 \chi + 2\left[\nabla_0\left(\log A\right)\right]\nabla_0 \chi + 2i\left(\nabla_0 S\right)\nabla_0 \chi - H_\rho \chi = 0. \tag{5.43}$$

[1] Eq.(5.39) does not invalidate eq. (5.38). $H_0\Psi$ includes terms of different order in $\hbar$, hence eq.(5.39) simply states that $H_\rho\Psi$ is $\mathcal{O}(\hbar)$ with respect to the larger terms of $H_0\Psi$.

Neglecting all terms which are not order $\mathcal{O}(\hbar)$ this becomes

$$2i\left(\nabla_0\chi\right)\left(\nabla_0 S\right) = H_\rho\chi. \tag{5.44}$$

Redefining the time variable and using that $\dot{q}^A = 2N\nabla^A S$, the above equation can be rewritten as a Schröedinger equation

$$i\frac{\partial\chi}{\partial t} = NH_\rho\chi. \tag{5.45}$$

Vilenkin proved that the probability distribution for Ψ, defined as in eq.(5.40), can be obtained with a first order WKB expansion of eq.(5.34) which, for the semiclassical variables, lead to:

$$j^A = |\chi|^2|A|^2\nabla_0^A S \equiv j_0^A\rho_\chi \tag{5.46}$$

Vilenkin showed that, in the last part of his paper, the probability distribution for the wave function can be written as the product of the probability distribution for Ψ_0 and the probability distribution for the variables ρ^I, hence:

$$\sigma(q,\rho,t) = \sigma_0(q,t)\sigma_\rho(\rho,q,t) = \sigma_0(q,t)|\chi(\rho,q(t),t)|^2. \tag{5.47}$$

Both these probability distributions can be normalized if the surface element $d\Sigma = d\Sigma_0 d\Omega_\rho$, where $d\Sigma_0$ is the surface space defined in the semiclassical subspace, is represented on the equal-time surface. In this case:

$$\int \sigma_0 d\Sigma_0 = 1, \qquad \int \sigma_\rho d\Omega_\rho = 1, \tag{5.48}$$

where $d\Omega_\rho = |detG_{AB}|^{1/2}d^m\rho$ and G_{AB} is the spacetime metric.

To conclude this subsection it is worth mentioning that the above computations are still valid if Ψ is a superposition of the form

$$\Psi(q,\rho) = \sum_k \Psi_k(q)\chi_k(q,\rho) \tag{5.49}$$

where each $\Psi_k(q)$ is given by $\Psi(q) = A(q)e^{\frac{i}{\hbar}S(q)}$. In this case the probability

distribution for Ψ becomes

$$\sigma(q,\rho,t) = \sum_k \sigma_{0k}(q,t)|\chi_k(q,\rho,t)|^2. \tag{5.50}$$

Vilenkin results are the main ingredients used in Chapter 6 and 7 to study the probability distribution of the Bianchi IX Universe.

5.3 Homogeneous cosmological models

The study of homogeneous models arise from breaking the hypothesis of space isotropy and, as seen in the Introduction 1, this is very well motivated. In this section we follow the description of these models as in [171–173].

The set of homogeneous but anisotropic cosmological models has been classified by Bianchi in 1898 [174] into 9 different types, corresponding to the independent groups of isometries for the three-dimensional space.
The dynamics of these models is characterized by the presence of three different scale factors associated to the evolution of the three independent spatial directions [175, 176]; they contain, as a subclass, the standard isotropic FLRW Universe.
The solution of the Einstein Equations for the simplest of this model, the Bianchi I, has been derived by Kasner in 1921 [177] (see also [175]), and takes the name of *Kasner solution*. This plays a key role in the understanding of the dynamical evolution toward the singularity not only for the Bianchi I model, but for all the 9 Bianchi Universes.

The Bianchi IX model, or Mixmaster, is the most general homogeneous model, together with the Bianchi VIII, and has an extremely important role in the study of the cosmological dynamics. Indeed, despite its spatial homogeneity, it possesses typical feature of the generic cosmologial solution [178–180], like a chaotic time evolution of the cosmic scale factors near the cosmological singularity, see also [181] and [182]. Providing the Hamiltonian formulation for the Mixmaster model, and introducing the so-calles *Misner variables* [183], it can be shown that its dynamics resembles the one of a two-dimensional point-particle in a time dependent potential [176]. Furthermore, it has been shown in [184], and later

reviewed in [178], that in its approach toward the singularity, the Mixmaster's dynamics exhibits an oscillatory regime represented by an infinite sequence of bounces of the point-particle against the potential wall.
In particular, in the asymptotic limit towards the singularity the potential term of the Bianchi IX dynamics resembles an infinite well with the morphology of an equilateral triangle with three open corners; these correspond to the non-singular Taub cosmology [185], which defines the limit when the Bianchi dynamics is associated to two equal scale factors of the three possible independent ones.
In the following we present the Kasner solution and study the dynamics of the Bianchi IX model toward is the singularity using both the canonical and the Misner variables.

5.3.1 Bianchi classification

As a general definition, a space is said to be homogeneous if its metric tensor admits an isometry group that maps the space onto itself, i.e a group of transformation which leaves the metric invariant. This group results to be generated by Killing vector fields.
Applying this concept to cosmology, a spacetime is said to be *homogeneous in space and time*, if the spacetime metric g_{ij} is the same in all points of space and time. Therefore under the isometry $\tau : x \to x'$, the line element

$$dl^2 = h_{\alpha\beta}(t, x)dx^\alpha dx^\beta \tag{5.51}$$

has to be invariant, meaning that

$$dl^2 = h_{\alpha\beta}(t, x')dx'^\alpha dx'^\beta \tag{5.52}$$

with the same functional dependence of $h_{\alpha\beta}$ on the new coordinates x'.
The metric tensor for a homogeneous spacetime is obtained choosing a basis of dual vector fields ω^a which are preserved under the isometries. In the general case of a non-Euclidean tridimensional homogeneous space there are three independent forms which are invariant under the transformation of the group of motions, which

can be written as

$$\omega^a = e^a_\alpha dx^\alpha, \tag{5.53}$$

where $\{e_a\}$ are the left-invariant basis vectors under the action of the Killing vectors. The line element dl^2 can be re-expressed as $dl^2 = \eta_{ab}(t)e^a_\alpha dx^\alpha e^b_\beta dx^\beta$.
Following the computation in [175, 181], it can be shown that the condition for the homogeneity of the spacetime becomes:

$$e^\alpha_a \frac{\partial e^\gamma}{\partial x^\alpha} - e^\beta_b \frac{\partial e^\gamma_a}{\partial x^\beta} = C^c_{\ ab} e^\gamma_c \tag{5.54}$$

where $C^c_{\ ab}$ are called *structure constants* of the group and for construction $C^c_{\ bc} = -C^c_{\ ba}$. Using this property, the last equation can be written as

$$C^f_{\ ab} C^d_{\ cf} + C^f_{\ bc} C^d_{\ af} + C^f_{\ ca} C^d_{\ bf} = 0. \tag{5.55}$$

To solve the problem of the classification of homogeneous spaces it is sufficient to identify all the *nonequivalent* sets of structure constants which satisfy eq.(5.55), which can be done using the tensor property of $C^c_{\ ab}$.
The structure constants $C^a_{\ bc}$ can be written as the sum of a symmetric and a antysymmetric part

$$C^a_{\ bc} = \epsilon_{bcd} n^{da} + \delta^a_c a_b - \delta^a_b a_c \rightarrow C^{ab} = n^{ab} + \epsilon^{abc} a_c \tag{5.56}$$

where $n^{ab} = n^{ba}$ and $a_c = C^b_{\ bc}$.
The homogeneity condition in eq. (5.55) therefore can be expressed as

$$n^{ab} a_b = 0 \tag{5.57}$$

and it is possible to determine the nine independent three-dimensional isometry groups assigning a dual vector $a_c = (a, 0, 0)$ and a symmetric matrix n^{ab}, which can be reduced in its diagonal form $n^{ab} = diag(n_1, n_2, n_3)$ without loss of generality.
This classification, reported in Table 5.1, has been derived by Bianchi in 1898.

Type	**a**	n_1	n_2	n_3
I	0	0	0	0
II	0	1	0	0
VII_0	0	1	1	0
VI_0	0	1	-1	0
IX	**0**	**1**	**1**	**1**
VIII	**0**	**1**	**1**	**-1**
III	1	0	1	-1
V	1	0	0	0
IV	1	0	0	1
VII_a	a	0	1	1
VI_a	a	0	1	-1

Table 5.1: Bianchi classification of inequivalent structure constants.

Bianchi type IX is the most general model in which the topology of the spatial surface is given by the three-sphere S^3 and it contains as special case the closed FLRW Universe.
Considering the basis of dual vector field ω^a, preserved under the group transformation (see eq. (5.53)), the spacetime metric tensor for a homogeneous spacetime can be written as

$$ds^2 = N(t)^2 dt^2 - \eta_{ab}\omega^a\omega^b \tag{5.58}$$

where $\eta_{ab}(t)e^a_\alpha(x^\gamma)e^b_\beta(x^\gamma) = h_{\alpha\beta}$, see above.
In a synchronous reference system, see Sec.5.1.3, it is possible to parameterize η_{ab} in such a way that is easier to understand how the above line element describes the properties of the Universe, i.e the expansion and anisotropies, in particular

$$\eta_{ab} = R_0^2 e^{2\alpha}\left(e^{2\beta}\right)_{ab} \tag{5.59}$$

where α and β are function of time only and $Tr\beta = 0$, so that $V_{Univ} \propto R_0^3 e^{3\alpha}$. This will be explained in more details in 5.3.5.

The Einstein Equations (EE) for an homogeneous spacetime, written in the tetradic basis ω^a, reduce to a system of ordinary differential equations which

involve function of time only (see [171] and [181]):

$$\begin{aligned} R^0_0 &= \frac{\partial}{\partial t}K^a_a - K^b_a K^a_b = k\left(T^0_0 - \frac{1}{2}T\right) \\ R^0_a &= K^c_b\left(C^b{}_{ca} - \delta^b_a C^d_{dc}\right) = kT^0_a \\ R^a_b &= \frac{1}{\sqrt{\eta}}\frac{\partial}{\partial t}(\sqrt{\eta}K^a_b) - {}^3R^a_b = k\left(T^a_b - \frac{1}{2}\delta^a_b T\right) \end{aligned} \tag{5.60}$$

where $K_{ab} = -\partial_t \eta_{ab}/2$ and

$${}^3R_{ab} = -\frac{1}{2}\left(C^{cd}{}_b C_{cda} - \frac{1}{2}C_b{}^{cd}C_{acd} - C^c{}_{cd}C_{ab}{}^d + C^c{}_{cd}C_{ba}{}^d\right) \tag{5.61}$$

5.3.2 Bianchi I model and the Kasner solution

The *Kasner solution*, which has been obtained by Kasner [186], is the simplest solution of the EE and solves them in the specific case of the vacuum Bianchi I Universe where, as can be seen in Table 5.1, $C^a{}_{bc} = 0$, $a = 0$ and, as a consequence, ${}^3R_{ab} = 0$.
Solving the system (5.60) (see [175, 181]), the resulting system of ordinary differential equations for η_{ab} is:

$$\dot{\eta}_{ab} = \frac{2}{t}\xi^c_a \eta_{cb}. \tag{5.62}$$

Denoting the eigenvalues of ξ^c_a as $(p_l, p_m, p_n) \in \mathbb{R}$ and its eigenvectors as $\mathbf{l}$, $\mathbf{m}$, $\mathbf{n}$, η_{ab} can be written as

$$\eta_{ab} = t^{2p_l} l_a l_b + t^{2p_m} m_a m_b + t^{2p_n} n_a n_b. \tag{5.63}$$

Choosing the direction of $\mathbf{l}$, $\mathbf{m}$ and $\mathbf{n}$ as the direction of $\{e^a\}$[1] (where the coordinates can be labeled as x^1, x^2, x^3), the space metric for the Bianchi I model becomes:

$$ds^2 = N^2(t)dt^2 - t^{2p_l}(dx^1)^2 - t^{2p_m}(dx^2)^2 - t^{2p_n}(dx^3)^2. \tag{5.64}$$

[1] Recall that $e^a_\alpha = \delta^a_\alpha$.

Here p_m, p_l, p_n are called *Kasner indices* and satisfy

$$p_l^2 + p_m^2 + p_m^2 = 1, \quad p_l + p_m + p_n = 1. \tag{5.65}$$

These indices are ordered according to

$$p_1 \leq p_2 \leq p_3 \tag{5.66}$$

and the variation range for each of them is

$$-\frac{1}{3} \leq p_1 \leq 0, \qquad 0 \leq p_2 \leq \frac{2}{3}, \qquad \frac{2}{3} \leq p_3 \leq 1. \tag{5.67}$$

As can be seen from the above inequalities, the Kasner indices are never equal to each other, except in the case $p_1 = p_2 = 0, p_3 = 1$ and $p_1 = -1/3, p_2 = p_3 = 2/3$. Moreover one is always negative and the other two positive. It is important to notice that the value $t = 0$ is a *non-eliminable* singularity for the metric in eq.(5.64) except for the peculiar case $p_l = p_m = 0, p_n = 1$ where it is possible to reduce the metric to a Minkowskian form using the transformation $t \sinh x^3 = \xi$, $t \cosh x^3 = \tau$.
The Kasner indices can be parameterized in terms of the Khalatnikov-Lifschitz parameter u:

$$p_1(u) = \frac{-u}{1+u+u^2}, \quad p_2(u) = \frac{1+u}{1+u+u^2}, \quad p_3(u) = \frac{u(1+u)}{1+u+u^2} \tag{5.68}$$

which holds for $1 \leq u < \infty$. Note that the parameter u can be uniquely defined as

$$u = -\frac{p_1}{(1-p_3)}. \tag{5.69}$$

For $u < 1$, as we explain more in detail in the next section, the Kasner indices transform as:

$$p_1\left(\frac{1}{u}\right) = p_1(u), \quad p_2\left(\frac{1}{u}\right) = p_3(u), \quad p_3\left(\frac{1}{u}\right) = p_2(u). \tag{5.70}$$

The line element in eq.(5.64) corresponds to a flat homogeneous but *anisotropic* space where volume grows with time while linear distances grow along two direc-

tions and decrease along the third one.

5.3.3 Dynamics of the Bianchi IX model

The Kasner solution is an exact solution for the EE when the Ricci tensor is of order higher than $1/t^2$ and therefore negligible. However this solution is unstable near the singularity since ${}^3R_{\alpha\beta}$ has additional terms dominant respect to t^{-2}.
In what follows we focus on the dynamical evolution of the Bianchi IX model for $t \to 0$.

Taking $\eta_{ab}(t)$ in eq.(5.63) to be diagonal and denoting the three frame vectors satisfying the homogeneity conditions as $\{l, m, n\}$, the spatial metric can be written as :

$$h_{\alpha\beta} = a^2(t) l_\alpha l_\beta + b^2(t) m_\alpha m_\beta + c^2(t) n_\alpha n_\beta, \tag{5.71}$$

and the Einstein equations become:

$$\begin{aligned}
-R^l_l &= \frac{(\dot{a}bc)^{\cdot}}{abc} + \frac{1}{2a^2b^2c^2}\left[\lambda_l^2 a^4 - \left(\lambda_m b^2 - \lambda_n c^2\right)^2\right] = 0 \\
-R^m_m &= \frac{(a\dot{b}c)^{\cdot}}{abc} + \frac{1}{2a^2b^2c^2}\left[\lambda_m^2 b^4 - \left(\lambda_l a^2 - \lambda_n c^2\right)^2\right] = 0 \\
-R^n_n &= \frac{(ab\dot{c})^{\cdot}}{abc} + \frac{1}{2a^2b^2c^2}\left[\lambda_n^2 c^4 - \left(\lambda_l a^2 - \lambda_m b^2\right)^2\right] = 0 \\
-R^0_0 &= \frac{\ddot{a}}{a} + \frac{\ddot{b}}{b} + \frac{\ddot{c}}{c} = 0.
\end{aligned} \tag{5.72}$$

where $(\lambda_l, \lambda_m, \lambda_n) = (1, 1, 1)$ being the structure constants of Bianchi IX.
The last terms on the rhs on all the above equation play the role of the perturbations to the Kasner solution. Note that, for the Bianchi I model $\lambda_l = \lambda_m = \lambda_c = 0$, hence there are no perturbation terms and the Kasner regime can continue indefinitely.
Before addressing the perturbation to the Kasner regime, note that comparing eq.(5.71) and eq.(5.64) when the Kasner solution is a valid approximation for the dynamics of the system, the scale factors can be approximated a

$$a(t) \sim t^{p_l}, \quad b(t) \sim t^{p_m}, \quad c(t) \sim t^{p_n}. \tag{5.73}$$

Let us now address how the rhs terms invalidate the Kasner regime.
If $p_l = p_1$, hence p_l is the smallest among the Kasner indices, it follows that it has to be the negative one, i.e $p_l < 0$, see eq.(5.67). Assuming that $p_m = p_2$, $p_n = p_3$, we can see that the terms on the rhs of the system in eq.(5.72) which are proportional to a^4, thus proportional to t^{4p_l} given eq.(5.73), grow for $t \to 0$. Therefore, they are no longer negligible when solving the EE toward the singularity.
The solution of the full system in eq.(5.72) with this assumption is

$$a(t) = t^{p'_l}, \quad b(t) = t^{p'_m}, \quad c(t) = t^{p'_n} \tag{5.74}$$

where the *new* Kasner indices are related to the old ones through the so-called *BKL map*:

$$p'_l = -\frac{p_1}{1+2p_1}, \quad p'_m = -\frac{2p_1+p_2}{1+2p_1}, \quad p'_n = \frac{p_3+2p_1}{1+2p_1}. \tag{5.75}$$

Clearly these new coefficients satisfy the Kasner relations in eq.(5.65).
From the above result we can see that the effect of the terms a^4 in eq.(5.72) on the Kasner regime is to *replace* a Kasner epoch with another one[1] where the negative Kasner index changes direction: if originally $p_l < 0$, now $p'_m < 0$.
In particular, looking at eq.(5.72), the perturbation to the Kasner regime caused by a^4 vanishes while that associated with b^4 grows until a new transition between a and b occurs with the same law.
To understand how long this process lasts, we can rewrite eq.(5.75) in terms of the parameter u introduced in eq.(5.68):

$$\begin{cases} p_l = p_1(u) \\ p_m = p_2(u) \\ p_n = p_3(u) \end{cases} \quad \to \begin{cases} p'_l = p_2(u-1) \\ p'_m = p_1(u-1) \\ p'_n = p_3(u-1) \end{cases} \tag{5.76}$$

Here it is clear that the exchange of the negative sign happens between the l and

[1] A *Kasner epoch* is defined as the period of time during which the solution of (5.72) is well approximated by (5.64).

m direction[1], while the n one remains unchanged.
Writing the parameter u as

$$u^0 = k^0 + x^0 \tag{5.77}$$

where $k^0 = [u^0]$ is the integer part and $x^0 < 1$ is the fractional, which can be rational or irrational, we can see that, given eq.(5.68) and eq.(5.70), the exchange between the l direction and the m one continues k^0 time. The collection of the total k^0 epochs is called *Kasner era*; during an era one of the three cosmic scale factors decreases monotonically towards the singularity.
After k^0 epochs, a new era starts: when u becomes $u < 1$ at the end of a Kasner epoch, according to eq.(5.70), the Kasner index along the **n** direction (which is p_3 in this case), becomes the smaller positive index, i.e $p_n = p_2$. Thus in the new Kasner epoch the exchanges of values is $l \to n$ or $m \to n$, depending on which one between p_l and p_m was the negative index during the k^0-th epoch of the previous era.
Let us notice that in terms of u, the BKL map (eq.(5.75)) becomes

$$u' = \begin{cases} u - 1 \quad for \quad u > 2 \\ \frac{1}{u-1} \quad for \quad u \leq 2, \end{cases} \tag{5.78}$$

which also explain eq.(5.70). When an era ends the new value of u is $u' = 1/x^0$.
To summarize, the Bianchi IX model evolves toward the singularity with an infinite series of successive Kasner eras: in each era the distances oscillate along two axes oscillates (in the case above these are l and m) and decrease along the third one (n).

5.3.3.1 Stochasticity of the Bianchi IX model

Belinsky, Kahlatnikov and Lifshitz, in [184] and [178] , showed that, for an arbitrary irrational initial value of u, the transition from a Kasner era to another is repeated infinitely many times up to the singularity.
They also demonstrated that the order in which the pair of axes are interchanged and the order in which eras of different length follow each other has a stochastic

[1]We are always considering the specific case where $p_l < 0$ when the dynamics evolution starts.

character.
To every s-th era corresponds a decreasing sequence of values for u, see eq.(5.78), which starts from $u^{(s)}_{max}$, $u^{(s-1)}_{max}$, ..., and arrives to $u^{(s)}_{min}$ where

$$u^{(s)}_{max} = k^{(s)} + x^{(s)}, \quad u^{(s)}_{min} = x^{(s)} < 1. \tag{5.79}$$

The next era starts when $u^{(s)}_{min}$ is reached, and starting value of the parameter u for this era, $u^{(s+1)}_{max}$, is given by

$$u^{(s+1)}_{max} = \frac{1}{x^{(s)}}, \qquad k^{(s+1)} = \left[\frac{1}{x^{(s)}}\right]. \tag{5.80}$$

If the sequence begins with $u^{(0)} = k^{(0)} + x^{(0)}$, then the lengths of the successive eras, $k^{(1)}, k^{(2)}, k^{(3)}, ...$ appear in the expansion for $x^{(0)}$ in the following way:

$$x^{(0)} = \cfrac{1}{k^{(1)} + \cfrac{1}{k^{(2)} + \cfrac{1}{k^{(3)} + ...}}} \tag{5.81}$$

The above sequence is *infinite* if u is an irrational number, while it has a finite number of iteration if u is *rational*. In this last case, the space of possible initial conditions would correspond to sets of zero measure and this, as we discuss in Chapter 7 brought the Belinskii, Kahlatnikov and Lifshitz to exclude rational values of u.

The map presented in eq.(5.80) is known to be stochastic in the sense that, in the limit $s \to \infty$, any initial probability distribution $w^{(1)}(x^{(1)})$ develops into a stationary distribution $w(x)$ which does not depend on the initial data.
As explained in [187], the distribution of $x^{(s)}$ in the interval (0,1), formulated by Gauss, but rigorously derived only in 1928 by R.O. Kuzmin [188] is:

$$w(x) = \frac{1}{(1+x)\log(2)}. \tag{5.82}$$

Note that this probability distribution, computed in the interval $(0, \epsilon)$, with $\epsilon \ll 1$, gives a very small number, which suggests that the probability to have small values of x, needed for $u \gg 1$, is small, but not null.
From eq.(5.82), noticing that x and k are not independent but admit a stationary

joint probability distribution

$$w(x,k) = \frac{1}{(k+x)(k+x+1)\ln(2)} \tag{5.83}$$

we can write

$$w(u) = \frac{1}{u(u+1)\ln(2)}. \tag{5.84}$$

In [189] the authors pointed out for the first time that the map in eq.(5.80) is the source of stochasticity in the cosmological oscillatory regime near a singularity. From a practical point of view, since the map in eq.(5.80) is stochastic and infinite it is possible to observe arbitrary small values $x^{(s)}$ and, accordingly, large lengths $k^{(s)}$ and therefore $u^{(s+1)}$.
The case of large values of u, $u \gg 1$, is called *small-oscillation regime* and produces, the following Kasner exponents:

$$p_1 \sim -\frac{1}{u}, \qquad p_2 \sim \frac{1}{u}, \qquad p_3 = 1 - \frac{1}{u^2} \tag{5.85}$$

which, in the limit considered, approach the values $(0,0,1)$. In [189] the authors proved that, starting from a generic $u^{(0)}$ the small oscillation regime is *always* reached.

5.3.4 Hamiltonian formulation of the Mixmaster model

The Hamiltonian formulation of the Bianchi IX dynamics allows to understand how the infinite sequence of Kasner epochs described in Sec.5.3.3, takes the form of a two-dimensional point particle performing an infinite series of bounces within a potential well.

To obtain the Hamiltonian of the system, the first step is to write the Einstein-Hilbert action (EH) in the specific case of a homogeneous model. To do that, we notice that the line element in eq.(5.58) can be rewritten in terms of 1-forms ω^a [181] as

$$\eta_{ab}\omega^a\omega^b = e^{q_a}\delta_{ab}\omega^a\omega^b \tag{5.86}$$

where $q^a = q^a(t)$ and ω^a, in the specific case of the Bianchi IX Universe, are

$$\begin{aligned} \omega^1 &= \sin\psi \sin\theta d\phi + \cos\psi d\theta \\ \omega^2 &= -\cos\psi \sin\theta d\phi + \sin\psi d\theta \\ \omega^3 &= \cos\theta d\phi + d\psi \end{aligned} \tag{5.87}$$

with $\theta \in [0, \pi)$, $\phi \in [0, 2\pi)$ and $\psi \in [0, 4\pi)$ are Euler angles, see [181] [176] [1] Eq.(5.86) is valid in the case of absence of matter, when $R_{0\alpha} = 0$ and it is possible to choose a diagonal $h_{\alpha\beta}$.
Carrying out the space integration of the EH action, using

$$\int \omega^1 \wedge \omega^2 \wedge \omega^3 = 4\pi^2, \tag{5.88}$$

the dynamical evolution of the Bianchi IX model is given by the variational principle[2]

$$\delta S_B = \delta \int_{t_1}^{t_2} \mathcal{L}_B(q_a, \dot{q}_b) dt = 0, \tag{5.89}$$

The Lagrangian $\mathcal{L}_B$ can be written explicitly, and it reads as

$$\mathcal{L}_B = \sqrt{-g}R = N\sqrt{\eta}\ ({}^3R + K_{ab}K^{ab} - K^2) \tag{5.90}$$

as already seen in eq.(5.6), where $\eta = det(\eta_{ab})$, ${}^3R$ is the spatial curvature, K_{ab} is the extrinsec curvature tensor and K is its trace.
Using the metric in eq.(5.86), the Lagrangian density becomes

$$\mathcal{L}_B = -\frac{8\pi^2\sqrt{\eta}}{k}\left[\frac{1}{N}\left(\dot{q}_l\dot{q}_m + \dot{q}_l\dot{q}_n + \dot{q}_m\dot{q}_n\right) - N\ {}^3R\right] \tag{5.91}$$

and we can write the Hamiltonian $\mathcal{H}_B$ for the Bianchi IX model performing a Legendre transformation.

[1] The simply connected covering space is obtained by extending the range of ψ to 4π, see [176].

[2] The subscript B here indicates that the action S and the Lagrangian density $\mathcal{L}$ are those of the Bianchi IX model.

Defining p_a as the conjugate to the generalized coordinates q_a, [1]

$$p_l \equiv -\frac{4\pi^2\sqrt{\eta}}{kN}(\dot{q}_m + \dot{q}_n), \quad p_m \equiv -\frac{4\pi^2\sqrt{\eta}}{kN}(\dot{q}_l + \dot{q}_n), \quad p_n \equiv -\frac{4\pi^2\sqrt{\eta}}{kN}(\dot{q}_l + \dot{q}_m), \tag{5.92}$$

and knowing that

$$N\mathcal{H}_B = \sum_{a=l,m,n} p_a\dot{q}^a - \mathcal{L}_B, \tag{5.93}$$

the Hamiltonian density $\mathcal{H}_B$ and the action S_B become

$$\mathcal{H}_B = \frac{k}{8\pi^2\sqrt{\eta}}\left[\sum_a (p_a)^2 - \frac{1}{2}\left(\sum_{a\neq b} p_b\right)^2 - \frac{64\pi^4}{k^2}\eta\ {}^3R\right] \tag{5.94}$$

$$S_B = \int dt\,(p_a\dot{q}^a - N\mathcal{H}_B)\,. \tag{5.95}$$

Note that $\mathcal{H}_B = 0$ is the scalar constraint for these models.

5.3.5 Dynamics of the Mixmaster model in the Misner variables

In 1969 Misner introduced the *Misner variables* [5], α, β_+, and β_-, to better understand how the evolution of both the expansion and anisotropies of the Bianchi IX model evolve as the Universe approaches the singularity.
He showed that using these coordinates the dynamics of the Mixmaster model can be reduced to the simple and very intuitive picture of a two-dimensional point particle moving within a closed potential domain. .

The variables q_a, introduced in eq.(5.86), can be written in terms of these new variables as

$$\begin{cases} q_1 = 2(\alpha + \beta_+ + \sqrt{3}\beta_-) \\ q_2 = 2(\alpha + \beta_+ - \sqrt{3}\beta_-) \\ q_3 = 2(\alpha - 2\beta_+). \end{cases} \tag{5.96}$$

and also the null-trace matrix β_{ab}, recalling eq.(5.59), can be re-expressed in

[1] These are *not* the *Kasner indices* introduced in the previous section.

terms of the Misner variables:

$$\begin{aligned}\beta_{11} &= \beta_+ + \sqrt{3}\beta_- \\ \beta_{22} &= \beta_+ - \sqrt{3}\beta_- \\ \beta_{33} &= -2\beta_+.\end{aligned} \tag{5.97}$$

As mentioned above, these coordinates have a clear physical meaning: the variable α is related to the Universe volume, in particular we have that $\mathcal{V} \sim e^{3\alpha}$, while $\beta_\pm$ describe the anisotropies in the different spatial directions.

Using the Misner variables $\mathcal{H}_B$ in eq.(5.94) becomes:

$$\mathcal{H}_B = \frac{k}{3(8\pi)^2} e^{-3\alpha} \left(-p_\alpha^2 + p_+^2 + p_-^2 + \mathcal{V}\right) \tag{5.98}$$

where

$$\mathcal{V} \equiv \frac{32\pi^4}{k^2} e^{4\alpha} V_{IX}(\beta_\pm) \tag{5.99}$$

and

$$V_{IX}(\beta_\pm) = e^{-8\beta_+} - 4e^{-2\beta_+} \cosh\left(2\sqrt{3}\beta_-\right) + 2e^{4\beta_+}\left[\cosh\left(4\sqrt{3}\beta_-\right) - 1\right] \tag{5.100}$$

is the potential for the Bianchi IX model.
In eq.(5.98), p_α and $p_\pm$ are the conjugate momenta to the respective Misner variables and, contrary to eq.(5.94), the kinetic term is diagonal, suggesting that it is possible to have a description resembling that of a point-particle.
It is also worth noticing that $\mathcal{V}$ is a function of both α, therefore time, and $\beta_\pm$, therefore the anisotropies.

The EE in the Misner variables are obtained using eq.(5.98) and imposing

$$\delta S_B = \delta \int \left(p_\alpha \dot{\alpha} + p_+ \dot{\beta}_+ + p_- \dot{\beta}_- - N\mathcal{H}_B\right) dt = 0. \tag{5.101}$$

for arbitrary independent variations of p_α, $p_\pm$, α, $\beta_\pm$, N.
The variation respect to N provides the super-Hamiltonian constraint, see eq.(5.18),

$$\mathcal{H}_B = 0. \tag{5.102}$$

The momenta p_α and $p_\pm$ are obtained varying eq.(5.101) respect to p_α and $p_\pm$ and inverting the results obtained:

$$p_\alpha = -\frac{6(4\pi)^2}{Nk}\dot{\alpha}e^{3\alpha}, \quad p_\pm = \frac{6(4\pi)^2}{Nk}\dot{\beta}_\pm e^{3\alpha}. \tag{5.103}$$

Analogously, the equations of motions can be written as

$$\begin{aligned} \dot{\alpha} &= N\frac{\partial \mathcal{H}_B}{\partial p_\alpha}, \quad \dot{p}_\alpha = -N\frac{\partial \mathcal{H}_B}{\partial \alpha}, \\ \dot{\beta}_\pm &= N\frac{\partial \mathcal{H}_B}{\partial p_\pm}, \quad \dot{p}_\pm = -N\frac{\partial \mathcal{H}_B}{\partial \beta_\pm}. \end{aligned} \tag{5.104}$$

Note that for the Kasner solution, the variables β_+ and β_- can be written in terms of α and the parameter u, introduced in eq.(5.68), as

$$\beta_+ = \frac{1}{2}\alpha\left(\frac{1-2u-2u^2}{1+u+u^2}\right), \quad \beta_- = -\frac{\sqrt{3}}{2}\alpha\left(\frac{2u+1}{1+u+u^2}\right) \tag{5.105}$$

Focusing on the potential $\mathcal{V}$ in eq.(5.99), this is a positive definite "potential well", which has the same symmetries as an equilateral triangle in the (β_+, β_-) plane and presents three open corner, see Fig.5.2.

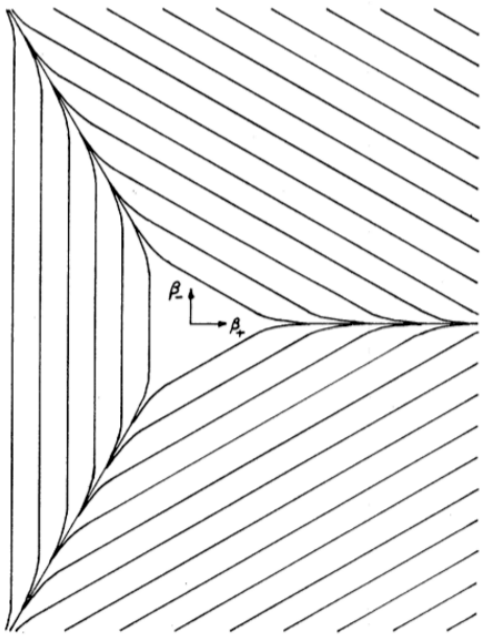

Figure 5.2: Equipotential lines for the Bianchi IX potential eq.(5.100) in the (β_-, β_+) plane. Plot from [5].

Near the origin, when $\beta_\pm = 0$, the equipotential lines are approximately circles, and the potential can be written as

$$V(\beta_\pm) = 24\left(\beta_-^2 + \beta_+^2\right), \tag{5.106}$$

while for large values of $|\beta_+|$ one finds:

$$V_{IX}(\beta_\pm) = \begin{cases} e^{-8\beta_+}, & \beta_+ \to -\infty, \quad |\beta_-| \ll 1 \\ 48\beta_-^2 e^{4\beta_+}, & \beta_+ \to +\infty, \quad |\beta_-| \ll 1 \end{cases}. \tag{5.107}$$

In the last part of Sec.5.3.4 we showed that the dynamical evolution of the Bianchi IX model toward the singularity is characterized by an infinite succession of Kasner epochs. Introducing the Misner variables and considering the set of equations (5.104), with the explicit form of the potential (5.99) and its simplified expressions (5.106) and (5.107), it is possible to see how this infinite succession of epochs can be interpreted as a point particle performing an infinite sequence of bounces against the potential well, see [181].

In [189] the authors used the equations presented above and the stochastic behavior of the parameter u discussed in Sec.5.3.3.1 to show that the Bianchi IX Universe enters *at least* one time deeply in one of the potential corners (see Fig.5.2) during its dynamical evolution.
The corner configuration is described by $u \gg 1$ and given the random character of the sequence of $k^{(s)}$, the parameter u assumes a very large value $\gg 1$ *at least* one time, see [189].
This configuration takes the name of *small oscillation regime*, see Sec.5.3.3.1, and lasts for many epochs, since k, as well as u, is $\gg 1$. Thus, the small oscillation regime is a *long regime* for the dynamics of the Mixmaster model.
However, the Universe *always* leaves this configuration. Despite the Universe spends a long time in the corner, it is a known result, see for example [181], that sooner or later it escapes the corner to restore the standard dynamics in the central region of the potential

Note that in the formulas presented in this section the Hamiltonian density $\mathcal{H}_B$ describes an empty Universe. In Chapter 6 we generalize it adding a scalar field ϕ and a cosmological constant Λ in order to obtain an inflationary scenario.

5.3.6 Taub Universe

The *Taub Universe*, introduced by Taub in [190], is an homogeneous cosmological model which presents a $SO(3)$ symmetry group. This Universe is considered an intermediate step between FLRW and the Mixmaster model since two of the three scale factors (which are all different in the Bianchi IX model) are the same.
Recalling the definition of the one forms in eq.(5.87), its line element can be written as [191] :

$$ds^2 = l^2 \left[F(dt^2) - A\left((\omega^1)^2 + (\omega^2)^2\right) - B(\omega^3)^2\right] \tag{5.108}$$

where l is a constant length, F, A and B are function of the time variable t.
The field equations $R_{ij} = 0$ can be satisfied choosing $F = A^m B^n$ and, given

Taub's choice $m = 2$ and $n = 1$, the functions A and B obtained are:

$$A = \frac{\cosh(t)}{2\left(1 + \cosh(t + a)\right)}, \quad B = \frac{1}{\cosh t}. \tag{5.109}$$

Therefore the model is *no longer singular* for $t \to 0$, but the singularity is at $t \to \pm\infty$. For further detail see [172].

Introducing the Misner variables, to get a better understanding of the model, the line element (5.108) can be rewritten as in (5.59)

$$ds^2 = N(t)^2 dt^2 - e^{2\alpha}\left(e^{2\beta}\right)_{ab}\omega^a\omega^b \tag{5.110}$$

where the anisotropy matrix β_{ab} only contains the anisotropy β_+

$$\beta_{ab} = diag(\beta_+, \beta_+, -2\beta_+). \tag{5.111}$$

Therefore the Taub model is a particular case of Bianchi IX model once $\beta_- \equiv 0$.

5.4 The generic cosmological solution

Since the first years of the '60s, the Landau School started investigating the dynamical characterization of the *generic cosmological solution* of the EE.
The first work in this direction was conduncted by Khalatnikov and Lifshits in 1963 [192] where they focused on the generalization of the Kasner solution to anisotropic and inhomogeneous cosmologies. In their derivation it was concluded that the asymptotic behavior of a generic inhomogeneous Universe towards the singularity is Kasner like. However, in order for this regime to survive up to the initial singularity, they had to impose an additional constraint on the metric. Hence, they reduced the number of physically arbitrary functions to three, one less than those necessary for the solution to be considered general.

In the following years Belinsky, Kalathnikov and Lifshitz, starting from the analysis of the dynamical evolution of the homogeneous Mixmaster model (see for example[184, 193]), showed that, even relaxing this additional constraint, it is possible to implement the idea of the infinite sequence of Kasner epochs towards

the cosmological singularity (see Sec. 5.3.3) to the dynamics of a generic inhomogeneous model [178], see Appendix C. See also [181] and [194] for a review. They discussed the idea that the generic cosmological solution dynamics resembles the one of the homogeneous indices of types VIII and IX also in [195, 196]. Interesting review papers on these findings are [187, 197–199].
This result is referred to as *BKL conjecture*.
Note that in [178], the inhomogeneous dynamics was described assuming the existence of a single relevant spatial scale of homogeneity and the standard time evolution was recovered on a small spatial scale, roughly identified with the average horizon size.
However, in [180] and [200] it was shown that the coupling between the space and time dependence of the metric tensor implies that smaller and smaller inhomogeneous scales are generated approaching the singularity (see [201] for a discussion on the impact that such a phenomenon can have on the primordial Universe turbolence, see also [202]). This phenomenon takes the name of *fragmentation process*.
In [179], Kirillov demonstrated that the spatial gradients growth can not destroy the standard oscillatory regime because they growth only logarithmically in time, and therefore they grow slower than the terms which induce the instability of the Kasner regime and the transition to a new one. Hence, despite the fragmentation process and the intrinsic inhomogeneity, the dynamical evolution of general cosmological models is still appropriately described by a sequence of Kasner regimes
.
On how to reconcile the generic mixmaster Universe with the highly symmetric isotropic model, at least on a local spatial regime, see [203], where the role of an inflationary regime is modeled via the effect of a massless scalar field plus a cosmological constant.

In this section we go trough the derivation of the BKL conjecture, and we present the Hamiltonian formulation for the inhomogeneous Universe, as formulated in [204]. Finally we introduce the concept of the *fragmentation process*, [180, 200] which is used in Chapter 7.

5.4.1 Generic cosmological solution in Misner variables

In Appendix C we review the derivation of the generalized Kasner solution done in [192] and [178], where the authors showed that the BKL map for inhomogeneous and anisotropic cosmologies retains in each space point the same form of the one valid for the homogeneous case, eq.(5.75). In this section we study the dynamics of this general cosmological model in the Misner variables.
In the ADM formalism the line element of a generic inhomogeneous cosmological model reads as

$$ds^2 = N(t,x)^2 dt^2 - h_{\alpha\beta}(dx^\alpha + N^\alpha dt)(dx^\beta + N^\beta dt) \tag{5.112}$$

where $h_{\alpha\beta} = e^{q_a(t,x)} l^a_\alpha l^b_\beta$ and the vectors l^a_α are linearly independent and have generic space-dependent components.
The dynamics of this system is given by the action

$$S = \int_{\Sigma\times\mathbb{R}} d^3x dt (p_a \partial_t q_a - N\mathcal{H} - N^\beta \mathcal{H}_\beta) \tag{5.113}$$

which can be rewritten in terms of Misner-like variables $\alpha(t,x)$ and $\beta_\pm(t,x)$, via a transformation analogous to the one in eq.(5.96)[1] as:

$$S = \int d^3x dt (p_\alpha \partial_t \alpha + p_+ \partial_t \beta_+ + p_- \partial_t \beta_- - N\mathcal{H} - N^\beta \mathcal{H}_\beta). \tag{5.114}$$

The super-Hamiltonian $\mathcal{H}$ admits the simplified expression

$$\mathcal{H} = \frac{k}{12} e^{-3\alpha} \left(-p_\alpha^2 + p_+^2 + p_-^2 + e^{4\alpha} V_G(\beta_+, \beta_-)\right) \tag{5.115}$$

where V_G is obtained neglecting the spatial gradients of the Misner variables.
This simplification is justified by the results presented in [179] by Kirillov, where he showed that these gradients increase *slower* towards the singularity (in a logarithmic way) than the time derivatives of the configuration variables. See also [181] for a simplified derivation of this result.

[1] Note that being in the inhomogenous case the Misner variables, as for the q_a, depend on the spatial coordinates.

The potential V_G is given by

$$V_G = \frac{1}{4}\left(\lambda_1^2 e^{4\beta_+ + 4\sqrt{3}\beta_-} + \lambda_2^2 e^{4\beta_+ - 4\sqrt{3}\beta_-} + \lambda_3^2 e^{-8\beta_+}\right) + \tag{5.116}$$

$$- \frac{1}{2}\left(\lambda_1\lambda_2 e^{4\beta_+} - \lambda_1\lambda_3 e^{-2\beta_+ + 2\sqrt{3}\beta_-} - \lambda_2\lambda_3 e^{-2\beta_+ - 2\sqrt{3}\beta_-}\right) \tag{5.117}$$

where $\lambda_a(x^\gamma) \equiv l_a \cdot \nabla \wedge l_a$.
The equipotential lines associated to this potential form, in each space point, a equilateral triangle with three open corners reaching infinity, exactly as in Fig.5.2. These three corners are equivalent. This can be seen simply rotating the coordinate plane (β_+, β_-) by an angle of $\pi/3$ to map one into another.
Using the Misner variables, the classical evolution of the system is summarized by the Hamilton-Jacobi equation

$$-\left(\frac{\partial S}{\partial \alpha}\right)^2 + \left(\frac{\partial S}{\partial \beta_+}\right)^2 + \left(\frac{\partial S}{\partial \beta_-}\right)^2 + V_G(\alpha, \beta_+\beta_-) = 0 \tag{5.118}$$

where we used that $p_a = \frac{\partial S}{\partial q^a}$.

Close to the cosmological singularity, when $\alpha \to -\infty$, the potential term becomes negligible and the solution of eq.(5.118) reads as

$$S = -\left(\sqrt{k_+^2 + k_-^2}\right)\alpha + k_+\beta_+ + k_-\beta_- \tag{5.119}$$

where $k_\pm = k_\pm(x^\gamma)$ are functions of the space coordinates only.
For the Jacobi prescription, the functional derivative of S respect to $k_\pm$ has to be equal to a stationary quantity, which we indicate with $\overline{\beta}_\pm(x^\gamma)$, therefore

$$\beta_\pm = \pi_\pm(x^\gamma)\alpha + \overline{\beta}_\pm(x^\gamma) \tag{5.120}$$

where

$$\pi_\pm \equiv \frac{p_\pm}{p_\alpha} = \frac{k_\pm}{\sqrt{k_+^2 + k_-^2}}. \tag{5.121}$$

Since the function $\pi_\pm$ must satisfy by definition $\pi_+^2 + \pi_-^2 = 1$, it is possible to set

$$\pi_+ = \cos\theta, \qquad \pi_- = \sin\theta. \tag{5.122}$$

In conclusion, the generic cosmological solution toward the Big Bang is isomorphic to the one of the Mixmaster model. This comes as a consequence of the fact that the spatial coordinates are involved in the problem only as parameters.

5.4.2 Fragmentation process

At the end of the 1990, Kirillov and Montani, in two different papers, respectively [200] and [180], introduced the idea of the *fragmentation process*, a peculiar mechanism, specific of the inhomogeneous Mixmaster model, taking place in the limit towards the singularity.
See [181] and [204] for a qualitative discussion. [1]

Deriving the generalized Kasner solution, see Appendix C, Belinskii, Khalatnikov and Lifshitz extended the BKL mechanism to inhomogeneous cosmologies under the assumption of local homogeneity [178]. To do that they assumed that the spatial variations of all spatial metric components possess the same characteristic length k, which can be considered as the average wave number.
However, in [201] the same Belinskii suggested that this hypothesis could cease to be valid as a natural consequence of the evolution of the system towards the singularity, and this is where the fragmentation process comes into play. This mechanism describes the effect produced by the iterative action of the BKL map, eq.(5.78), on the spatial dependence of the Kasner index functions.
Let us start by noticing that eq.(C.3) does not require for the three Kasner indices $p_a(x^\gamma)$ to have the same ordering in all points of space: as long as the conditions in eq.(C.3) are satisfied, the different Kasner indices can vary their ordering an infinite number of time through space, in agreement with the oscillatory-like behavior of their spatial dependence.[2]
Given that the BKL map in the inhomogeneous case has the same form of the

[1] In this section we use the terminology and notation introduced in [180]
[2] This behavior is a consequence of the iteration of the BKL map (5.75).

BKL map for the homogeneous Mixmaster , see eq.(5.78), point by point, this has also the same general properties; in particular, it shows a strong dependency on the initial conditions.
Assuming that, as initial condition, $u = u^{(0)}(x^\gamma)$, the Kasner index functions $p_a^0(x^\gamma)$ assume close values if computed in two very close points, x_1 and x_2, i.e $p_a^{(0)}(x_1) \sim p_a^{(0)}(x_2)$.[1] However, given the strong dependence of the map from the initial conditions, the trajectories emerging from these two space points result to be exponentially different after few steps of the map! Moreover, since $p_a(x^\gamma) \in [-1/3, 1]$, which is quite a restricted interval, the spatial dependence acquires an oscillatory-like behavior.

Let us now study the iterative effect of the BKL map on the manifold.
In the simplest case, it is possible to assume, as initial condition at a fixed instant of time t_0, that

1. All the space points are described by a generalized Kasner metric

2. The Kasner index functions have the same ordering in all the manifold and that they are described by a narrow interval of u values, i.e $u \in [K, K+1]$, where K is an integer.

When both these conditions are satisfied, the manifold is said to be composed of only one "island".
Using the notation introduced in Sec.5.3.3, at t_0 the u parameter can be written as $u^0(x^\gamma) = K^0 + X^0(x^\gamma)$, where $X^0(x^\gamma)$ takes all values in $[0, 1)$.[2]
As the system evolves towards the singularity, its dynamics is controlled by the ihomogeneous BKL map, which point by point is given by eq.(5.78), so the Universe evolves for n Kasner epochs, where n is such that $K - n = 0$. After the last epoch, the integer part of u goes to zero, and $u < 1$; the Kasner era ends and a new one starts.
The new u parameter, given eq.(5.78), starts from $u^1(x^\gamma) = 1/X^0(x^\gamma)$ and takes all the values in the interval $[1, \infty)$. Hence only space points which are very close

[1] This is due to the continuity of the three-manifold.

[2] Note that in this section we indicating the fractional part of u with X and not x, to not generate confusion with the space coordinates.

at the end of the first era will be in the same island when the new era starts (i.e. they have the same K^1) while space points which are further part will find themselves different islands. Therefore, in the new era, the manifold can be separated in many islands, according to the value of the integer K^1 in the different regions, see Fig.5.3.

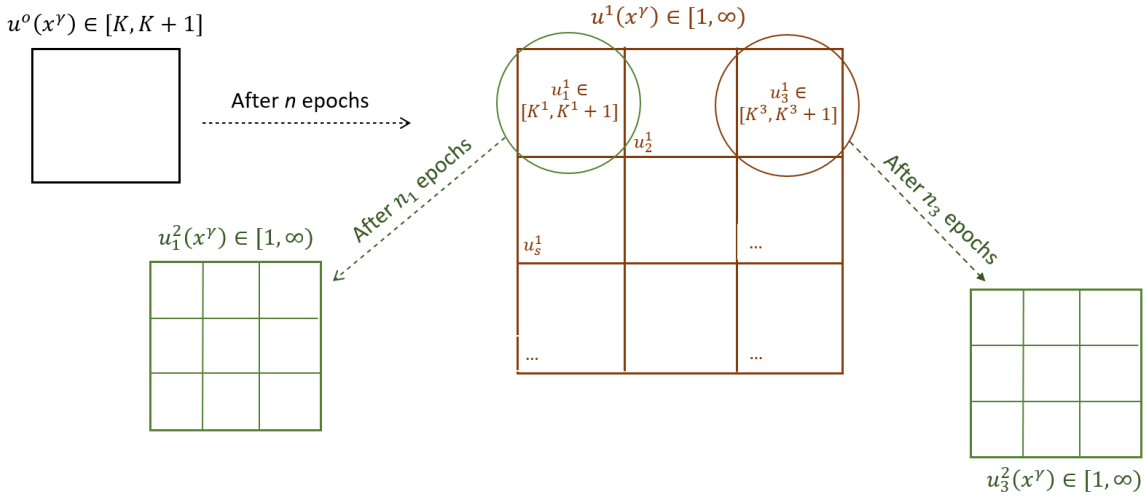

Figure 5.3: Diagram for the fragmentation process.

For each of these islands, the parameter $u(x^\gamma)$ has the form

$$u^1(x^\gamma)_s = s + X_s^1(x^\gamma), \qquad s \in N, X^1(x^\gamma) \in [0, 1), \tag{5.123}$$

where s indicates the different islands.
As the system continues its evolution toward the singularity, the scheme just illustrated can be iterated: each of these islands is decomposed into an infinite number of new islands according to the scheme

$$u_s^{(2)}(x^\gamma) = \frac{1}{X_s^{(1)}(x^\gamma)}. \tag{5.124}$$

This scheme can be repeated indefinitely and produce, progressively, the fragmentation of space into smaller and smaller subregions corresponding to the formation of new islands.

This phenomenon is called *fragmentation process.*

Therefore, summarizing, the fragmentation process is responsible for the formation of smaller and smaller "local patches" when the inhomogeneous model is studied in the limit towards the singularity. Note that all the points in the sam patch are causally connected and therefore follow the same evolution.

To conclude this section is worth mentioning that, while it might seem that the presence of the fragmentation process could deform the BKL map because of the progressive increase of the spatial gradients, it has been demonstrated by a qualitative analysis that this is not the case. [180, 181].

Chapter 6

Quantum dynamics of the corner of the Bianchi IX model in WKB approximation

This chapter is based on the work published in [8].

In this chapter we analyse the Bianchi IX Universe dynamics within the corner region, see Fig.5.2. The study is done in two cases: in the vacuum and in the presence of both a massless scalar field ϕ and a cosmological constant term Λ.

We investigate the dynamics in terms of WKB scenario for which the isotropic Misner variables (the volume) and one of the two anisotropic ones (and ϕ when present) are treated on a semi-classical level, while the remaining anisotropy degree of freedom, the one trapped in the corner, is described on a pure quantum level. We show that the quantum dynamics always reduces to the one of a time-dependent Schr̈oedinger equation for a harmonic potential with a time dependent frequency. The vacuum case is treated in the limits of an expanding and a collapsing Universe, hence for $t \to \infty$ and $t \to 0$ respectively, while the dynamics in presence of ϕ and Λ is studied only for $t \to \infty$. In both analysis the quantum dynamics of the anisotropy variable is associated to a decaying standard deviation of its probability density, corresponding to a suppression of the quantum anisotropy associated. In the vacuum case, for $t \to 0$, the corner configuration becomes an attractor for the dynamics and the evolution resembles that one of

a Taub cosmology. This suggests that if the Bianchi dynamics enters enough in the potential corner, then the initial singularity is removed and a Taub picture emerges.
The case when ϕ and Λ are present is studied since it mimics well the de Sitter phase of an inflationary Universe. Here we demonstrated that both the classical and quantum anisotropies are exponentially suppressed, so that the resulting dynamics corresponds to an isotropic closed Robertson-Walker geometry.

The chapter is organized as follow. In Sec.6.1, after reviewing some of the main results obtained by the Landau school for the Bianchi IX model, we describe the aim of our study and we quickly summarize the results obtained. In Sec.6.2, we apply the Vilenkin approach, introduced in Sec.5.2.2, to the dynamics of the Bianchi IX model and we separate the Misner variables into a semi-classical and a quantum subsets. In Sec.6.2.1 we describe how to solve a Schr"oedinger-like equation for an harmonic oscillator with a time dependent frequency and we use these results in the both Sec.6.2.2 and 6.2.3. In these section we compute the probability density for the quantum subset of the wave function of the Universe to understand the dynamics of the point-Universe in the vacuum and in presence of Λ and ϕ. Finally, in Sec.6.3 we summarize the conclusions.

6.1 Introduction

The Bianchi IX model, as mentioned in Sec.5.3, has been the subject of numerous studies since the '60s, for two main reasons:

1. It possess some of the features of the generic cosmological solution, like a chaotic time evolution of the cosmic scale factors near the cosmological singularity. Hence people hoped that a deeper understanding of its dynamics could help them shed some light on more general cosmologies.

2. Its dynamics, given the introduction of the Misner variable, see Sec.5.3.5, becomes incredible simple: the Mixmaster model can be described as a two

dimensional point-particle in a time dependent potential. In this representation, the chaotic features mentioned above correspond to an infinite sequence of bounces of the point particle against the potential walls.

In particular there have been numerous studies which focused on the dynamics of the Bianchi IX model toward the singularity. In the asymptotic limit to the cosmological singularity, the potential term of the Bianchi IX dynamics resembles an infinite well having the morphology of an equilateral triangle with three open corners in the vertices of such a triangular configuration, see Fig5.2; they correspond to the non-singular Taub cosmology [185], described in Sec.5.3.6.
In [189] the authors showed that for $t \to 0$ there is always a situation where the point-Universe is deeply inside one of the potential corners and the two very close scale factors rapidly oscillate. This regime takes the name of "small oscillations" [184]. However, despite the Bianchi IX model spends a long time in this configuration, it is a well known result [181] that sooner or later it escapes this regime to restore the standard dynamics in the central region of the potential well and, furthermore, the probability that small oscillations take place again is strongly suppressed, see also Sec.5.3.5.
These results have been obtained assuming that all the variables involved (the Misner variables) are classical.

In the present chapter we study the peculiar situation in which the Bianchi IX dynamics is trapped in a corner of the potential and the small degree of anisotropy, which is oscillating, is in a quantum regime. In particular our aim is to understand if, once the point-Universe is deeply inside the corner and one of the anisotropy variables is small enough to be considered quantum, the Universe escapes, as in the classical case described above, or something different might happen.
We chose the initial conditions such that the point-universe finds itself deeply inside the right corner of the potential, hence we consider the corner configuration for which $|\beta_-| \ll 1$ and $\beta_+ \to \infty$. As mentioned, we study two different cases: Bianchi IX in the vacuum, and in presence of a massless scalar field ϕ and a cosmological constant Λ, able to mimic an inflationary-like paradigm. The paradigm

we address corresponds to the WKB proposal of Vilenkin (see [168] and Sec.5.2.2) for the interpretation of the wave-function of a small quantum subsystem of the Minisuperspace.
The idea is that a part of the primordial Universe (the volume, the macroscopic anisotropies and ϕ when present) has reached a quasi-classical limit and can therefore play the role of a clock for the small quantum subsystem, which corresponds to the small anisotropy variable trapped in the corner, close to a zero value. In particular, since the point-Universe dynamics starts in the right corner of the potential, in our example β_- is the quantum variable while α and β_+ are the semi-classical ones. A similar scenario has already been implemented when both β_- and β_+ are treated as quantum variables. This framework, reffered to as quasi-isotropic Universe, has been studied in the case of the Bianchi IX Universe and of the Taub Universe, see [205] and [206] respectively. In both cases, it has been shown that the small quantum degrees of freedom are naturally suppressed by the Universe exponential expansion during the de Sitter phase. For a better characterization of the concept of smallness of the quantum subsystem in the Vilenkin BKL scenario, see [207].

In the vacuum case, we study the evolution of the Bianchi IX model in two different situations

1. for an expanding Universe, therefore $t \to \infty$
2. for a collapsing Universe, i.e. $t \to 0$.

In the first scenario we shown that when the volume expands and the classical anisotropy increases towards larger values, the standard deviation of the probability distribution associated to the small quantum anisotropy degree of freedom is damped to zero. If we consider this picture in the direction of a collapsing Universe instead, we get that the frequency of the harmonic oscillator associated to the quantum anisotropy takes a constant value. Therefore, the classical component of the Universe takes the form of a Taub Universe, possessing a small fluctuating additional anisotropy. It is known [185] that the Taub model has a singularity in the future, but is a non-singular finite Universe volume in the past. Thus if we start with a point Universe entering the corner for $t \to 0$, the approach

to the initial singularity would be stopped.
In this respect, differently from the pure classical behaviour (see [181, 184]), using the Vilenkin approximation, i.e considering the small anisotropy as a quantum degree of freedom, the existence of the initial singularity could be removed. The backward extension of a Mixmaster dynamics sooner or later would deeply enters the corner and the limiting initial configuration of the Universe would be a finite volume Universe, endowed with a small stationary distribution for the relic quantum anisotropy. This conjecture could offer a more general paradigm if we recall that the Bianchi IX model is the prototype for the generic cosmological solution [181], [178].
When ϕ and Λ are included in the dynamics, we consider the limit of an asymptotic exponentially expanding Universe, i.e $t \to \infty$, according to a de Sitter phase of an inflationary paradigm. We show that both the classical macroscopic anisotropy, and the small quantum one are exponentially suppressed as the volume expands. By other words, we are implementing a new dynamical scheme for the isotropization of the Bianchi IX dynamics. This issue completes the analysis in [205], where the depicted scenario corresponds to the case of two small quantum anisotropies, i.e. the case when the point-particle is close to the potential center.

The results showed in this chapter seem to be of more cosmological interests, since we expect, due to the time reversibility of the Einsteinian dynamics, that also in the expanding picture the Bianchi IX Universe spends long time in the corner configuration. This consideration makes plausible that, on one hand the small anisotropy degree of freedom is in a quantum regime, and on the other hand, the cosmological constant term has time to grow, and therefore the de Sitter phase has time to start.

6.2 Application of the Vilenkin approach to the Bianchi IX Universe

In this section we apply the Vilenkin approach to the Bianchi IX model. In particular, following the computation presented in Sec.5.2.2, we derive the Schröedinger-

like equation for the Mixmaster model and we write the full expression for the probability density of the wave function of the Universe.

The starting point for our computation is the Hamiltonian of the system expressed in terms of the Misner variables:

$$\mathcal{H}_{IX} = \frac{Nk}{3(8\pi)^2} e^{-3\alpha} \left(-p_\alpha^2 + p_+^2 + p_-^2 + p_\phi^2 + \frac{32\pi^4}{k^2} e^{4\alpha} V_{IX} + \Lambda e^{6\alpha} \right). \tag{6.1}$$

This Hamiltonian is obtained from eq.(5.98) and includes a scalar field ϕ and a cosmological constant Λ. The massless scalar field ϕ well approximated the slow-rolling dynamics, i.e $\dot{\phi}^2 \ll V(\phi)$, when the potential term is essentially constant, therefore its presence, as discussed in the introduction, makes our analysis more interesting, from a cosmological point of view.
In the following we set $N(t) = 1$, preferring to work in a *synchronous reference frame*, see Sec.5.1.3.

To implement the Vilenkin approach on the Mixmaster model it is necessary to separate dynamical variables of the system, hence the Misner variables α, β_+ and β_-, into semi-classical and quantum. Since our aim is to study how the system evolves starting from the *corner configuration*, we chose α and β_+ as semi-classical variables, and β_- as the quantum one. Thus, the anisotropic Misner variables are

$$\beta_+ \to \infty, \qquad |\beta_-| \ll 1. \tag{6.2}$$

Assuming these initial conditions, the point-Universe starts its dynamics from a specific region of the (β_+, β_-) plane, the right corner of the potential, see Fig.5.2. Given eq.(6.2), the potential V_{IX} in eq.(6.1) can be approximated as:

$$V_{IX} \simeq 48 e^{4\beta_+} \beta_-^2. \tag{6.3}$$

Note that the potential level surfaces for a fixed value of the variable α are invariant under a rotation of $\pi/3$. Thus we can choose a specific corner without any loss of generality: it is in fact possible to map each corner into another one through a $\pi/3$ rotation in their plane, of the anisotropy variables coordinates β_+ and β_-.

Recalling eq.(5.40), the wave function of the Universe Ψ can be written explicitly including the scalar field ϕ as:

$$\Psi = \Psi_0 \chi = A(\alpha, \beta_+, \phi) e^{\frac{i}{\hbar} S(\alpha, \beta_+, \phi)} \chi(\alpha, \beta_+, \phi, \beta_-). \tag{6.4}$$

and following the same steps highlighted in [168], the WdW equation for the Bianchi IX wave function of the Universe becomes:

$$\hat{\mathcal{H}}_{IX}\Psi = \frac{k}{3(8\pi)^2} e^{-3\alpha} \left(\hbar^2\partial_\alpha^2 - \hbar^2\partial_+^2 - \hbar^2\partial_-^2 - \hbar^2\partial_\phi^2\right)\Psi + \tag{6.5}$$

$$+ \frac{k}{3(8\pi)^2} e^{-3\alpha} \left(\frac{32\pi^4}{k^2} e^{4\alpha} V_{IX} + \Lambda e^{6\alpha}\right)\Psi = 0. \tag{6.6}$$

where we used that $p_a = -i\hbar\partial/\partial q^a$. In the following $\mathcal{V}_{IX} \equiv \frac{32\pi^4}{k^2} e^{4\alpha} V_{IX} = 24\pi^2 \beta_-^2 e^{4(\alpha+\beta_+)}$.

The total Hamiltonian $\mathcal{H}_{IX}$ can be written in terms of a semi-classical and quantum Hamiltonian, respectively $\mathcal{H}_0$ and $\mathcal{H}_q$, as in eq.(5.38):

$$\begin{cases} \mathcal{H}_0 &= K e^{-3\alpha}\left(\hbar^2\partial_\alpha^2 - \hbar^2\partial_+^2 - \hbar^2\partial_\phi^2 + \Lambda e^{6\alpha}\right) \\ \mathcal{H}_q &= K e^{3\alpha}(-\hbar^2\partial_-^2 + \mathcal{V}_{IX}) \end{cases} \rightarrow \hat{\mathcal{H}}_{IX}\Psi = (\mathcal{H}_0 + \mathcal{H}_q)\Psi \tag{6.7}$$

where $K = k/(3(8\pi)^2)$.

Expanding the conjugate momenta p_a in their operator form, eq. (6.5) becomes:

$$\begin{aligned}\hat{\mathcal{H}}_{IX}\Psi = Ke^{-3\alpha}\hbar^2\Big[&(\partial_\alpha^2 A)\chi + \frac{i}{\hbar}(\partial_\alpha A)(\partial_\alpha S)\chi + (\partial_\alpha A)(\partial_\alpha\chi) + \frac{1}{\hbar}(\partial_\alpha^2 S)A\chi \\ &+ \frac{1}{\hbar}(\partial_\alpha S)(\partial_\alpha A)\chi + \left(\frac{i}{\hbar}\partial_\alpha S\right)^2 A\chi + \frac{i}{\hbar}(\partial_\alpha S)(\partial_\alpha\chi)A + (\partial_\alpha A)(\partial_\alpha\chi) + \\ &\frac{i}{\hbar}(\partial_\alpha S)(\partial_\alpha\chi) + A\partial_\alpha^2\chi - (\partial_+^2 A)\chi - \frac{i}{\hbar}(\partial_+ A)(\partial_+ S)\chi - (\partial_+ A)(\partial_+\chi) + \\ &- \frac{1}{\hbar}(\partial_+^2 S)A\chi - \frac{1}{\hbar}(\partial_+ S)(\partial_+ A)\chi - \left(\frac{i}{\hbar}\partial_+ S\right)^2 A\chi + \\ &- \frac{i}{\hbar}(\partial_+ S)(\partial_+\chi)A - (\partial_+ A)(\partial_+\chi) - \frac{i}{\hbar}(\partial_+ S)(\partial_+\chi) - A\partial_+^2\chi + \\ &- (\partial_\phi^2 A)\chi - \frac{i}{\phi}(\partial_\phi A)(\partial_\phi S)\chi - (\partial_\phi A)(\partial_\phi\chi) - \frac{1}{\hbar}(\partial_\phi^2 S)A\chi \\ &- \frac{1}{\hbar}(\partial_\alpha S)(\partial_\phi A)\chi - \left(\frac{i}{\hbar}\partial_\phi S\right)^2 A\chi - \frac{i}{\hbar}(\partial_\phi S)(\partial_\phi\chi)A - (\partial_\phi A)(\partial_\phi\chi) + \\ &- \frac{i}{\hbar}(\partial_\phi S)(\partial_\phi\chi) - A\partial_\phi^2\chi + \frac{1}{\hbar^2}\Lambda e^{6\alpha}A + A\mathcal{H}_q\chi\Big] = 0.\end{aligned} \tag{6.8}$$

Considering the equation order by order in $\hbar$, we obtain the following three equations:

$$\mathcal{O}(1) \to -(\partial_\alpha S)^2 + (\partial_+ S)^2 + (\partial_\phi S)^2 + \Lambda e^{6\alpha} = 0 \tag{6.9}$$

$$\begin{aligned}\mathcal{O}(\hbar) \to &2i\left(\partial_\alpha S\partial_\alpha A - \partial_+ S\partial_+ A - \partial_\phi S\partial_\phi A\right) + Ai\left(\partial_\alpha^2 S - \partial_+^2 S - \partial_\phi^2 S\right) + \\ &2Ai\left(\partial_\alpha S\partial_\alpha\chi - \partial_+ S\partial_+\chi - \partial_\phi S\partial_\phi\chi\right) + A\mathcal{H}_q\chi = 0\end{aligned} \tag{6.10}$$

$$\mathcal{O}(\hbar^2) \to -2\left(\partial_\alpha A\partial_\alpha\chi - \partial_+ A\partial_+\chi - \partial_\phi A\partial_\phi\chi\right) + A\left(\partial_\alpha^2\chi - \partial_+^2\chi - \partial_\phi^2\chi\right) \tag{6.11}$$

The first equation, as expected, is the Hamilton-Jacobi equation for the action S and involves only the semiclassical variables.
Before focusing on eq.(6.10), let us note that the Hamiltonian of the quantum subsystem $\mathcal{H}_q$ appears in this equation since one of the hypothesis of the Vilenkin approach is that $\mathcal{H}_q\Psi/\mathcal{H}_0\Psi \sim \mathcal{O}(\hbar)$.

Using the *adiabatic approximation* (see eq.(5.37)), eq.(6.10) can be separated

in its semi-classical and its quantum components:

$$2\left(\partial_\alpha S\partial_\alpha A-\partial_+ S\partial_+ A-\partial_\phi S\partial_\phi A\right)+A\left(\partial_\alpha^2 S-\partial_+^2 S-\partial_\phi^2 S\right)=0 \tag{6.12}$$

$$2i\left(\partial_\alpha S\partial_\alpha \chi-\partial_+ S\partial_+ \chi-\partial_\phi S\partial_\phi \chi\right)+\mathcal{H}_q\chi=0. \tag{6.13}$$

Eq.(6.12) is the continuity equation for the amplitude A, which can be used to determine its explicit expression, while (6.13) can be used to compute the probability distribution for χ.
Knowing that $p_a=\frac{\partial S}{\partial q^a}$ and deriving the semiclassical variables and their momenta from equations (5.104)

$$\dot{\alpha}=-2p_\alpha e^{-3\alpha}K, \quad \rightarrow \quad p_\alpha=-\frac{e^{3\alpha}\dot{\alpha}}{2K} \tag{6.14}$$

$$\dot{\beta_+}=2p_+ e^{-3\alpha}K, \quad \rightarrow \quad p_+=-\frac{e^{3\alpha}\dot{\beta}_+}{2K} \tag{6.15}$$

$$\dot{\phi}=2p_\phi e^{-3\alpha}K, \quad \rightarrow \quad p_\phi=-\frac{e^{3\alpha}\dot{\phi}}{2K} \tag{6.16}$$

eq.(6.13) can be rewritten as

$$2i\frac{e^{3\alpha}}{2K}\left(\dot{\alpha}\frac{\partial\chi}{\partial\alpha}+\dot{\beta_+}\frac{\partial\chi}{\partial\beta_+}+\dot{\phi}\frac{\partial\chi}{\partial\phi}\right)=\mathcal{H}_q\chi. \tag{6.17}$$

where $\chi=\chi(\alpha(t),\beta_+(t),\phi(t),\beta_-)$, as highlighted in (6.4)[1].
Finally, the above equation becomes

$$i\frac{d\chi}{dt}=Ke^{-3\alpha}\mathcal{H}_q\chi, \tag{6.18}$$

which can be written as a Schröedinger-like equation introducing a new time variable τ:

$$\tau=K\int e^{-3\alpha}dt. \tag{6.19}$$

Following this substitution, (6.18) becomes:

$$i\frac{d\chi}{d\tau}=\mathcal{H}_q\chi. \tag{6.20}$$

[1]Note that χ depends on time through the semi-classical variables.

Solving this equation provides us with the form of χ, which is key to write the probability density of the full wave function Ψ:

$$\sigma(\alpha, \beta_+, \phi, \beta_-) = \sigma_0(\alpha(\tau), \beta_+(\tau), \phi(\tau))|\chi(\beta_-, \tau)|^2. \tag{6.21}$$

Here $\sigma_0 = |A(\alpha(\tau), \beta_+(\tau), \phi(\tau))|^2$ and $|\chi|^2$ is indeed the solution of eq.(6.20), see Sec.5.2.2.

6.2.1 Resolution of the Schröedinger equation for an harmonic oscillator with time dependent frequency

In this section we focus on solving eq.(6.20) in order to derive the expression for $|\chi|^2$.

Eq. (6.20) written explicitly, resembles the Schröedinger equation of a harmonic oscillator with a time-dependent frequency $\omega^2(\tau) \equiv 24\pi^2 e^{4(\alpha+\beta_+)}$ and unitary mass[1]:

$$i\frac{d\chi}{d\tau} = \left(\frac{p_-^2}{2} + 12\pi^2 e^{4(\alpha+\beta_+)}\beta_-^2\right)\chi. \tag{6.22}$$

In [208–210], the authors developed a technique to solve this particular type of equations which, as summarised by Pedrosa in [211], is based on the *invariant method*.

According to this, the general solution of an equation of the form (6.22) is given by:

$$\chi = \sum_n c_n e^{i\alpha_n(\tau)}\phi_n(\beta_-, \tau) = \sum_n c_n \chi_n(\beta_-, \tau), \tag{6.23}$$

where

- c_n are constants that weight the different $\chi_n(\beta_-, \tau)$,
- $\alpha_n(\tau)$ is a phase function given by

$$\alpha_n(\tau) = -\left(n + \frac{1}{2}\right)\int_0^\tau \frac{1}{\rho}^2 d\tau' \tag{6.24}$$

[1]We redefined τ as $\tau' = 2\tau$

- ϕ_n is the eigenfunction of the invariant $I(\tau)$ for the Hamiltonian $\mathcal{H}_q$

$$\phi_n(\beta_-, \tau) = \Omega_n exp\left[\frac{i}{2\hbar}\left(\frac{\dot{\rho}}{\rho} + \frac{i}{\rho^2}\right)\beta_-^2\right]\mathcal{H}_n\left[\left(\frac{1}{\hbar}\right)^{1/2}\frac{\beta_-}{\rho}\right]. \tag{6.25}$$

  Here $\Omega_n = \left[\frac{1}{\sqrt{\pi\hbar}\ n!\ 2^n}\right]$, $\mathcal{H}_n$ is the Hermite polynomial of order n and ρ is a complex quantity which satisfies the auxiliary equation

$$\ddot{\rho} + \omega^2(\tau)\rho - \frac{1}{\rho^3} = 0. \tag{6.26}$$

  Note that $\dot{}$ indicates the differentiation respect to the time variable ρ depends to, hence τ.

Eq.(6.26) can be really difficult to solve analitycally since $\omega^2(\tau)$ is a general function, but in [209] and [210] the authors gave an alternative way to obtain the explicit expression for ρ, according to which ρ can written be as a linear combination of $f(\tau)$ and $g(\tau)$, solutions of

$$\frac{d^2q}{dt^2} + \omega^2(\tau)q = 0. \tag{6.27}$$

In the following we use this last possibility, when the above equation can be solved analytically, or we compute ρ numerically solving eq.(6.26).

6.2.2 Bianchi IX in the vacuum

In this Section we are going to study the dynamical evolution of the Mixmaster model in the simplest case, the vacuum, for both an expanding and a collapsing Universe. In particular, we compute $|\chi|^2$ to understand if, during its dynamical evolution, the point-Universe leaves the corner region.

The Hamiltonian of the system is simpler than the complete one presented in eq.(6.1) and is given by

$$\mathcal{H} = e^{-3\alpha}K\left(p_\alpha^2 + p_+^2 + p_-^2 + \mathcal{V}_{IX}\right) \tag{6.28}$$

where, again, the quantum part of the Hamiltonian is the one defined in eq.(6.8), i.e $\mathcal{H}_q = e^{-3\alpha}K\left(p_-^2 + 24\pi^2\beta_-^2 e^{4(\alpha+\beta_+)}\right)$ and $\mathcal{H}_0 = e^{-3\alpha}K(-p_\alpha^2 + p_+^2)$.
To compute the solution of (6.20) we need to write the time-dependent frequency $\omega^2(\tau)$ explicitly as a function of the time variable τ. This can be done using the Hamiltonian above and eq.(5.104).

In particular, the time derivative of the variable α and its conjugate momenta become

$$\dot{\alpha} = \frac{\partial\alpha}{\partial p_\alpha} = \frac{\partial\mathcal{H}_0}{\partial t} = -p_\alpha K e^{-3\alpha} \tag{6.29}$$

$$\dot{p_\alpha} = \frac{\partial p_\alpha}{\partial t} = -\frac{\partial\mathcal{H}_0}{\partial\alpha} = -3\mathcal{H}_0 = 0 \tag{6.30}$$

Note that the time variable in the above equations is the synchronous time t and not the new time variable τ, eq. (6.19).
The last equality in eq. (6.30) has been derived from the semiclassical Super-Hamiltonian constraint (5.18) $\mathcal{H}_0 = 0$ and its immediate consequence is that

$$p_\alpha = const. \tag{6.31}$$

The sign of p_α can be deduced from eq.(6.29). As mentioned in Sec.5.3.5, α is the Misner semi-classical variable which characterizes the volume of the Universe ($\mathcal{V} \sim e^{3\alpha}$), hence $\dot{\alpha}$ indicates how $\mathcal{V}$ changes in time, and from eq.(6.29), the sign of $\dot{\alpha}$ depends on the sign of p_α. Our analysis is based on an expanding Universe, where $\dot{\alpha} > 0$, thus it is possible to impose, without loss of generality, $p_\alpha < 0$.
With this in mind, eq.(6.29) can be integrated obtaining

$$e^{3\alpha} = 6|p_\alpha|Kt \tag{6.32}$$

which gives

$$\alpha(t) = \frac{1}{3}\log 6|p_\alpha|K + \frac{1}{3}\log t \quad \rightarrow \quad \alpha(t) \propto \frac{1}{3}\log t. \tag{6.33}$$

To write ω^2 as a function of τ, the next step is to write t as a function of this time variable.

Substituting eq.(6.33) in eq.(6.19) we can write $\tau(t)$ and therefore $t(\tau)$ as:

$$\tau(t) = \frac{1}{6|p_\alpha|}\log t \quad \rightarrow \quad t(\tau) = e^{6|p_\alpha|\tau} \tag{6.34}$$

Finally, using the last equation in eq.(6.33) we obtain the expression for $\alpha(\tau)$:

$$\alpha(\tau) = \frac{1}{3}\log 6|p_\alpha|K + 2|p_\alpha|\tau. \tag{6.35}$$

Let us note that, from eq.(6.34):

$$t \rightarrow 0, \quad \tau \rightarrow -\infty \tag{6.36}$$

$$t \rightarrow +\infty, \quad \tau \rightarrow +\infty. \tag{6.37}$$

The next step is to use the above results to compute $\beta_+(\tau)$ to have the full expression of the time-dependent frequency $\omega(\tau)^2$ necessary to solve the Schröedinger-like equation, eq.(6.20).

In the following subsection we compute $\beta_+(\tau)$ in two cases: for an expanding Universe, see Sec.6.2.2.1, and for a collapsing one, see Sec.6.2.2.2.

6.2.2.1 Bianchi IX in the vacuum: expanding Universe

In this section we consider the dynamical evolution when the semi-classical anisotropy variable β_+ increases in the direction of an expanding Universe, hence $\dot{\beta}_+(t) > 0$. Physically this means that, while the Universe expands, therefore $\alpha(t)$ grows, the point-particle Universe moves deeper into the corner.
To find the explicit expression for $\beta_+(t)$, and consequently for $\beta_+(\tau)$, we follow the same arguments presented in the previous subsection for the computation of $\alpha(t)$.
From the system in eq.(5.104),

$$\dot{\beta_+} = \frac{\partial \mathcal{H}_0}{\partial p_+} = 2p_+ K e^{3\alpha} \tag{6.38}$$

$$\dot{p}_+ = -\frac{\partial \mathcal{H}_0}{\partial \beta_+} = 0 \quad \rightarrow \quad p_+ = const \tag{6.39}$$

and integrating the first equation,

$$\beta_+(t) = \frac{1}{3}\frac{p_+}{|p_\alpha|}\log t + \beta_0 \tag{6.40}$$

where β_0 is an integration constant.
The ratio $p_+/|p_\alpha|$ can be simplified using the Hamilton-Jacobi equation:

$$\left(\frac{\partial S}{\partial \alpha}\right)^2 - \left(\frac{\partial S}{\partial \beta_+}\right)^2 = 0, \tag{6.41}$$

which leads to

$$p_\alpha = \pm p_+ \quad \rightarrow \quad p_+ = \pm|p_\alpha|. \tag{6.42}$$

As mentioned above, in this section we are interested in studying the dynamical evolution for $t \to \infty$ (hence $\dot{\alpha} > 0$) when the point-Universe moves deeper into the corner, $\dot{\beta}_+ > 0$, and, given eq.(6.38), this condition is satisfied if $p_+ > 0$.
Finally, imposing $p_+ = |p_\alpha|$, using eq.(6.34), $\beta_+(t)$ can be written as:

$$\beta_+(\tau) = \beta_0 + 2|p_\alpha|\tau. \tag{6.43}$$

Comparing the above equation with eq.(6.35), it is interesting to notice that both the semiclassical Misner variables have the same time-dependency.

Substituting eq.(6.35) and eq.(6.43) into the expression of the time-dependent frequency $\omega(\tau)^2$, we obtain

$$\omega^2(\tau) = 24\pi^2 e^{4(\alpha(\tau)+\beta(\tau))} = 24\pi^2 e^{4(\alpha_0+\beta_0)} e^{16|p_\alpha|\tau} \propto Ce^{k\tau}, \tag{6.44}$$

with C and k constants.

The last step to compute $|\chi|^2$ is to solve the Schröedinger-like equation, eq.(6.22) which, in the specific case of an expanding Bianchi IX Universe in the vacuum, can be written as

$$i\hbar\frac{\partial \chi}{\partial \tau} = \left(\frac{p_-^2}{2} + Ce^{k\tau}\beta_-^2\right)\chi. \tag{6.45}$$

In Sec.6.2.1 we see how the expression for χ depends on the c-number quantity $\rho(\tau)$, which can be computed either from eq,(6.26) or from eq.(6.27). Given the expression for $\omega^2(\tau)$, we did not find any analytical solution for eq.(6.26), hence we determined an expression for $\rho(\tau)$ as a linear combination of $f(\tau)$ and $g(\tau)$, solutions of

$$\frac{d^2q}{d\tau^2} + Ce^{k\tau} = 0. \tag{6.46}$$

In particular,

$$f(\tau) = J_0\left[\frac{2\sqrt{C}\sqrt{e^{k\tau}}}{k}\right] \tag{6.47}$$

$$g(\tau) = N_0\left[\frac{2\sqrt{C}\sqrt{e^{k\tau}}}{k}\right] \tag{6.48}$$

where J_0 and N_0 represent the Bessel functions of the first and second kind. It follows that

$$\rho(\tau) = \frac{\pi}{2k}\sqrt{J_0^2\left[\frac{2\sqrt{C}\sqrt{e^{k\tau}}}{k}\right] + \frac{64k^2N_0^2\left[\frac{2\sqrt{C}\sqrt{e^{k\tau}}}{k}\right]}{\pi^2} + \frac{8\sqrt{3}J_0\left[\frac{2\sqrt{C}\sqrt{e^{k\tau}}}{k}\right]N_0\left[\frac{2\sqrt{C}\sqrt{e^{k\tau}}}{k}\right]}{\pi}} \tag{6.49}$$

At this point we can to solve eq.(6.45) substituting eq.(6.49), $\phi_n(\tau)$ and $\alpha_n(\tau)$, in eq.(6.23).

Once χ is known, the resulting probability density $|\chi|^2$ can be written as:

$$|\chi(\tau,\beta_-)|^2 = \left(\sum_n c_n\chi_n(\tau,\beta_-)\right)\left(\sum_m c_m\chi_m(\tau,\beta_-)\right)^*. \tag{6.50}$$

where c_n are constants.

Using the property of the inner product and the orthogonality of the different wavefunctions χ_n[1],

$$c_n = \int \chi(\tau_0,\beta_-)\chi_n^*(\tau_0,\beta_-)d\beta_- \tag{6.51}$$

[1]This expression for c_n is true for every τ because the c_n are time independent.

where $\chi(\tau_0) = \chi_0$ is the function χ at the initial time τ_0. We choose χ_0 such that

$$|\chi_0|^2 = \frac{1}{2\pi} e^{-\frac{\beta_-^2}{2\sigma^2}}. \tag{6.52}$$

which is in agreement with our assumption that initially the system is deeply inside the right corner of the potential: at τ_0 the probability density of the quantum part of the wave function has a Gaussian shape peaked around $\beta_- = 0$.

To study the dynamical evolution in time of the probability density for χ, we report the plots $|\chi|^2$ at different time as a function of the quantum anisotropy variable β_- in Fig.6.1.

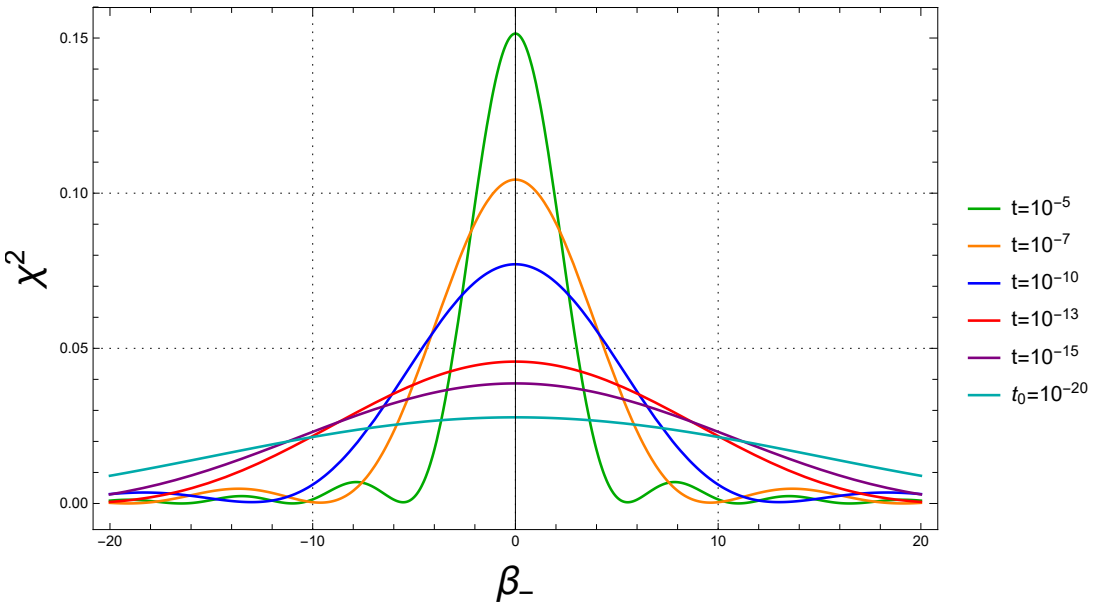

Figure 6.1: Probability density function for different values of the synchronous time variable for Bianchi IX in the vacuum in the case $\beta_+ = 2|p_\alpha|\tau$, for an expanding Universe.

From this plot, we see that as β_+ grows in time, i.e the point-Universe moves deeper in the corner, $|\chi|^2$ peaks even more around $\beta_- = 0$.

To write the full expression of σ, as in eq.(6.21), we compute the probability density of the semiclassical variables α and β_+, i.e. $\sigma_0 = |A(\alpha, \beta_+)|^2$. Assuming

that the amplitude $A(\alpha, \beta_+)$ can be factorize as

$$A(\alpha, \beta_+) = A_1(\alpha)A_2(\beta_+), \tag{6.53}$$

it can be computed using eq.(6.9) and eq.(6.12).
From (6.9)

$$(\partial_\alpha S_0) = -(\partial_+ S_0) \tag{6.54}$$

and assuming that $S_0 = S_0(\alpha) + S_0(\beta)$, this leads to

$$\begin{cases} S_0(\alpha) = W\alpha \\ S_0(\beta_+) = -W\beta_+ \end{cases} \quad \rightarrow S_0(\alpha, \beta_+) = W(\alpha - \beta_+). \tag{6.55}$$

where W is a constant.

Substituting this expression into (6.12) we obtain:

$$\frac{2}{A_1}\frac{\partial A_1}{\partial \alpha}(W) + \frac{\partial W}{\partial \alpha} - \frac{2}{A_2}\frac{\partial A_2}{\partial \beta_+}(W) - \frac{\partial W}{\partial \beta_+} = 0. \tag{6.56}$$

which, since A is separable, can be solved solving the following system

$$\begin{aligned} \frac{2}{A_1}\frac{\partial A_1}{\partial \alpha}(W) + \frac{\partial W}{\partial \alpha} &= \frac{2}{A_1}\frac{\partial A_1}{\partial \alpha}(W) = c1 \\ \frac{2}{A_2}\frac{\partial A_2}{\partial \beta_+}(W) + \frac{\partial W}{\partial \beta_+} &= \frac{2}{A_2}\frac{\partial A_2}{\partial \beta_+}(W) = -c1. \end{aligned}$$

Recognizing that $W = p_\alpha$, the final expression for the amplitude A is:

$$A(\alpha, \beta_+) = e^{c1/(2p_\alpha)(\alpha - \beta_+)}. \tag{6.57}$$

To summarize, in this section we show that if the initial probability density for χ is a Gaussian packet peaked in $\beta_- = 0$, namely $|\chi_n(\tau_0)|^2$, as β_+ grows in time (thus the point-Universe moves deeper in the corner) the Gaussian packet tends to peak even more around $\beta_- = 0$. This result is shown in Fig.6.1.
As a straightforward consequence the right corner in Fig.5.2 becomes an attractor for the global system dynamics. Therefore the Universe models a Taub cosmological model, see Sec.5.3.6, to a greater degree.

6.2.2.2 Bianchi IX in the vacuum: collapsing Universe

In this section we consider the Bianchi IX model in vacuum when β_+ decreases for $t \to \infty$. In this case the point-Universe enters deeply in the corner for $t \to 0$, hence for a collapsing Universe. The equations of motion and the Hamilton-Jacobi equation do not change compared to those of the previous case, hence

$$\beta_+(t) = \beta_0 + \frac{1}{3}\frac{p_+}{|p_\alpha|}\log t, \qquad p_+ = \pm p_\alpha. \tag{6.58}$$

However, the initial assumption that $\dot{\beta}_+ < 0$ translates in $p_+ < 0$; from the above equation this means that $p_+ = -|p_\alpha|$.
The semi-classical anisotropic variable becomes:

$$\beta_+(\tau) = \beta_0 - 2p_\alpha\tau \tag{6.59}$$

from which

$$\alpha(\tau) + \beta_+(\tau) = \beta_0. \tag{6.60}$$

and the frequency $\omega^2(\tau)$ reads as

$$\omega^2(\tau) = 16e^{4(\alpha(\tau)+\beta_+(\tau))} = 16e^{4\beta_0} \tag{6.61}$$

which is a constant.

Given the simple expression for $\omega^2(\tau)$, in this case we can solve eq.(6.26) analytically as in [210], and it results:

$$\rho(\tau) = \frac{1}{\sqrt{\omega(\tau)}} = \frac{1}{2}e^{-\beta_0} = const. \tag{6.62}$$

It follows that the eigenfunctions χ_n, which depend on time through $\rho(\tau)$, see eq. (6.25), which is constant, are now time independent; hence the probability density distribution $|\chi|^2$ does not evolve in time, but it is defined simply by choosing its shape at the initial time.
As in the previous case, we compute A to have the full expression for σ, and given

that $p_\alpha = p_+$, we obtain:

$$A(\alpha, \beta_+) = e^{c1/(2W)(\alpha+\beta_+)}. \tag{6.63}$$

In summary, the standard deviation of the initial Gaussian $|\chi|^2$ remains unchanged during the evolution when we evolve the point-Universe toward the singularity. This reflects the fact that, evolving the system for $t \to 0$, the Schröedinger equation for the quantum variable is that of a harmonic oscillator with constant frequency.

6.2.3 Bianchi IX model in presence of cosmological constant and scalar field

Finally we study the Bianchi IX model in an expanding scenario in the presence of a cosmological constant Λ and a scalar field ϕ in order to mimic the slow-rolling phase of an inflationary scenario [212].
As mentioned before, the scalar field is such that $\dot{\phi} \ll V(\phi)$, and $V(\phi) \propto \alpha$, so this can be neglected compared to the cosmological constant and the $\mathcal{V}$ term.

In this case the Hamiltonian takes the form:

$$\mathcal{H} = e^{-3\alpha} K \left(-p_\alpha^2 + p_+^2 + p_\phi^2 + p_-^2 + \mathcal{V}_{IX} + \Lambda e^{6\alpha} \right). \tag{6.64}$$

and while $\mathcal{H}_q$ does not change respect to the previous case,
$\mathcal{H}_0 = e^{-3\alpha} \left(-p_\alpha^2 + p_+^2 + p_\phi^2 + \Lambda e^{6\alpha} \right)$.
The equations of motion for the semi-classical variables are:

$$\dot{\alpha} = -2 p_\alpha K e^{-3\alpha}, \qquad \dot{\beta}_+ = 2 p_+ K e^{3\alpha} \tag{6.65}$$

where p_α can be obtained from the Hamilton-Jacobi equation (6.9):

$$p_\alpha = \pm \sqrt{p_+^2 + p_\phi^2 + \Lambda e^{6\alpha}}. \tag{6.66}$$

Again, since $\dot{\alpha} > 0$ in an expanding Universe, $p_\alpha < 0$, i.e $p_\alpha = -\sqrt{p_+^2 + p_\phi^2 + \Lambda e^{6\alpha}}$.

Substituting this expression in eq.(6.65) and solving the the differential equation, we obtain

$$\alpha(t) = \frac{1}{3}\log\left[\sqrt{\frac{p_+^2+p_\phi^2}{\Lambda}}\sinh\left(3\sqrt{\Lambda}\,(2Kt+J)\right)\right] \tag{6.67}$$

where J is an integration constant. and it follows that the new time variable τ, introduced in eq.(6.19), becomes

$$\tau(t) = \frac{1}{6\sqrt{p_+^2+p_\phi^2}}\log\left[\tanh\left(\frac{3}{2}\sqrt{\Lambda}(2Kt+J)\right)\right], \qquad -\infty < \tau < 0. \tag{6.68}$$

To write down the explicit expression for the semi-classical variables $\alpha(\tau)$ and $\beta_+(\tau)$ we substitute eq.(6.68) into eq.(6.65) obtaining:

$$\alpha(\tau) = \frac{1}{3}\log\left[\sqrt{\frac{p_+^2+p_\phi^2}{\Lambda}}\sinh\left[2\tanh^{-1}\left(e^{6\tau\sqrt{p_+^2+p_\phi^2}}\right)\right]\right], \tag{6.69}$$

$$\beta_+(\tau) = \beta_0 + 2p_+\tau \tag{6.70}$$

where

$$-\infty < \alpha < \infty$$
$$-\infty < \beta_+ < \beta_0.$$

We can now write explicitly the time-dependent frequency $\omega^2(\tau)$, which results to have a much more complicated expression than the previous cases:

$$\omega^2(\tau) = 16e^{4(\beta_0+8p_+\tau)}\left[\sqrt{\frac{p_+^2+p_\phi^2}{\Lambda}}\sinh\left[2\tanh^{-1}\left(e^{6\tau\sqrt{p_+^2+p_\phi^2}}\right)\right]\right]. \tag{6.71}$$

Given the complexity of this equation, were not able to solve analytically neither eq.(6.26) nor the simpler eq.(6.27), and eq.(6.26) has been solved numerically for different values of t. In Fig.6.2 we report the plots of $|\chi|^2$ obtained.

We notice that, as in the case analyzed in Sec.6.2.2.1, the probability density of the quantum part of the wavefunction peaks around β_0 as the Universe ex-

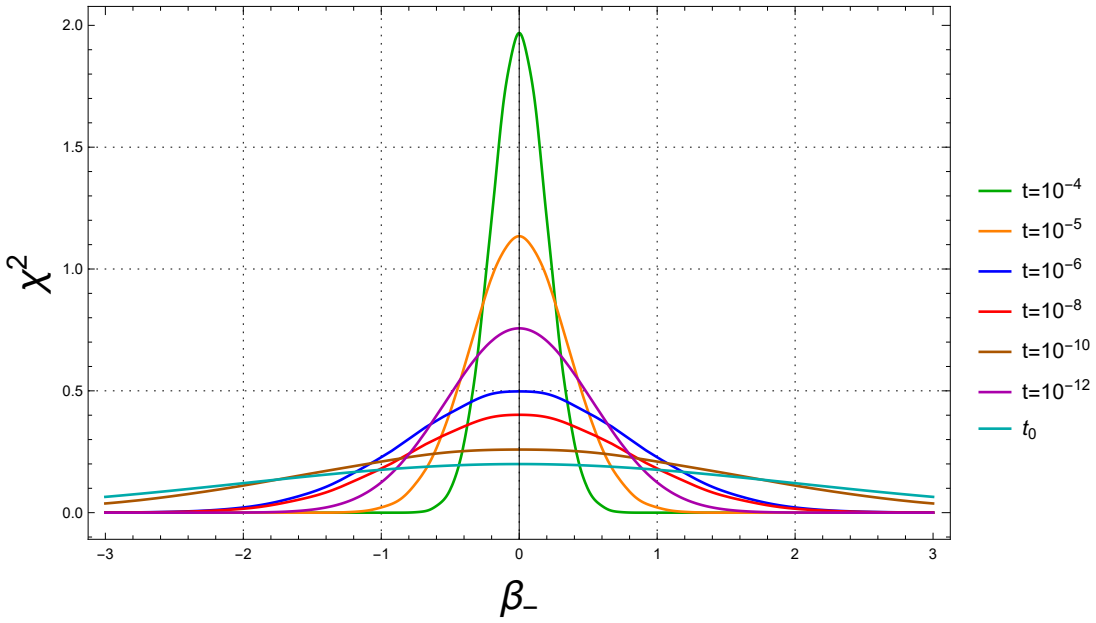

Figure 6.2: Probability density function for different values of the synchronous time variable for Bianchi IX in presence of a scalar field ϕ and a cosmological constant Λ.

pands.

It is worth mentioning that we realized different plots of $|\chi|^2$ changing the standard deviation σ in eq.(6.52) and the numerical value of Λ, but in all cases analyzed the results are consistent with those proposed in Fig.6.2.

Finally, we compute the semi-classical probability distribution assuming that

$$A(\alpha, \beta_+, \phi) = A_1(\alpha)A_2(\beta_+)A_3(\phi). \tag{6.72}$$

Following the same computation as in Sec.6.2.2.1, we obtain:

$$A_1(\alpha) = \frac{Exp\left[\frac{c1\tanh^{-1}\left(\sqrt{\frac{p_+^2+p_\phi^2+\Lambda e^{6\alpha}}{p_+^2+p_\phi^2}}\right)}{6\sqrt{p_+^2+p_\phi^2+\Lambda e^{6\alpha}}}\right]}{\left(p_+^2+p_\phi^2+\Lambda e^{6\alpha}\right)^{1/4}}$$
$$A_2(\beta_+) = Exp\left[\frac{c_2}{2p_+}\beta_+\right]$$
$$A_3(\phi) = Exp\left[-\frac{c_1+c_2}{2p_\phi}\phi\right]$$

with c_1 and c_2 constants. Looking at Fig.6.2, we conclude that, unlike for the Bianchi IX in the vacuum, there is not a well defined trend of the probability density evolution in time.
However, as the Universe evolves in time, the variable β_+ leans to a constant value β_0, and the variable β_- tends to peak around the value $\beta_- = 0$; thus the presence of the cosmological constant tends to isotropize the Universe.

6.3 Conclusion

In this chapter we analysed the Bianchi IX cosmology in both vacuum and when ϕ and Λ are present, in the situation in which the point-Universe is trapped in a corner of the scalar curvature potential. Our aim was to understand how its dynamics changes compared to the results obtained by the Landau Scool, see e.g [189], if one of the anisotropies is in a quantum regime.

To study the dynamical evolution of the system we adopted the WKB decoupling of the quasi-classical degrees of freedom, the Misner variables α and β_+ (and ϕ when present), from a microscopic fully quantum degree of freedom, the small anisotropy variable β_-, trapped in the corner. Then, we computed the probability density of the wave function of the Universe, focusing on its quantum part, to understand if the point-Universe escapes the corner configuration as in the classical regime or the presence of a quantum degree of freedom changes the

dynamics substantially.
To answer this question, we had to solve a time dependent Schröedinger equation with a quadratic potential, which resembled the equation of a harmonic oscillator with time-dependent frequency.
We demonstrated that, both with and without matter, the solution of this equation suggests that the small quantum anisotropy β_- is strongly suppressed via the dynamics of the quasi-classical variables.

In the vacuum case, considering the situation when the point-Universe enters the corner with an expanding Universe (Sec.6.2.2.1), we find a suppression of the quantum variable β_-, as its standard deviation decays in time. We therefore concluded that the corner of the potential is an attractor for the point-particle Universe; once the Universe enters in the corner, it cannot escape any more.

Following this analysis, we also studied the limit in which the system approaches the cosmological singularity, see Sec.6.2.2.2. In this case we found that the variance associated to the anisotropic variable has a constant character, hence the probability density of the quantum anistropy variable does not change in time. This conclusion has a very deep meaning on the whole structure of the Bianchi IX dynamics. When $\beta_- \simeq 0$, the resulting cosmology is indistinguishable from a Taub Universe (Sec.5.3.6), which is not a singular model in the limit $\alpha \to -\infty$. Since the emergence of a long regime of the classical Bianchi IX dynamics within the a corner has been convincingly established [181], if the proposed picture is applicable, i.e. the smallness of the β_- values justify its quantum treatment, then the singular behaviour of the Bianchi IX Universe can be removed.
This result, in view of the prototype character of the Bianchi IX cosmology versus the generic cosmological solution [178], [182] could have a deep implication on the notion of the cosmological singularity as a general property of the Einstein equations, under cosmological hypotheses.

Finally in the last section, Sec.6.2.3, we studied the Bianchi IX dynamics in presence of ϕ and Λ, again in an expanding picture, i.e. for $\alpha \to \infty$. The aim of this analysis was to mimic the behavior of the Bianchi IX Universe if the de Sitter phase, which is associated to the inflationary paradigm for the primordial Universe, takes place when a corner evolution is performed by the point-Universe.

In this case we demonstrated that, in the limit of applicability of the WKB proposed scheme, the Universe naturally isotropizes since the classical anisotropy degree of freedom β_+ is suppressed while the fully quantum variable, i.e. β_-, is characterized by a decaying standard deviation. In other words, starting with a Gaussian distribution for β_-, its natural evolution in the future is towards a Dirac delta-function around the zero value.
Thus, this study offers a new paradigm for the Bianchi IX cosmology isotropization, based on the idea that the de Sitter phase is associated with a corner regime of the model.
To conclude, the study conducted in this chapter, generalizes and completes the results discussed in [205], where the Bianchi IX isotropization is faced in the same WKB scenario, but starting with two very small quantum anisotropy variables, i.e. assuming that the de Sitter phase starts when the point-Universe is in the center of the potential, already near to an isotropic configuration.

Chapter 7

A scenario for a singularity free generic cosmological solution

This section is based on the work published in [9].

We develop a scenario for the emergence of a non-singular generic cosmological solution based on the a WKB characterization of one of the two anisotropy degrees of freedom. We investigate the dynamics of the so-called inhomogeneous Mixmaster in the "corner" configuration and inferring that one of the two anisotropic variables becomes small enough to explore the uncertainty principle. Then, we apply a standard WKB approximation to the dynamics of the Universe which has macroscopic volume, one macroscopic anisotropy and one microscopic quantum degree of freedom.
Our study demonstrates the possibility that the Universe acquires a *non-singular* classical behavior, retaining the quantum degree of freedom as a small oscillating ripple on a stationary Universe. The role of the so-called "fragmentation process" is also taken into account in outlining the generality of such a behavior in independent local space regions.

The Chapter is organized as follow. In Sec.7.1, we motivate our study, provide the hyphotesis on which it is based and we give a brief overview of the results. In Sec.7.2 we review the main equations presented in Sec.5.4 and then we investigate more in detail the structure of the generic inhomogeneous model Hamiltonian

in the corner configuration. In Sec.7.3 we prove that it is possible to apply the Vilenkin paradigm to the corner configuration, and we investigate the structure of the inhomogeneous Mixmaster in this setup showing how the cosmological singularity can be removed. In Sec.7.4 we show how the corner configuration can statistically be reached in each point of the space, and finally, in Sec.7.5 we draw the conclusions.

7.1 Introduction

Following the results obtained in [8], presented in Chapter6, in this chapter we apply a similar idea to the inhomogeneous Mixmaster Universe, see Sec.5.4. The idea is to challenge the result, present in the works of Belinskii, Khalatnikov and Lifshitz, that the singularity is always present in the generic inhomogeneous solution.
The results of this study are presented in [9].

One of the most important constribution of the Landau School to theoretical cosmology consisted of the dynamical characterization of the generic cosmological solution in the vicinity of a singularity, as showed in [178, 184] (see also [181] and Sec.5.4). These studies, together with Hawking and Penrose theorem [213], seem to suggest that the presence of a singular point in the past of our actual universe should be regarded as a general feature of the Einsteinian cosmology and not as a consequence of the high symmetry of the isotropic Universe geometry.
The same conclusion was reached by Misner in [214] and Montani and Benini in their studies on the generic cosmological solution conducted using the canonical quantum gravity in the metric approach [215]. Ashtekar, on the other hand, showed that, if the canonical quantization scheme is riformulated in Loop Quantum cosmology, the situation is different, see the work in [216].

Also in [217] the authors constructed a singularity-free generic cosmological solution; in this case they used the semi-classical Polymer dynamics, which could be considered as a quasi-classical behavior of Loop quantum Cosmology for the evolution toward the singularity.

Given the amount of studies questioning the presence (or absence) of the singularity in the generic cosmological model, we decided to examine the possibility of a singularity free inhomogeneous Mixmaster also in the peculiar scenario of the *long era*, see the end of Sec.5.3.5.
In particular, we investigate the possibility that, when such configuration is addressed (according to the analysis in [8]), one of the two anisotropic degrees of freedom is small enough to approach a quantum behavior since it can explore the uncertainty principle in its own phase space. Then, we apply the WKB scenario proposed in [168] and we demonstrate that the resulting Universe is a classical non-singular one, plus a small quantum anisotropy.
Using the language of the standard Hamiltonian formalism we outline how, when the universe performs a long era in any corner of the potential term, there is a separation taking place between the classical macroscopic components of the inhomogeneous Mixmaster and a small quantum subset, made up of one of the two anisotropic variable.

The assessment of this scenario relies on two known results mentioned in Sec. 5.4:

- There always exists a non-null probability, as showed in [189], that the parameter u, which characterizes a Kasner regime, acquires large values such that the system dynamics evolves deeply in the corner configuration, where one of the anisotropy variable is very small.

- The existence of the fragmentation process discussed in [180, 200]. According to this, rational values taken by the function $u(x^i)$ across space can not be excluded from the evolution of the BKL map, therefore even few steps of the BKL map ensure the existence f large values of u in the neighborhood of certain space surface.

Note that, while our analysis is developed toward the singularity, we can consider a time reversed picture which is able to connect the standard inhomogeneous Mixmaster to a primordial non-singular generic solution as soon as the small quantum anisotropy degree of freedom is able to become a classical variable, i.e. as soon as the Universe escapes the corner.

7.2 Inhomogeneous Mixmaster in the corner configuration

In the ADM formalism the line element for a generic inhomogeneous cosmological model, written in terms of the Misner variables, reads as

$$ds^2 = N^2 dt^2 - e^{2\alpha}\left(e^{2\beta}\right)_{ab} l^a_\alpha l^b_\beta, \tag{7.1}$$

where β_{ab} is given by eq.(5.97), and the action S_G and the super-Hamiltonian for this generic model are given by eq.(5.114), and eq.(5.115):

$$S_G = \int d^3x dt (p_\alpha \partial_t \alpha + p_+ \partial_t \beta_+ + p_- \partial_t \beta_- - N\mathcal{H} - N^\beta \mathcal{H}_\beta) \tag{7.2}$$

$$\mathcal{H} = \frac{k}{12} e^{-3\alpha}(-p_\alpha^2 + p_+^2 + p_-^2 + e^{4\alpha} V_G(\beta_+, \beta_-)) \tag{7.3}$$

The potential $V_G(\beta_+, \beta_-)$ is obtained neglecting the spatial gradients of the Misner variables in the spatial curvature, which is justified by the work of Kirillov [179]. This scenario leads to the inhomogeneous Mixmaster model where, within each smooth spatial scale (roughly the horizon scale), the dynamics is isomorphic to the homogeneous Mixmaster, [184, 214]. However, as seen in Sec.5.4.2 for this model the chaotic time evolution couples to the spatial dependence and increasingly small scales are generated for the space variation of the Misner variables, but without destroying the dynamical scheme of infinite sequence of Kasner regimes.

The classical dynamics of a generic cosmological model is described by the Hamilton equations associated to the Misner variables and by the secondary constraints, see eq.(5.18), obtained varying the action S_G respect to N and N^i, namely:

$$\mathcal{H} = \mathcal{H}_i = 0. \tag{7.4}$$

These can be written explicitly as

$$-p_\alpha^2 + p_+^2 + p_-^2 + e^{4\alpha} V_G = 0 \tag{7.5}$$

$$p_\alpha \partial_i \alpha + p_+ \partial_i \beta_+ + p_- \partial_i \beta_- = 0, \tag{7.6}$$

where in the super-momentum constraint we kept only the dominant contribution. The potential V_G is given by eq.(5.116): the equipotential lines associated to this potential form, in each space point a curvilinear equilateral triangle having three open corner reaching infinity.

If the initial singularity is identified with the instant of time when the spatial volume of the Universe (i.e. the three-metric determinant) vanishes, then we can fix that singularity with the limiting value $\alpha \to -\infty$. In this limit V_G tends to become an infinite well in which center $\beta_+ \sim \beta_- \sim 0$ (actually for an increasing region as the singularity is approached) the potential term can be neglected. The dynamics of the system is described by the generalized Kasner solution, see AppendixC, during which p_α and $p_\pm$ are constant in time and:

$$\frac{d\beta_\pm}{d\alpha} = \frac{p_\pm}{p_\alpha} \equiv \pi_\pm(\bar{x}^i), \to \beta_\pm = \pi_\pm(\bar{x}^i)\alpha + \bar{\beta}_\pm(\bar{x}^i), \tag{7.7}$$

where $\bar{\beta}_\pm$ denote generic space functions and it is possible to identify

$$\pi_+ = \cos\theta, \qquad \pi_- = \sin\theta \tag{7.8}$$

since by definition they have to satisfy $\pi_+^2 + \pi_-^2 = 1$. The function $\theta(x^i)$ is angle of incidence of the particle off the potential wall and changes at each bounce, see Fig.7.1

In this chapter, as in [8], we are interested in the dynamics of the inhomogeneous Mixmaster Universe in the corner configuration, i.e. when the point-Universe is deeply inside the corner of the potential. As mentioned in Sec.5.4.1, the three corners, see Fig.7.1, are equivalent since it is possible to map one into another simply by rotating the coordinate plane $\{\beta_+, \beta_-\}$ by $\pi/3$. Hence, without loss of generality, in the following we are going to consider the corner along side the axis $\beta_- = 0$.
This configuration, from a physical point of view, corresponds to deal with the *long oscillations* regime, see Sec.5.3.5, where two space directions scale almost with the same oscillating time law and the remaining one decays monotonically toward the singularity.

Looking at the plot in Fig.7.1, it is possible to see that if the system reaches a configuration deeply inside the corner, such that $\beta_- \sim 0$, then θ is small and it follows that

$$\pi_- = \sin\theta \simeq \theta \simeq \epsilon \ll 1 \tag{7.9}$$

Choosing a space coordinate system $\bar{x}^i$ such that $\lambda_1(\bar{x}^i) = \lambda_2(\bar{x}^i) = \lambda_3(\bar{x}^i) \equiv \lambda(\bar{x}^i)$, the potential V_G becomes

$$V_G = \frac{1}{4}\lambda^2\left(2e^{4\beta_+}\cosh\left(4\sqrt{3}\beta_-\right) + e^{-8\beta_+}\right) - \frac{1}{2}\lambda^2\left(e^{4\beta_+} - 2e^{-2\beta_+}\cosh\left(2\sqrt{3}\beta_-\right)\right) \tag{7.10}$$

which matches with the expression of the potential for the homogeneous Mixmaster, see eq.(5.100).
Inside the corner, where $\beta_+ \gg 1, |\beta_-| \ll 1$, it is possible to expand V_G to $\mathcal{O}(\beta_-^2)$, which results in

$$V_G = 12\lambda^2 e^{4\beta_+}\beta_-^2. \tag{7.11}$$

In this configuration, the super Hamiltonian constraint in eq.(7.4) reads as

$$-p_\alpha^2 + p_+^2 + \mathcal{H}^- = 0 \tag{7.12}$$

where $\mathcal{H}^- = p_-^2 + 12\lambda^2 e^{4(\alpha+\beta_+)}\beta_-^2$ is a small contribution.

7.3 Quantum small oscillation

In order to use Vilenkin approach [168], we have to show that one of the Misner variables can be small enough to approach a quantum behavior.
To understand why this is possible, let us fix α to a finite value. In the corner configuration, as said in the previous section, $|\beta_-| \ll 1$, hence the coordinate interval for this variable $\Delta\beta_-$ is of order

$$\Delta\beta_- \sim 2\beta_+\theta = 2\beta_+\epsilon. \tag{7.13}$$

where the last equality comes from eq.(7.9). This can be understood looking at Fig.7.1.

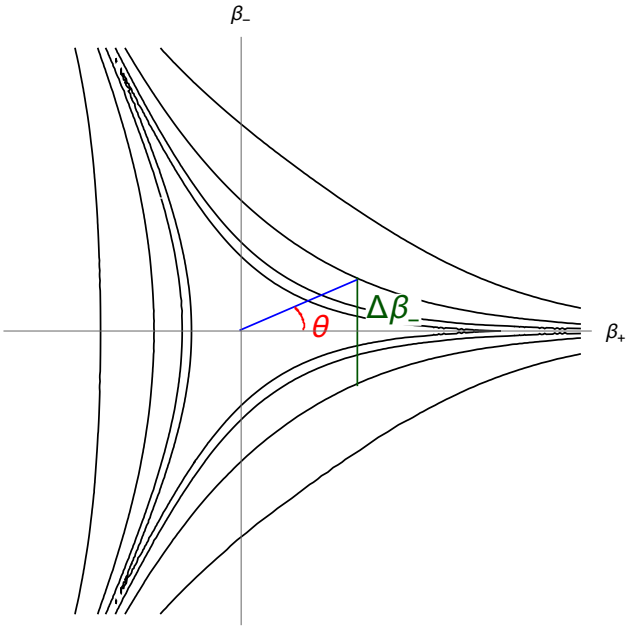

Figure 7.1: Equilateral triangle formed by the equipotential lines in each space point. The segment $\Delta\beta$ is in green, while the angle θ is represented in red.

Moreover, according to the general Kasner solution (see Appendix C), and to the first equality in eq.(7.7), comparing the kinetic and potential term in $\mathcal{H}^-$ defined above, it results

$$\frac{\mathcal{H}^-}{p_\alpha^2} \sim \frac{\mathcal{H}^-}{p_+^2} \sim \pi_-^2 \sim \theta^2 = \epsilon^2. \tag{7.14}$$

In the first part we used that, since $\mathcal{H}^-$ is a small contribution to $\mathcal{H}$, from the super-Hamiltonian constraint in eq.(7.12) $p_\alpha^2 = p_+^2$, while in the last part we used eq.(7.7). The function $\theta(\bar{x}^i)$, as mentioned before, changes at every bounce of the point-Universe against the potential wall and, being generated by the BKL map, rapidly acquires a random behavior.
The stochasticity of the BKL is what gives us the possibility to decouple the system: if the point-Universe is reflected such that θ, and therefore ϵ, is of order $\sqrt{\hbar}$, then the Hamiltonian constraint in eq.(7.12) can be decoupled into a classical part and a quantum one, according to the analysis in [168]. The classical part is associated to the variables α and β_+, while the small quantum subsystem, which

lives on the space-time defined by the classical components, is constituted by the anisotropy degree of freedom β_-.

In other words, we are inferring that, when $\epsilon \sim \mathcal{O}(\sqrt{\hbar})$, the variable β_- is small enough to explore the uncertainty principle with

$$\Delta\beta_- \leq 2\sqrt{\hbar}\beta_+, \qquad \Delta p_- \geq \frac{1}{4}\frac{\sqrt{\hbar}}{\beta_+}. \tag{7.15}$$

According to what we just said, the quantum subsystem shows to have the smallness requirement postulated in [168] and precised in [207]. Therefore, in analogy with the wave function of the Universe for the homogeneous case (eq. (5.40)), the Universe wave function can be written as

$$\Psi = e^{i\frac{\Sigma(\alpha,\beta_+)}{\hbar}}\Phi(\alpha,\beta_+,\beta_-), \tag{7.16}$$

where Σ is associated to the classical system and depends on the semi-classical variables α and β_+, while Φ describes the quantum sub-component. Note also that Ψ is a functional
According to the scheme developed in [168], the functional derivative of Φ with respect to the space field $\beta_-(\bar{x}^i)$ are of order $1/\hbar$, hence $\mathcal{H}^-\Phi \propto \mathcal{O}(\hbar)$.

To obtain the dynamical implication of the state functions eq.(7.16), we need to apply the canonical version of the super-Hamiltonian and super-momentum constraint, respectively (7.12) and (7.6), i.e:

$$\left[\hbar^2\frac{\delta^2}{\delta\alpha^2} - \hbar^2\frac{\delta^2}{\delta\beta_+^2} + \hat{\mathcal{H}}^-\right]\Psi = 0 \tag{7.17}$$

$$i\hbar\left(\partial_i\alpha\frac{\delta}{\delta\alpha} + \partial_i\beta_+\frac{\delta}{\delta\beta_+} + \partial_i\beta_-\frac{\delta}{\delta\beta_-}\right)\Psi = 0 \tag{7.18}$$

where the symbol δ denotes functional derivatives. Note that eq.(7.17) is the analogous of the eq.(6.5) written for the homogeneous Mixmaster case.
Following the same steps presented in Sec.6.2 it is possible to separate the above equation according to the order of $\hbar$ of the various terms. At the zero-th order in $\hbar$ the equations obtained are the classical Hamilton-Jacobi super-Hamiltonian and super-momentum equations for the semi-classical Misner variables α and β_+,

i.e:

$$-\left(\frac{\delta\Sigma}{\delta\alpha}\right)^2+\left(\frac{\delta\Sigma}{\delta\beta_+}\right)^2=0 \tag{7.19}$$

$$\frac{\delta\Sigma}{\delta\alpha}\partial_i\alpha+\frac{\delta\Sigma}{\delta\beta_+}\partial_i\beta_+=0. \tag{7.20}$$

From the above system, the classical component is associated to the reduced action

$$S_{Class}=\int dtdx^3\left(p_\alpha\partial_t\alpha+p_+\partial_t\beta_+-\frac{N}{12}e^{-3\alpha}\left(-p_\alpha^2+p_+^2\right)-N^i\left(p_\alpha\partial_i\alpha+p_+\partial_i\beta_+\right)\right). \tag{7.21}$$

Expanding eq. (7.17) ad eq. (7.18) at 1st order in $\hbar$, it is possible to write a Schröedinger-like equation for the quantum functional Φ.
The equation of order $\mathcal{O}(\hbar)$ from eq.(7.17) and eq.(7.18) are respectively

$$i\left(\frac{\delta^2\Sigma}{\delta\alpha^2}-\frac{\delta^2\Sigma}{\delta\beta_+^2}\right)\Phi+2i\left(\frac{\delta\Sigma}{\delta\alpha}\frac{\delta\Phi}{\delta\alpha}-\frac{\delta\Sigma}{\delta\beta_+}\frac{\delta\Phi}{\delta\beta_+}\right)+\mathcal{H}^-\Phi=0 \tag{7.22}$$

$$i\left[\partial_i\alpha\frac{\delta\Phi}{\delta\alpha}+\partial_i\beta_+\frac{\delta\Phi}{\delta\beta_+}+\partial_i\beta_-\frac{\delta\Phi}{\delta\beta_-}\right]=0, \tag{7.23}$$

and the last one can be separated into an equation for the semi-classical variables and one for the quantum one:

$$\partial_i\alpha\frac{\delta\Phi}{\delta\alpha}+\partial_i\beta_+\frac{\delta\Phi}{\delta\beta_+}=0 \tag{7.24}$$

$$\partial_i\beta_-\frac{\delta\Phi}{\delta\beta_-}=0. \tag{7.25}$$

where eq.(7.24) states the invariance of the wave functional Φ respect to the space coordinates in the classical line element.

From eq.(7.22) it is possible to see that the functional Φ obeys the equation:

$$i\hbar\partial_t\Phi=\int dx^3\frac{N}{12}e^{-3\alpha}\left(\hat{\mathcal{H}}^-+i\hbar\left(\frac{\delta^2\Sigma}{\delta\alpha^2}-\frac{\delta^2\Sigma}{\delta\beta_+^2}\right)\Phi\right), \tag{7.26}$$

where

$$\partial_t \Phi \equiv \int dx^3 \left[\left(\partial_t \alpha \frac{\delta}{\delta \beta_+} + \partial_t \beta_+ \frac{\delta}{\delta \beta_+} \right) \Phi \right]. \tag{7.27}$$

In the last equation, $\partial_t \alpha$ and $\partial_t \beta_+$ can be computed from the reduced action eq.(7.21) and via the identification of the momenta with the corresponding functional derivatives of Σ.

This analysis differs slightly from the approach presented in chapter 6 because we are dealing with a functional formalism, due to the inhomogeneity of the model considered and we are taking the variables α and β_+ as strictly classica. This last difference result in the last term of eq.(7.26). Assuming that $\Sigma(\alpha, \beta_+)$ is separable in the variables α and β_+, it is easy to check that eq.(7.19) admits the following solution:

$$\Sigma = \int d^3x K(x^i)(\alpha + \beta_+). \tag{7.28}$$

According to the Hamilton Jacobi method, this yields to the classical relation

$$\alpha + \beta_+ = \beta_0(x^i) \tag{7.29}$$

which is the analogous in the inhomogeneous case of the result found in eq.(6.60). Substituting the last equation into the quantum Hamiltonian $\hat{\mathcal{H}}^-$, this becomes

$$\hat{\mathcal{H}}^- = p_-^2 + 24C^2 e^{4\beta_0} \beta_-^2. \tag{7.30}$$

Note that, in order for Σ in eq.(7.28) to satisfy the super-momentum equation (7.20) it is enough to require that β_0 is constant.

Before using eq. (7.28) and eq (7.30) to solve the dynamics of the quantum subsystem of the inhomogeneous Mixmaster, let us write explicitly the line-element of the system.
Following the computation presented in Sec.6.2, we can write the relation between the variable α and the synchronous time variable t. From eq.(7.21) and from the semi-classical Hamiltonian $\mathcal{H}_0 = k/12 e^{-3\alpha}(-p_\alpha^2 + p_+^2)$, it follows that

$$\alpha(t) = \frac{1}{3} \log \frac{t}{t_0}, \tag{7.31}$$

where t_0 is a generic instant.
Substituting eq.(7.29) in the transformation analogous to eq.(5.96), we obtain that

$$\begin{cases} q_1(x^i,t) = 2\beta_0 + 2\sqrt{3}\beta_- \\ q_2(x^i,t) = 2\beta_0 - 2\sqrt{3}\beta_- \\ q_3(x^i,t) = 2(\alpha - 2\beta_0 + 2\alpha). \end{cases} \tag{7.32}$$

In the specific case we are analyzing, where $\beta_- \ll 1$, it follows that $q_1(t,x) = q_2(t,x) = 2\beta_0$.
Choosing without any loss of generality $\overrightarrow{l}^3$ along the coordinate x^3, using the transformation for $q_3(x^i,t)$ in eq.(7.32) and substituting the solution for $\alpha(t)$ (see eq.(7.31)), the line element in eq.(7.1) becomes:

$$ds^2 = dt^2 - \left(\frac{t}{t_0}\right)^2 e^{-4\beta_0}(dx^3)^2 - (dl_2)^2 \tag{7.33}$$

where $(dl_2)^2$ is a static two-dimensional line element on the plane $\{x^1, x^2\}$.
The line element above, as well known [178, 184], is *Taub-like*, therefore it is associated to a *non-singular* cosmological model. Moreover this becomes static after changing coordinates : $t' = (t/t_0)\cosh x^3$ and $(x^3)' = (t/t_0)\sinh x^{31}$.

Now let us go back to eq.(7.26).
Using the expression of Σ in eq.(7.28) and introducing the time variable τ defined via the lapse function $N = 12e^{3\alpha}$, eq.(7.26) reduces to the simpler form:

$$i\hbar\partial_\tau\Phi = \int d^3x\hat{\mathcal{H}}^-\Phi \tag{7.34}$$

where $\hat{\mathcal{H}}^-$ is defined in eq.(7.30).
The dynamical decoupling of the space points, i.e of each space region sufficiently smooth (so that the spatial gradient can be considered negligible), allows to reduce the Superspace on which the wave function Φ is defined, to the collection of local Minisuperspace, one for each point x^i.
Thus we can write

$$\Phi = \Pi_{x^i}\phi_{x^i}(\tau,\beta_-). \tag{7.35}$$

[1] This is true if $e^{2\beta_0} = t_0$.

where the local wave functions ϕ_{x^i} satisfy the equations obtained from (7.34):

$$i\hbar\partial_\tau\phi_{x^i} = \{-\hbar^2\partial^2_{\beta_-} + 24C^2(x^i)e^{4\beta_0}\beta^2_-\}\phi_{x^i}. \tag{7.36}$$

At $\mathcal{O}(\hbar)$ the functional Φ has to satisfy, at the same time, eq.(7.34) and eq.(7.25). However, taking Φ as the product of local wavefunctions ϕ_{x^i}, it already satisfies the supermomentum constraint in eq.(7.25); eq.(7.35) in fact corresponds to deal locally with the condition $\partial_i\beta_- \simeq 0$.
Here we are implementing the BKL conjecture based on the idea that the scale of spatial gradients is larger than the quantum correlation length. The concept of *quantum causality* is therefore introduced, according to which space regions evolving independently are not in causal contact.

Going back to solving eq.(7.36), this has the same morphology as eq.(6.20) obtained in the homogeneous case. Hence, also in this case, the different local wave functions ϕ_{x^i} are solution of a Schröedinger-like equation for a quantum harmonic oscillator with a frequency constant in time, each in each space point. It is well known that the solution of such equations can be localized non spreading wavefunctions, see Sec.6.2.2.2. In particular, for each localized ϕ_{x^i} at τ_0, where τ_0 is a generic instant of time,

$$|\phi_{x^i}(\tau)|^2 = |\phi_{x^i}(\tau_0)|^2 \tag{7.37}$$

for every τ.
Therefore, if $\phi_{x^i}(\tau_0)$ is such that its probability density is Gaussian, Φ, defined as a superposition of ϕ_{x^i} in eq.(7.35), has the morphology of non spreading and localized quantum harmonic oscillators, each in each space point.
We expect that the variable β_- can be represented by localized state because when it enters the corner is a classical degree of freedom and its available domain remains of order $\hbar\beta_+$ in that configuration.

Thus, we can conclude that, if our scheme is reliably applicable to the Universe dynamics deeply entering the corner, the cosmological singularity is removed in every local Minisuperspace. The line-element describing the model, see eq.(7.33), is the one of a classical non-singular space time on which very small quantum

fluctuations of the variable β_- live.
This intriguing picture is well-established when referred to the single spatial point (causal region), but to understand how it works for the Universe as a whole, it is necessary to develop some consideration on the BKL map [178, 184] and on the fragmentation process [180], see also [200]. These considerations are the focus of the next section.

To conclude this section it is worth to emphasize that the picture proposed above can be reversed in time. Hence it would be possible to start with a non-singular Universe with a small quantum anisotropy and, as the space volume increases (i.e. α increases), this degree of freedom becomes classical; in this way the dynamics comes out of the corner configuration and the full configurational domain is restored . This means that, in this scenario, the generic inhomogeneous cosmological solution can emerge from a non-singular initial configuration and evolves toward the standard oscillatory regime discussed in [184], [178].

7.4 Inhomogeneous BKL map

Introducing the parameter $u(x^i)$ as in [184], which, again, is the generalization to the inhomogeneous case of the parameter u introduced in eq.(5.68) for the homogeneous Mixmaster, and using eq.(5.105) in the definition of $\pi_\pm(x^i)$, see eq.(7.7), these can be written as [176]:

$$\pi_+ = \frac{1}{2}\left(\frac{1-2u-2u^2}{1+u+u^2}\right), \qquad \pi_- = \frac{\sqrt{3}}{2}\left(\frac{2u-1}{1+u+u^2}\right). \tag{7.38}$$

Since we are focusing on the limit in which $\theta \ll 1$ (Fig.7.1) so that the point-Universe is deep inside the potential corner, we can restrict the expressions in eq.(7.38) to the limit $u \gg 1$ (note that $\theta \simeq \sqrt{3}/u$).

To understand when such large value appears we have to consider the BKL map, presented in [184], which provides the values u' generated from the value u via the effect of the potential wall in the standard oscillatory regime, i.e;

$$\text{for} \quad u > 1, \quad u' = u - 1, \quad \text{for} \quad u \leq 1, \quad u' = \frac{1}{u-1}. \tag{7.39}$$

7. A SCENARIO FOR A SINGULARITY FREE GENERIC COSMOLOGICAL SOLUTION

As mentioned in Sec.5.3.3.1, the evolution of the map depends on the initial value u^0.
All the initial rational values of the parameters $u = u^0$ are evolved for a *finite* number of the BKL map steps; after this $u \to \infty$ is recovered (i.e $\theta = 0$ is reached and the point-Universe is deeply inside the corner).

Irrational values of u^0, instead, evolve *indefinitely* and the BKL map outlines a strong (exponential) instability with respect to the initial condition: hence, modifying the value of an irrational u^0 by a very small amount, the sequence of values generated by the map iteration becomes uncorrelated with respect to the sequence associated to u^0 just after a few steps.
Note that in [184] and [178], the authors excluded the rational values of u^0 in their analysis of the map, see Sec.5.3.3.1, because being of zero measure on the real axis, they turn out to be non general conditions.
However, in the following years, the idea of excluding some specific points (the rational u^0 initial values) has been revisited.
Firstly because, from a purely logical point of view, it does not make much sense to exclude *only* some specific values for the parameter u since this itself is not an exact "concept". This parameter has in fact been introduced to approximately describe the Kasner solution which, again, is an approximate regime which can be obtained only by neglecting the potential wall.
Furthermore, assigning over the inhomogeneous space the initial condition $u = u^0(x^i)$, it is not possible to exclude the rational values of u simply for continuity reason.

Thus, each spatial region containing surfaces on which u is rational, enters deeply in the corner after a certain number of iterations of the map and the corner scenario can be implemented close enough to one of such regions. As a direct consequence, *both* rational and irrational u values, in this picture, can reach the corner configuration.

Actually, when the parameter u is thought as a physical parameter, we have to assign its values with a given uncertainty; this consideration, together with the instability of the BKL map, leads to think of u as a statistically distributed variable. As seen in Sec.5.3.3.1, it can be shown that it admits the following

steady probability density:

$$w(u) = \frac{1}{\ln 2}\frac{1}{u(u+1)}. \tag{7.40}$$

The BKL map has, especially when is expressed in terms of the fractional part of the parameter u, "strong mixing" properties [218]; starting from a generic irrational u all the other irrational values (including very large one), sooner or later, are generated.
This ensures that, also from a statistical point of view, in each point of the space it is possible to reach the conditions needed for the system to enter in the corner. This can also be noticed recalling the inhomogeneous Mixmaster is subjected to the fragmentation process, see Sec.5.4.2.
According to this the iteration of the BKL map towards the singularity causes the fragmentation of space in a series of smaller and smaller "islands" in which the points are causally connected.
Without any loss of generality, but simply using the general knowledge that the irrational numbers are dense in reals, each irrational u_i belongs to the neighborhood of a rational value u_r "nearby", i.e. belongs to the same causal region. As a consequence, for $\alpha \to -\infty$, since the rational value u_r reaches the corner ($u_r \to \infty$), all the irrational values u_i in its local patch reach the corner as well, being causally connected.
To summarize, the fragmentation process allows for each spatial region containing surfaces on which u is rational, to enter deeply in the corner.

This is extremely important because it provides an additional method for the u_i to reach the corner configuration.

In [180] it has also been argued how the iteration of the BKL map in two close space points gives uncorrelated values of the parameter u just after few steps and thus is at the ground of the progressive increasing of the spatial gradients towards the singularity. As a consequence of this result, the proposed scenario takes place in different instant of time in dynamical independent regions of space.
However this does not change the analysis presented above since once the system enters in the corner, the BKL map is no longer applicable. Furthermore, once we can separate semi-classical and quantum variables, the increasing behavior of the

spatial gradients is naturally stopped.
Each smooth space region is characterized by a non-singular static space-time and the statistical properties of the BKL map are reflected only on the specific initial conditions at which the corner dynamics is implemented.

7.5 Conclusion

In this section we investigated the possibility to obtain a non-singular generic cosmological solution as a results of a quantum behavior of the small anisotropy β_- within a deep corner configuration.
In other words, the Universe's dynamics has been separated into a classical non-singular one, plus a quantum effect. The dynamics of the quantum variable β_- is obtained solving a Schröedinger-like equation for an harmonic oscillator with time-independent frequency, and it results in a simple small oscillation of β_- itself.
To establish this configuration we inferred that, for a large values of the parameter u, the variable β_- is extremely small and well inside the corner of the potential, so that it explores the uncertainty principle, see eq.(7.15).
To characterize the generality of this scheme, we used two effects:

1. In each assigned space point the iteration of the BKL map is associated to a significant probability for a very long era, i.e. the system dynamics can be trapped in the potential corner, see [189].

2. The existence of the fragmentation process [180] in the inhomogeneous Mixmaster, i.e. the impossibility to exclude rational values of u in a continuous representation $u(x^i)$, contrary to what was done in [184] and [178].
   This process generates on all the corresponding space surfaces exactly the limit $\beta_- \equiv 0$, with associated neighborhoods where a long era must take place.

The analysis presented completes and generalizes the consideration made in [8], where the WKB approach was used in the the homogeneous case. Related topics have been discussed in [205, 206].

The basic motivation for such generalization consists in the natural character that the corner configuration acquires in the inhomogeneous picture, as effect of the fragmentation process. This means that few iterations of the map can be enough to generate very high values of u in correspondence of all the rational values of the initially assigned function $u^0(x^i)$.

In conclusion, the present analysis revives, on a slightly different level, the original (pre-"BKL map") Lifshit and Khalatnikov idea that the anisotropy of the Universe could resolve its singularity.

7. A SCENARIO FOR A SINGULARITY FREE GENERIC COSMOLOGICAL SOLUTION

Chapter 8

Final remarks

The formulation of the Inflationary theory opened the door to a series of new questions concerning the beginning of the Universe. In this thesis we focused on the following: *How can inflation be realized? What was the Universe like before this exponential expansion?*
In particular, the first part of this work focused on a particular subgroup of inflationary models, the multifield models.
After explaining some of the reasons that brought people to investigate multifield models, and after giving a brief description of their dynamics in Chapter 2, in Chapter 3 we looked at conditions the masses of the scalar fields must satisfy to drive a successful period of inflation.
We developed a new type of inflationary attractor, which we called *fat inflation*, that can be achieved when all the scalar fields' masses are heavier than the Hubble scale, i.e $H < M_{Inf}$.
In particular, we showed that fat inflation avoids the η-problem, which would prevent inflation to happen; this type of attractor in fact satisfies the slow-roll conditions. Moreover, unavoidably requiring a curved non-geodesic trajectory, fat inflation can also have interesting implications for the dS conjectures.

Hoping to derive similar results for the interesting case of multifield inflationary models in a SUGRA framework, we noticed that rapid-turn models in supergravity are rare. In Chapter 4, after describing different forms of two-field inflation which may occur in SUGRA, we focused on finding a way to build highly

non-geodesic multifield inflationary models in supergravity. For concreteness we concentrated in particular on *multifield axion inflation*. We observed that by tuning the superpotential and the Kähler potential it is possible to construct a successful multifield inflationary model (hence ensuring a small ϵ) with a large turning rate. We studied in detail the EGNO model and a no-scale inspired model and, for both of them, we demonstrated how to appropriately fine-tune the models' parameters to increase Ω/H.

These results lead us to conjecture that large dimensionless turning rates are *rare* in (theoretically motivated) supergravity constructions, however they can easily be achieved by introducing an additional parameter in the Kähler potential. In the cases we analysed we obtained large turning rates as a consequence of large field space curvature.

To conclude the review of the first part of this thesis it is worth mentioning some future prospects of the work presented in Chapter 3 and 4.
In the second part of [6] my collaborators showed how it is possible to construct an explicit fat inflation model in string theory, in particular a D5-brane model, which is consistent with the Planck data. In light of this, it would be interesting to revisit D-brane models, e.g. D3-brane multifield inflation, which have been studied in the standard inflationary attractor with small turns. This would also be important in view of the recent theoretical constraints on standard slow-roll inflation.
Focusing on the results discussed in Chapter 4, it would be interesting to understand if it is possible to have theoretically motivated SUGRA multifield models which present large turning rates. Moreover, we found that tachyons appear to be a ubiquitous feature of rapid-turn inflation in supergravity, however more study in this sense might be needed.

In the second part of this thesis we focused on the understanding of the dynamics of the Universe *before* inflation. As we mentioned in the introduction, since inflation smooths and homogenises the Universe just few moments after its beginning, it is possible to consider more general cosmologies near the singularity. In Chapter 6 we analysed the Bianchi IX Universe within the corner region of its

potential using the Vilenkin approach introduced in Chapter 5. Our intent was to understand how the dynamics of this model changes compared to the "classical" one derived by the Landau Schools when we treat one of the anisotropic variables on a quantum level. We studied this model in two cases: first in the vacuum, and secondly in the presence of a scalar field ϕ along with a cosmological constant Λ. In the first case, considering an expanding Universe ($t \to \infty$), we found that the presence of a quantum anisotropic variable makes the corner of the Bianchi IX potential an attractor for the point-particle Universe. For a collapsing Universe ($t \to 0$), instead, we concluded that the resulting cosmology is indistinguishable from a Taub Universe, which suggests that the singular behavior of the Bianchi IX Universe can be removed. Finally, analysing the dynamics of the Mixmaster model in the presence of ϕ and Λ in an expanding picture we demonstrated that the Universe naturally isotropizes.
In Chapter 7, following the result obtained in Chapter 6 for an empty collapsing Universe, we investigated the possibility to obtain a non-singular generic cosmological solution adopting the same configuration used in the previous chapter, i.e. the Vilenkin WKB approximation. To establish this configuration, we inferred that one of the anisotropic variables is extremely small and well inside the potential's corner, where the uncertainty principle applies. We motivated this scheme recalling that there is a significant probability for the Universe to be trapped in the corner and that the inhomogeneous Mixmaster is subjected to the fragmentation process (as motivated in Chapter 5).
Once we proved that the Vilenkin approach can be implemented to the inhomogeneous Mixmaster, we demonstrated the possibility that the Universe acquires a *non-singular* classical behavior simply following the steps already implemented for the homogeneous case.

Summarising, in the last two Chapters of this thesis we showed that the dynamics of general cosmologies near the singularity differ deeply from those proposed by the Landau School in the '80s when it is possible to separate variables into semiclassical and quantum ones. In particular, this framework allows us to obtain a non-singular (in)homogeneous Mixmaster model and it provides an isotropization mechanism for the Bianchi IX model.

An interesting follow-up to this work would be the study of a quantum Bianchi IX model, or inhomogeneous Mixmaster: how would the dynamics of these models change near the singularity if *all* the variables can be considered quantum? In particular, it would be interesting to understand if it is still possible to remove the singularity (for a collapsing Universe) and isotropize the Universe (for an expanding Universe).

Appendix A

Primordial fluctuations for single field models

In the rest of this section we will briefly sketch the computations of the quantum fluctuation generated during inflation in a pure de Sitter and massless case. A more extensive derivation can be found in [32–36] and in references therein.

Let's start by noticing that a perturbation in the scalar field produces inevitably a fluctuation in the energy momentum tensor, hence in the metric $g_{\mu\nu}$:

$$\phi(t, x^i) = \phi^0(t) + \delta\phi(t, x^i) \quad \rightarrow \quad g^0_{\mu\nu}(t) + \delta g_{\mu\nu}(t, x^i) \tag{A.1}$$

The most general scalar-tensor decomposition of the metric is

$$ds^2 = -(1 + 2\Phi)dt^2 + 2a\partial_i B dx^i dt + a^2 \left[(1 - 2\Psi)\delta_{ij} + E_{ij}\right] dx^i dx^j. \tag{A.2}$$

where E_{ij} is a traceless symmetric tensor and can be decomposed as $E_{ij} = \partial_i\partial_j E - \frac{1}{3}\delta_{ij}\nabla^2 E + h_{ij}$. Here Φ, Ψ and E are the scalar degrees of freedom and h_{ij} is the tensor one.
The spatial metric perturbation, together with the field perturbation, can be split into two vector, two scalar and one tensor mode. However not all of these are physical degrees of freedom and one scalar and one vector mode can be removed

with the following reparametrization invariance

$$x^\mu \to \xi^\mu(t, \mathbf{x}). \tag{A.3}$$

This leaves us with one scalar and one tensor mode.
The scalar perturbations, coupling to the energy density, lead to the inhomogeneities and anistropies that we see today in the CMB, while the tensor ones induce polarization in the CMB spectrum, see e.g. [219–221].
In the following we will focus exclusively on the scalar perturbations.
For the purpose of the computation, it is useful to fix a gauge. The most used in literature are: *comoving gauge*, where the inflationary perturbation is zero, $\delta\phi = 0$, and the *spatially flat gauge* where instead the metric perturbation is set equal to zero.
In the following we will use the comoving gauge, following [39][1], where

$$\delta\phi = 0, \quad g_{ij} = a^2(t)\left((1 + 2\mathcal{R})\delta_{ij} + h_{ij}\right). \tag{A.4}$$

Here $\mathcal{R}$ and h are the physical degrees of freedom, $\mathcal{R}$ parametrizes the scalar fluctuations and h_{ij} parametrizes the tensor fluctuation.
In particular, h_{ij} is a traceless matrix which contains the two tensor degrees of freedom and $\mathcal{R}$ is the *comoving curvature perturbation*, which measures the curvature of the spatial hypersurfaces in the gauge, and it is defined as [2]

$$\mathcal{R} \equiv \Psi. \tag{A.5}$$

Focusing only on the scalar fluctuations, the scalar part of the second order action $S_\mathcal{R}$, derived in [36, 39], is given by

$$S_{\mathcal{R}^2} = \int d^4x a^3 \left[\epsilon\left(\dot{\mathcal{R}}^2 - \frac{1}{a^2}\left(\nabla\mathcal{R}\right)^2\right)\right] \tag{A.6}$$

where ϵ is the slow-roll parameter defined in eq.(2.50).

[1] In sec 2.3.4 we will use the spatially flat gauge following [79]

[2] The general expression for $\mathcal{R}$ is $\mathcal{R} \equiv \Psi + \frac{H}{\dot{\phi}}\delta\phi$. In the spatially flat gauge, defined by $\Psi = 0$, $\mathcal{R}$ is defined as $\mathcal{R} = \frac{H}{\dot{\phi}}\delta\phi$.

To perform the quantization of the curvature perturbations, it is convenient to introduce a new variable z, the canonically normalized *Mukhanov-Sasaki* variable [222–224],

$$v = z\mathcal{R}, \qquad z^2 \equiv a^2 \frac{\dot{\phi}^2}{H^2} = 2a^2\epsilon \tag{A.7}$$

and move to the conformal time $\tau = (aH)^{-1}$.
The action becomes

$$S_{v^2} = \frac{1}{2}\int d\tau d^3x \left[(v')^2 + (\partial_i v)^2 + \frac{z''}{z}v^2\right]. \tag{A.8}$$

To quantize the theory v has to be promoted to a quantum operator [225]

$$\hat{v}(t,\mathbf{x}) = \int \frac{d^3\mathbf{k}}{(2\pi)^3}\left[v_k(\tau)\hat{a}_\mathbf{k}e^{i\mathbf{k}\cdot\mathbf{x}} + v_k^*\hat{a}_\mathbf{k}^\dagger e^{-i\mathbf{k}\cdot\mathbf{x}}\right] \tag{A.9}$$

where $\hat{a}_\mathbf{k}$ and $\hat{a}_\mathbf{p}^\dagger$ satisfy

$$\left[\hat{a}_\mathbf{k}, \hat{a}_\mathbf{p}^\dagger\right] = (2\pi)^3\delta(\mathbf{k}-\mathbf{p}), \qquad [\hat{a}_\mathbf{k}, \hat{a}_\mathbf{p}] = \left[\hat{a}_\mathbf{k}^\dagger, \hat{a}_\mathbf{p}^\dagger\right] = 0. \tag{A.10}$$

and the quantum zero-point fluctuation is given by

$$\langle\hat{v}^\dagger(\tau,\mathbf{k})\hat{v}(\tau,\mathbf{k}')|0\rangle = |v_k(\tau)|^2\delta^3(\mathbf{k}-\mathbf{k}') \tag{A.11}$$

The mode functions v_k satisfy a modified Klein-Gordon equation in conformal time

$$v_k'' + \left(k^2 - \frac{z''}{z}\right)v_k = 0 \tag{A.12}$$

which, assuming true de Sitter ($H' = 0, a = -1/(H\tau)$) becomes

$$v_k'' + \left(k^2 - \frac{2}{\tau^2}\right)v_k = 0. \tag{A.13}$$

One can prove that the solution of the above equation is:

$$v_k(\tau) = \alpha\frac{e^{-ik\tau}}{\sqrt{2k}}\left(1 - \frac{i}{k\tau}\right) + \beta\frac{e^{ik\tau}}{\sqrt{2k}}\left(1 + \frac{i}{k\tau}\right) \tag{A.14}$$

where α and β can be fixed selecting the Bunch-Davies vacuum initial condition. Finally, eq.(A.14) becomes

$$v_k = \frac{e^{-ik\tau}}{\sqrt{2k}}\left(1 - \frac{i}{k\tau}\right) \tag{A.15}$$

In the super-horizon limit, when $k \gg aH$, that is $k\tau \to 0$, recalling that $\tau = -1/(aH)$, corresponds to

$$\lim_{k\tau\to 0} v_k = -\frac{i}{\sqrt{2k^3}\tau}, \quad \to \quad R_k \propto \frac{1}{k^{3/2}}. \tag{A.16}$$

This results implies that once the perturbations exit the Hubble radius they freeze $\mathcal{R} \sim const$, as it can be seen in Fig.2.5. When inflation ends and the Hubble radius starts to grow, the super-horizon mode k re-enters inside the horizon and starts oscillating; its oscillating amplitude, initially, is as big as it was when k crossed the Hubble radius during the inflation. This explains how the small fluctuations, which source the large scale structures, derive from the inflationary dynamics.

Finally, we compute the power spectrum of $\mathcal{R}$ defined as [39, 107, 226]

$$\frac{k^3}{2\pi^2}\langle \mathcal{R}(\mathbf{k})\mathcal{R}(\mathbf{k}')\rangle \equiv (2\pi)^3\delta^3\left(\mathbf{k}+\mathbf{k}'\right)\Delta^2_{\mathcal{R}}(k). \tag{A.17}$$

Recalling that $\mathcal{R} = v/(a\sqrt{2\epsilon})$ and using eq. (A.11), the dimensionless power spectrum $\Delta^2_{\mathcal{R}}$ can be evaluated at horizon crossing $k = a_* H_*$

$$\Delta^2_{\mathcal{R}}(k) = \frac{H^2}{8\pi^2\epsilon}\Big|_{k=a_*H_*}. \tag{A.18}$$

Note that $k = a_* H_*$ is usually taken to be 60-70 e-folds before the end of inflation, when $\epsilon \to 1$.
A direct consequence of eq.(A.18) is that it constraints the slow-roll parameter ϵ relatively to the scale of the potential $V \sim H^2$.

Tensor perturbation

The above computations have been done focusing on the scalar perturbations only. However, as mentioned at the beginning of this section, the inflaton quan-

tum fluctuations generate metric perturbations which include both scalar tensor degrees of freedom where the tensor ones are associated to the polarization of gravitational waves (h_+ and $h_\times$). Following the same step used to determine the scalar power spectrum, it can be proven that the dimensionless tensor power spectrum is

$$\Delta_t^2(k) = \frac{2H^2}{\pi^2}\Big|_{k=a_* H_*} \tag{A.19}$$

A. PRIMORDIAL FLUCTUATIONS FOR SINGLE FIELD MODELS

Appendix B

Results from survey of supergravity models

In this Appendix we display various Supergravity inflationary models we found in the literature. For each model we report: Kähler potential K, Superpotential W, initial conditions (ICs), wheter the inflation ends or not (Inflation ends if $N_{end} = 60$), largest value for the dimensionless turning rate ω^2_{end} and the parameters' range analysed.

Table B.1: Searched SUGRA models

Model	K	W	ICs	N_{end}	ω^2_{end}	Ref	Scanned range
EGNO[1]	(4.95)	(4.96)	$\phi^1 = 0.6496$ $\phi^2 = 1.719$ $\pi^1 = -0.2204$ $\pi^2 = -0.6702$ $a = 0.966$ $p = 3.055$ $c = 2258$ $\alpha \equiv 1$ $S \equiv 0$	60.0	10.58	[4]	$\phi^1 \in (0.0, 1.0)$ $\phi^2 \in (0.0, 5.0)$ $\pi^1 \in (-\sqrt{2}, \sqrt{2})$ $\pi^2 \in (-\sqrt{2}, \sqrt{2})$ $a \in (0.0, 1.0)$ $p \in (0, 2\pi)$ $c \in (0, 3000)$

(To be continued)

[1]Note that these parameters are not limited to $p = 0$, like the parameters presented in Section 4.3.5.2. They were found during a scan with `Inflation.jl` and `BlackBoxOptim.jl` as described above.

Model	K	W	ICs	$N_{\rm end}$	$\omega^2_{\rm end}$	Ref	Scanned range
2	$-3\log[\Phi+\bar{\Phi}-S\bar{S}]$	$\lambda-\mu\Phi$ $+\beta S+\gamma\Phi S$	$\phi^1=14.59$ $\phi^2=5.237$ $\phi^3=19.75$ $\phi^4=4.783$ $\pi^1=-0.8464$ $\pi^2=0.8382$ $\pi^3=-0.5993$ $\pi^4=-0.4731$ $\lambda=3.386*10^{-4}$ $\mu=5*10^{-5}$ $\beta=3.447*10^{-4}$ $\gamma=7.987*10^{-4}$	60.0	$\sim 10^{-9}$	[157]	$\phi^i\in(0.0,20.0)$ $\lambda\in(0.0,10^{-3})$ $\mu\in(0.0,10^{-3})$ $\beta\in(0.0,10^{-3})$ $\gamma\in(0.0,10^{-3})$
3	$-3\log[1+\frac{1}{6}(\Phi-\bar{\Phi})^2$ $-\frac{1}{3}S\bar{S}]$	$-S\left(\Phi^2-\frac{v^2}{2}\right)$	$\phi^1=0.7162$ $\phi^2=0.01539$ $\phi^3=2.441$ $\phi^4=0.005576$ $\pi^1=-1.026$ $\pi^2=-0.6852$ $\pi^3=1.392$ $\pi^4=-0.9465$ $v=0.5917$	60.0	0.004	[100]	$\phi^1\in(0.0,5.0)$ $\phi^2\in(0.0,\sqrt{3})$ $\phi^3\in(0.0,\sqrt{6})$ $\phi^4\in(0.0,\sqrt{6})$ $\pi^i\in(-\sqrt{2},\sqrt{2})$ $v\in(0.0,20.0)$

(To be continued)

Model	K	W	ICs	$N_{\rm end}$	$\omega^2_{\rm end}$	Ref	Scanned range
4.1	$\frac{(\Phi+\bar{\Phi})^2}{2}+S\bar{S}$	$S(1-e^{-\alpha\Phi})$	$\phi^1=-0.04236$ $\phi^2=0.4779$ $\phi^3=9.098$ $\phi^4=0.1057$ $\pi^1=-0.07004$ $\pi^2=-0.01171$ $\pi^3=0.3973$ $\pi^4=0.93$ $\alpha=0.4813$	60.0	0.00297	[154]	$\phi^1\in(-2.0,2.0)$ $\phi^2\in(0.0,10.0)$ $\phi^3\in(0.0,10.0)$ $\phi^4\in(0.0,10.0)$ $\pi^i\in(-\sqrt{2},\sqrt{2})$ $\alpha\in(0.0,10.0)$
4.2	$-\frac{(\Phi+\bar{\Phi})^2}{2}+S\bar{S}$	$S\sin\left(\frac{\alpha\Phi}{2}\right)$	$\phi^1=1.921$ $\phi^2=0.1958$ $\phi^3=0.03938$ $\phi^4=0.1432$ $\pi^1=0.7423$ $\pi^2=1.408$ $\pi^3=-0.04178$ $\pi^4=-0.6481$ $\alpha=2.107$	13.27	$\sim 10^{-8}$	[154]	$\phi^1\in(-2.0,2.0)$ $\phi^2\in(0.0,10.0)$ $\phi^3\in(0.0,10.0)$ $\phi^4\in(0.0,10.0)$ $\pi^i\in(-\sqrt{2},\sqrt{2})$ $\alpha\in(0.0,10.0)$

(To be continued)

Model	K	W	ICs	$N_{\rm end}$	$\omega^2_{\rm end}$	Ref	Scanned range
4.3	$-\frac{(\Phi+\bar{\Phi})^2}{2}+S\bar{S}$	$S(A\sin(\Phi\alpha/2)$ $+B\sin(\Phi\beta/2))$	$\phi^1=1.874$ $\phi^2=0.7861$ $\phi^3=0.09951$ $\phi^4=0.8866$ $\pi^1=-0.5719$ $\pi^2=1.136$ $\pi^3=0.02645$ $\pi^4=1.19$ $\alpha=1.325$ $\beta=4.175$ $A=3.718$ $B=1.402$	60.0	0.0025	[154]	$\phi^1\in(-2.0,2.0)$ $\phi^2\in(0.0,10.0)$ $\phi^3\in(0.0,10.0)$ $\phi^4\in(0.0,10.0)$ $\pi^i\in(-\sqrt{2},\sqrt{2})$ $\alpha\in(0.0,10.0)$ $\beta\in(0.0,10.0)$ $A\in(0.0,10.0)$ $B\in(0.0,10.0)$,

(To be continued)

Model	K	W	ICs	$N_{\rm end}$	$\omega^2_{\rm end}$	Ref	Scanned range
5	$-3\log(\Phi+\bar{\Phi})+$ $-\log(S+\bar{S})$	$-if+ihS$ $+iq\Phi$	$\phi^1=0.2574$ $\phi^2=2.173$ $\phi^3=1.203$ $\phi^4=9.63$ $\pi^1=-0.2818$ $\pi^2=-0.01292$ $\pi^3=-1.37$ $\pi^4=-0.00025$ $h=1.7*10^{-11}$ $q=3.625$ $f=2.599$	0.6489	0.0014	[156]	$\phi^i\in(0.0,10.0)$ $\pi^i\in(-\sqrt{2},\sqrt{2})$ $h\in(0.0,10.0)$ $q\in(0.0,10.0)$ $f\in(0.0,10.0)$
6	$\Phi\bar{\Phi}$	$\Phi-\frac{c+if}{\sqrt{2}}$	$\phi^1=0.9854$ $\phi^2=0.09409$ $\pi^1=-0.2266$ $\pi^2=-0.6254$ $c=0.07026$ $f=0.1019$	60.0	$\sim10^{-5}$	[155]	$\phi^1\in(0.0,1.0)$ $\phi^2\in(0.0,1.0)$ $\pi^i\in(-\sqrt{2},\sqrt{2})$ $c\in(0.0,2.0)$ $f\in(0.0,2.0)$

(To be continued)

Model	K	W	ICs	$N_{\rm end}$	$\omega^2_{\rm end}$	Ref	Scanned range
Poly$N$	$-3\log(\Phi+\bar{\Phi})$ $+S\bar{S}$	$S\sum_{n=0}^{N}\frac{p_n\Phi^n}{n!}$	$\phi^1=1.777$ $\phi^2=0.3429$ $\pi^1=-0.5227$ $\pi^2=-1.292$ $S\equiv 0$ $p_0=93.3$ $p_1=73.06$ $p_2=31.9$ $p_3=98.48$ $p_4=-3.389$ $p_5=57.9$ $p_6=69.24$ $p_7=-70.46$ $p_8=-85.69$ $p_9=-61.32$ $p_{10}=-19.51$ $N=10$	60.0	0.0033	-	$\phi^1\in(10^{-6},10^2)$ $\phi^2\in(-10^2,10^2)$ $\pi^i\in(-\sqrt{2},\sqrt{2})$ $p_i\in(-10^2,10^2)$ $N\in\{1,\ldots,10\}$

(To be continued)

Model	K	W	ICs	$N_{\rm end}$	$\omega^2_{\rm end}$	Ref	Scanned range
QPolyN	$-3\log(\Phi+\bar{\Phi})$ $+S\bar{S}$	$S\sum_{n=0}^{N}\frac{p_n\Phi^n}{\Phi^{N+1}n!}$	$\phi^1=1.992$ $\phi^2=-8.307$ $\pi^1=-1.233$ $\pi^2=0.9123$ $S\equiv 0$ $p_0=-27.69$ $p_1=33.45$ $p_2=27.29$ $p_3=-93.18$ $p_4=-51.78$ $p_5=23.04$ $p_6=16.54$ $p_7=67.45$ $p_8=78.78$ $p_9=38.83$ $p_{10}=58.3$ $N=10$	60.0	$\sim 10^{-4}$	-	$\phi^1\in(10^{-6},10^2)$ $\phi^2\in(-10^2,10^2)$ $\pi^i\in(-\sqrt{2},\sqrt{2})$ $p_i\in(-10^2,10^2)$ $N\in\{1,\ldots,10\}$

(To be continued)

Model	K	W	ICs	$N_{\rm end}$	$\omega^2_{\rm end}$	Ref	Scanned range
EPoly$N$	$-3\log(\Phi+\bar{\Phi})$ $+S\bar{S}$	$S\sum_{n=0}^{N}\frac{p_n e^{n\Phi}}{n!}$	$\phi^1=0.5322$ $\phi^2=15.81$ $\pi^1=-0.4712$ $\pi^2=0.1758$ $S\equiv 0$ $p_0=-3.048$ $p_1=-41.88$ $p_2=-52.78$ $p_3=97.38$ $p_4=53.4$ $p_5=75.42$ $p_6=36.84$ $p_7=73.26$ $p_8=20.15$ $p_9=32.92$ $p_{10}=36.91$ $N=10$	60.0	0.54	-	$\phi^1\in(10^{-6},10^2)$ $\phi^2\in(-10^2,10^2)$ $\pi^i\in(-\sqrt{2},\sqrt{2})$ $p_i\in(-10^2,10^2)$ $N\in\{1,\ldots,10\}$

(To be continued)

Model	K	W	ICs	$N_{\rm end}$	$\omega^2_{\rm end}$	Ref	Scanned range
Poly$N\alpha$ [1]	$-3\alpha\log(\Phi+\bar{\Phi})$ $+S\bar{S}$	$S\sum_{n=0}^{N}\frac{p_n\Phi^n}{n!}$	$\phi^1=1.735$ $\phi^2=-37.83$ $\pi^1=-0.4471$ $\pi^2=0.2346$ $\alpha=0.001984$ $S\equiv 0$ $p_0=69.23$ $p_1=-6.451$ $N\equiv 1$	60.0	16.28	-	$\phi^1\in(10^{-6},10^2)$ $\phi^2\in(-10^2,10^2)$ $\pi^i\in(-\sqrt{2},\sqrt{2})$ $\alpha\in(10^{-3},10.0)$ $p_i\in(-10^2,10^2)$
Mono$N\alpha$ [2]	$-3\alpha\log(\Phi+\bar{\Phi})$	Φ^N	$\phi^1=0.9469$ $\phi^2=10.09$ $\pi^1=-0.06989$ $\pi^2=-1.065$ $\alpha=0.9966$ $N=9.976$	60.0	1.294	-	$\phi^1\in(10^{-3},10^2)$ $\phi^2\in(0.0,10^2)$ $\pi^i\in(-\sqrt{2},\sqrt{2})$ $\alpha\in(10^{-3},1.0)$ $N\in(2.0,10.0)$

(To be continued)

[1] Although we present results for $N=1$, we searched up to $N=10$ without qualitatively different results. We also searched the similar models QPoly$N\alpha$ and EPoly$N\alpha$ (with this Kähler potential, but the same superpotentials as QPoly$N$ and EPoly$N$ respectively) and found a similarly large turning rate. As we understand from Section 4.3.5.1, the dynamics of this construction do not show a strong dependence on the structure of the superpotential in the rapid-turn regime.

[2] Note that for this example, the quoted values are barely inflationary, with an $\epsilon > 0.95$.

Model	K	W	ICs	$N_{\rm end}$	$\omega^2_{\rm end}$	Ref	Scanned range
Racetrack [1]	$-3\alpha \log\left(\Phi + \bar{\Phi}\right)$	$Ae^{-a\Phi} + e^{-b\Phi}$	$\phi^1 = 0.8386$ $\phi^2 = 64.83$ $\pi^1 = 0.1642$ $\pi^2 = 0.8657$ $\alpha = 0.9097$ $a = 0.1189$ $b = 9.857$ $A = 7.964$	17.74	$\sim 10^{-8}$	[158]	$\phi^1 \in (0.01, 1.0)$ $\phi^2 \in (0.0, 100.0)$ $\pi^i \in (\sqrt{2}, \sqrt{2})$ $\alpha \in (10^{-3}, 1.0)$ $a \in (0.0, 10.0)$ $b \in (0.0, 10.0)$ $A \in (0.0, 10.0)$

[1] Note that this is the original racetrack model without an uplifting term, which was included in [158].

Appendix C

Kasner solution for inhomogeneous cosmologies

In [192] the Kasner solution was extended, for the first time, to the inhomogeneous and anisotropic case. In this paper the authors showed that, near the singularity, this can be written as:

$$\begin{cases} dl^2 = h_{\alpha\beta} dx^\alpha dx^\beta \\ h_{\alpha\beta} = a^2 l_\alpha l_\beta + b^2 m_\alpha m_\beta + c^2 n_\alpha n_\beta \end{cases} \tag{C.1}$$

where, as in the Mixmaster model (see Sec.5.3.3)

$$a \sim t^{p_l}, \quad b \sim t^{p_m}, \quad c \sim t^{p_n}. \tag{C.2}$$

Dealing with inhomogeneous model, in this case both p_i and the reference vectors $\mathbf{l}, \mathbf{m}, \mathbf{n}$ are functions of the spatial coordinates x^γ and the Kasner indices, which in the homogeneous case have to satisfy eq.(5.65), in this case satisfy

$$p_l(x^\gamma) + p_m(x^\gamma) + p_n(x^\gamma) = p_l^2(x^\gamma) + p_m^2(x^\gamma) + p_n^2(x^\gamma) = 1. \tag{C.3}$$

The Kasner indices can be parametrized as in eq.(5.68), where, analogously to eq.(5.69),

$$u(x^\gamma) = -\frac{p_1(x^\gamma)}{1 - p_3(x^\gamma)} \tag{C.4}$$

Assuming without loss of generality $p_l(x^\gamma) = p_1(x^\gamma)$, $p_m(x^\gamma) = p_2(x^\gamma)$ and $p_n(x^\gamma) = p_3(x^\gamma)$, going from one Kasner epoch to another, the indices transform as in eq.(5.75).
The result presented in [192], was obtained from the gravitational field equations $R_{00} = 0$ and $R_{\alpha\beta} = 0$ keeping only terms with time derivatives and neglecting all of those containing spatial derivatives and, to be valid up to the singularity, required an additional constraint[1]:

$$l \cdot \nabla \wedge l = 0. \tag{C.5}$$

Eq.(C.5) reduces the number of arbitrary functions to formulate the Cauchy problem to three, one less that those needed to to deal with a general case. In [178] the authors investigated the implication of removing the constraint (C.5).
The Kasner behavior in eq.(C.1) is obtained, as mentioned above, neglecting the triadic projection of ${}^3R^a_b$ in the vacuum EE. This can be done if

$$R^l_l, R^m_m, R^n_n \ll t^{-2}. \tag{C.6}$$

These conditions can be written in terms of the 3-metric diagonal and off-diagonal projection as

$$\eta_{lm} \ll \sqrt{\eta_{ll}\eta_{mm}}, \quad \eta_{ln} \ll \sqrt{\eta_{ll}\eta_{nn}}, \quad \eta_{mn} \ll \sqrt{\eta_{nn}\eta_{mm}}. \tag{C.7}$$

These inequalities allow to write down the following conditions for the off-diagonal Ricci tensor's terms

$${}^3R_{lm} \ll ab/t^2, \quad {}^3R_{ln} \ll ac/t^2, \quad {}^3R_{mn} \ll bc/t^2. \tag{C.8}$$

Therefore, if it is true that we can neglect the off diagonal term in the metric projection, it is possible to neglect the off diagonal component of the Ricci tensor in the EE.
Finally, computing the diagonal terms ${}^3R^l_l, {}^3R^m_m, {}^3R^n_n$, these show the following

[1]Without this condition, if $p_l(x^\gamma) = p_1 < 0$, the Kasner dynamics ceases to be valid for $t \to 0$.

proportionality:

$$ {}^3R^l_l \propto k^2a^4/(\Lambda^2t^2), \quad {}^3R^m_m \propto k^2b^4/(\Lambda^2t^2), \quad {}^3R^n_n \propto k^2c^4/(\Lambda^2t^2) \tag{C.9} $$

where $\Lambda = abc$ and $1/k$ denotes the order of magnitude of spatial distances oever which the metric changes.
Hence, eq. (C.6) give the following inequalities

$$ a\sqrt{k/\Lambda} \ll 1, \quad b\sqrt{k/\Lambda} \ll 1, \quad c\sqrt{k/\Lambda} \ll 1 \tag{C.10} $$

which are the *sufficient* conditions for the existence of the generalized Kasner solution (C.1). It is important to notice that these conditions do not impose *any* restrictions on the degree of the spatial inhomogeneity.
When, for $t = t_r \to 0$, one of the above condition does not old anymore (for example $a|_{t=tr}\sqrt{k/\Lambda} \sim 1$) the Kasner solution, as in homogeneous model (see Sec5.3.3), it is not valid anymore, and in the EE it is necessary to take into account perturbation terms, which are the analogous of those appearing in eq. (5.72) on the rhs.
In the case chosen above, in which the perturbation is on the l direction, the equations for the Ricci tensor become

$$ -R^l_l = \frac{(\dot{a}bc)\dot{}}{abc} + \frac{\nu^2}{2b^2c^2}a^2 = 0 \tag{C.11} $$

$$ -R^m_m = \frac{(a\dot{b}c)\dot{}}{abc} - \frac{\nu^2}{2b^2c^2}a^2 = 0 \tag{C.12} $$

$$ -R^n_n = \frac{(ab\dot{c})\dot{}}{abc} - \frac{\nu^2}{2b^2c^2}a^2 = 0 \tag{C.13} $$

$$ -R^0_0 = \frac{\ddot{a}}{a} + \frac{\ddot{b}}{b} + \frac{\ddot{c}}{c} = 0 \tag{C.14} $$

where ν is no longer a constant, but a function of the space-coordinates

$$ \nu(x^\gamma) = \frac{l \cdot \nabla \wedge l}{l \cdot [m \wedge n]}. \tag{C.15} $$

The system of equation obtained, eq.(C.11), is a system of ordinary differential equations respect to time. The space coordinates enter *only* parametrically, hence

the solution is not affected by this change, and also in the inhomogenous model it remains valid the law of alternation of the Kasner exponents.

Appendix D

Internship

In this Section we briefly summarise some of the work done during the industrial placement at Mobileum.

D.1 What is a GT?

A Global Title (GT) is an address used in a telecommunication protocol to route signaling messages on telecommunications networks. It is a unique identifier of each physical component of the network.
Whenever a person sends an SMS, starts a call or browses the internet, his mobile device exchanges an enormous amount of encrypted messages with the network to ensure that all these actions can be done and are done in the right way. All these encrypted messages contain the GT number of both the network's part which sends *and* which receives the messages.
To clarify this idea we can use a practical example. In Fig.D.1 we show the Location Update procedure, which is done by our mobile phone every couple of minutes (or every time we send a message or do a call).

Every arrow in the Fig.D.1 is an encrypted message sent by a GT to another GT.
But why do we care so much about GTs and the way they encode their messages? Learning how to recognize a legitimate encoded message from a "fake" one would prevents numerous hackers' attacks! It is quite common in fact that hackers try

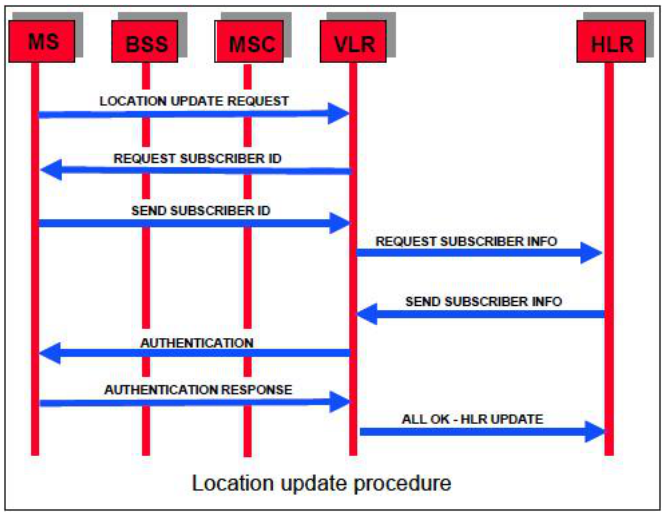

Figure D.1: How the Location Update procedure is performed. Each arrow is an encrypted message sent from a GT to another. MS, VLR and HLR are the three GTs involved in this exchange. MS is the subscriber.

to infiltrate into the telecommunication networks to try to steal sensitive data. For example, returning to the example above, if an hacker pretends to be the GT named VLR, he would be able to receive from HLR all the data of the subscriber.

D.1.1 Encoding of messages

The encoding of a signalling message is split into several layers. Here we decided to split the layers into two groups:

1. **Group 1**: features that change over the short life of the message from source to destination. They are *rigidly* defined, therefore all the GTs have to encode these according to the same protocols.

2. **Group 2**: these features are constant over the life of a message. In this case different GTs can encode them in slightly different ways, i.e. there is a possibility for ”individual expression”.

If we examine the features in Group 2, we further see that there are 4 classes of features:

1. *Application meaningful data* – e.g. IMSI, MSISDN, Calling Party, Called SSN. These are useful fields for the application (whether it is an SEP or STP)

2. *Protocol level data* – e.g. TCAP OTID, Calling Party Encoding Scheme, Application Context Name and Version, TCAP invoke ID. These are explicit parameters in the message but used for decoding the message correctly. They are of no real interest to the end application.

3. *Low level encoding data* – e.g. type of TLV tag encoding, type of TLV length encoding, order of SCCP mandatory parameters, use of XUDT, use of SCCP class. These are hidden in most decodes of a message.

4. *Statistical data* – e.g. length of SCCP over time, length of TCAP User Info over time. These features are numeric and so are possibly treated with stochastic methods.

The first layer is what the hacker wants to fake; he also has to make sure that layers 2 and 3 are sufficiently correct to transmit the message across the network. 4 is observable over a sample.

In Fig.D.2 we report an example of an encoded message (it's only a part of the full message). Each couple of bit has a specific meaning and represents a layer of the message. The one highlighted in this case is the GT identifier of the network component which is receiving the message. Note that in the following

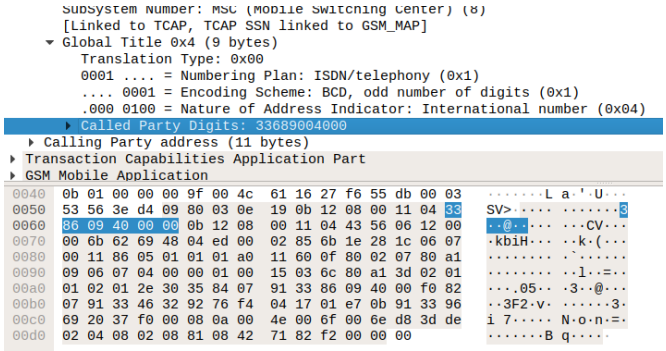

Figure D.2: Example of an encoded message using Wireshark.

we refer to these messages' layers as features.

The encoding method of these messages is defined in ITU X.690 ASN.1. The TCAP layer in particular, which is in the *protocol level data*, consists of a hierarchy of tag-length-values (TLVs) and it is described as a hierarchy because each value can itself consist of other TLVs. A TLV construction is a byte array which contain a tag indicating the role of the parameter (called *identifier*), a *length* specifying the tag's length in bytes and the *values* itself, which is the parameter of interest. The *tag* and the *length* values reveal, indirectly, some elaborations of encoding, hence they can be important as well.

The tag can be encoded with specific bits set, to mean different things:

1. If bit 6 is set, the tag is treated as a constructor, otherwise is treated it as a primitive.

2. If tag < 31, the tag is treated as short form, so bits 1-5 define the tag.

3. If tag bits 1-5 > 30, the tag is treated as long form and subsequent bytes are needed to define the tag.

A constructor does not have much value or use. It just means that there is a group of TLVs following. A primitive however is a useful thing: it is an important parameter, such as an IMSI (international mobile subscriber identity, it identifies uniquely every user of a cellular network). Programmers of stacks can decide whether to use constructors or not. Some use them a lot, others not at all.

Once the tag has been decoded, we move onto (typically) the second byte, to get the length:

1. If bit 8 == 0, the length is in short form, i.e. the length occupies this byte only

2. If bit 8 == 1 and bits 1-7 != 0, the length is long form, i.e. the length is given over multiple following bytes, all connected to make a more capacious integer.

3. If bit 8 == 1 and bits 1-7 are 0, the length is given in indefinite form. If this is the case, no length is given.

The enormous flexibility here has allowed some advanced hackers to manage to hide shellcode in messages to attack the signalling stacks directly.
However, this flexibility is also useful for us, because it requires programmers to make choices, and many of those choices are visible in the coding of the message.

D.1.2 Purpose of the study

The question we hope to answer is: can we use all this information to judge whether a message is really coming from a specific GT and not from an hacker? In other words, can we "fingerprint" a message from a GT?
We hope that, if this is the case, we are able to discern between real GT's signalling messages and messages sent by hackers who "fake" to be a GT and aim to interfere in the telecommunication networks.

A *perfect fingerprint* is a pattern of features that:

- is forever always present in the encoding of messages from a GT.
- is never seen in messages from other GTs

We immediately concede that in this analysis we are likely to see, instead, *families of GTs* which present the same fingerprint because they are written by the same programmer.
Therefore, in our study we are likely to see families of GTs, each sharing the same fingerprint.

An *anomaly*, on the other hand, has two meanings here:

- A message from a GT that has some outrageous values for various features, as in a specially crafted packet by an advanced hacker. E.g. suddenly seeing a value of 100 for $tcap - user - info - len$ when normally its value is 0.
- A message that looks normal within the entire sample of all GTs, however, is clearly written in a different style to the usual one for that specific GT.

This distinction caused confusion for about half the study because different approaches can be taken to each. While both can be approached by unsupervised learning, classifiers, and statistical analysis, the second one can also be

approached with supervised learning, and this ultimately gave superior results, as we show later.[1].

During the internship our main goal has been to use Machine Learning algorithms to understand if different GTs could be clustered into families, hence they do encode messages in a similar way, and to train "anomaly detectors" which aim was to isolate anomalous messages among a dataset.
All the studies have been conducted on datasets containing messages sent by numerous GTs.

In the following we describe the final part of the data analysis carried out during the placement.

D.2 Data analysis - First part

The dataset used for this analysis is `data_original`, and it comprises of 86030 messages (rows) sent from 6001 different GTs, and 56 features (columns) which are both numerical and categorical. These features represent some of the couple of bit present in Fig.D.2. The features' selection has been done by Mobileum's engineers.
We are not going in detail about the different features, however it is worth mentioning the following ones: `op_code` and the pointers `p1`, `p2` and `p3`. As mentioned above each GT sends encrypted messages for a variety of reasons: `op_code` encodes the "reason" for the relative message.
This is important because one of the assumption we do is that each GT encrypts messages with the same `op_code` in the same way.
We comment on the importance of `p1`, `p2` and `p3` later in the study.

D.2.1 Statistical analysis

The first step is to manipulate the dataset such that it contains only *numerical* features: this allows us to do some basic statistical analysis on it.
The dataset with only numerical feature is referred to as `data_num`. From Fig.D.3

[1] Another important problem faced during the project was to understand how to correctly identify the important features (i.e. layers) in a .pcap message, see Fig.**??**.

we can see that none the numerical features seem to follow any evident distribution. Applying a PowerTransform function to the dataset, which applies a power

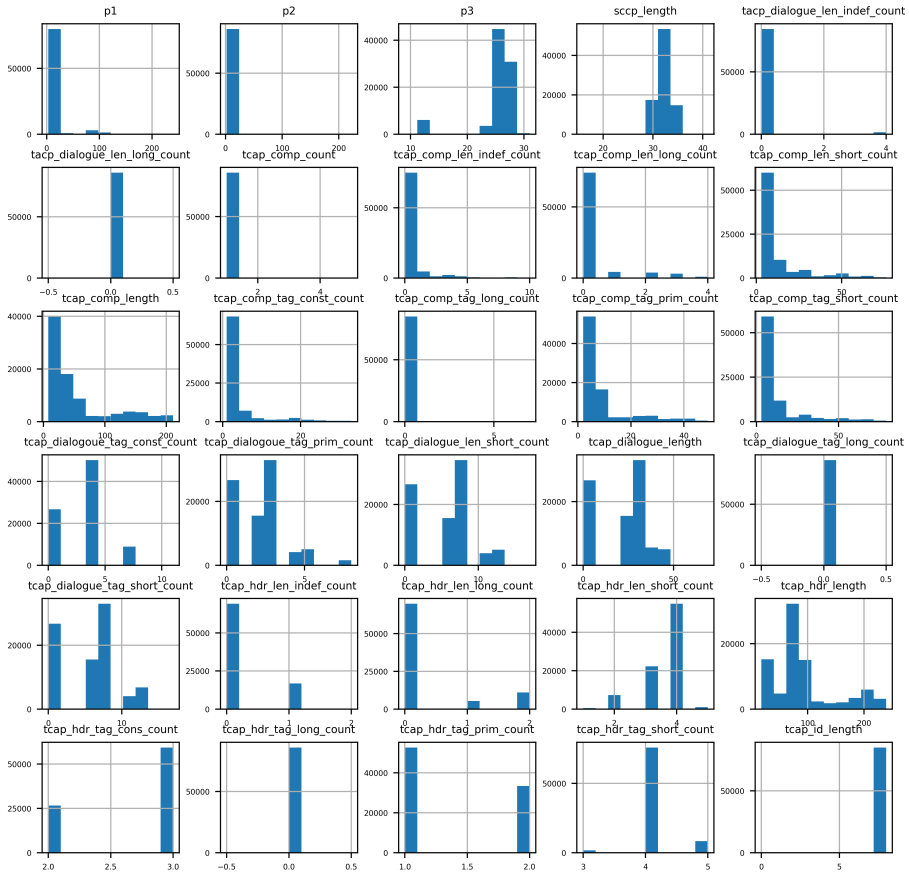

Figure D.3: Histograms representing the distribution of the numerical features of `data_num`.

transform featurewise to make data more Gaussian-like, we obtain the histograms in Fig.D.4

Also in this case, after "forcing" the data to assume a gaussian distribution, the features cannot be considered gaussian at all and it seems that there is no

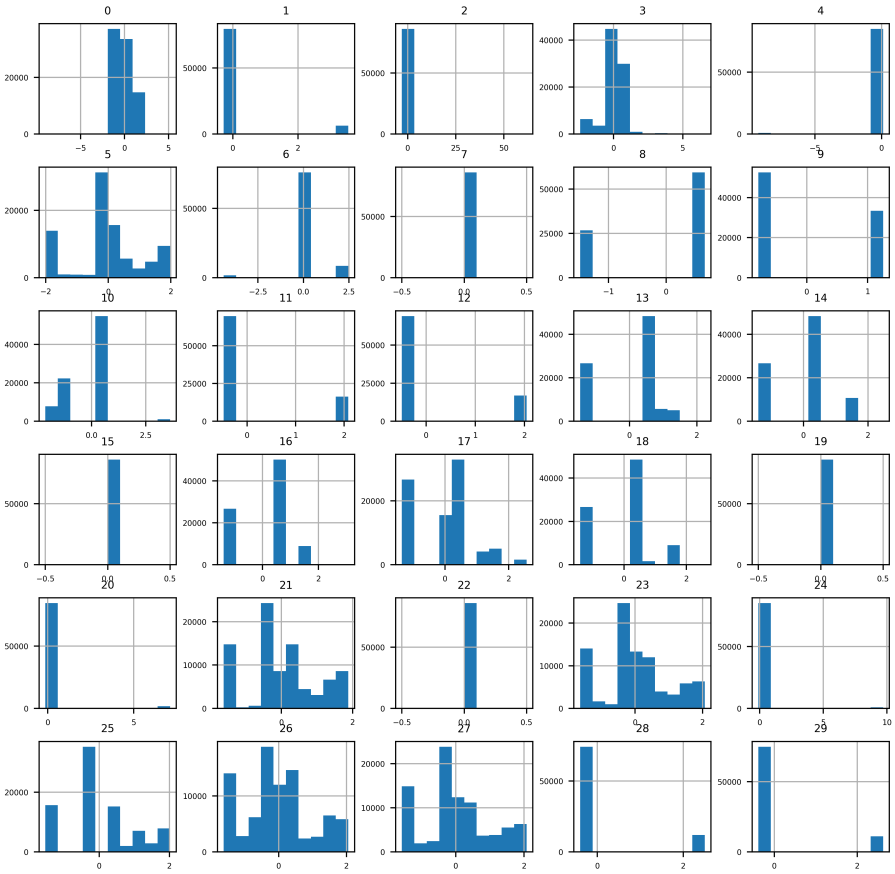

Figure D.4: Histograms representing the distribution of the numerical features of `data_num`. Note that the title of the single picture is not a feature name anymore since the *powertransformation* modifies the features themselves.

hidden correlation among the features. Hence a more in depth analysis is necessary.

D.2.2 Can we talk about GTs' families?

In this section we try to give an answer to the question introduces above *Can GTs be clustered into families?*

Correlation

Knowing, as showed in the previous subsection, that the numerical features do not follow any specific distribution, the first step to answer this question is to understand if there is any correlation among the different features.
The *correlation* is a statistical parameter used to determine when a change in a variable causes a change in another variable, therefore we aim to understand if there is any dependence among some of the features.
Correlation can be computed only for the numerical features and its most common formulation, the Pearson one, is given by:

$$\rho_{X,Y} = \frac{cov(X,Y)}{\sigma_X \sigma_Y} \tag{D.1}$$

where X and Y are the considered features, $\sigma_{X/Y}$ is the standard deviation of X or Y and $cov(X,Y)$ is the covariance matrix.
In our case, however, we decide to use the Spearman correlation. In fact, Pearson's correlation assesses only linear relationships, while Spearman's correlation assesses monotonic relationships (whether linear or not) hence it is more general.

The correlation matrix has been plotted using the `seaborn` package. We computed the correlation matrices for 4 different GTs (we only used GTs for which we have more than 500 messages in order to have a good sample size) and we plotted the results obtained on a heatmap; colors on the map indicate the value of the correlation among two particular features. The heatmaps can be found at the end of the document, in Sec.D.6.

Each line and each column refers to a numerical feature, and the values in the squares represent the correlation value among the 2 features intersecting in that square. A value ~ 0 indicates that there is almost no correlation among the features for that GT, while a value ~ 1 (or ~ -1) indicates that the features are

highly correlated (or anti-correlated).
All the heatmaps present some blank rows/columns; this represent features which present only one value for a specific GT.
Looking carefully at the different heatmaps, it is possible to notice that two of them are more similar than the others. In particular, the correlation matrices for $GT = 351930000133$ and for $GT = 351930000433$ (Fig.D.29 and Fig.D.31) are almost identical, while they present more differences with the correlation matrix of $GT = 22376000066$ (Fig.(D.28)) and of $GT = 447937113433$ in Fig.(D.31).
This suggests that it might actually be possible to cluster GTs into families, since some of them present a similar behavior. In particular $GT = 351930000133$ and for $GT = 351930000433$ might belong to the same family.
We only presented four heatmaps here, but plotting heatmaps for other GTs we had confirmation of this hypothesis.

Clustering algorithms

To confirm the idea that GTs can be grouped into families, we use the DBSCAN and KMeans algorithms on a new dataframe built starting from the correlation values. [1].
We construct the new dataframe considering only the GTs for which we have more than 50 messages each. Moreover, for each of these GTs, we compute the correlation matrix, as explained before, which returns a $30x30$ matrix[2]. We then transformed this 2D matrix in a dataset's raw (hence we transformed the matrix in a 1 dimensional array).
The final dataset, `correlation`, contains 365 entrances with 901 of features: one is the GT identifier, while 900 derive from the correlation matrix.
As said previously the correlation matrices contain null values when a certain features remain constant for all the dataset; eliminating these constant features, `correlation` comprises of "only" 717 features.
After a little bit of data manipulation we reduce the number of features implementing a Principal Component Analysis (PCA) algorithm. We go from 717 to

[1] We implemented both the clustering algorithms using *scikit-learn* methods and functions in python.
[2] There are 30 numerical features in `data_original`

only 12, after proving that these 12 features explain the 95% of variance in the dataset.
Now we can apply the KMeans and DBSCAN clustering algorithm.
Let us start with the KMeans algorithm.
The most important hyperparameter to set when using this algorithm is the number of clusters (k) that we want our data cluste into. This is also the only one we actively focus on during this study while we leave the other hyperparameters with their default values.
To choose a correct number of clusters to fit the data we use both the elbow method and the silhouette method. We fit the KMeans algorithm on the data 19 times, each time setting a different number of clusters (from 2 to 20). Both the mentioned methods give the best results when the number of clusters is 8.
Therefore, we chose $k = 8$ for KMeans, and running the algorithm on `correlation`, this assigns a *label* to each GT. The assigned label identifies the cluster (or family) to which the GT belongs to.

We use the DBSCAN algorithm to check the labels assigned by the KMeans method.
DBSCAN does not require the number of clusters as hyperparameter, differently from KMeans, but it requires the parameter ϵ, defined as "the maximum distance between two samples for one to be considered as in the neighborhood of the other".
To provide a reasonable value for ϵ we compute the distances in the 12 dimensional features space among the GTs data point, and we chose an ϵ value compatible with them, in particular $\epsilon = 5$.
As for the KMeans method, we use the default values for the other hyperaparameters.
Fitting the data using DBSCAN, we obtain a second set of *labels* for each GT. The biggest difference between KMeans and DBSCAN is that the latter does not assign all the data to a cluster; thus not all the GTs are labelled using this algorithm. In this case we manually set the GT's label as -1.
We report part of the results obtained in Table 1.

GT	Label KM	Label DB	GT	Label KM	Label DB
22899999797	6	0	34656000213	0	1
351930000433	6	0	22376000066	0	1
351930000133	6	0	41789310321	1	2
41789310020	0	1	41789310311	1	2
41789310003	0	1	34656027000	6	0
41789310204	0	1	34656000212	0	1
41789310206	0	1	22507939831	0	1
33689002650	4	2	22376000067	0	1
33689002190	4	2	34656000243	0	1
33689002620	4	2	41789310312	1	2
34656000233	0	1	22507939832	0	1
41789310205	0	1	22507939833	0	1
34656000235	0	1	22376000064	0	1
34656000226	0	1	3519330000111	1	3
34656000216	0	1	351930003441	5	4
41789310322	1	2	34656073000	6	0

Table D.1: GTs' labels obtained running KMeans and DBSCAN.

We can see from this table that in most cases the two clustering algorithms agree on the which GTs belong to the same cluster.
This is a further proof which supports the idea that there are different GT's families.

To provide a visual interpretation of the results obtained, we encode the messages sent by the GTs in color boxes, as in Fig.D.5.

We refer to particular square as [number of raw, number of columns].
Square [5,5] (in yellow in the example plot Fig.D.5) does not contain any information, and it has been added to set the color scale; similarly [5,0], [5,1], [5,2] and [5,3] are manually set to 0.
Square [5,4] is probably the most important: it encodes the feature `op_code` (hence which type of message is the one analysed). All the other squares, in order from [0,0] to [4,5], represent numerical features[1].

In the following we present 20 color boxes (i.e. 20 messages) for 4 different

[1]to provide this graphical encoding, we scaled and normalized the data.

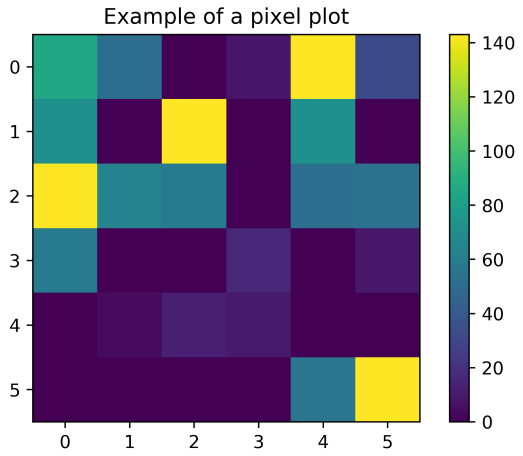

Figure D.5: Colour box example of a random message sent by $GT = 22899999797$

GTs and 2 different values of `op_code`. Two of these GTs have been classified as belonging to the same clusters by both KMeans and DBSCAN, see Table 1, while the others belong to different clusters. From the plots we can see how GTs belonging to the same cluster encode the same type of messages (messages with the same `op_code`) almost always in the same way.
The GTs selected for these plots all sent messages with operation code = 56, and three of them send also messages with operation code = 2.

The GTs which belong to the same family, GT=22899999797 and GT=351930000133, present the same sort of patterns for the messages they sen, see Fig.D.6 and Fig.D.7 while both the others GTs show different patterns (they share some, but some are different), see Fig.D.8 and Fig.D.9.
The same kind of study can be done for the same GTs but a different operation code, in particular, `op_code` = 2.

Also in this case GT = 22899999797 and GT = 351930000133 show the same pattern, see Fig.D.10 and D.11 while GT = 41789310204 shows a different one, see Fig.D.12. It was not possible to show GT = 351930003441 since it sent less than 20 messages with operation code = 2.

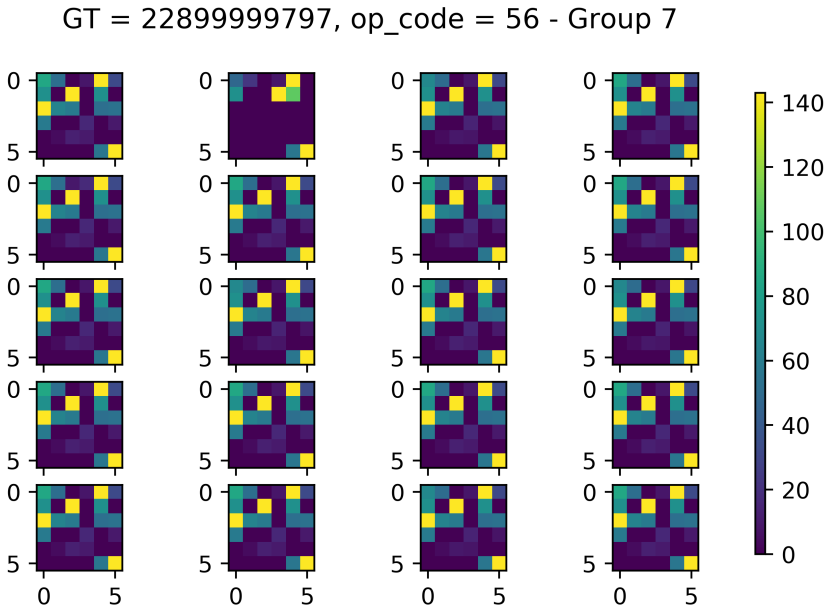

Figure D.6: Colour boxes for GT = 22899999797 and operation code = 56

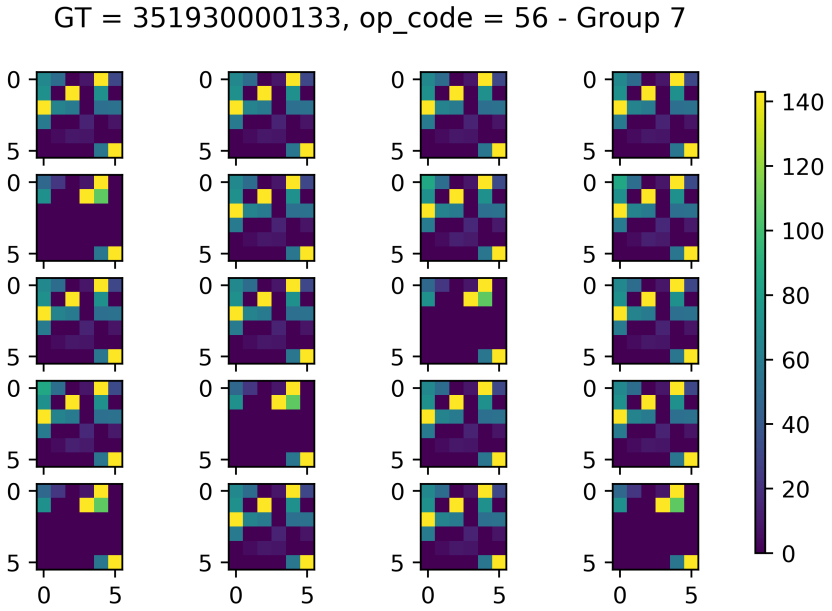

Figure D.7: Colour boxes for GT = 351930000133 and operation code = 56

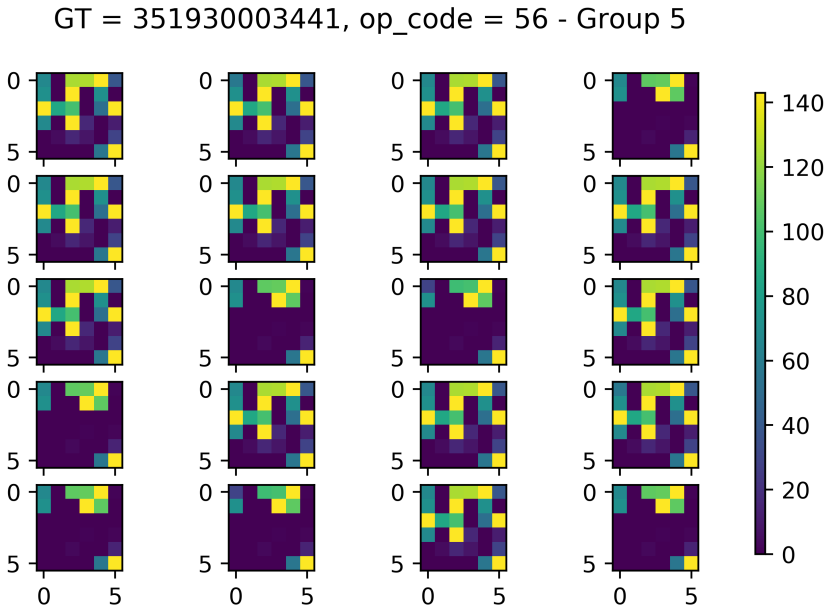

Figure D.8: Colour boxes for GT = 351930003441 and operation code = 56

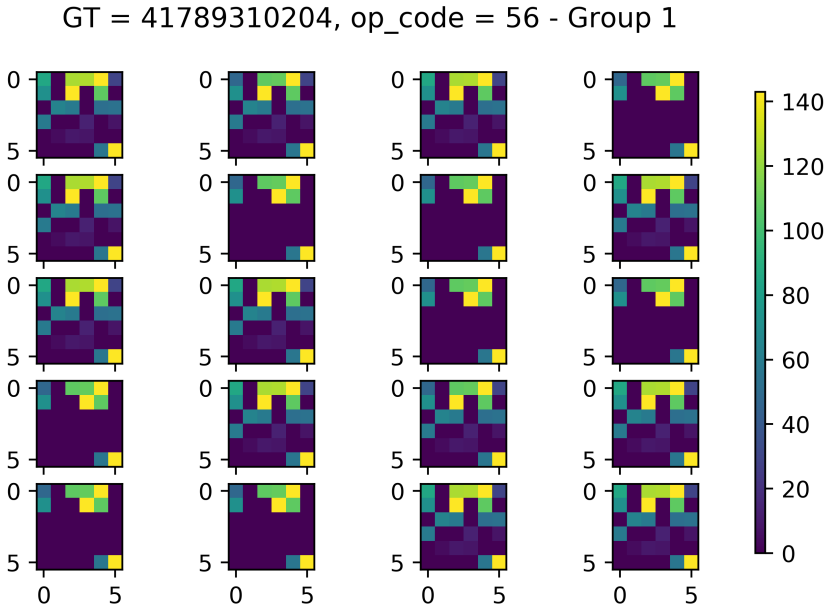

Figure D.9: Colour boxes for GT = 41789310204 and operation code = 56

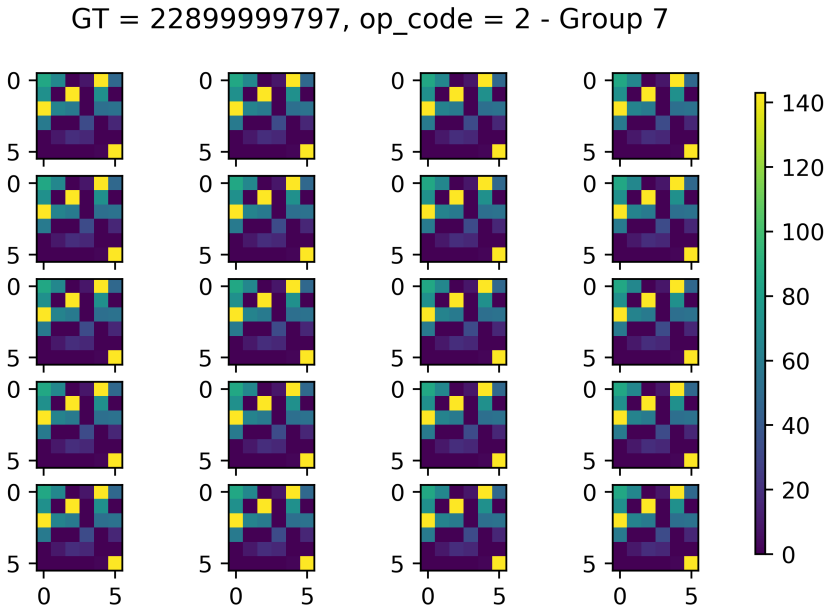

Figure D.10: Colour boxes for GT = 22899999797 and operation code = 2

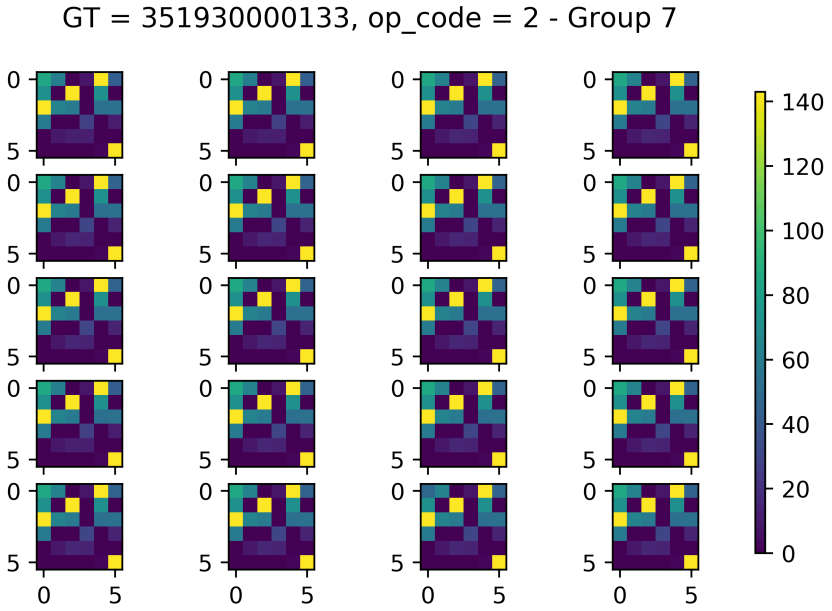

Figure D.11: Colour boxes for GT = 351930000133 and operation code = 2

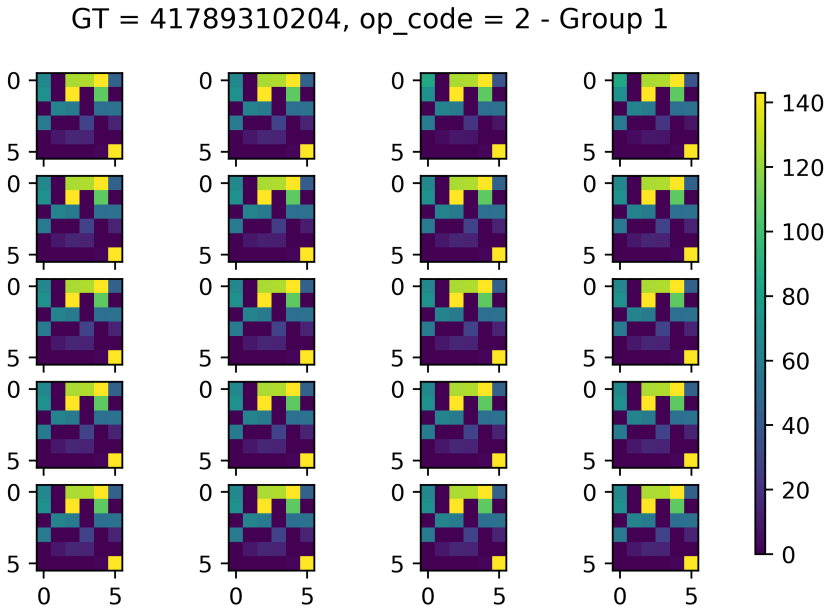

Figure D.12: Colour boxes for GT = 41789310204 and operation code = 2

D.2.3 Is a GT always consistent within itself?

Using the same colour box graphs used in the previous subsection, we want to examine how many patterns a single GT uses to send messages with the same op_code.

The plots presented in the previous subsection, Fig.D.6, Fig. D.7, Fig. D.8, etc.., show how these GTs are consistent in the way they encode messages with the same `op_code`: all the 20 color boxes look very similar among them.

As an additional proof, we chose a different GT which sends mostly messages with different operation code and analyse its "color boxes". We chose GT = 33689002190 and operation code = 7,3.

Also in this case we can see that the 20 messages sent are encoded in incredibly similar way.

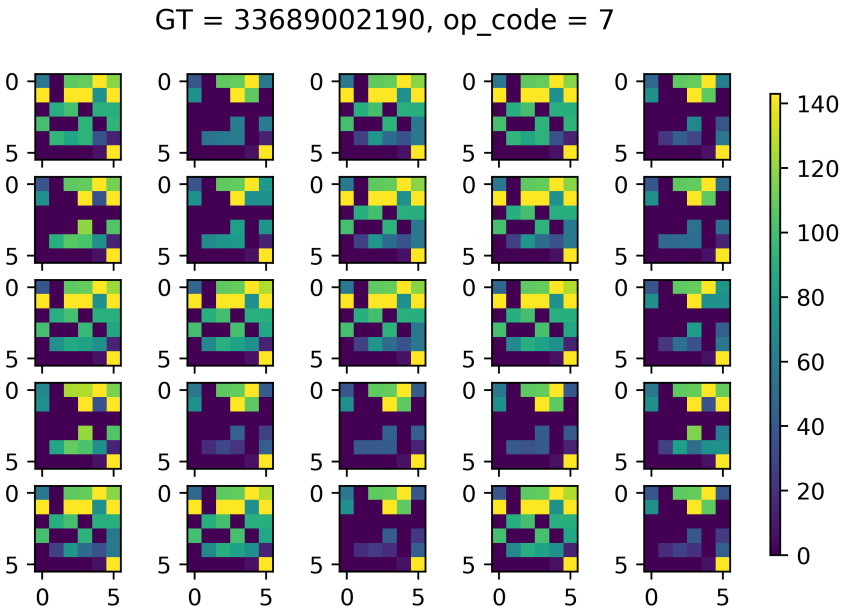

Figure D.13: Colour boxes for GT = 33689002190 and operation code = 7

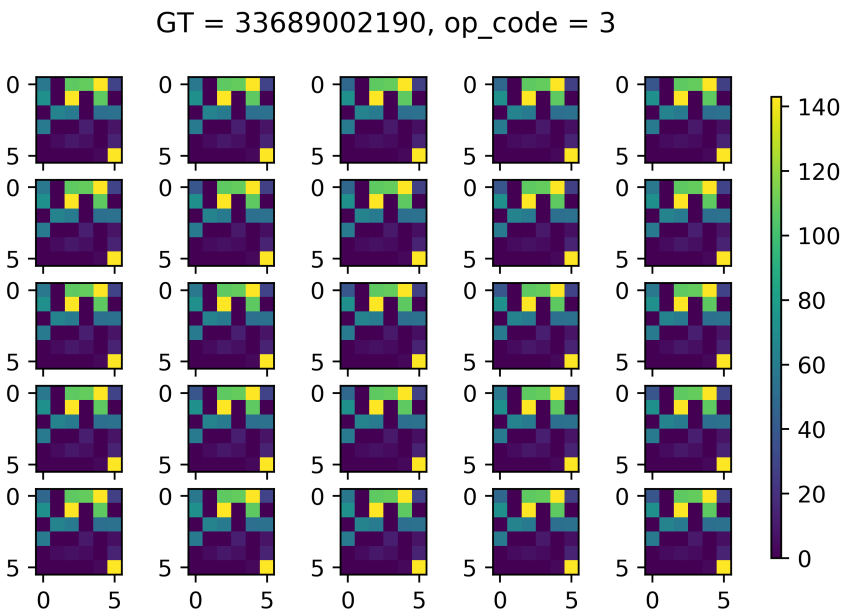

Figure D.14: Colour boxes for GT = 33689002190 and operation code = 3

D.3 First Outlier study

In this section we present the first study we carried to study and analyse possible outliers. This study is done on the dataset *1515155608A*

In this case we transform the values of `op_code` into a numerical feature (in fact even if its value is a number, it is a categorical feature since each value represents a type of message). To do that we use the `get_dummies` method which realizes a one hot encoding; the feature (`op_code` in this case) is encoded using a dummy encoding scheme that creates a binary column for each category and returns a sparse matrix or a dense array (depending on the sparse parameter). Here is a small example:

GT	`op_code`
22899999797	56
351930000433	2
351930000133	56
41789310020	23

→

GT	op_code_56	op_code_2	op_code_23
22899999797	1	0	0
351930000433	0	1	0
351930000133	1	0	0
41789310020	0	0	1

We focus our attention on 12 GTs, each of which sent more than 500 messages. The dataset containing only these 12 GTs and the numerical features is called `data_num`.

`data_num` is composed of 7509 total messages (rows) and 73 features (columns). We, again, apply a PCA algorithm to `data_num` reducing the number of features to 2 and 3. The dataset created are, respectively `data_num_PCA2` and `data_num_PCA3`. This allows us to represent the messages in a 2D and 3D space.

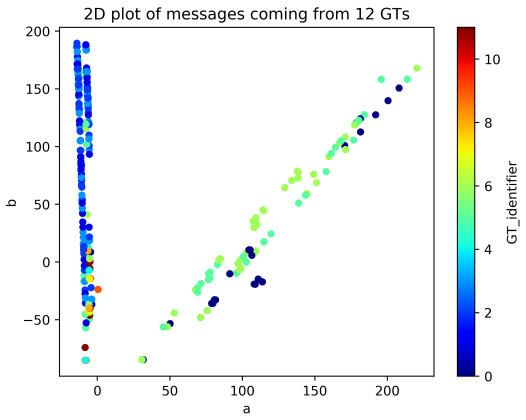

Figure D.15: In this plot we present a plot of the data in `data_num_PCA2`. a and b are the features obtained from the PCA reduction. The different color of the points represents different GTs.

It is worth mentioning that, even if this dimensional reduction induces a substantial change of dimension in the feature space, the new features (a and b in the 2D case, a, b and c in the 3D case) account for the 90% (and above) of variance among the data, hence we are quite confident that the results obtained in these reduced spaces are general enough.

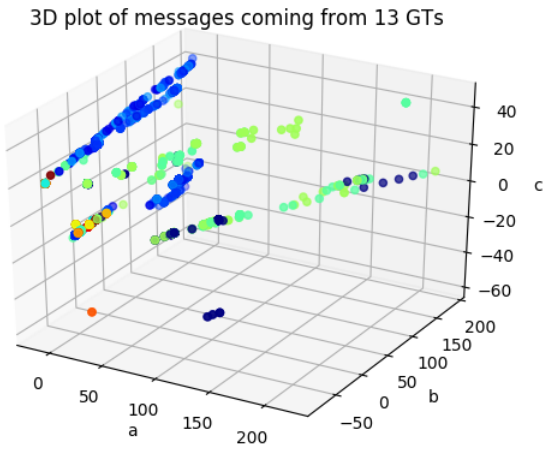

Figure D.16: In this plot we present a plot of the data in `data_num_PCA3`. a, b and c are the features obtained from the PCA reduction. The different color of the points represents different GTs.

Looking at Fig.D.15 and Fig.D.16 we can see that messages sent by some GTs lie consistently on the same line, while messages sent by different GTs can lie on different lines. An example of this are GT_identifier 0 (dark blue) and GT_identifier 3 and 4 (lighter blue). We can see that they lie on total different line (Fig.D.15) or, better, on total different planes (Fig. D.16).

In the following we are going to use this information to create a dataset which can be used to train an anomalies detection ML algorithm.
The idea is to build a dataset containing messages coming from 2 GTs which lie onto different planes (which we call GT1 and GT2), and to consider messages coming from GT1 as "normal" and messages coming from GT2 as "outliers" (respect to those sent by GT1).
To realize this dataset we follow the following steps:

- We define GT1 = GT = 22899999797 (GT_identifier = 0) and GT2 = GT = 33689002620 (GT_identifier = 2).
- From `data_num_PCA3` we extract 5% of GT2's messages and we add them

to a dataset comprising only of the messages sent by GT1; in this way we create a dataset which contains 5% of outliers.

The final dataset `data_num_PCA3_outlier` is composed of 760 rows, 38 of which are outliers, and 4 columns (one contains the GT number, the other three are the a, b and c features obtained using the PCA).

To try to solve the outlier problem, thus to correctly identify as outliers the 38 messages sent by GT2, we use the *Isolation Forest* (IF) algorithm.
The IF algorithm used is the built-in algorithm in the *scikit-learn* package.
We set the hyperparameters for this algorithm as following:

```
RANDOM = 42

#isolation forest
is_for = IsolationForest(max_samples = 256,
contamination = 0.05, max_features = 1, n_estimator = 100,
random_state = RANDOM )
```

where

- *max_samples*: in the original paper it has been defined as *min(256,n_samples)*. Here it has been choose as 256.
- *max_features*: it is the number of features to drawn from the train dataset to train each base estimator. Its default value is 1.
- *n_estimator*: it is the number of base estimator in the ensemble. Its default value is 100.
- *contamination_rate*: it is defined as *n_outlier*/total_data; in this case it is 0.02.
- *random_state* : it controls the pseudo-randomness of the selection of the feature and split values. I fixed it to be *random_state* = RANDOM.

Note that we fixed *random_state* to guarantee the reproducibility of the results. The IF is an unsupervised learning algorithm, therefore we removed the GT column from the data before running the algorithm, but we use this information to check the accuracy of the results. The confusion matrix obtained using IF is

$$c_X = \begin{bmatrix} 16 & 22 \\ 22 & 700 \end{bmatrix}$$

The IF recognizes as outlier 16 of the 38 outliers present in the dataset, and it wrongly classifies as outlier 22 of the 760 legitimate messages.

D.4 Second outliers study

In this section we describe a study realized on 2 datasets, namely *1515155608A*, the same used in the previous section with 86030 messages and *1482233452_722272*, with more than 1 million messages. Both of them contain the same features described above.
Also in this study we aim to use the IF algorithm to detect outliers in both the datasets.

In this section we focus on the following features: *p1*, *p2* and *p3* which show an important correlation in both datasets. This can be seen in Fig.D.17 where we present a small sample of 1515155608A.

frame	GT	op_code	sccp_type	sccp_length	sccp_class_handling	p1	p2	p3	sccp_called_address_indicator	sccp_calling_address_indicator	...
89964	351930000133	2	9	35	81	108	2	13	12	12	...
62183	41789310205	56	9	31	80	3	14	25	12	12	...
54649	34656000233	56	9	30	81	3	14	25	12	12	...
28449	41789310206	56	9	31	80	3	14	25	12	12	...
36216	351930000133	56	9	33	81	86	2	13	12	12	...
59707	41789310020	56	9	35	80	3	16	27	12	12	...
80538	33689002650	7	9	32	1	3	14	25	12	12	...
134835	41789310206	56	9	35	80	3	16	27	12	12	...
148518	34656000233	67	9	32	81	3	16	27	12	12	...
43973	33689002620	3	9	30	81	3	14	25	12	12	...
75792	41789310205	56	9	31	80	3	14	25	12	12	...
112830	41789310205	56	9	31	80	3	14	25	12	12	...
88275	351930000133	56	9	31	81	40	2	13	12	12	...
128335	351930000133	56	9	33	81	3	15	26	12	12	...
40063	22899999797	56	9	35	81	88	2	13	12	12	...

Figure D.17: Small sample of data from 1515155608A . It is possible to see a pattern for $p1$, $p2$ and $p3$.

Studying the data closely, we identified two main patterns:

1. When `p1` = 3, `p2` and `p3` vary, but they remain correlated. In particular, if `p2` = 14 → `p3` = 25, if `p2` = 16, `p3` = 27, if `p2`= 16, `p3` = 27.

2. If `p1` ≠ 3, hence it varies, `p2` and `p3` are always related (e.g. `p2` = 2 → `p2` = 13).

As a consequence the pointers values can be easily predicted, which makes easier to detect a "suspicious" pointer's value.

In both datasets, we add two features depending on the pointers values:

1. `p_order`: This is a categorical feature that expresses the numerical order of the pointer, i.e if: `p1` = 3, `p2` = 14, `p3` = 27, `p_order` = 123.

2. `pointers_PCA`: we apply the PCA analysis to `p1`, `p2`, `p3` in order to "collect" them in only one feature, which is a numerical feature.

As mentioned at the beginning, the main purpose of this section is to study how to implement and optimize the IF to detect outliers, however both the 1515155608A and 1482233452_722272 are "outliers free", since they only contain legitimate messages, hence we introduce some[1].

Once the anomalies are introduced we create 5 different sets of data which differ for the features they contain.
In particular:

1. *X*: it contains `p1,p2,p3` and `p_order`, plus all the features not related to the pointers' values.

2. *X2*: it contains only `p1, p2, p3`, plus all the features not related to the pointers' values.

3. *X3*: it contains only `p_order`, plus all the features not related to the pointers' values.

[1]In doing so we kept in mind that the number of anomalies in a dataset has to been very small compared to the total number of instances (in the previous section we used 5% of contamination in a valid dataset).

4. *X4*:it contains only `pointers_PCA`, plus all the features not related to the pointers' values.

5. *X5* : it contains both `pointers_PCA` and `p1,p2,p3`, plus all the features not related to the pointers' values.

Before entering in the details of the study of both the datasets, we briefly summarize the steps we are going to take:

1. We select a single GT from the dataset and we reduce the initial dataset to messages sent *only* by this GT.

2. We manually modify a small portion of this new dataset to create outliers.

3. We transform `op_code` and `p_order` in numerical features using the `get_dummies` method.

4. We manipulate and preprocess the data scaling them.

5. We implement the IF algorithm and report the results.

6. We optimizing the IF algorithm's hyperparameters.

D.4.1 Analysis on 1515155608A

For this dataset, we chose the following GT:

$$GT = 33689002650 \qquad n_{counts} = 557 \tag{D.2}$$

where n_{counts} is the total number of the GT's messages present in the dataset. This GT's `p1`'s value is always `p1`= 3, hence, from what we said above, we expect a certain correlation among `p2` and `p3` as follows:

1. $p1 = 3$, $p2 = 14$, $p3 = 25$ in 531 cases.

2. $p1 = 3$, $p2 = 16$, $p3 = 27$ in only 2 cases.

3. $p1 = 3$, $p2 = 13$, $p3 = 24$, in 24 cases.

We decide to create outliers in two different ways:

1. We abruptly change the pointers' values , so that the pointers order changes as well.

2. We slightly change the pointers' values, so that the modifies values are similar to the original ones. In this case the pointers order does not necessarily change.

Random changing of the pointers values

Here we modify randomly some pointers' value. In particular, we modify 12 data out of a total of 557 as shown in Fig.D.18b creating the new dataset `data_num_outlier`. This dataset contains the 12 anomalies and 545 normal inputs. In Fig.D.18a we present some of the original data.

frame	GT	sccp_length	p1	p2	p3
1846	33689002650	32.0	3.0	14.0	25.0
2730	33689002650	31.0	3.0	14.0	25.0
2934	33689002650	32.0	3.0	14.0	25.0
2939	33689002650	32.0	3.0	14.0	25.0
3238	33689002650	32.0	3.0	14.0	25.0
3388	33689002650	32.0	3.0	13.0	24.0
3502	33689002650	33.0	3.0	14.0	25.0

(a) Small sample of the GT's original pointers values.

frame	sccp_length	p1	p2	p3
53664	31	118	2	24
10985	32	34	2	12
169695	32	30	3	25
169689	32	33	2	11
169527	32	46	2	10
145486	30	18	1	1
180822	32	21	3	37
5739	31	37	2	13
129308	32	30	20	1
78088	31	75	2	13
133408	30	45	45	100
75154	30	10	65	2

(b) Modified pointer's values.

Figure D.18: Example of original and modified pointers' values for 1515155608A.

Plotting the values of the three pointers in a 3D space for all the instance in `data_num_outlier`, we obtain Fig.(D.19).

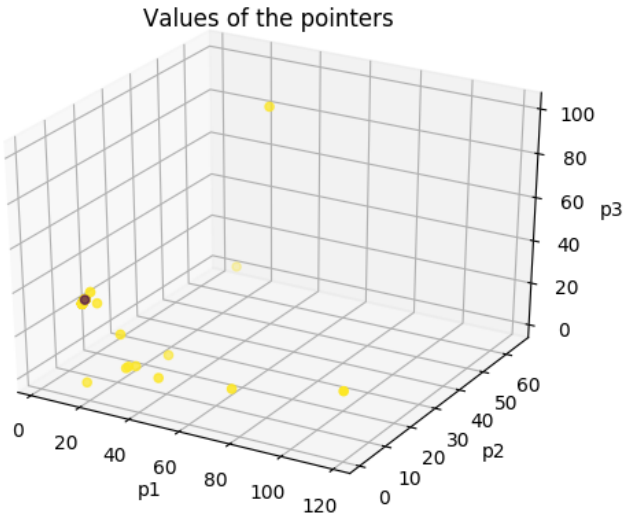

Figure D.19: Scatter plots of the pointers values. The points in yellow are outliers, while points in purple are normal points.

Before preprocess the data, we add a *label* column (hence a new feature) to `data_num_outlier`. The value of this feature is $+1$ is the message is a normal one, while it is -1 if the instance to which it refers it is an outlier. We are going to use this to evaluate the performance of the ML algorithm we use to fit the data. As mentioned, we use IF, which is an unsupervised ML algorithm. We preprocess the data using the `MinMaxScaler` function of *sklearn*: this allow us to scale the data to a given range; we chose to scale every feature in the range $(0, 1)$. Before using IF we need to define the *contamination rate*, i.e. the percentage of expected outliers; since we modified 12 instances over the 557 total ones, $contamination = 0.02$.
Thus, the IF used is:

$\mathrm{RANDOM} = 0$

$\#isolation\ forest$

```
is_for = IsolationForest(max_samples = 256,
contamination = 0.02, max_features = 1,
 n_estimator = 100, random_state = RANDOM )
```

To avoid possible overfitting, and considering the deeply skewed nature of the data, we decide to use the stratified cross-validation method with $k = 6$. The number of folds has been choose such that it is possible to have 2 anomalous messages in every fold .
We use the stratified version of the cross-validation since outliers and normal instances are not present with the same proportion in the dataset.

To check the IF performance we compute the *f1_score* for every fit. We fit each of the 5 datasets described above six times with the IF algorithm and in Table (D.2) we report the average *f1_score* for each dataset.

dataset	*f1 score*
X	0.7272
X2	0.1818
X3	0
X4	0.1666
X5	0.8333

Table D.2: Average *f1_score* computed over 5 fit of the data for the 5 datasets introduced above. This is obtained using the `cross_val_score` function. Parameters used: max_samples =256, contamination = 0.02, max_features = 1, random_state = 0, n_estimator = 100

The *confusion matrices* for the datasets are:

$$c_X = \begin{bmatrix} 8 & 4 \\ 2 & 543 \end{bmatrix}, \quad c_{X2} = \begin{bmatrix} 7 & 5 \\ 3 & 542 \end{bmatrix}, \quad c_{X3} = \begin{bmatrix} 0 & 12 \\ 16 & 529 \end{bmatrix}$$

$$c_{X4} = \begin{bmatrix} 2 & 10 \\ 12 & 533 \end{bmatrix}, \; c_{X5} = \begin{bmatrix} 10 & 2 \\ 2 & 543 \end{bmatrix}$$

From Table D.2 and the confusion matrices above, we can see that the datasets which give better results are *X* and *X5*.

Why do we think that these dataframes have the best *f1_score*?
The anomalies we manually introduced are very different from the "normal" in-

stances, therefore `p_order` and `pointers_PCA`, being derived features (derived from the original three features `p1`, `p2`, `p3`), are completely different as well.
Both *X* and *X5* include pointers values `p1`, `p2`, `p3` and the derived features; hence they do contain more features which are sensitive to the anomalies.
We think that this might be one of the reasons for which the IF algorithm performs better on *X* and *X5*.

To optimize the *f1_score*, hence to have a better anomalies detector, we use the `GridSearchCV` function.
This function scans over a specified range of hyperparameters for a given estimator (IF in this case) and tries to find the hyperparameters which can optimize the algorithm. To use this function we have to indicate an estimator, a set of parameters and a scoring function: in this specific case the estimator is the IF algorithm, the parameters are *max_samples*, *max_features*, *n_estimator* and *contamination_rate*, while the scoring function choose is the *f1_score*.
From Table D.2, the highest *f1_score* was 0.83 for the *X5* dataset, thus we decide to optimize the IF's hyperparameters over this dataframe. The `GridSearchCV` function suggests to keep most of the hyperparameters as the one indicated in the code above but to use $max\_samples = 200$.
The *f1_score* for the *X5* dataset after the IF's optimization is

$$f1\_score = 0.88 \tag{D.3}$$

while the confusion matrix returns:

$$c = \begin{bmatrix} 11 & 1 \\ 2 & 543 \end{bmatrix}$$

We also try to optimize the *f1_score* changing the PCA function used in *X4* and *X5*.
As mentioned in the introduction of this section, the feature `pointers_PCA` has been obtained applying the PCA transformation, which is one of the most common and immediate dimensional reduction technique. The PCA is a linear dimensionality reduction technique that uses the single value decomposition of the data to project it to a lower dimensional space. Therefore it does not always

perform as expected when data are not linearly separable.
The generalized version of PCA for data which are non linearly separable is called Kernel PCA, which is a non-linear dimensional reduction technique. The kernel shape can be set by the user and we chose a gaussian kernel.
We substitute the `pointers_PCA` values in *X4* and *X5* with the `pointers_Kernel_PCA` values obtained with this new dimensional reduction technique and we run IF on the new datasets. Using again `GridSearchCV` function to optimize IF on the dataset, we obtain the same confusion matrices presented above. Thus, we conclude that in this case the possible non-linearity of the pointers' values does not influence the algorithm.

Finally, we create a new dataset *X6*, which contains *only* pointers values and `pointers_PCA`.
Applying the IF algorithm used before, we obtain a perfect confusion matrix

$$c = \begin{bmatrix} 12 & 0 \\ 0 & 545 \end{bmatrix}$$

The *f1_score* in this case is 1, thus the IF algorithm recognizes all the outliers in *X6*, as we would have expected.

Small changes of the pointers values

In this section we study what happens if we modify the pointers values so that, except in one case, the pointers order stays the same, see Fig. (D.20).

In Fig.(D.21) we can see the 3D plot for pointers values in this case.

We also provide a second graph which helps to visualize how the feature `pointers_PCA` can be representative of `p1`, `p2`, `p3`, see Fig.D.22. Here we can see that, even reduced the dimensionality space from three (the three pointers' values) to one (`pointers_PCA`) , the outliers stand out respect to the normal instances.

Following the same steps of the previous section, we use the `StratifiedKFold` function, with $k = 6$ folds, and the IF algorithm with the following hyperparameters

```
#isolation forest with initial parameter
```

frame	label	sccp_length	p1	p2	p3
5739	-1	31	3	26	50
10985	-1	32	2	2	10
53664	-1	31	3	11	15
75154	-1	30	3	50	76
78088	-1	31	3	20	25
129308	-1	32	3	1	40
133408	-1	30	9	20	25
145486	-1	30	3	12	50
169527	-1	32	3	14	20
169689	-1	32	10	26	40
169695	-1	32	3	30	30
180822	-1	32	3	30	45

Figure D.20: Outliers realized modifying slightly the pointers' values. The pointers order does not change.

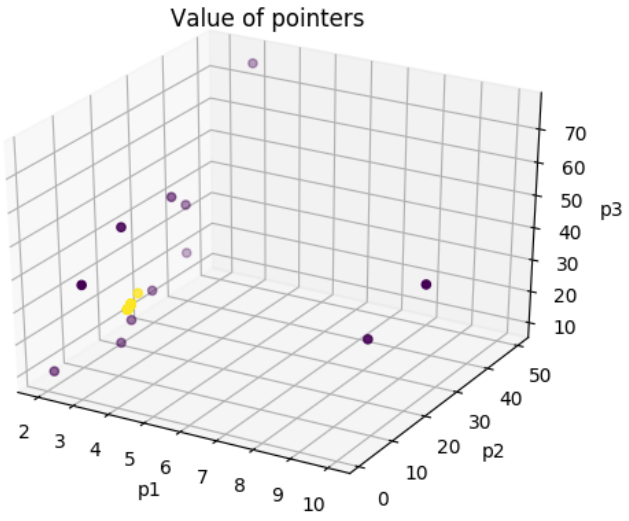

Figure D.21: Scatter plots of the pointers values. The points in purple are outliers, while points in yellow are normal points.

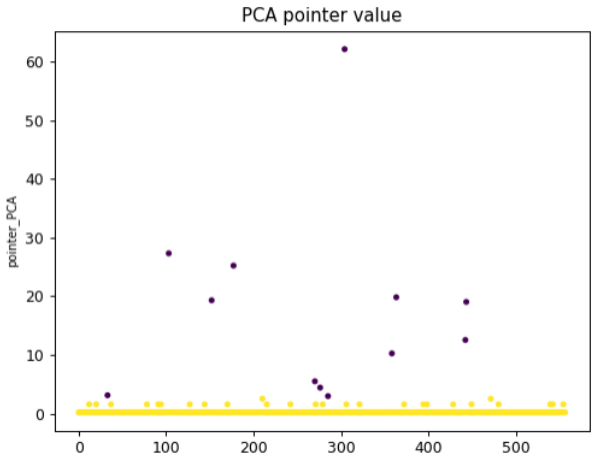

Figure D.22: Scatter plots of the *pointers_PCA* values. In purple we have the outliers, in yellow we have the real instances.

```
is_for = IsolationForest(max_samples = 256,
 contamination = 0.03, max_features = 1,
random_state = RANDOM , n_estimators =100)
```

Applying this algorithm to the 5 different datasets, we compute confusion matrices and *f1_scores*. We report the *f1_scores*' values in Tab (D.3) and the confusion matrices are The *confusion matrices* for the datasets are:

$$c_X = \begin{bmatrix} 2 & 10 \\ 15 & 530 \end{bmatrix}, \quad c_{X2} = \begin{bmatrix} 8 & 4 \\ 7 & 538 \end{bmatrix}, \quad c_{X3} = \begin{bmatrix} 0 & 12 \\ 20 & 525 \end{bmatrix}$$

$$c_{X4} = \begin{bmatrix} 1 & 11 \\ 16 & 529 \end{bmatrix}, \; c_{X5} = \begin{bmatrix} 8 & 4 \\ 10 & 535 \end{bmatrix}$$

From both the confusion matrices and Table D.3 we see that *X2* and *X5* are the datasets where the IF was most successfull.
In general, comparing the results presented in Table D.2 and Table D.3, we can notice that the *f1_score* is lower in the second case.
Moreover, when we modify the pointers's values only slightly, X does not present a high f1 score. We think that this might be the case since the additional feature present in X (*p_order*) does not bring any additional information in this case: we did not modify the pointers order for the outliers, hence it is not an informative

dataset	*f1 score*
X	0.095
X2	0.5896
X3	0
X4	0.0476
X5	0.5420

Table D.3: Average *f1_score* on 6 fit with IF for 5 datasets. Parameters used: max_samples =256, contamination = 0.03, max_features = 1, random_state = 42, n_estimator = 100

feature.

The highest *f1_scores* are associated to `X2` and `X5`. To optmize the results for both dataframes, we use the `GridSearchCV` function on each of the dataframe. For the dataframe *X2* the best hyperparameters results to be :

```
IsolationForest(behaviour='deprecated', bootstrap=False,
contamination=0.025, max_features=1,
max_samples=350, n_estimators=100,
n_jobs=None, random_state=0,
 verbose=0, warm_start=False)
```

Using them we obtain

$$f1\_score = 0.6923, \quad c_{X2} = \begin{bmatrix} 9 & 3 \\ 5 & 540 \end{bmatrix} \tag{D.4}$$

Optimizing the hyperparameters for *X5* we obtain the following hyperparameters

```
IsolationForest(behaviour='deprecated',
bootstrap=False, contamination=0.035,
max_features=1, max_samples=300,
 n_estimators=100, n_jobs=None,
random_state=0, verbose=0, warm_start=False)
```

which leads to

$$f1\_score = 0.6, \quad c_{X5} = \begin{bmatrix} 9 & 3 \\ 9 & 536 \end{bmatrix} \tag{D.5}$$

It is possible to see that also optimizing the hyperparameters, *X2* seems to be the dataframe that better describes the data in this case.

As in the previous case we also run IF on a dataset containing `pointers_Kernel_PCA` we do not obtain any improvement in either *f1_score* or the confusion matrix.

Lastly, we apply the IF to datasets containing *only* the parameters of interest, thus we create the following datasets considering only the features `p1`, `p2`, `p3`, `p_order` and `pointers_PCA`. The new dataframe are the analogous of *X*, *X2*, ... but containing *only* pointers' related features.
In particular:

- *Xp_1* : it contains `p1`, `p2`, `p3` and `p_order` (as a numerical features)
- *Xp_2*: it contains `p1` `p2`, `p3`.
- *Xp_3*: it contains `p_order`.
- *Xp_4*: it contains `pointers_PCA`.
- *Xp_5*: it contains `p1`, `p2`, `p3` and `pointers_PCA`.

Using IF with the same initial hyperparameters of above, we obtain the *f1_score* reported in Table D.4 and the following confusion matrices:

$$c_{Xp\_1} = \begin{bmatrix} 10 & 2 \\ 2 & 543 \end{bmatrix}, \quad c_{Xp\_2} = \begin{bmatrix} 10 & 2 \\ 2 & 543 \end{bmatrix}, \quad c_{Xp\_3} = \begin{bmatrix} 0 & 12 \\ 0 & 545 \end{bmatrix}$$

$$c_{Xp\_4} = \begin{bmatrix} 12 & 0 \\ 0 & 545 \end{bmatrix}, \; c_{Xp\_5} = \begin{bmatrix} 10 & 2 \\ 2 & 543 \end{bmatrix}$$

dataset	*f1 score*
X_p	0.8278
X2_p	0.8278
X3_p	0
X4_p	1
X5_p	0.8278

Table D.4: Average *f1_score* on 6 run of the IF algorithm for 5 datasets.

From these we conclude that *X3* does not contain enough information for the IF to correctly identify the anomalies, while *X*, *X2* and *X5* correctly classify

10 out of 12 anomalies. The anomalous pointers values which have not been recognized are reported in Table D.5. Note that all of these are very similar to the original (non modified) pointers' values.

p1	p2	p3
3	14	20
3	20	25

Table D.5: Pointers' value not recognised by the IF algorithm.

The *Xp_4*, which checks only the PCA values, is the only one to have a *f1_score* = 1.

D.4.2 Analysis on 1482233452_722272

From this dataset we isolate the messages sent by the following GT

$$GT = 34656000235 \qquad n_{counts} = 20254 \tag{D.6}$$

This GT presents the following pointers values:

1. p1 = 3, p2 = 14, p3 = 25 , for 5027 messages
2. p1 = 3, p2 = 15, p3 = 26, for 1076 messages
3. p1 = 3, p2 = 16, p3 = 27, for 13701 messages

In this case we modify 102 of the total 20254 messages, some of which are shown in Fig.(D.23). The outliers in this case are a mix: in some cases we do not modify the pointers order, in other cases we do.

frame	sccp_length	label	p1	p2	p3
1124	32	-1	3	30	70
63112	32	-1	5	12	80
72673	32	-1	2	80	45
89606	32	-1	3	10	10
99097	30	-1	40	45	25
...	...	...	...	...	...
2517326	30	-1	21	14	25
2529876	30	-1	3	21	45
2544999	30	-1	12	35	79
2557823	32	-1	3	42	27
2565122	30	-1	8	12	25

Figure D.23: Some of the outliers present in this study.

The dataset containing the outliers is called `data_num_outlier_big`. From this, exactly as in the previous section, Sec.(D.4), we create *X1*, *X2*, *X3*, *X4*, *X5*, and we add the *label* column.

Plotting `p1`, `p2` and `p3` in a 3D space for all the instance in `data_num_outliers`, we obtain the plot presented in Fig.D.24.

The 1D scatter plot obtained plotting `pointers_PCA` is reported in Fig.D.25.

To apply the IF to the 5 different datasets, we set the *contamination_rate* as:

$$contamination\_rate = 102/20254 = 0.005 \tag{D.7}$$

Also in this case we use the `StratifiedKFold` function, and the code we run to fit the data with the IF is the following:

```
skfold = StratifiedKFold(n_splits=10)

is_for = IsolationForest(max_samples = 256,
contamination = contamination_parameter,
 max_features = 1, random_state = 42 , n_estimators =100)
```

The *f1_score*'s values obtained for the different datasets are reported in Table. (D.6)

The confusion matrices are:

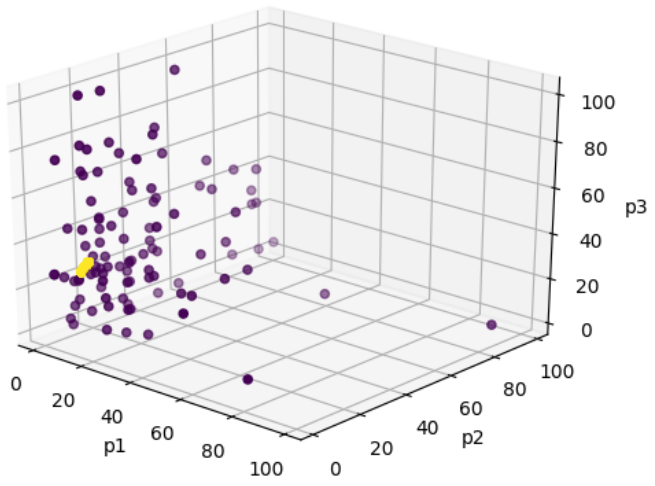

Figure D.24: 3D plot of the pointers values in the dataset `big_dataset`. Points in purple are putliers, points in yellow are legitimate.

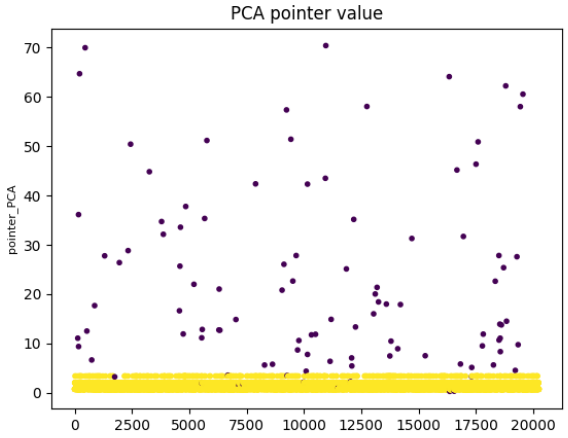

Figure D.25: Scatter plot of the pointers_PCA values. Purple points are outliers, yellow point are legitimate data.

$$c_{X1} = \begin{bmatrix} 2 & 101 \\ 0 & 20151 \end{bmatrix}, \quad c_{X2} = \begin{bmatrix} 2 & 101 \\ 0 & 20151 \end{bmatrix}, \quad c_{X3} = \begin{bmatrix} 0 & 102 \\ 0 & 20151 \end{bmatrix}$$

dataset	*f1 score*
X	0.0348
X2	0.0348
X3	0
X4	0.0182
X5	0.0825

Table D.6: Average *f1_score* on 6 fit with IF for 5 datasets. Parameters used: max_samples =256, contamination = 0.005, max_features = 1, random_state = 42, n_estimator = 100

$$c_{X4} = \begin{bmatrix} 1 & 98 \\ 0 & 20151 \end{bmatrix}, \; c_{X5} = \begin{bmatrix} 5 & 98 \\ 0 & 20151 \end{bmatrix}$$

From these results we can see that the IF does not produce a satisfactory outlier detection, at least with its standard hyperparameters.
We use the `GridSearchCV` function to optimize the IF fit on *X5*, which from Table.**??** is the most promising dataset.
The best *f1_score* for *X5* is obtained with the following IF function:

```
is_for_GSCV_X5 = IsolationForest(behaviour='deprecated',
  bootstrap=False,   contamination=0.015,
   max_features=5, max_samples=350, n_estimators=200,
   n_jobs=None, random_state=42, verbose=0, warm_start=False)
```

which gives

$$f1score = 0.25, \quad c_{X5} = \begin{bmatrix} 15 & 88 \\ 1 & 20151 \end{bmatrix}. \tag{D.8}$$

With the new hyperparameters there is a large improvement of the anomaly detection ability of the IF, however this is not still good enough. On 102 outliers, *only* 15 were detected.

Finally, we construct 5 new datasets *Xp_1*, ..., *Xp_5* (defined in the previous subsection) and we compute their *f1_scores* and confusion matrices using the standard IF hyperparameters. The results of the *f1_score* are presented in Table. (D.7), while the confusion matrices are:

$$c_{Xp\_1} = \begin{bmatrix} 75 & 28 \\ 0 & 20151 \end{bmatrix}, \quad c_{Xp\_2} = \begin{bmatrix} 39 & 64 \\ 0 & 20151 \end{bmatrix}, \quad c_{Xp\_3} = \begin{bmatrix} 58 & 45 \\ 0 & 20151 \end{bmatrix}$$

$$c_{Xp\_4} = \begin{bmatrix} 93 & 10 \\ 0 & 20151 \end{bmatrix}, \; c_{Xp\_5} = \begin{bmatrix} 35 & 68 \\ 0 & 20151 \end{bmatrix}$$

dataset	*f1 score*
X	0.8427
X2	0.5493
X3	0.7205
X4	0.9499
X5	0.5072

Table D.7: Average f1 score for 5 dataset containing only features related to the pointers values.

Comparing these matrices with those of the datasets *X1*, ..., *X5* we can see see that there is a substantial improvement, as expected.

D.5 Supervised Learning approach - Random Forest

In this section we try to use a Supervised Learning approach to detect outliers. The idea is to combine in a single dataset messages sent by a specific GT, which we refer to as GT1, and messages coming from other random GTs.
We plan to use a Random Forest (RF) algorithm.

The datasets used for this study are **feature_small_v3** and **feature_small_v4**, which have features very similar to those described in the Sec. D.2, with only few differences:

- *sccp_class_handling* is removed. It is substituted with 2 categorical features *sccp_class*, which can assume values in the range [0,1] and *sccp_handling* with values [0,8].
- *sccp_ptr_order* is introduced: this describes the order of the pointers in the message.
- A feature *tcap_user_comp_length* was added. This is a numerical feature not often used in messages.

D.5.1 Study done on feature_small_v3.csv

This dataset contains 85966 messages sent by 6001 different GTs.

The main idea is to train a supervised machine learning algorithm (Random Forest) to distinguish between messages sent by different GTs looking at their features patterns.

D.5.1.1 First case with only 2 GTs

We consider two GTs:

1. GT1 = 22899999797 , which sent 760 messages.
2. GT2 = 351930000433, which sent 748 messages.

and we create a dataset containing all the messages coming from GT1 and GT2. We include ad additional column labeled *label*, which takes different values according to which GT the messages are sent. If $GT = GT1 \rightarrow label = 1$, if $GT = GT2 \rightarrow label = 0$.

The final dataset, `GT_tot` comprises of 1508 messages and 56 features (including *label* and GT), see Fig.(D.26).

frame_number	GT	op_code	sccp_type	sccp_len	sccp_class	sccp_handling	p1	p2	p3	sccp_ptr_order	...	tcap_comp_count	tcap_invokeID
121572	22899999797	56	9	35	1	8	88	2	13	231	...	1	1
51911	351930000433	56	9	31	1	8	40	2	13	231	...	1	2
46982	22899999797	56	9	35	1	8	88	2	13	231	...	1	1
122824	22899999797	56	9	35	1	8	88	2	13	231	...	1	1
60253	351930000433	44	9	32	1	0	123	2	13	231	...	2	3
...	...	...	...	...	...	...	...	...	...	...	...	...	...
46319	351930000433	56	9	31	1	8	40	2	13	231	...	1	2
102579	351930000433	56	9	33	1	8	86	2	13	231	...	1	1
105780	351930000433	2	9	35	1	8	108	2	13	231	...	1	1
164486	351930000433	56	9	35	1	8	88	2	13	231	...	1	1
44599	351930000433	56	9	31	1	8	40	2	13	231	...	1	2

1508 rows × 56 columns

Figure D.26: Some data from `GT_tot`

We use the `get_dummies` function of `pandas` to convert *all* the categorical features into numerical ones.

feature	importance
sccp_calling_es	0.75
sccp_len	0.030
tcap_comp_tag_short_count	0.027
p1	0.025
tacp_comp_length	0.022

Table D.8: Features importance in the case of GT1 = 22899999797 and GT_outliers = GT2

We also eliminate the GT column, leaving the *label* column as identifier on which GT sent the message. As final result, `GT_tot` has 92 columns (features).

We train the RF on 1206 data (80% of the total) and test it on the remaining 302 (20% of the total)
We obtain the following results:

$$accuracy\_score = 1.0, \qquad c_{Xp\_4} = \begin{bmatrix} 150 & 0 \\ 0 & 152 \end{bmatrix} \tag{D.9}$$

All the messages coming from GT1 and GT2 were correctly classified.

To have a better understanding of which features mostly influenced the RF classification, we compute the `feature_importance` using a *property* of the `RandomForestClassifier` in *scikit-learn*. The results are reported in Table.D.8.

D.5.1.2 Multiple GTs

Following the success of the previous study, we decide to create a dataset `GT_tot2` containing messages sent form GT1 and other 148 messages (which are our outliers in this case) coming from 5 different GTs:

1. GT3 = 447802000257, 29 messages
2. GT4 = 628112907133, 29 messages
3. GT5 = 201059969650, 19 messages
4. GT6 = 48501999945, 39 messages
5. GT7 = 33609009700, 32 messages

feature	importance
p1	0.153
sccp_ptr_order	0.246
p2	0.120
p3	0.092
sccp_calling_ssn	0.104

Table D.9: Features importance in the case of GT1 = 22899999797 and GT_outliers = GT3/GT4/GT5/GT6/GT7.

The final dataset has a total of 908 messages, 70% of which are legitimate (coming from GT1).
Again, we transform all the categorical features into numerical ones. As a result, `GT_tot2` has 908 rows and 100 columns.
We train the RF on 80% of the dataset (726 data) and test it on the remaining 182 instances. The split between train and test dataset is done in a stratified way to take into account that there is a misproportion between legitimate and outliers messages.
Using the standard hyperparameters for the RF, we obtain the following results:

$$accuracy\_score = 1, \qquad c_{Xp\_4} = \begin{bmatrix} 30 & 0 \\ 0 & 152 \end{bmatrix} \tag{D.10}$$

Running `feature_importance` we obtain the results shown in Table D.9.

D.5.2 Study done on feature_small_v4.csv

In this section we extend the study realized on *feature_small_v3.csv* on a much larger dataset, *feature_small_v4.csv*.

We create a dataset containing messages sent by GT1 and we randomly add messages sent by other GTs. This is done using a function `outlier`:

```
def outlier(dataset, GT_list, n_outlier, max_rep):
```

where

- `dataset` contains the data from which the outliers messages are drown.
- `GT_list` is the list of GTs whose messages are *outliers*

- `n_outlier` is the total number of outliers we want in the dataset.
- `max_rep` is the maximum number of outliers sent from *the same* GT that we want in the dataset.

We chose

$$GT1 = 256771101050, \qquad n_{counts} = 95316 \tag{D.11}$$

The dataset containing only the messages sent by GT1 is `gg256771101050.csv` while the one including GT1 and the outliers is `data`.

Using the function `outlier` we apply the RF algorithm on `data` and we compute its accuracy. We create three different `data` datasets modifying each time the number of outliers messages.
In particular, for the three datasets we use the following n_outliers and max_reps:

1. n_outliers 10000, max_rep = 30
2. n_outliers 1000, max_rep = 12
3. n_outliers 50, max_rep = 3

For each study we iterate the following steps 200 times:

1. Call the function `outliers` to generate a dataset containing the desired number of outliers.
2. Concatenate this with `gg256771101050.csv` to create `data`.
3. Split `data` into a training dataset and a testing dataset, taking into account the different proportion of legitimate-outlier messages.
4. Fit a RF with standard hyperparameters over the train data and run this on the test data.
5. Compute the confusion matrix, the *f1_score* and the accuracy.

n outliers	accuracy	f1 score
10000	$0.998 \pm 5 \cdot 10^{-7}$	$0.998 \pm 6 \cdot 10^{-7}$
1000	$0.996 \pm 1 \cdot 10^{-5}$	$0.996 \pm 1 \cdot 10^{-5}$
50	0.958 ± 0.002	0.954 ± 0.003

Table D.10: Table reporting the averaged values of f1 score and accuracy obtained from the studies on *random_forest_small_v4.csv*

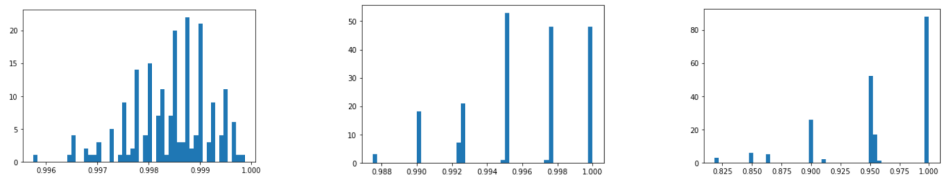

(a) Histogram of the accuracy values when n_outliers=10000.

(b) Histogram of the accuracy values when n_outliers=1000.

(c) Histogram of the accuracy values when n_outliers=50.

Figure D.27: Histograms of the accuracy values for the three cases described

.

Each run provides an accuracy value and a *f1_score* value, hence running RF 200 times, we can compute and average and a standard deviation for them. This are reported in Table D.10.

We can also plot the accuracy values in histograms for the three cases analysed, see Fig.D.27.

From Table D.10 we can see that when there is a big imbalance among messages (3rd case, when there are only 50 outliers) RF does not perform as well as in the previous two cases.

We repeat the same study comparing two Supervised Learning algorithms: RF and XGBOOST (XG).
In this case we repeat the same steps described above, but we iterate them for only 10 times instead than 200. The results are shown in Table.D.11.

From TableD.11 it results that, using the standard hyperparameters for both the algorithms, RF performs better: it has a better accuracy and *f1_score*.

metric	RF_1	XG_1	RF_2	XG_2	RF_3	XG_3
accuracy	0.9983	0.9979	0.9955	0.9933	9826	0.9442
f1 score	0.9979	0.9974	0.9955	0.9932	0.9817	0.9401

Table D.11: Table of the accuracy and f1 score values for Random Forest (RF) and XGBOOST (XG) for different number of outliers (_1 means 1st case, _2 2nd case and so on).

D.6 Heatmaps

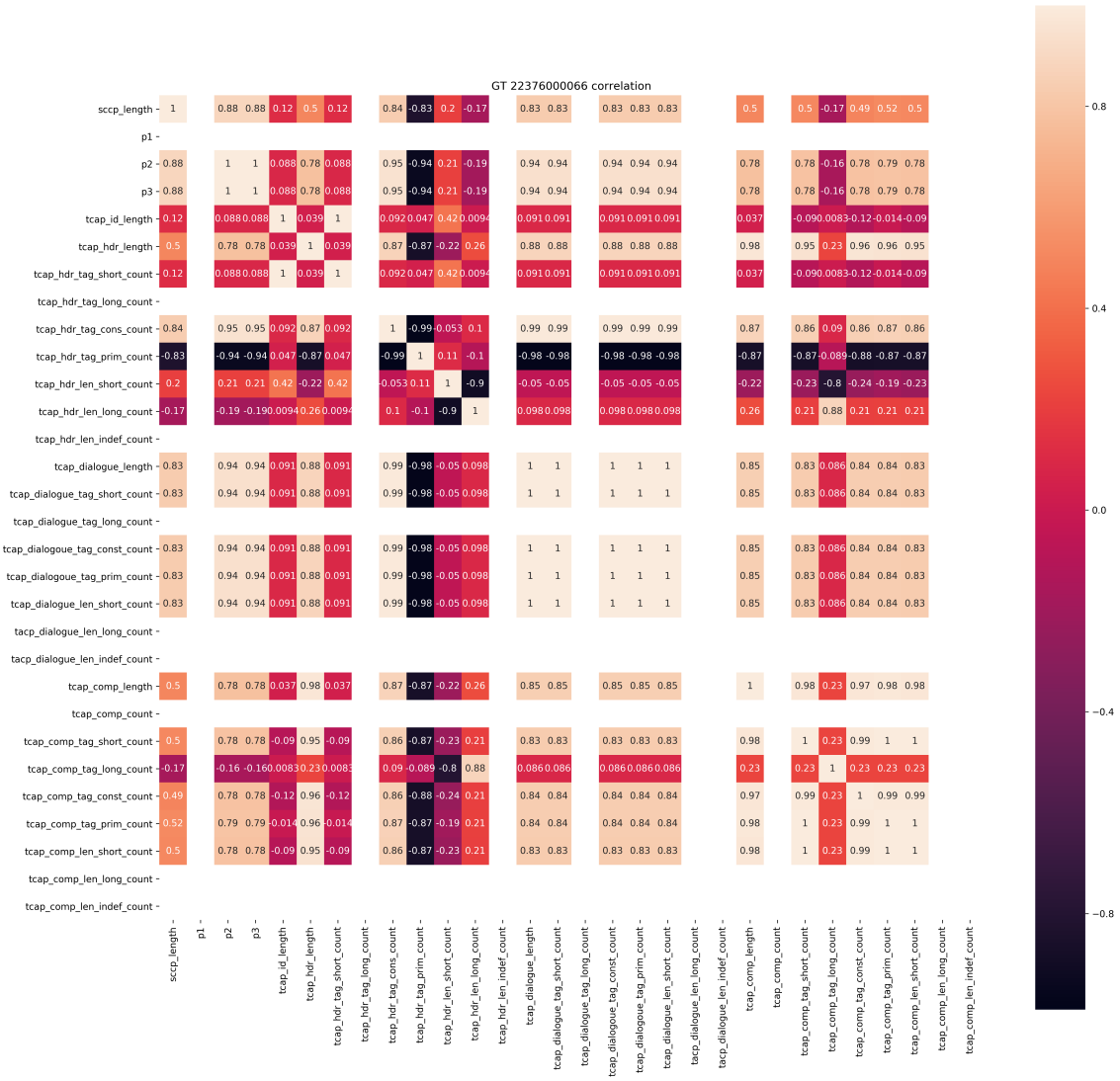

Figure D.28: Correlations for $GT_1 = 22376000066$ prova plot

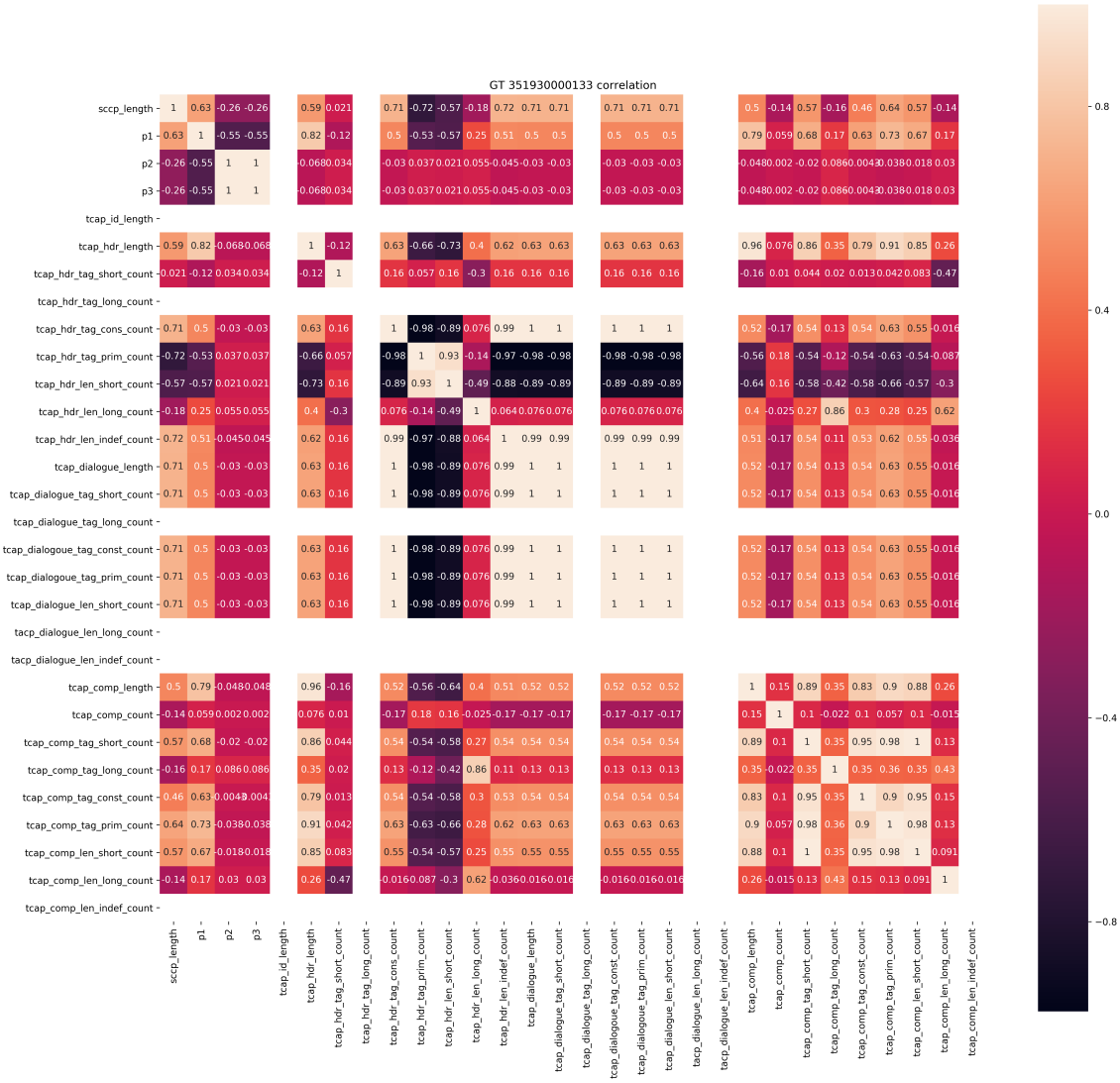

Figure D.29: Correlations for $GT_2 = 351930000133$

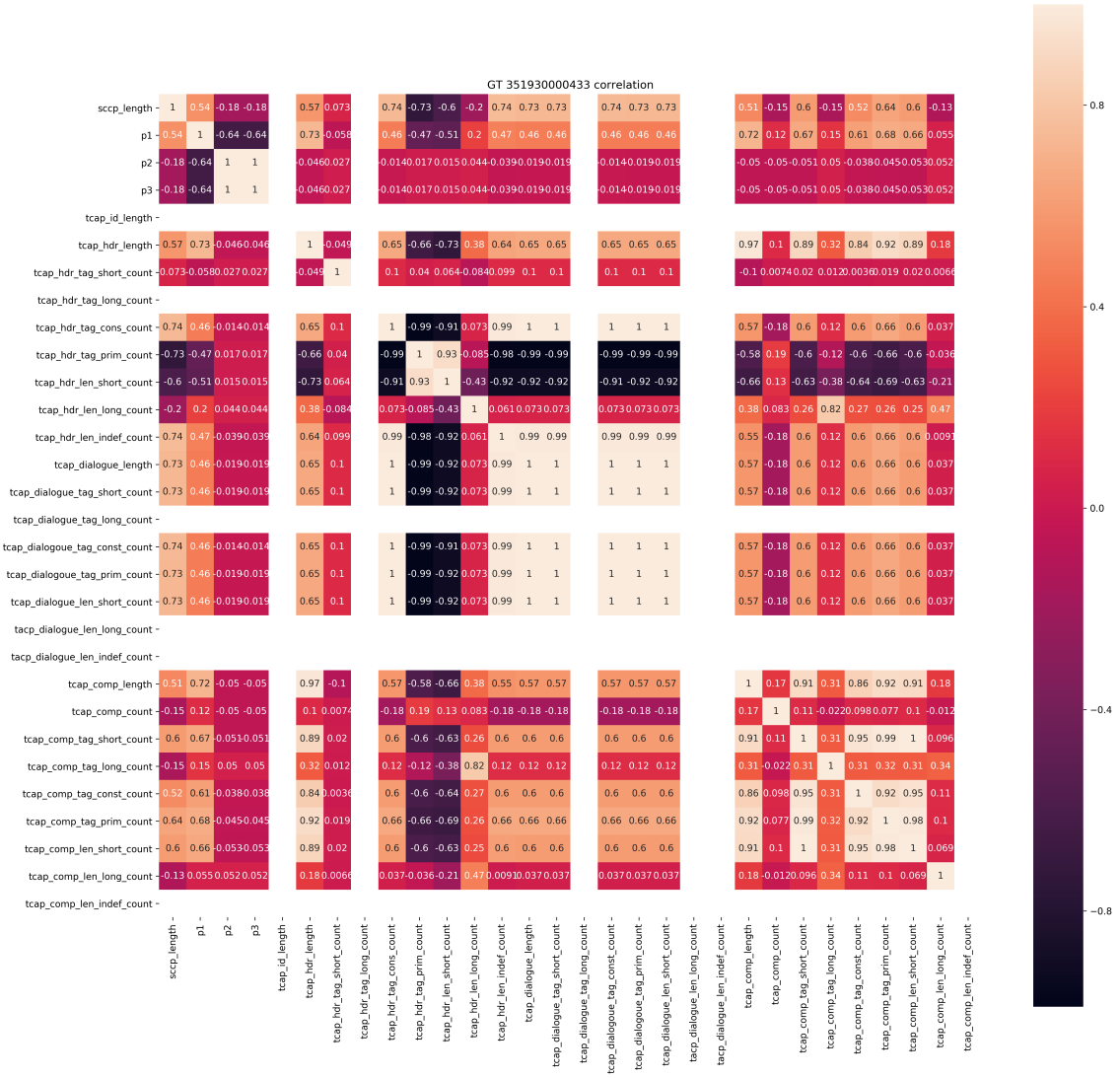

Figure D.30: Correlations for $GT_3 = 351930000433$

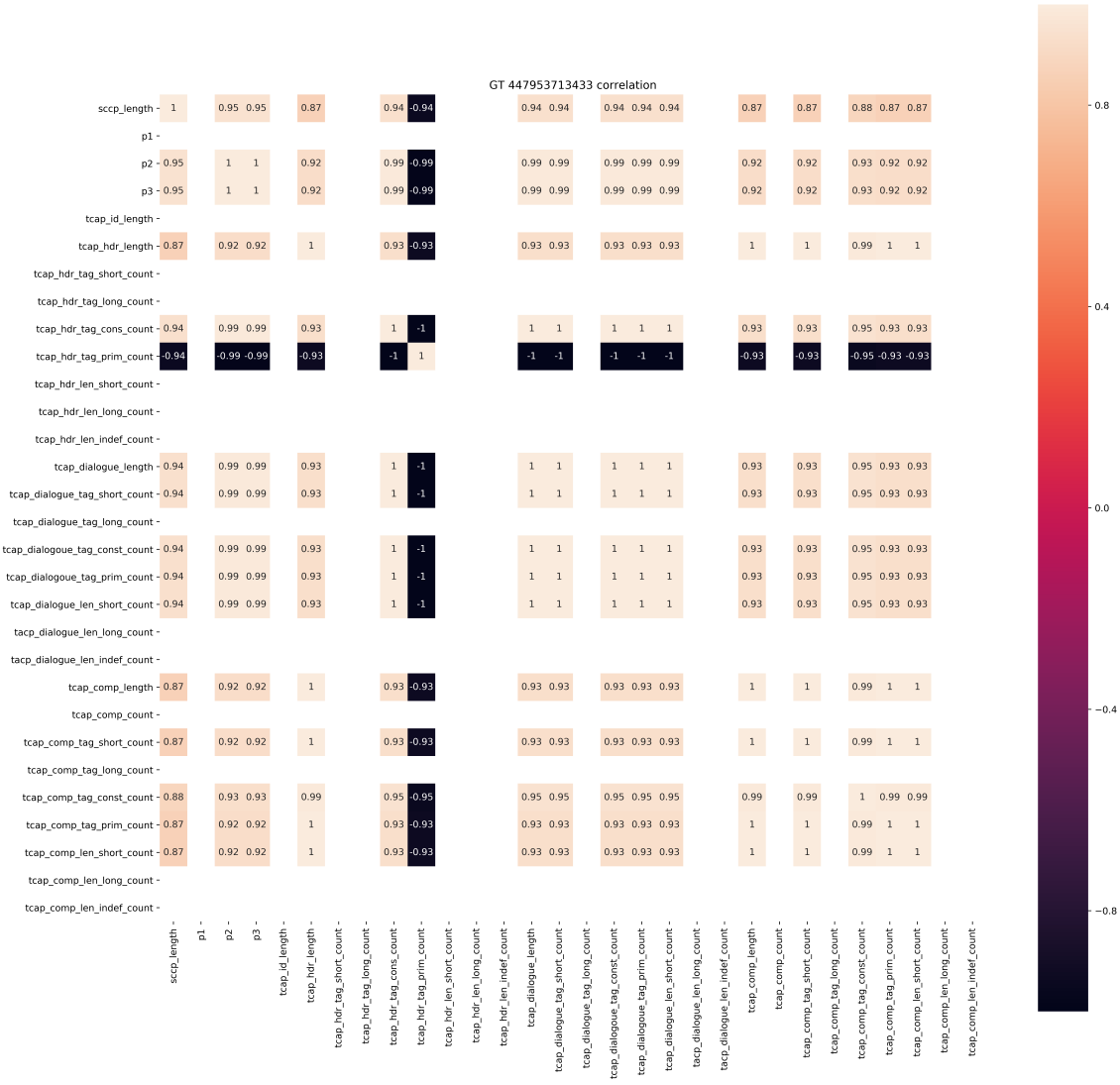

Figure D.31: Correlations for $GT_4 = 447953713433$

Bibliography

[1] N. Aghanim *et al.*, "Planck 2018 results. VI. Cosmological parameters," *Astron. Astrophys.*, vol. 641, p. A6, 2020. [Erratum: Astron.Astrophys. 652, C4 (2021)]. xi, 10, 27, 56

[2] Y. Akrami *et al.*, "Planck 2018 results. X. Constraints on inflation," 2018. xi, 27, 28, 56

[3] P. Christodoulidis, D. Roest, and E. I. Sfakianakis, "Angular inflation in multi-field α-attractors," *JCAP*, vol. 11, p. 002, 2019. xii, 37, 60, 71, 72, 73, 78, 81, 82, 84

[4] J. Ellis, M. A. G. Garcia, D. V. Nanopoulos, and K. A. Olive, "A No-Scale Inflationary Model to Fit Them All," *JCAP*, vol. 08, p. 044, 2014. xiii, 89, 102, 104, 105, 108, 202

[5] C. W. Misner, "Mixmaster universe," *Phys. Rev. Lett.*, vol. 22, pp. 1071–1074, May 1969. xiv, 135, 138

[6] D. Chakraborty, R. Chiovoloni, O. Loaiza-Brito, G. Niz, and I. Zavala, "Fat inflatons, large turns and the -problem," *Journal of Cosmology and Astroparticle Physics*, vol. 2020, p. 020–020, Jan 2020. 3, 55, 56, 78, 108, 192

[7] V. Aragam, R. Chiovoloni, S. Paban, R. Rosati, and I. Zavala, "Rapid-turn inflation in supergravity is rare and tachyonic," *Journal of Cosmology and Astroparticle Physics*, vol. 2022, p. 002, mar 2022. 4, 64, 77

[8] R. Chiovoloni, G. Montani, and V. Cascioli, "Quantum dynamics of the corner of the bianchi ix model in the wkb approximation," *Physical Review D*, vol. 102, Oct 2020. 4, 149, 174, 175, 177, 188

[9] G. Montani and R. Chiovoloni, "Scenario for a singularity-free generic cosmological solution," *Physical Review D*, vol. 103, Jun 2021. 4, 173, 174

[10] E. Hubble, "A Relation between Distance and Radial Velocity among Extra-Galactic Nebulae," *Proceedings of the National Academy of Science*, vol. 15, pp. 168–173, Mar. 1929. 6

[11] A. G. Riess, S. Casertano, W. Yuan, L. M. Macri, and D. Scolnic, "Large magellanic cloud cepheid standards provide a 1determination of the hubble constant and stronger evidence for physics beyond Λcdm," *The Astrophysical Journal*, vol. 876, p. 85, May 2019. 7

[12] G. C. F. Chen *et al.*, "A SHARP view of H0LiCOW: H_0 from three time-delay gravitational lens systems with adaptive optics imaging," *Mon. Not. Roy. Astron. Soc.*, vol. 490, no. 2, pp. 1743–1773, 2019. 7

[13] W. L. Freedman, , *et al.*, "The carnegie-chicago hubble program. viii. an independent determination of the hubble constant based on the tip of the red giant branch*," *The Astrophysical Journal*, vol. 882, p. 34, Aug 2019. 7

[14] C. Huang *et al.*, "Hubble space telescope observations of mira variables in the sn ia host ngc 1559: An alternative candle to measure the hubble constant," *The Astrophysical Journal*, vol. 889, p. 5, 01 2020. 7

[15] P. Shah, P. Lemos, and O. Lahav, "A buyer's guide to the hubble constant," *The Astronomy and Astrophysics Review*, vol. 29, Dec 2021. 7

[16] N. Aghanim, Y. Akrami, M. Ashdown, J. Aumont, C. Baccigalupi, M. Ballardini, A. J. Banday, R. B. Barreiro, N. Bartolo, and et al., "Planck 2018 results," *Astronomy and Astrophysics*, vol. 641, p. A6, Sep 2020. 7, 13

[17] A. Friedmann, "Über die krümmung des raumes," vol. 10, pp. 377–386, 1922. 7

[18] G. Lemaître, "Un univers homogène de masse constante et de rayon croissant rendant compte de la vitesse radiale des nébuleuses extra-galactiques," vol. 47, pp. 49–59, 1927. 7

[19] G. Lemaître, "Expansion of the universe, a homogeneous universe of constant mass and increasing radius accounting for the radial velocity of extra-galactic nebulæ," vol. 91, pp. 483–490, 1931. 7

[20] H. P. Robertson, "Kinematics and world-structure," vol. 82, p. 284, 1935. 7

[21] A. G. Walker, "On milne's theory of world-structure," vol. 42, pp. 90–127, 1937. 7

[22] A. Friedman, "On the Curvature of space," *Z. Phys.*, vol. 10, pp. 377–386, 1922. 8

[23] R. A. Alpher, H. Bethe, and G. Gamow, "The origin of chemical elements," *Phys. Rev.*, vol. 73, pp. 803–804, 1948. 9

[24] A. A. Penzias and R. W. Wilson, "A Measurement of excess antenna temperature at 4080-Mc/s," *Astrophys. J.*, vol. 142, pp. 419–421, 1965. 10

[25] G. F. Smoot *et al.*, "Structure in the COBE differential microwave radiometer first year maps," *Astrophys. J. Lett.*, vol. 396, pp. L1–L5, 1992. 10, 27

[26] D. N. Spergel *et al.*, "First-year wilkinson microwave anisotropy probe (wmap) observations: Determination of cosmological parameters," *The Astrophysical Journal Supplement Series*, vol. 148, p. 175–194, Sep 2003. 10

[27] E. Komatsu and others., "Five-year wilkinson wilkinson microwave anisotropy probe observations: cosmological interpretations," *The Astrophysical Journal Supplement Series*, vol. 180, p. 330–376, Feb 2009. 10

[28] J. P. Preskill, "Cosmological production of superheavy magnetic monopoles," *Physical Review Letters*, vol. 43, no. 19, p. 1365, 1979. 15

[29] A. A. Starobinsky, "A New Type of Isotropic Cosmological Models Without Singularity," *Phys. Lett. B*, vol. 91, pp. 99–102, 1980. 15, 80, 88

[30] A. H. Guth, "The Inflationary Universe: A Possible Solution to the Horizon and Flatness Problems," *Phys.Rev.*, vol. D23, pp. 347–356, 1981. 15, 31, 56

[31] A. Albrecht and P. J. Steinhardt, "Cosmology for Grand Unified Theories with Radiatively Induced Symmetry Breaking," *Phys.Rev.Lett.*, vol. 48, pp. 1220–1223, 1982. 16, 56

[32] F. Bernardeau, S. Colombi, E. Gaztañaga, and R. Scoccimarro, "Large-scale structure of the universe and cosmological perturbation theory," *Physics Reports*, vol. 367, p. 1–248, Sep 2002. 25, 195

[33] V. Mukhanov, H. Feldman, and R. Brandenberger, "Theory of cosmological perturbations," *Physics Reports*, vol. 215, no. 5, pp. 203–333, 1992. 25, 195

[34] A. Riotto, "Inflation and the theory of cosmological perturbations," 2017. 25, 195

[35] N. Bretón, J. Cervantes-Cota, and M. Salgad, "The early universe and observational cosmology," 2004. 25, 195

[36] D. Baumann, "Tasi lectures on inflation," 2012. 25, 195, 196

[37] P. Ade, N. Aghanim, Z. Ahmed, R. Aikin, K. Alexander, M. Arnaud, J. Aumont, C. Baccigalupi, A. Banday, D. Barkats, and et al., "Joint analysis of bicep2/keck array and planck data," *Physical Review Letters*, vol. 114, Mar 2015. 28

[38] P. Ade and et al., "Improved constraints on primordial gravitational waves using planck , wmap, and bicep/keck observations through the 2018 observing season," *Physical Review Letters*, vol. 127, Oct 2021. 28

[39] J. Maldacena, "Non-gaussian features of primordial fluctuations in single field inflationary models," *Journal of High Energy Physics*, vol. 2003, p. 013–013, May 2003. 29, 30, 196, 198

[40] V. Acquaviva, N. Bartolo, S. Matarrese, and A. Riotto, "Gauge-invariant second-order perturbations and non-gaussianity from inflation," *Nuclear Physics B*, vol. 667, p. 119–148, Sep 2003. 29

[41] N. Bartolo, E. Komatsu, S. Matarrese, and A. Riotto, "Non-gaussianity from inflation: theory and observations," *Physics Reports*, vol. 402, p. 103–266, Nov 2004. 29

[42] M. Liguori, E. Sefusatti, J. R. Fergusson, and E. P. S. Shellard, "Primordial non-gaussianity and bispectrum measurements in the cosmic microwave background and large-scale structure," *Advances in Astronomy*, vol. 2010, p. 1–64, 2010. 29

[43] X. Chen, "Primordial non-gaussianities from inflation models," *Advances in Astronomy*, vol. 2010, p. 1–43, 2010. 29

[44] Y. Wang, "Inflation, cosmic perturbations and non-gaussianities," *Communications in Theoretical Physics*, vol. 62, p. 109–166, Jul 2014. 29

[45] P. D. Meerburg *et al.*, "Primordial Non-Gaussianity," 2019. 29, 31, 33

[46] A. P. S. Yadav and B. D. Wandelt, "Primordial non-gaussianity in the cosmic microwave background," *Advances in Astronomy*, vol. 2010, p. 1–27, 2010. 30

[47] Y. Akrami *et al.*, "Planck 2018 results. IX. Constraints on primordial non-Gaussianity," 2019. 30, 56

[48] P. Creminelli, "On non-gaussianities in single-field inflation," *Journal of Cosmology and Astroparticle Physics*, vol. 2003, p. 003–003, Oct 2003. 30

[49] D. Baumann, D. Green, and R. A. Porto, "B-modes and the nature of inflation," *Journal of Cosmology and Astroparticle Physics*, vol. 2015, pp. 016–016, jan 2015. 30

[50] M. Alvarez *et al.*, "Testing Inflation with Large Scale Structure: Connecting Hopes with Reality," 12 2014. 30

[51] A. Aghamousa *et al.*, "The DESI Experiment Part I: Science,Targeting, and Survey Design," 2016. 31, 33

[52] P. A. Abell *et al.*, "LSST Science Book, Version 2.0," 2009. 31, 33

[53] L. Amendola *et al.*, "Cosmology and fundamental physics with the Euclid satellite," *Living Rev. Rel.*, vol. 21, no. 1, p. 2, 2018. 31, 33

[54] S. Camera, M. G. Santos, and R. Maartens, "Probing primordial non-Gaussianity with SKA galaxy redshift surveys: a fully relativistic analysis," *Mon. Not. Roy. Astron. Soc.*, vol. 448, no. 2, pp. 1035–1043, 2015. [Erratum: Mon. Not. Roy. Astron. Soc.467,no.2,1505(2017)]. 31, 33

[55] G. Obied, H. Ooguri, L. Spodyneiko, and C. Vafa, "De Sitter Space and the Swampland," 6 2018. 32, 45, 78, 81

[56] H. Ooguri, E. Palti, G. Shiu, and C. Vafa, "Distance and de Sitter Conjectures on the Swampland," *Phys. Lett. B*, vol. 788, pp. 180–184, 2019. 32, 45, 78, 81

[57] A. Achucarro and G. A. Palma, "The string swampland constraints require multi-field inflation," *JCAP*, vol. 1902, p. 041, 2019. 32, 44, 46, 47, 72, 78, 79

[58] K. N. Abazajian *et al.*, "CMB-S4 Science Book, First Edition," 2016. 33

[59] T. Essinger-Hileman *et al.*, "CLASS: The Cosmology Large Angular Scale Surveyor," *Proc. SPIE Int. Soc. Opt. Eng.*, vol. 9153, p. 91531I, 2014. 33

[60] T. Matsumura *et al.*, "Mission design of LiteBIRD," 2013. [J. Low. Temp. Phys.176,733(2014)]. 33

[61] J. Aguirre *et al.*, "The Simons Observatory: Science goals and forecasts," *JCAP*, vol. 1902, p. 056, 2019. 33

[62] S. Hanany *et al.*, "PICO: Probe of Inflation and Cosmic Origins," 2019. 33

[63] S. Groot Nibbelink and B. J. W. van Tent, "Density perturbations arising from multiple field slow roll inflation," 11 2000. 33

[64] S. Groot Nibbelink and B. J. W. van Tent, "Scalar perturbations during multiple field slow-roll inflation," *Class. Quant. Grav.*, vol. 19, pp. 613–640, 2002. 33, 63

[65] A. Achúcarro, J.-O. Gong, S. Hardeman, G. A. Palma, and S. P. Patil, "Mass hierarchies and nondecoupling in multi-scalar-field dynamics," *Physical Review D*, vol. 84, Aug 2011. 33

[66] A. Achucarro, J.-O. Gong, S. Hardeman, G. A. Palma, and S. P. Patil, "Features of heavy physics in the CMB power spectrum," *JCAP*, vol. 1101, p. 030, 2011. 33, 37, 44, 57, 63, 64, 74

[67] S. Céspedes and G. A. Palma, "Cosmic inflation in a landscape of heavy-fields," *Journal of Cosmology and Astroparticle Physics*, vol. 2013, p. 051–051, Oct 2013. 35, 57, 74

[68] A. Hetz and G. A. Palma, "Sound Speed of Primordial Fluctuations in Supergravity Inflation," *Phys. Rev. Lett.*, vol. 117, no. 10, p. 101301, 2016. 37, 41, 78, 79, 84

[69] V. Aragam, S. Paban, and R. Rosati, "The Multi-Field, Rapid-Turn Inflationary Solution," *JHEP*, vol. 03, p. 009, 2021. 38, 89

[70] J.-O. Gong, "Multi-field inflation and cosmological perturbations," *International Journal of Modern Physics D*, vol. 26, p. 1740003, Jan 2017. 42

[71] S. Groot Nibbelink and B. J. W. van Tent, "Scalar perturbations during multiple field slow-roll inflation," *Class. Quant. Grav.*, vol. 19, pp. 613–640, 2002. 42

[72] M. Sasaki and E. D. Stewart, "A General analytic formula for the spectral index of the density perturbations produced during inflation," *Prog. Theor. Phys.*, vol. 95, pp. 71–78, 1996. 42, 63

[73] D. Langlois and S. Renaux-Petel, "Perturbations in generalized multi-field inflation," *JCAP*, vol. 0804, p. 017, 2008. 42, 63

[74] S. Garcia-Saenz, S. Renaux-Petel, and J. Ronayne, "Primordial fluctuations and non-Gaussianities in sidetracked inflation," *JCAP*, vol. 1807, no. 07, p. 057, 2018. 42, 43, 62, 64, 67, 73, 74, 84, 86

[75] A. Achúcarro, V. Atal, C. Germani, and G. A. Palma, "Cumulative effects in inflation with ultra-light entropy modes," *Journal of Cosmology and Astroparticle Physics*, vol. 2017, p. 013–013, Feb 2017. 42

[76] C. Gordon, D. Wands, B. A. Bassett, and R. Maartens, "Adiabatic and entropy perturbations from inflation," *Phys. Rev.*, vol. D63, p. 023506, 2001. 43, 63

[77] A. Achucarro, V. Atal, S. Cespedes, J.-O. Gong, G. A. Palma, and S. P. Patil, "Heavy fields, reduced speeds of sound and decoupling during inflation," *Phys. Rev.*, vol. D86, p. 121301, 2012. 44, 57, 63, 64, 74

[78] S. Cespedes, V. Atal, and G. A. Palma, "On the importance of heavy fields during inflation," *JCAP*, vol. 1205, p. 008, 2012. 44, 57, 63

[79] S. Renaux-Petel and K. Turzynski, "Geometrical Destabilization of Inflation," *Phys. Rev. Lett.*, vol. 117, no. 14, p. 141301, 2016. 44, 63, 196

[80] C. Vafa, "The String landscape and the swampland," 2005. 44

[81] H. Ooguri and C. Vafa, "On the Geometry of the String Landscape and the Swampland," *Nucl. Phys.*, vol. B766, pp. 21–33, 2007. 45, 74

[82] R. Bousso, "A covariant entropy conjecture," *Journal of High Energy Physics*, vol. 1999, p. 004–004, Jul 1999. 45

[83] P. Agrawal, G. Obied, P. J. Steinhardt, and C. Vafa, "On the cosmological implications of the string swampland," *Physics Letters B*, vol. 784, p. 271–276, Sep 2018. 46

[84] R. Bravo, G. A. Palma, and S. Riquelme, "A Tip for Landscape Riders: Multi-Field Inflation Can Fulfill the Swampland Distance Conjecture," 2019. 46, 74

[85] S. Weinberg, "The cosmological constant problem," *Rev. Mod. Phys.*, vol. 61, pp. 1–23, Jan 1989. 47

[86] G. 't Hooft, "Naturalness, chiral symmetry, and spontaneous chiral symmetry breaking," *NATO Sci. Ser. B*, vol. 59, pp. 135–157, 1980. 47

[87] A. Hook, "Tasi lectures on the strong cp problem and axions," 2021. 47

[88] J. Wess and B. Zumino, "Supergauge transformations in four dimensions," *Nuclear Physics B*, vol. 70, no. 1, pp. 39–50, 1974. 48

[89] D. V. Volkov and V. P. Akulov, "Possible universal neutrino interaction," *JETP Lett.*, vol. 16, pp. 438–440, 1972. 48

[90] D. Z. Freedman, P. van Nieuwenhuizen, and S. Ferrara, "Progress toward a theory of supergravity," *Phys. Rev. D*, vol. 13, pp. 3214–3218, Jun 1976. 48

[91] S. Deser and B. Zumino, "Consistent Supergravity," *Phys. Lett. B*, vol. 62, p. 335, 1976. 48

[92] M. Yamaguchi, "Supergravity-based inflation models: a review," *Classical and Quantum Gravity*, vol. 28, p. 103001, Apr 2011. 49, 54

[93] M. B. Green, J. H. Schwarz, and E. Witten, *Superstring theory. Vol.2: Loop amplitudes, anomalies and phenomenology.* 7 1988. 49, 50

[94] L. Álvarez Gaumé, C. Gómez, and R. Jimenez, "Minimal inflation," *Physics Letters B*, vol. 690, p. 68–72, Jun 2010. 50

[95] L. Álvarez Gaumé, C. Gómez, and R. Jimenez, "A minimal inflation scenario," *Journal of Cosmology and Astroparticle Physics*, vol. 2011, p. 027–027, Mar 2011. 50

[96] A. Achucarro, S. Mooij, P. Ortiz, and M. Postma, "Sgoldstino inflation," *JCAP*, vol. 1208, p. 013, 2012. 50

[97] A. Borghese, D. Roest, and I. Zavala, "A geometric bound on f-term inflation," *Journal of High Energy Physics*, vol. 2012, Sep 2012. 50

[98] D. Roest, M. Scalisi, and I. Zavala, "Kähler potentials for Planck inflation," *JCAP*, vol. 11, p. 007, 2013. 50, 83, 108

[99] M. Kawasaki, M. Yamaguchi, and T. Yanagida, "Natural chaotic inflation in supergravity," *Physical Review Letters*, vol. 85, p. 3572–3575, Oct 2000. 50, 54

[100] R. Kallosh and A. Linde, "New models of chaotic inflation in supergravity," *JCAP*, vol. 11, p. 011, 2010. 50, 54, 89, 203

[101] M. B. Einhorn and D. R. Timothy Jones, "Inflation with non-minimal gravitational couplings in supergravity," *Journal of High Energy Physics*, vol. 2010, Mar 2010. 50

[102] S. Ferrara, R. Kallosh, A. Linde, A. Marrani, and A. Van Proeyen, "Jordan frame supergravity and inflation in the nmssm," *Physical Review D*, vol. 82, Aug 2010. 50

[103] H. M. Lee, "Chaotic inflation in jordan frame supergravity," *Journal of Cosmology and Astroparticle Physics*, vol. 2010, p. 003–003, Aug 2010. 50

[104] S. Ferrara, R. Kallosh, A. Linde, A. Marrani, and A. Van Proeyen, "Superconformal symmetry, nmssm, and inflation," *Physical Review D*, vol. 83, Jan 2011. 50

[105] R. Kallosh, A. Linde, and T. Rube, "General inflaton potentials in supergravity," *Physical Review D*, vol. 83, Feb 2011. 51, 54, 83, 95, 108

[106] S. Ferrara, R. Kallosh, and A. Linde, "Cosmology with nilpotent superfields," *Journal of High Energy Physics*, vol. 2014, Oct 2014. 51, 95, 108

[107] D. Baumann and L. McAllister, "Inflation and string theory," 2014. 52, 198

[108] E. J. Copeland, A. R. Liddle, D. H. Lyth, E. D. Stewart, and D. Wands, "False vacuum inflation with einstein gravity," *Phys. Rev. D*, vol. 49, pp. 6410–6433, Jun 1994. 52

[109] M. K. Gaillard, H. Murayama, and K. A. Olive, "Preserving flat directions during inflation," *Physics Letters B*, vol. 355, no. 1, pp. 71–77, 1995. 52

[110] C. Kolda and J. March-Russell, "Supersymmetric d-term inflation, reheating, and affleck-dine baryogenesis," *Physical Review D*, vol. 60, May 1999. 52

[111] N. Arkani-Hamed, H.-C. Cheng, P. Creminelli, and L. Randall, "Pseudonatural inflation," *JCAP*, vol. 07, p. 003, 2003. 52

[112] L. McAllister and E. Silverstein, "String cosmology: a review," *General Relativity and Gravitation*, vol. 40, p. 565–605, Jan 2008. 53

[113] D. V. Nanopoulos, K. A. Olive, M. Srednicki, and K. Tamvakis, "Primordial Inflation in Simple Supergravity," *Phys. Lett. B*, vol. 123, pp. 41–44, 1983. 54

[114] B. A. Ovrut and P. J. Steinhardt, "Supersymmetry and inflation: A new approach," *Physics Letters B*, vol. 133, no. 3, pp. 161–168, 1983. 54

[115] A. B. Goncharov and A. D. Linde, "Chaotic Inflation in Supergravity," *Phys. Lett. B*, vol. 139, pp. 27–30, 1984. 54

[116] G. B. Gelmini, C. Kounnas, and D. V. Nanopoulos, "Primordial inflation with flat supergravity potentials," *Nuclear Physics*, vol. 250, pp. 177–198, 1985. 54

[117] H. Murayama, H. Suzuki, T. Yanagida, and J. Yokoyama, "Chaotic inflation and baryogenesis in supergravity," *Physical Review D*, vol. 50, p. R2356–R2360, Aug 1994. 54

[118] P. Binétruy and G. Dvali, "D-term inflation," *Physics Letters B*, vol. 388, p. 241–246, Nov 1996. 54

[119] E. Halyo, "Hybrid inflation from supergravity d-terms," *Physics Letters B*, vol. 387, p. 43–47, Oct 1996. 54

[120] A. D. Linde, "A New Inflationary Universe Scenario: A Possible Solution of the Horizon, Flatness, Homogeneity, Isotropy and Primordial Monopole Problems," *Phys.Lett.*, vol. B108, pp. 389–393, 1982. 56

[121] T. Bjorkmo, "Rapid-Turn Inflationary Attractors," *Phys. Rev. Lett.*, vol. 122, no. 25, p. 251301, 2019. 57, 62, 79, 89

[122] A. Berera, "Warm inflation solution to the eta problem," p. AHEP2003/069, 2004. [PoSAHEP2003,069(2003)]. 57

[123] M. Bastero-Gil, A. Berera, R. O. Ramos, and J. G. Rosa, "Towards a reliable effective field theory of inflation," 2019. 57

[124] I.-S. Yang, "Strong multifield slowroll condition and spiral inflation," *Physical Review D*, vol. 85, Jun 2012. 58

[125] A. R. Brown, "Hyperbolic Inflation," *Phys. Rev. Lett.*, vol. 121, no. 25, p. 251601, 2018. 62, 84

[126] T. Bjorkmo and M. C. D. Marsh, "Hyperinflation generalised: from its attractor mechanism to its tension with the "swampland conditions"," *JHEP*, vol. 04, p. 172, 2019. 62, 79, 89

[127] P. Christodoulidis, D. Roest, and E. I. Sfakianakis, "Scaling attractors in multi-field inflation," *Journal of Cosmology and Astroparticle Physics*, pp. 059–059, 2019. 62, 78

[128] P. Christodoulidis, D. Roest, and E. I. Sfakianakis, "Attractors, Bifurcations and Curvature in Multi-field Inflation," *JCAP*, vol. 08, p. 006, 2020. 62, 80, 82

[129] A. Achucarro, V. Atal, and Y. Welling, "On the viability of $m^2\phi^2$ and natural inflation," *JCAP*, vol. 1507, p. 008, 2015. 64, 67, 73

[130] A. Achúcarro, E. J. Copeland, O. Iarygina, G. A. Palma, D.-G. Wang, and Y. Welling, "Shift-symmetric orbital inflation: Single field or multifield?," *Phys. Rev. D*, vol. 102, no. 2, p. 021302, 2020. 64, 67, 73, 74, 80

[131] A. Achucarro and Y. Welling, "Orbital Inflation: inflating along an angular isometry of field space," 2019. 64, 79, 84

[132] L. Covi, M. Gomez-Reino, C. Gross, J. Louis, G. A. Palma, and C. A. Scrucca, "Constraints on modular inflation in supergravity and string theory," *JHEP*, vol. 08, p. 055, 2008. 64

[133] G. Barenboim and W.-I. Park, "Spiral Inflation," *Phys. Lett.*, vol. B741, pp. 252–255, 2015. 67, 73

[134] J. J. Blanco-Pillado, C. P. Burgess, J. M. Cline, C. Escoda, M. Gomez-Reino, R. Kallosh, A. D. Linde, and F. Quevedo, "Racetrack inflation," *JHEP*, vol. 11, p. 063, 2004. 67, 73

[135] V. Aragam, S. Paban, and R. Rosati, "Multi-field Inflation in High-Slope Potentials," *JCAP*, vol. 04, p. 022, 2020. 67, 73, 75, 79

[136] S. K. Garg and C. Krishnan, "Bounds on Slow Roll and the de Sitter Swampland," *JHEP*, vol. 11, p. 075, 2019. 78, 81

[137] D. I. Kaiser and E. I. Sfakianakis, "Multifield Inflation after Planck: The Case for Nonminimal Couplings," *Phys. Rev. Lett.*, vol. 112, no. 1, p. 011302, 2014. 78

[138] P. Christodoulidis, D. Roest, and R. Rosati, "Many-field Inflation: Universality or Prior Dependence?," *JCAP*, vol. 04, p. 021, 2020. 78, 80

[139] X. Chen, G. A. Palma, B. Scheihing Hitschfeld, and S. Sypsas, "Reconstructing the Inflationary Landscape with Cosmological Data," *Phys. Rev. Lett.*, vol. 121, no. 16, p. 161302, 2018. 78

[140] X. Chen, G. A. Palma, W. Riquelme, B. Scheihing Hitschfeld, and S. Sypsas, "Landscape tomography through primordial non-Gaussianity," *Phys. Rev. D*, vol. 98, no. 8, p. 083528, 2018. 78

[141] A. Slosar *et al.*, "Scratches from the Past: Inflationary Archaeology through Features in the Power Spectrum of Primordial Fluctuations," *Bull. Am. Astron. Soc.*, vol. 51, no. 3, p. 98, 2019. 78

[142] M. Braglia, X. Chen, and D. K. Hazra, "Comparing multi-field primordial feature models with the Planck data," *JCAP*, vol. 06, p. 005, 2021. 78

[143] M. Braglia, X. Chen, and D. K. Hazra, "Primordial Standard Clock Models and CMB Residual Anomalies," 8 2021. 78

[144] J. Fumagalli, S. Renaux-Petel, J. W. Ronayne, and L. T. Witkowski, "Turning in the landscape: a new mechanism for generating Primordial Black Holes," 4 2020. 78

[145] M. Braglia, D. K. Hazra, F. Finelli, G. F. Smoot, L. Sriramkumar, and A. A. Starobinsky, "Generating PBHs and small-scale GWs in two-field models of inflation," *JCAP*, vol. 08, p. 001, 2020. 78

[146] G. A. Palma, S. Sypsas, and C. Zenteno, "Seeding primordial black holes in multifield inflation," *Phys. Rev. Lett.*, vol. 125, no. 12, p. 121301, 2020. 78

[147] L. Anguelova, "On Primordial Black Holes from Rapid Turns in Two-field Models," *JCAP*, vol. 06, p. 004, 2021. 78

[148] E. Barausse *et al.*, "Prospects for Fundamental Physics with LISA," *Gen. Rel. Grav.*, vol. 52, no. 8, p. 81, 2020. 78

[149] J. Fumagalli, S. Renaux-Petel, and L. T. Witkowski, "Oscillations in the stochastic gravitational wave background from sharp features and particle production during inflation," *JCAP*, vol. 08, p. 030, 2021. 78

[150] J. Fumagalli, S. e. Renaux-Petel, and L. T. Witkowski, "Resonant features in the stochastic gravitational wave background," *JCAP*, vol. 08, p. 059, 2021. 78

[151] G. Domènech, "Scalar Induced Gravitational Waves Review," *Universe*, vol. 7, no. 11, p. 398, 2021. 78

[152] L. Pinol, "Multifield inflation beyond $N_{\rm field} = 2$: non-Gaussianities and single-field effective theory," *JCAP*, vol. 04, p. 002, 2021. 79

[153] S. V. Ketov, "Multi-Field versus Single-Field in the Supergravity Models of Inflation and Primordial Black Holes," *Universe*, vol. 7, no. 5, p. 115, 2021. 84

[154] R. Kallosh, A. Linde, and B. Vercnocke, "Natural Inflation in Supergravity and Beyond," *Phys. Rev. D*, vol. 90, no. 4, p. 041303, 2014. 89, 204, 205

[155] G. Germán, J. C. Hidalgo, F. X. Linares Cedeño, A. Montiel, and J. A. Vázquez, "Simple supergravity model of inflation constrained with Planck 2018 data," *Phys. Rev. D*, vol. 101, no. 2, p. 023507, 2020. 89, 206

[156] R. Blumenhagen, A. Font, M. Fuchs, D. Herschmann, and E. Plauschinn, "Towards Axionic Starobinsky-like Inflation in String Theory," *Phys. Lett. B*, vol. 746, pp. 217–222, 2015. 89, 206

[157] Y. Aldabergenov, "Volkov–Akulov–Starobinsky supergravity revisited," *Eur. Phys. J. C*, vol. 80, no. 4, p. 329, 2020. 89, 203

[158] J. J. Blanco-Pillado, C. P. Burgess, J. M. Cline, C. Escoda, M. Gomez-Reino, R. Kallosh, A. D. Linde, and F. Quevedo, "Racetrack inflation," *JHEP*, vol. 11, p. 063, 2004. 89, 211

[159] R.Rosati, "Inflation.jl – a julia package for numerical evaluation of cosmic inflation models using the transport method," July 2020. 90

[160] E. Cremmer, S. Ferrara, C. Kounnas, and D. V. Nanopoulos, "Naturally Vanishing Cosmological Constant in N=1 Supergravity," *Phys. Lett. B*, vol. 133, p. 61, 1983. 100

[161] J. Calderón-Infante, A. M. Uranga, and I. Valenzuela, "The Convex Hull Swampland Distance Conjecture and Bounds on Non-geodesics," *JHEP*, vol. 03, p. 299, 2021. 109

[162] J. P. Conlon and F. Quevedo, "Kahler moduli inflation," *JHEP*, vol. 01, p. 146, 2006. 109

[163] J. R. Bond, L. Kofman, S. Prokushkin, and P. M. Vaudrevange, "Roulette inflation with Kahler moduli and their axions," *Phys. Rev. D*, vol. 75, p. 123511, 2007. 109

[164] J. J. Blanco-Pillado, D. Buck, E. J. Copeland, M. Gomez-Reino, and N. J. Nunes, "Kahler Moduli Inflation Revisited," *JHEP*, vol. 01, p. 081, 2010. 109

[165] D. Andriot, "Tachyonic de Sitter Solutions of 10d Type II Supergravities," *Fortsch. Phys.*, vol. 69, no. 7, p. 2100063, 2021. 109

[166] R. Arnowitt, S. Deser, and C. W. Misner, "Republication of: The dynamics of general relativity," *General Relativity and Gravitation*, vol. 40, p. 1997–2027, Aug 2008. 112

[167] R. Arnowitt, S. Deser, and C. W. Misner, "Canonical variables for general relativity," *Phys. Rev.*, vol. 117, pp. 1595–1602, Mar 1960. 113

[168] A. Vilenkin, "The Interpretation of the Wave Function of the Universe," *Phys. Rev. D*, vol. 39, p. 1116, 1989. 119, 120, 152, 155, 175, 178, 179, 180

[169] B. S. DeWitt, "Quantum theory of gravity. i. the canonical theory," *Phys. Rev.*, vol. 160, pp. 1113–1148, Aug 1967. 120

[170] A. Vilenkin, "Boundary conditions in quantum cosmology," *Phys. Rev. D*, vol. 33, pp. 3560–3569, Jun 1986. 120

[171] L. D. Landau and E. M. Lifschits, *The Classical Theory of Fields*, vol. Volume 2 of *Course of Theoretical Physics*. Oxford: Pergamon Press, 1975. 123, 127

[172] M. P. Ryan and L. C. Shepley, *Homogeneous Relativistic Cosmologies*. Princeton Series in Physics, Princeton: Princeton University Press, 1975. 123, 140

[173] H. Stephani, D. Kramer, M. MacCallum, C. Hoenselaers, and E. Herlt, *Exact Solutions of Einstein's Field Equations*. Cambridge Monographs on Mathematical Physics, Cambridge University Press, 2 ed., 2003. 123

[174] L. Bianchi, "Sugli spazi a tre dimensioni che ammettono un gruppo continuo di movimenti," *Memorie della Societa Italiana delle Scienze. detta dei XL. (3)*, vol. 11, pp. 267–352, 1897. 123

[175] L. D. Landau and E. M. Lifschits, *The Classical Theory of Fields*, vol. Volume 2 of *Course of Theoretical Physics*. Oxford: Pergamon Press, 1975. 123, 125, 127

[176] C. W. Misner, K. S. Thorne, and J. A. Wheeler, *Gravitation*. San Francisco: W. H. Freeman, 1973. 123, 134, 185

[177] E. Kasner, "Geometrical theorems on Einstein's cosmological equations," *Am. J. Math.*, vol. 43, pp. 217–221, 1921. 123

[178] V. Belinsky, I. Khalatnikov, and E. Lifshitz, "A General Solution of the Einstein Equations with a Time Singularity," *Adv. Phys.*, vol. 31, pp. 639–667, 1982. 123, 124, 131, 141, 142, 144, 153, 171, 174, 183, 185, 186, 188, 214

[179] A. Kirillov, "On the nature of the spatial distribution of metric inhomogeneities in the general solution of the einstein equations near a cosmological singularity," *Journal of Experimental and Theoretical Physics*, vol. 76, pp. 355–358, 01 1993. 123, 141, 142, 176

[180] G. Montani, "On the general behaviour of the universe near the cosmological singularity," *Classical and Quantum Gravity*, vol. 12, pp. 2505–2517, 1995. 123, 141, 144, 147, 175, 185, 187, 188

[181] G. Montani, M. V. Battisti, R. Benini, and G. Imponente, *Primordial cosmology*. Singapore: World Scientific, 2009. 123, 125, 127, 133, 134, 138, 139, 141, 142, 144, 147, 151, 153, 171, 174

[182] G. Imponente and G. Montani, "Covariance of the mixmaster chaoticity," *Physical Review D*, vol. 63, Mar 2001. 123, 171

[183] R. Arnowitt, S. Deser, and C. W. Misner, "Canonical variables for general relativity," *Phys. Rev.*, vol. 117, pp. 1595–1602, Mar 1960. 123

[184] V. Belinsky, I. Khalatnikov, and E. Lifshitz, "Oscillatory approach to a singular point in the relativistic cosmology," *Adv. Phys.*, vol. 19, pp. 525–573, 1970. 123, 131, 140, 151, 153, 174, 176, 183, 185, 186, 188

[185] C. W. Misner and A. H. Taub, "A singularity-free empty universe," *Sov.Phys. JETP*, vol. 28, p. 122, 1969. 124, 151, 152

[186] J. Wainwright and A. Krasinski, "Republication of: Geometrical theorems on einstein's cosmological equations (by e. kasner)," *General Relativity and Gravitation*, vol. 40, pp. 865–876, 2008. 127

[187] V. A. Belinski, "On the cosmological singularity," *International Journal of Modern Physics D*, vol. 23, p. 1430016, Jun 2014. 132, 141

[188] R. Kuzmin, "Sur un probleme de Gauss," *Atti del Congresso Internazionale dei Matematici, Bologna*, vol. 6, p. 83, 1928. 132

[189] E. M. Lifshitz, I. M. Lifshitz, and I. M. Khalatnikov, "Asymptotic analysis of oscillatory mode of approach to a singularity in homogeneous cosmological models," *Journal of Experimental and Theoretical Physics*, 1970. 133, 139, 151, 170, 175, 188

[190] A. H. Taub, "Empty space-times admitting a three parameter group of motions," *Annals Math.*, vol. 53, pp. 472–490, 1951. 139

[191] S. Bonanos, "On the stability of the taub universe," *Communications in Mathematical Physics*, vol. 22, pp. 190–222, 1971. 139

[192] E. M. Lifshitz and I. M. Khalatnikov, "Investigations in relativistic cosmology," *Adv. Phys.*, vol. 12, pp. 185–249, 1963. 140, 142, 213, 214

[193] M. Ryan, "The oscillatory regime near the singularity in bianchi-type ix universes," *Annals of Physics*, vol. 70, pp. 301–322, 04 1972. 140

[194] G. Montani, M. V. Battisti, R. Benini, and G. Imponente, "Classical and quantum features of the mixmaster singularity," *International Journal of Modern Physics A*, vol. 23, p. 2353–2503, Jul 2008. 141

[195] V. Belinsky and I. Khalatnikov, "General solution of the gravitational equations with a physical oscillatory singularity," *Soviet Physics JETP*, vol. 32, pp. 169–172, 1971. 141

[196] V. Belinsky, I. Khalatnikov, and L. E.M., "Construction of a general cosmological solution of the einstein equation with a time singularity," *Soviet Physics JETP*, vol. 35, p. 838, 1972. 141

[197] B. K. Berger, "Approach to the singularity in spatially inhomogeneous cosmologies," in *1999 UAB-GIT International Conference on Differential Equations and Mathematical Physics*, 6 2001. 141

[198] B. K. Berger, D. Garfinkle, J. Isenberg, V. Moncrief, and M. Weaver, "The singularity in generic gravitational collapse is spacelike, local and oscillatory," *Modern Physics Letters A*, vol. 13, p. 1565–1573, Jun 1998. 141

[199] J. D. Barrow and F. J. Tipler, "Analysis of the generic singularity studies by belinskii, khalatnikov, and lifschitz," *Physics Reports*, vol. 56, pp. 371–402, 1979. 141

[200] A. Kirillov and A. Kochnev, "Cellular structure of space in the vicinity of a time singularity in the einstein equations," *Pis ma Zhurnal Eksperimental noi i Teoreticheskoi Fiziki*, vol. 46, pp. 345–348, 10 1987. 141, 144, 175, 185

[201] V. Belinskii, "Turbulence of a gravitational field near a cosmolological singularity," *JETP*, vol. 56, no. 9, p. 421, 1992. 141, 144

[202] J. D. Barrow, "Multifractality in the general cosmological solution of Einstein's equations," *Phys. Rev. D*, vol. 102, no. 4, p. 041501, 2020. 141

[203] A. A. Kirillov and G. Montani, "Quasi isotropization of the inhomogeneous mixmaster universe induced by an inflationary process," *Phys. Rev. D*, vol. 66, p. 064010, 2002. 141

[204] G. Imponente and G. Montani, "Classical and quantum behavior of the generic cosmological solution," *AIP Conference Proceedings*, 2006. 141, 144

[205] M. V. Battisti, R. Belvedere, and G. Montani, "Semiclassical suppression of weak anisotropies of a generic universe," *EPL (Europhysics Letters)*, vol. 86, p. 69001, Jun 2009. 152, 153, 172, 188

[206] M. De Angelis and G. Montani, "Dynamics of quantum anisotropies in a taub universe in the wkb approximation," *Physical Review D*, vol. 101, May 2020. 152, 188

[207] L. Agostini, F. Cianfrani, and G. Montani, "Probabilistic interpretation of the wave function for the bianchi i model," *Phys. Rev. D*, vol. 95, p. 126010, Jun 2017. 152, 180

[208] H. R. Lewis and W. B. Riesenfeld, "An Exact quantum theory of the time dependent harmonic oscillator and of a charged particle time dependent electromagnetic field," *J. Math. Phys.*, vol. 10, pp. 1458–1473, 1969. 158

[209] H. R. Lewis, "Classical and quantum systems with time-dependent harmonic-oscillator-type hamiltonians," *Phys. Rev. Lett.*, vol. 18, pp. 510–512, Mar 1967. 158, 159

[210] H. R. Lewis, "Class of exact invariants for classical and quantum time-dependent harmonic oscillators," *J. Math. Phys.*, vol. 9, pp. 1976–1986, 1968. 158, 159, 166

[211] I. A. Pedrosa, "Exact wave functions of a harmonic oscillator with time-dependent mass and frequency," *Phys. Rev. A*, vol. 55, pp. 3219–3221, Apr 1997. 158

[212] E. W. Kolb and M. S. Turner, *The Early Universe*, vol. 69. 1990. 167

[213] S. W. Hawking and R. Penrose, "The Singularities of gravitational collapse and cosmology," *Proc. Roy. Soc. Lond. A*, vol. 314, pp. 529–548, 1970. 174

[214] C. W. Misner, "Quantum cosmology. 1.," *Phys. Rev.*, vol. 186, pp. 1319–1327, 1969. 174, 176

[215] R. Benini and G. Montani, "Inhomogeneous Quantum Mixmaster: from Classical toward Quantum Mechanics," *Class. Quant. Grav.*, vol. 24, pp. 387–404, 2007. 174

[216] A. Ashtekar, A. Henderson, and D. Sloan, "A Hamiltonian Formulation of the BKL Conjecture," *Phys. Rev. D*, vol. 83, p. 084024, 2011. 174

[217] S. Antonini and G. Montani, "Singularity-free and non-chaotic inhomogeneous Mixmaster in polymer representation for the volume of the universe," *Phys. Lett. B*, vol. 790, pp. 475–483, 2019. 174

[218] J. D. Barrow, "Chaotic behavior in general relativity," *Phys. Rept.*, vol. 85, pp. 1–49, 1982. 187

[219] U. Seljak, "Measuring polarization in the cosmic microwave background," *The Astrophysical Journal*, vol. 482, p. 6–16, Jun 1997. 196

[220] M. Kamionkowski, A. Kosowsky, and A. Stebbins, "A probe of primordial gravity waves and vorticity," *Physical Review Letters*, vol. 78, p. 2058–2061, Mar 1997. 196

[221] M. Kamionkowski, A. Kosowsky, and A. Stebbins, "Statistics of cosmic microwave background polarization," *Physical Review D*, vol. 55, p. 7368–7388, Jun 1997. 196

[222] M. Sasaki, "Large Scale Quantum Fluctuations in the Inflationary Universe," *Progress of Theoretical Physics*, vol. 76, pp. 1036–1046, 11 1986. 197

[223] M. Sasaki, "Gauge-Invariant Scalar Perturbations in the New Inflationary Universe," *Progress of Theoretical Physics*, vol. 70, pp. 394–411, 08 1983. 197

[224] V. F. Mukhanov, "Quantum Theory of Gauge Invariant Cosmological Perturbations," *Sov. Phys. JETP*, vol. 67, pp. 1297–1302, 1988. 197

[225] N. D. Birrell and P. C. W. Davies, *Quantum Fields in Curved Space*. Cambridge Monographs on Mathematical Physics, Cambridge University Press, 1982. 197

[226] W. H. Kinney, "Horizon crossing and inflation with large η," *Physical Review D*, vol. 72, Jul 2005. 198